
Precision Matters: Measurement of the W boson mass and width with the ATLAS detector at $\sqrt{s} = 7$ TeV and the activity of the Underlying Event in Z boson events at $\sqrt{s} = 13$ TeV

*Dissertation
zur Erlangung des Grades
"Doktor der Naturwissenschaften"*

Fachbereich Physik, Mathematik und Informatik
Johannes Gutenberg Universität, Mainz

Lennart Adam

geb. in Worms
Mainz, den 05.02.2021

1. Berichterstatter:

████████████████████

2. Berichterstatter:

████████████████████

Datum der mündlichen Prüfung: 05.02.2021

Ownership declaration

Hereby I, Lennart Adam, declare that I have completed the present thesis, entitled: *Precision Matters: Measurement of the W boson mass and width with the ATLAS detector at $\sqrt{s} = 7$ TeV and the activity of the Underlying Event in Z boson events at $\sqrt{s} = 13$ TeV* independently, making use only of the specified literature and aids. It is entirely the product of my own doctoral work, unless stated otherwise.

Mainz, den 15.10.2020

Signature

© Lennart Adam 2020

Abstract

The Standard Model is today the most powerful theory to describe and predict the behaviour and quantities of elementary particles. A set of free parameters are not directly predicted, but linked via quantum physics relations to other quantities of the Standard Model. Precise measurements of these parameters are therefore crucial to probe the Standard Model and serve as a test of its consistency. The mass of the W boson plays a key role among these parameters, because the theoretical prediction currently outperforms the precision of its experimentally measured value. It is therefore a natural target to probe for a possible tension, which could yield hints to new physics. This thesis presents an improved measurement of the mass of the W boson with the ATLAS detector at a centre-of-mass energy of 7 TeV. The legacy ATLAS measurement is re-evaluated using a profile likelihood ratio fit. An improvement of about 2 MeV on the uncertainty is accomplished and sets the path for the target precision. The introduced fit method enhances the sensitivity of the measurement and allows a first determination of the decay width of the W boson with LHC data. The precision of the width measurement is compatible to the current world average and provides an additional parameter for the consistency tests. The second part of this thesis presents measurements of charged-particle distributions sensitive to the properties of the underlying event in events containing a Z boson decaying into a muon pair at a centre-of-mass energy of 13 TeV. The measurement is a standard candle for hadron-colliders and serves as ancillary measurement for the future measurement of the mass of the W boson. The measured distributions provide crucial feedback to the tested Monte Carlo generators, which will in turn promote the measurement of the transverse momentum of the W boson.

Keywords: Drell-Yan, Underlying Event, W boson mass, W boson width, ATLAS experiment

Zusammenfassung

Das Standard Model der Elementarteilchenphysik ist bis zum heutigen Tag die mächtigste Theorie zur Beschreibung der Eigenschaften und Reaktionen von Elementarteilchen. Einige Parameter des Modells werden nicht direkt vorhergesagt, sind aber über Quantenkorrekturen untereinander verknüpft. Präzisionsmessungen dieser Parameter testen daher die intrinsische Konsistenz des Standard Modells. Die Messung der Masse des W Bosons trägt in diesem Zusammenhang eine Schlüsselrolle, da die theoretische Vorhersage wesentlich genauer ist als die aktuell beste Messung. Sie ist daher geeignet, um mögliche Widersprüche zwischen Messung und Theorie herauszuarbeiten und Ansätze für neue Physik zu offenbaren. Diese Dissertation stellt eine verbesserte Messung der Masse des W Bosons mit dem ATLAS Detektor bei einer Schwerpunktsenergie von 7 TeV vor. Die Originalmessung wird mit einem Profile Likelihood Fit neu evaluiert. Mit dieser Neuerung wird die Unsicherheit der Messung um etwa 2 MeV verbessert und bestätigt den Erfolg des Ansatzes. Die neue Fitmethode verbessert außerdem die Sensitivität auf die Zerfallsbreite des W Bosons und erlaubt dessen erste Messung am LHC. Die Präzision ist vergleichbar mit der des aktuellen globalen Mittelwerts und bietet einen weiteren Parameter für Konsistenztests. Der zweite Teil dieser Arbeit ist eine Messung von Verteilungen geladener Teilchen, die sensitiv auf die Eigenschaften des Underlying Event sind. Diese Verteilungen werden in Kollisionsereignissen bei einer Schwerpunktsenergie von 13 TeV gemessen, in denen ein Z Boson produziert wurde, das in ein Myonenpaar zerfällt. Es handelt sich um eine Standardmessung für Hadronen-Beschleuniger und dient als Ergänzungsmessung für die zukünftigen Messungen der Masse und Zerfallsbreite des W Bosons. Die gemessenen Verteilungen werden außerdem als Richtwert für Monte Carlo Generatoren verwendet.



Contents

1	Introduction	2
I	Common theoretical and instrumental concepts	6
2	Theoretical Background for High Energy Physics	8
2.1	The Standard Model of particle physics	8
2.1.1	The elementary building blocks	8
2.1.2	The quantitative picture and calculus of the Standard Model	10
2.2	The Electroweak sector	12
2.2.1	Quantum-electrodynamics and local gauge symmetry	12
2.2.2	The electroweak unification	13
2.2.3	Spontaneous Symmetry Breaking of the electroweak sector	15
2.3	Quantum-Chromo-Dynamics	17
2.4	Probing Standard Model physics in proton-proton collisions	18
2.4.1	General phenomenology of pp collisions	18
2.4.2	The proton structure captured in Parton Distribution Functions	19
2.4.3	The hard scattering process and vector boson production	20
2.4.4	Transverse momentum of vector bosons	22
2.4.5	Decay kinematics of vector bosons	23
2.4.6	The soft part of the collision - the underlying event	24
2.5	Limitations of the Standard Model	25
2.6	Objectives of precision measurements	26
3	Experimental Setup	30
3.1	The Large Hadron Collider	30
3.1.1	The accelerator complex	30
3.1.2	Beam characteristics and luminosity	31
3.2	A Thoroidal LHC AparatuS (ATLAS) - the giant	33
3.2.1	The Inner Detector	34
3.2.2	The calorimeters	36
3.2.3	The Muon spectrometer	37
3.2.4	Object reconstruction	38
3.2.5	The Trigger system	42
4	Event Simulation	44
4.1	The hard process: Matrix Element and parton showers	44
4.2	The soft parts and its parameters	46
4.2.1	Hadronization models	46
4.2.2	The Multi-parton interaction (MPI) models	47
4.3	Detector Simulation with GEANT4	48
4.4	Detector Corrections and Uncertainty Estimation	49
4.4.1	Inner Detector Tracking Performance and related Uncertainties for the 2015 dataset	49

4.4.2	Muon reconstruction performance and related systematic uncertainties	51
4.4.3	Pile Up correction	53
4.4.4	Beam spot size (primary vertex reconstruction)	54
II	On the road to precision with the ATLAS experiment	56
5	Reanalysis of the W boson mass and a first measurement of its width with the ATLAS detector	58
5.1	Motivation to re-analyze the m_W measurement	58
5.2	Overview and measurement strategy	60
5.3	Signal process selection	63
5.3.1	Event selection	63
5.3.2	Muon selection	63
5.3.3	Hadronic recoil reconstruction	64
5.3.4	W boson candidate selection	64
5.4	Data and Monte-Carlo simulation samples	65
5.4.1	The 2011 pp collision data	65
5.4.2	Simulation setup for the signal process	66
5.4.3	Simulation setup for the background processes	67
5.4.4	Validation of the re-analysis selection criteria	68
5.5	Data-based background estimation for Multi-Jet contribution	70
5.5.1	Event yield of the multi-jet (MJ) background	70
5.5.2	Shape construction of the MJ background	72
5.6	Physics modelling corrections	73
5.6.1	Electroweak Corrections	73
5.6.2	Rapidity and angular coefficient corrections	74
5.6.3	Boson transverse momentum corrections	74
5.6.4	Reweighting procedure	75
5.6.5	Uncertainties in the QCD modelling	76
5.7	Detector calibrations for the muon reconstruction	77
5.7.1	Muon momentum scale calibration	78
5.7.2	Muon selection efficiency	79
5.8	Detector calibrations for the hadronic recoil	80
5.8.1	Modelling of the event activity	80
5.8.2	Response corrections	82
5.9	The template fits	82
5.9.1	The legacy χ^2 -fit approach	83
5.9.2	General aspects of the Profile Likelihood fit	86
5.9.3	Implementation of the Profile Likelihood Ratio (PLH)-fit	87
5.9.4	Template fits with a PLH: Morphing	88
5.9.5	Validation of the reanalysis process	91
5.9.6	Migration of the legacy uncertainties to the PLH fit approach	92
5.10	First results for m_W using a PLH fit	93
5.11	Measuring Γ_W using a PLH fit	98
5.11.1	Adaptions for the Γ_W fit setup	98
5.11.2	First results for Γ_W using a PLH fit	99
5.12	Conclusion for the measurements of m_W and Γ_W	101

6	Measurement of the activity of the Underlying Event	104
6.1	Motivation and Outline	104
6.2	Measurement strategy for the Underlying Event (UE) activity	106
6.2.1	Becoming sensitive to the UE: UE regions	106
6.2.2	Observables sensitive to the activity of the UE	107
6.2.3	Enhancing MPI sensitivity: Transverse Thrust	108
6.3	Data and Monte-Carlo simulation samples	111
6.3.1	Event and object selection	111
6.3.2	The 2015 <i>pp</i> collision data	114
6.3.3	Setup of the Monte-Carlo generators	115
6.3.4	Background processes	117
6.3.5	Control distributions	119
6.4	Correction to particle level: Unfolding	120
6.4.1	Unfolding preparations: Monte-Carlo corrections	120
6.4.2	Bayesian iterative unfolding	120
6.4.3	Non-fiducial signal correction and event efficiency correction	123
6.4.4	The response matrix and number of iterations	124
6.4.5	Unfolding validation	127
6.5	Pile-up correction via unfolding	130
6.5.1	Consistency validation: Pile-up intervals	130
6.5.2	Data-driven pile-up correction: The HBOM algorithm	131
6.6	Uncertainties	136
6.6.1	Statistical Uncertainties	136
6.6.2	Systematic Uncertainties	136
6.6.3	Relative uncertainties and discussion	139
6.7	Unfolded observables and comparison with model predictions	142
6.7.1	Underlying-event activity as a function of p_T^Z	142
6.7.2	Differential distributions and generator performance	147
6.7.3	Comparison with other centre-of-mass energies	159
6.8	Conclusion	160
7	Conclusion and final remarks	164
	Acknowledgement	167
III	Appendix	170
	References	181
	List of Figures	189
	List of Tables	191
	List of Abbreviations	196
A	Track reconstruction with irradiated sensors	197
A.1	A model for pixel digitization including radiation damage effects	197
A.1.1	Radiation damage effects	197
A.1.2	Interpolation method for an irradiated electric field	198

B	Additional material for the measurement of m_W and Γ_W	200
B.1	Validation of the reanalysis process	200
B.2	Ranking plots for the measurement of m_W using a profile likelihood ratio fit	200
B.3	First results for Γ_W using a profile likelihood ratio fit in m_T	202
C	Additional material for the measurement of the UE activity	204
C.1	Convention for the visualization of the UE activity	204
C.2	The HBOM algorithm	205
C.2.1	Validation of the HBOM Algorithm	205
D	Curriculum vitae	208

1.

Introduction

Curiosity and the fundamental desire to understand the world and its guiding principles are an innate quality of mankind. A simple example is a three-year-old, who is repeatedly asking 'Why?' and questions even the most ordinary matters. The mature equivalent is maybe a particle physicist, because the explanation of some process is often deduced from its substructure, and the elementary constituents of matter should naturally represent the end of the chain of reasoning.

The Standard Model (SM) of particle physics provides the best description of the elementary particles and their interactions until the present day. It was developed in the 1960's and confirmed in many experiments. The last milestone, which experimentally completed the theory predictions, was the discovery of the Higgs boson [1, 2] in 2012. Particle physics entered a new era of exploration with this discovery, because no other new particles are predicted by the SM, although many questions are left unanswered. For instance, the SM does not explain, why is there a preponderance of matter over antimatter or what is the nature of dark matter.

Therefore the SM is obviously not complete. There are experiments, which perform direct searches for other non-SM particles, in order to probe extensions of the SM. But consistency tests of the SM represent a different, rather primordial approach to carve out the shortcomings of the theory. They are driven by precision measurements of the SM parameters and serve as a powerful tool to assess the validity of the theory.

The quantities of the elementary particles, such as mass and life-time, and the coupling constants, which describe the interaction strengths, are the input parameters for the consistency tests of the SM. The Large Hadron Collider (LHC) is the largest particle collider in the world and operates at unprecedented collision energies. These are needed to produce heavy, elementary particles. The particles or rather their decay products are measured with the ATLAS detector. This thesis presents a set of measurements, which either directly contribute to the precision tests or support future precision measurements. The first two measurements presented in Chapter 5 determine the mass m_W and the decay width Γ_W of the W boson. These two values are of great importance to the consistency tests. The heart of the analysis is the evaluation of a new fit approach, which on one hand improves the legacy measurement of m_W , and on the other hand provides sufficient sensitivity to allow the first measurement of Γ_W at the LHC. The second major content of this thesis is the measurement of the activity of the underlying event (UE) in Z boson events in Chapter 6, which was published in [3]. The UE accumulates the majority of the low-energetic processes in a proton-proton (pp) collision. It is an irreducible background to hadron collider observables and the measurement is a standard candle for any hadron collider. The setting in this thesis is on one hand optimized to reduce the related uncertainties on the measurement of m_W . On the other hand, specialized observables are introduced to improve the sensitivity to certain subprocesses of the UE, namely multiple parton interaction (MPI).

This thesis starts in Chapter 2 to equip the reader with the fundamentals of the SM theory concept. The focus is set on the interdependencies of the different parameters and highlights open questions.

Any valid theory is required to withstand experimental tests. These are conducted

with the ATLAS detector at the LHC in the scope of this thesis. Chapter 3 introduces the basic concepts of the collider and highlights the functionality of the detector. It emphasizes the reconstruction of muons and charged particles with the ATLAS detector, which are essential to the presented measurements.

The introductory part is completed with Chapter 4. It elaborates the functionality of Monte-Carlo simulations. They are the essential link between the theory predictions and the actual measurement in the context of High Energy Physics (High Energy Physics). The Monte-Carlo simulation generators transform the theoretical predictions into explicit quantities, which are compatible with the measurement.

The measurements of m_W and Γ_W are presented in Chapter 5. The chapter starts with a brief overview of the measurement principle and subsequently sketches the different calibrations and uncertainty estimates, which are needed for the competitive precision of both measurements.

Chapter 6 follows a similar structure, in order to guide to the measurement of the UE activity. It emphasizes the enhanced sensitivity to individual processes contributing to the UE. Only a fraction of all results is presented to sustain a better clarity.

The final conclusion in Chapter 7 sets the results of this thesis into context with ongoing measurements.



Part I

Common theoretical and instrumental concepts



2.

Theoretical Background for High Energy Physics

The Standard Model of Particle Physics is one of the most successful theories in modern physics, because it provides all predictions for the processes on smallest scales. So far, all expectations meet the experimental results. However, the opposite statement is not true: Several details and observations lack of an explanation by the SM in its current formulation. The most prominent one are the hints of dark matter or the matter-anti-matter-asymmetry in our universe. It is therefore obvious, that the SM is not yet the full story of particle physics. This thesis provides inputs and support measurements for an important consistency test of the SM in the electroweak sector.

The theoretical introduction of this chapter equips the reader with the basic concepts of the SM theory, i.e. a simple introduction of its elementary particles and their relations (Sec. 2.1). The theoretical foundation of the different forces is sketched to motivate different aspects of the final measurements (Sec. 2.2 and Sec. 2.3). The principle of electroweak symmetry breaking is presented, because it yields the relations among the free parameters of the SM for the consistency tests.

This thesis focuses on LHC data recorded with the ATLAS detector, therefore different aspects of pp -collision phenomenology are illustrated in the final section, Sec. 2.4. The theoretical introduction of this chapter concludes with the limitations of the SM and the corresponding role of precision measurements to tackle these frontiers (Sec. 2.5 and Sec. 2.6).

2.1 The Standard Model of particle physics

2.1.1 The elementary building blocks

It appeals to the human perception to build everything from elementary building blocks, because one could conclude, that all properties are hence deducible from the blueprint. The SM provides the toolkit to build matter objects out of a finite number of elementary particles.

The SM distinguishes two classes of elementary particles: fermions and bosons. The first ones are characterized by half-integer spin and henceforth obey the Fermi-Dirac statistics [4]. The fermions are the building blocks of matter.

The bosons with an integer spin are the mediator particles. They are exchanged among the fermions and mediate at least three out of four fundamental forces. The one, which is not confirmed, is gravity. It is not described in the context of the SM. To present knowledge, the gravitational force is negligible in the scales of elementary particles, which are discussed within the scope of this thesis. It is a subject of present research to incorporate Gravity into the picture of the SM.

Nevertheless, three forces are described within the SM driving the elementary interactions: the electromagnetism, the weak and the strong force. All three of them are discussed in dedicated sections (Sec. 2.2 and Sec. 2.3). A key principle of the SM is, that each force carrier couples to particles, only if they carry the corresponding charge. The photon or γ transmits the electromagnetic force and acts on particles with the non-zero electromagnetic charge Q . The W and Z bosons are the mediators of the weak interaction and couple to particles with non-vanishing weak isospin T . In contrast to the photon, they are massive particles with a rather short lifetime.

This fact limits the weak interaction to be present only at short ranges. The strong interaction is also present only on subatomic scales. The gluons mediate the strong force and couple to the colour charge of a particle. They further carry this kind of charge themselves, so that they are self-interacting, which is believed to cause the short range of the strong force. The colour charge is depicted in three different types, red, green and blue. The unique feature, which motivates the naming of the colour charge, is the analogy of additive colour mixing, while the electromagnetic charge and the isospin are represented with rational numbers and obey the corresponding addition theorems. The combination of one red, one blue and one green charge adds up to a colourless or colour-neutral state, which is then left untouched by the strong force.

The class of fermions is further subdivided in quarks and leptons. Each of these is structured in three generations ordered in mass and particular charges. The generations hold similar characteristics and are represented by two particles. The lepton generations are electrons (e), muons (μ) and taus (τ). All of them have a neutrino partner of the corresponding lepton flavour. The neutrino masses are still unknown, but upper limits are set by present experiments [5]. The neutrinos carry a weak isospin, but are neutral with respect to other charges. Hence, they interact only via the weak force. Electron, muon and tau leptons also interact with the W and Z bosons and couple additionally to the photon due to their electromagnetic charge.

The three quark generations consist of quark pairs, namely up-, down-quark and charm-, strange-quark and bottom-, top-quark. All of these carry an electromagnetic charge, weak isospin and colour. Hence, they couple to all four types of force mediator bosons, γ , W , Z and gluons. Only the first generation of leptons is stable and represents the matter of everyday life. The particles of higher generations are heavier and decay into the lighter ones.

The last piece of the SM toolkit is the Higgs boson. It introduces mass to all particles within the SM via the concept of the electroweak-symmetry breaking also known as Higgs mechanism [6]. The latter one yields implicit relations among the SM particle properties, which motivate the studies detailed in Chapter 5.

Figure 2.1 illustrates all elementary particles of the SM and their corresponding properties, such as their rest masses. The figure emphasizes the structure of classes and generations. The masses and coupling strengths are not determined within the formalism of the SM. They are free parameters and need to be provided by measurements to complete the theory. The measurement of the mass of the W boson is the anchor point of this thesis. It plays a special role among the free parameters of the SM, as m_W holds implicit links to the other parameters. The quantitative dependencies are outlined in detail in Sec. 2.2.3 and Sec. 2.6. A precise measurement of m_W serves as a consistency check for the up to now most successful theory, the SM.

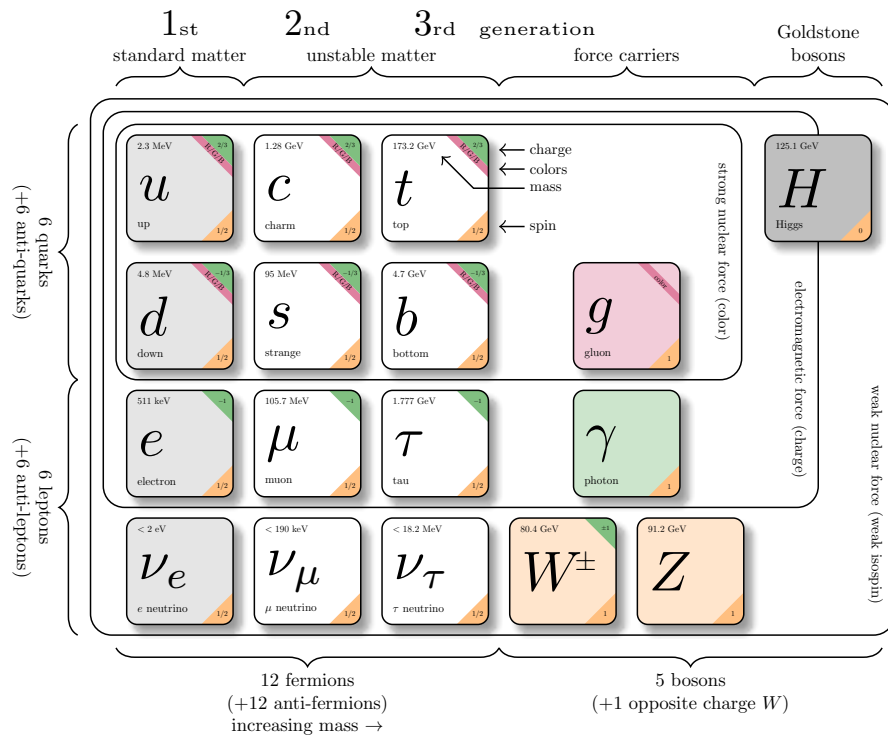


Figure 2.1: Summary table of all SM particles ordered in the different families. The surrounding black rectangles indicate to which force the fermions on the left couple. The figure is based on [7].

2.1.2 The quantitative picture and calculus of the Standard Model

The previous section introduced the actors playing a role in the SM of particle physics. The yet missing part are the interactions between them.

The SM is a gauge quantum field theory. It contains the symmetries of the unitary product group of

$$SU(3)_C \times SU(2)_L \times U(1)_Y \quad (2.1)$$

The fundamental objects, i.e. the elementary particles introduced in Sec. 2.1.1, represent excitations of the different quantum fields. Fermions are described by Dirac-spinors $\psi(x)$, while gauge bosons are described by vector fields $A_\mu(x)$. The dynamics of the quantum fields and states are determined by the Lagrangian density (short Lagrangian or \mathcal{L}). The *principle of least action* allows to derive the Euler-Lagrange equations or the equations of motion respectively from the Lagrangian. A key principle of the SM is, that the Lagrangian of the SM holds the differentiable symmetries mentioned above. In other words, the Lagrangian is invariant under some types of field variations ($\Phi + \delta\Phi$). Therefore, there must exist a conserved quantity following Noether's theorem, namely the different charges. A representative example is given in Sec. 2.2.1, which exemplifies the occurrence of the electromagnetic charge, when demanding the local gauge invariance.

The symmetries in 2.1 correspond to the different forces and each one is associated to a certain charge. The $SU(3)$ symmetry describes the Quantum Chromodynamics (QCD), the theory framework of the strong force. It conserves the colour charge (C). The electroweak sector represents the unification of the electromagnetism and the

weak forces. It is invariant under $SU(2)_L \times U(1)_Y$. The force couples to the weak hypercharge (Y). The index L refers to the fact, that the weak force acts only on left-handed particles. The following sections specify these symmetry considerations to express the corresponding SM Lagrangian. Also the peculiarities of the different forces will be sketched.

The Lagrangian defines, which particle interactions are allowed in the SM. The probability for the possible interactions to take place are derived via the Feynman rules, which are themselves determined by the Lagrangian. The mathematical expressions are usually illustrated with Feynman diagrams [8]. They present a fundamental process, which contributes to the matrix element amplitude. Fermi's golden rule connects the matrix element amplitude with the available phase space and calculates the cross-section of a specific process. The cross-section σ is the quantity, which can be measured in experiments.

All possible Feynman diagrams have to be taken into account to calculate the exact amplitude of a process. The processes illustrated in Fig. 2.2 present the same initial and final state, and therefore both contribute to the same processes. The number of vertices of a Feynman diagram defines its order, which reflects the suppression of the contribution as power of the coupling constant α . The full cross-section σ is described as an expansion of all orders:

$$\sigma = \sum_{n=1}^A \sigma^{(n)} \alpha^n \quad (2.2)$$

with A being the highest of available coefficients $\sigma^{(n)}$. The ideal case would be $A \rightarrow \infty$, but the current research provides calculations up to the range of third order. The example in Fig. 2.2 (a) presents a Leading order (LO) diagram ($n = 1$), while Fig. 2.2 (b) is a Next-to-Next-to-Leading order (NNLO) diagram ($n = 2$). Lower orders serve as an approximation of the process, because the higher the order the lower its contribution to the matrix element due to the suppression by α^n with $\alpha < 1$.

Loop diagrams of higher orders, such as the example in Fig. 2.2 (b), lead to divergences in the calculation of $\sigma^{(n)}$, when the integration covers all possible momenta of the loop particles. The cut-off scale Λ tames these divergences by setting a limit for the energy scale of the integrated particle momenta. The calculation of its infinite limit is determined at the end of the integration process. The divergent terms are realized as corrections $\delta\alpha$ to the coupling constant:

$$\alpha_{physical} = \alpha + \delta\alpha \quad (2.3)$$

The infinite limit of $\delta\alpha$ is compensated by infinities of the bare coupling constant, which yields the physically measured value. The compensating effects are e.g. illustrated by charge-screening due to the vacuum polarization. The result is depicted as renormalized coupling constant. The scale Λ can be adapted to the referred force, e.g. Λ_{QCD} . The process links the measured finite coupling to the occurring infinities in the calculation. The corresponding corrections create a dependency of the coupling constant on the momentum transfer Q^2 . It is further accompanied by a second but unphysical renormalization scale μ_R . The cross-section calculation depends on the choice of μ_R for a finite number of orders ($\alpha_S(\mu_R^2)$), but the dependency vanishes in the sum of all orders. The inclusion of higher order diagrams lowers the dependency on μ_R . This scale dependency is usually considered as theoretical uncertainty on the process.

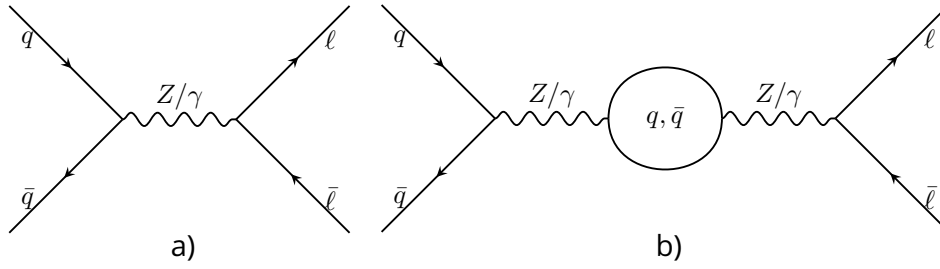


Figure 2.2: (a) The lowest order diagram for the Drell-Yan process, usually referred to as LO diagram. (b) Higher order correction with a virtual fermion loop. It corresponds to a NNLO correction.

2.2 The Electroweak sector

2.2.1 Quantum-electrodynamics and local gauge symmetry

The Quantum Electrodynamics (QED) is the modern correspondence of the classical theory of electromagnetism, which was firstly formulated by James Clerk Maxwell around 1860. The QED describes the interaction of electromagnetically charged fermions and photons, or in other words light and matter. In the following, it will be exemplarily illustrated, how the Lagrangian of the QED evolves from the equation of motion of free particles. The key requirement is local gauge invariance, a fundamental principle of the SM. The same principle could be transferred to the other forces, but it will not be illustrated in similar detail. The chain of reasoning presented here follows Ref.[9].

A free fermion of mass m , which is described by the fermion field $\psi(x)$, obeys the Dirac equation ¹:

$$(i\gamma^\mu \partial_\mu - m)\psi(x) = 0 \quad (2.4)$$

It is linked to the following Lagrangian:

$$\mathcal{L} = \bar{\psi}(x)(i\gamma^\mu \partial_\mu - m)\psi(x) \quad (2.5)$$

The notation follows the literature with γ^μ representing the Gamma matrices.

A local phase transformation is presented with the following substitution:

$$\psi(x) \rightarrow \psi'(x) = e^{i\alpha(x)}\psi(x) \quad (2.6)$$

It would spoil the global $U(1)$ symmetry of Eq. 2.5, if this substitution is applied on its own. Hence, also the derivative is replaced by the covariant derivative (\mathcal{D}_μ) in order to maintain the invariance under the local gauge transformation:

$$\partial_\mu \rightarrow \mathcal{D}_\mu = \partial_\mu + iQA_\mu(x) \quad (2.7)$$

Noether's theorem argues that Q is a conserved charge. It is identified as the electromagnetic charge. The required invariance introduces also the gauge field $A_\mu(x)$, which appears to be the photon field. It transforms as:

$$A_\mu(x) \rightarrow A'_\mu(x) = A_\mu - \frac{1}{Q}\partial_\mu\alpha(x) \quad (2.8)$$

¹a relativistic wave equation derived by Paul Dirac in 1928

The final Lagrangian of the QED emerges, when Eq. 2.7 is inserted into Eq. 2.5. Furthermore, the kinetic term $\frac{1}{4}F_{\mu\nu}F^{\mu\nu}$ has to be added, where $F_{\mu\nu} = \partial_\mu A_\nu - \partial_\nu A_\mu$. It represents the photon propagator and allows the photon to be massless and free:

$$\mathcal{L}_{\text{QED}} = \bar{\psi}(i\gamma^\mu\partial_\mu - m)\psi - Q\bar{\psi}\gamma^\mu A_\mu\psi - \frac{1}{4}F_{\mu\nu}F^{\mu\nu} \quad (2.9)$$

The full Lagrangian is invariant under local phase transformations. The first part still resembles the Dirac equation and hence the propagation of a fermion. The important consequence is the middle term, which describes the interaction of this fermion (ψ) with the photon field, A_μ . The fact, that the photon is massless agrees with the infinite range of the electromagnetic force, as it was already described in the classical theory.

Demanding local gauge invariance under a certain symmetry introduces further bosonic fields for the weak and the strong force. The latter one requires a non-Abelian $SU(3)$ symmetry, while the weak interaction and QED are united obeying the invariance under the non-Abelian $SU(2) \times U(1)$ symmetry. The following chapters, Sec. 2.2.2 and Sec. 2.3, explain the corresponding consequences, but avoid a detailed derivation.

2.2.2 The electroweak unification

The previous chapter introduced the QED to demonstrate the appearance of bosonic fields, if local gauge invariance is demanded for a Lagrangian. However, in the scope of high energy physics QED emerges in the electroweak theory. The electromagnetic and the weak force unify into one above a certain energy threshold. This unification and its consequences are explained in the following.

The development of a theory framework of the weak force was motivated by experimental results in the first half of the twentieth century. The tables turned, when the final formulation predicted new massive gauge bosons, which were confirmed by experiment several decades later.

The weak theory started with Enrico Fermi explaining the β -decay of the Neutron with a new force. Later the Wu-Experiment [10] proved, that this weak force violates parity and couples only to left-handed fermions and right-handed anti-fermions. The latter fact lead to the suggestion by Feynman and Gell-Mann to employ a *vector minus axial-vector* (V-A) or left-handed Lagrangian for the weak force. Finally, Glashow, Weinberg and Salam unified the weak and electromagnetic force to the electroweak one. This is therefore also known as *GWS-model*. The formerly mentioned electromagnetic charge Q is described as a linear combination of the weak hypercharge Y and a component of the weak isospin T . The weak hypercharge Y results from a local gauge invariance under $U(1)$ of the corresponding Lagrangian. The concept to incorporate the local $U(1)$ is inspired by the formalism used for the QED. And the weak isospin T is the charge related to a $SU(2)$ symmetry. The latter symmetry is needed for a doublet describing the left-handed particles and right-handed anti-particles respectively. The combination of both symmetries is the $SU(2)_L \times U(1)_Y$.

The corresponding gauge transformation is defined for left and right handed spinors independently:

$$\begin{aligned} \psi_L &\rightarrow \psi'_L = e^{i\theta(x)T + i\beta(x)Y} \psi_L \\ \psi_R &\rightarrow \psi'_R = e^{i\beta(x)Y} \psi_R \end{aligned} \quad (2.10)$$

where the left and right-handed components are derived from the Dirac spinor ψ by:

$$\begin{aligned}\psi_L &= \frac{1}{2}(1 - \gamma_5)\psi \\ \psi_R &= \frac{1}{2}(1 + \gamma_5)\psi\end{aligned}\quad (2.11)$$

The transformation $\beta(x)$ is equal to the illustration in Sec. 2.2.1. The local parameters β and θ are arbitrary. The weak isospin T is presented by the generators of $SU(2)$, $T_i = \sigma_i/2$, with σ_i being the Pauli matrices. The electromagnetic charge Q is constructed as:

$$Q = T_3 + \frac{Y}{2}\quad (2.12)$$

The covariant derivatives require then four gauge boson fields to maintain the local gauge invariance:

$$\begin{aligned}\mathcal{D}_\mu\psi_L(x) &= [\partial_\mu - igW_\mu(x) - ig'YB_\mu(x)]\psi_L(x) \\ \mathcal{D}_\mu\psi_R(x) &= [\partial_\mu - ig'YB_\mu(x)]\psi_L(x)\end{aligned}\quad (2.13)$$

The isotriplet W_μ consists of three components corresponding to the generators of $SU(2)$, $W_\mu = \frac{\sigma_i}{2}W_\mu^i(x)$. The related coupling constant for $SU(2)$ is g . B_μ is the isosinglet corresponding to the generators of $U(1)$ with the associated coupling constant g' .

The Lagrangian for the $SU(2) \times U(1)$ group is:

$$\mathcal{L}_{EWK} = i\bar{\psi}_L\gamma_\mu\mathcal{D}_\mu\psi_L + i\bar{\psi}_R\gamma_\mu\mathcal{D}_\mu\psi_R - \frac{1}{4}B_{\mu\nu}B^{\mu\nu} - \frac{1}{4}W_{\mu\nu}W^{\mu\nu}\quad (2.14)$$

The kinetic terms are defined as:

$$\begin{aligned}W_{\mu\nu}^i &= \partial_\mu W_\nu^i - \partial_\nu W_\mu^i + g\epsilon^{ijk}W_\mu^jW_\nu^k \\ B_{\mu\nu} &= \partial_\mu B_\nu - \partial_\nu B_\mu\end{aligned}\quad (2.15)$$

The characteristics of the isosinglet are already discussed in Sec. 2.2.1. A major difference for the isotriplet is the self-coupling expressed in the third term. The four generators of the symmetry group correspond to four *massless* gauge boson fields, $W_\mu^1, W_\mu^2, W_\mu^3, B_\mu$. The existence of any mass term would violate the gauge symmetry of the electroweak Lagrangian. The mixing of different gauge fields yields the physically observed boson fields and creates the already known electromagnetic field:

$$\begin{aligned}\begin{pmatrix} A_\mu \\ Z_\mu \end{pmatrix} &= \begin{pmatrix} \cos\theta_W & \sin\theta_W \\ -\sin\theta_W & \cos\theta_W \end{pmatrix} \begin{pmatrix} B_\mu \\ W_\mu^3 \end{pmatrix} \\ W_\mu^\pm &= \frac{1}{\sqrt{2}}(W_\mu^1 \mp iW_\mu^2)\end{aligned}\quad (2.16)$$

The rotation of B_μ and W_μ^3 into A_μ and Z_μ is described by the weak mixing angle θ_W . The mixing angle is a geometrical interpretation of the relation between the couplings of $SU(2)_L$, $U(1)_Y$ and the QED:

$$\begin{aligned}\sin^2\theta_W &\equiv \frac{g'^2}{g^2 + g'^2} = 1 - \frac{g^2}{g^2 + g'^2} = 1 - \frac{m_W^2}{m_Z^2} \\ \Rightarrow e &= g \sin\theta_W = g' \cos\theta_W\end{aligned}\quad (2.17)$$

The latter relation yields the more common presentation of the electromagnetic coupling constant α_{EM}^2 :

$$\alpha_{EM} \equiv \frac{e^2}{4\pi} = \frac{g^2 g'^2}{4\pi(g^2 + g'^2)}\quad (2.18)$$

²It is also referred to as the fine structure constant α .

The electromagnetic and weak (electroweak) gauge bosons hold two noticeable properties, which are related to self-coupling term: The W and Z both carry weak hypercharge, so that couple to each other. And the photon couples to the W bosons, as they carry the electromagnetic charge. They further differ from the photon with respect to their mass. As physical mass eigenstates are combinations of the massless fields, they should appear to be massless themselves. However, the fact, that the weak force is limited to short ranges, suggests that the force carriers are massive. This contradiction is resolved by spontaneous symmetry breaking of the electroweak gauge symmetry. The corresponding formalism is called the *Higgs mechanism*, which is briefly described in the following section.

2.2.3 Spontaneous Symmetry Breaking of the electroweak sector

The Higgs mechanism [6, 11] is attributed to Peter Higgs, Francois Englert and Robert Brout. It reveals, that a gauge boson can acquire mass, if it is coupled to a scalar field, that acquires a vacuum expectation value. It solves the conflict of the experimental observation of massive gauge bosons, which are predicted to be massless under the assumption of gauge invariance. The latter permits the simple inclusion of mass terms into the Lagrangian.

The electroweak Lagrangian introduced in Eq. 2.14 is extended with an additional complex scalar field ϕ . The simplest representation matching the $SU(2)_L$ symmetry is a doublet $\phi(x)$ obeying the following Lagrangian:

$$\phi(x) = \begin{pmatrix} \phi^{(+)}(x) \\ \phi^{(0)}(x) \end{pmatrix} \quad (2.19)$$

with $\phi^{(+)}$ presenting the charged part, while $\phi^{(0)}$ is neutral. Both fields carry a hypercharge of 1.

$$\begin{aligned} \mathcal{L}_{SSB} &= (\mathcal{D}_\mu \phi)^\dagger (\mathcal{D}^\mu \phi) - V(x) \\ &= (\mathcal{D}_\mu \phi)^\dagger (\mathcal{D}^\mu \phi) - \mu^2 \phi^\dagger \phi - \lambda (\phi^\dagger \phi)^2 \end{aligned} \quad (2.20)$$

The covariant derivatives are equal to the definition in Eq. 2.13 to preserve the invariance under $SU(2)_L \times U(1)_Y$. The last two terms in the second line describe the potential $V(x)$. It is shaped like a 'Mexican hat' (see illustration Fig. 2.3), if $\lambda > 0$ and $\mu^2 < 0$. The potential is unstable at its symmetric centre ($\phi(x=0)$), but there is an infinite number of stable minima on the circle in the $\phi^{(+)}, \phi^{(0)}$ -plane with the radius $-\frac{\mu^2}{\lambda} (= \phi^{(0)2} + \phi^{(+2)} \equiv \frac{\nu}{\sqrt{2}})$.

The system will choose one particular minimum as a ground state. The global rotational symmetry is henceforth broken by this choice, although the Lagrangian holds its symmetric properties. This process motivates the term of *spontaneous symmetry breaking* (SSB). The vacuum expectation value of the system is (by convention):

$$\langle |\phi| \rangle = \frac{\nu}{\sqrt{2}} \quad (2.21)$$

The scalar doublet can be parametrized by expanding ϕ about the vacuum expectation value. This expansion requires four real scalar fields. An appropriate $SU(2) \times U(1)$ gauge transformation eliminates three of these fields. These vanishing fields correspond to the so called *Goldstone* bosons in terms of the mechanism. The remaining scalar field is termed as *Higgs field*, $H(x)$. The parametrization of the doublet ϕ becomes:

$$\phi(x) = \frac{1}{\sqrt{2}} \begin{pmatrix} 0 \\ \nu + H(x) \end{pmatrix} \quad (2.22)$$

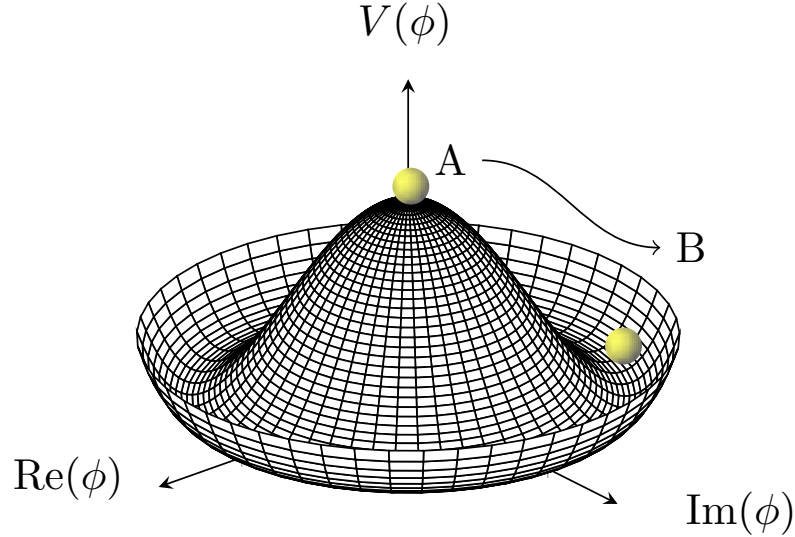


Figure 2.3: Illustration of the ‘Mexican hat’-shaped Higgs potential. The position A is the unstable symmetric center. As soon as the system transfers to position B somewhere on the circle of minima, the original symmetry will be broken.

The Higgs field describes the small deviations of ϕ from its vacuum expectation value. If the covariant derivatives in Eq. 2.20 act on the parametrization, the kinetic part of Lagrangian transforms into the following expression (when applying the representation of Z and A_μ from Eq. 2.16):

$$(\mathcal{D}_\mu \phi)^\dagger (\mathcal{D}^\mu \phi) \phi = \frac{1}{2} \partial_\mu H \partial^\mu H + (\nu + H)^2 \left(\frac{g^2}{4} W_\mu^\dagger W^\mu + \frac{g^2}{8 \cos^2 \theta_W} Z_\mu Z^\mu \right) \quad (2.23)$$

The last two terms reveal now a mass for the W and Z bosons, while the photon remains massless. Furthermore, the mass terms are related via the weak mixing angle:

$$m_Z \cos \theta_W = m_W = \frac{1}{2} \nu g \quad (2.24)$$

The full Higgs Lagrangian (\mathcal{L}_{SSB}) yields a mass term for the Higgs boson with:

$$m_H = \sqrt{-2\mu^2} = \nu \sqrt{2\lambda} \quad (2.25)$$

The parameters μ, λ, ν are not fixed by the theory and require a direct measurement. They can be expressed by a further relation, namely the Fermi constant G_F :

$$G_F \equiv \nu^{-2} = \frac{\lambda^2}{2|\mu^2|} \quad (2.26)$$

The discovery of the Higgs boson at the LHC [1, 2] confirmed its existence with $m_H = 125 \text{ GeV}$ and completed the electroweak sector.

Also the fermions appear to be massive, although it is not required by the theory so far. The observation of massive fermions is incorporated into the SM by coupling the fermion fields to the scalar fields ϕ as well. The corresponding Lagrangian is called the *Yukawa Lagrangian*. The fermion masses are proportional to the vacuum

expectation value of ϕ . The Yukawa coupling fixes the proportionality for each fermion field. All the fermion masses (or the Yukawa couplings) are further free parameters of the SM. However, the Yukawa Lagrangian is not further discussed, because this thesis focus on the relations of m_W .

2.3 Quantum-Chromo-Dynamics

The evolution of the Quantum Field Theory (QFT) of the strong force was initiated by the technical breakthroughs in accelerator and spectroscopy techniques. Back in the 1950's a continuously growing zoo of baryons and mesons was discovered. Murray Gell-Mann and George Zweig proposed, that all these particles are formed of more fundamental ones: the quarks [12, 13]. The properties of these bound states come with the need of an additional quantum number in order to comply with Pauli's exclusion principle. The new quantum number is termed today as *colour charge*, which motivates the term of *Quantum-Chromo-Dynamics* for the corresponding QFT. Colour charge exists in the quantities of *(anti-)red*, *(anti-)blue* and *(anti-)green*. The combination of all three colours or one colour and its anti-colour yields a colour-neutral state, which reasons the analogy from visible colours.

The number and properties of the newly discovered hadrons revealed an underlying $SU(3)$ symmetry for the quark interactions. The corresponding local gauge transformation of a quark field $q(x)$ is described as:

$$q(x) \rightarrow e^{-i\alpha_a(x)T_a(x)}q(x) \quad (2.27)$$

The $SU(3)$ symmetry group inherits eight generators. These are represented by the eight Gell-Mann matrices ($\lambda_a = 2T_a, a \in [1, \dots, 8]$), here combined with a scaling parameter α_a . The matrices hold the following commutation relation:

$$[\lambda^a, \lambda^b] = if^{abc}\lambda^c \quad (2.28)$$

where f^{abc} is the structure constant of the group. The generators correspond to eight bosonic fields in the context of a QFT. These fields are termed as *gluon* fields G_μ^a . The invariance under $SU(3)$ requires the following covariant derivative:

$$\partial_\mu q(x) \rightarrow \mathcal{D}_\mu q(x) = [\partial_\mu - ig_s Y T^a G_\mu^a(x)]q(x) \quad (2.29)$$

with g_s being the strong coupling constant. The coupling constant is usually referred to with an alternative expression, namely $\alpha_s \equiv g_s^2/4\pi$. Additionally, the gluon fields transform as:

$$G_\mu^a \rightarrow G_\mu^a - \frac{1}{g_s} \partial_\mu \alpha_a - f_{abc} \alpha_b G_\mu^c \quad (2.30)$$

The kinetic term of gluon fields is derived via the commutation relation of the covariant derivatives and yields the following gluon field strength tensor:

$$G_{\mu\nu}^a = \partial_\mu G_\nu^a - \partial_\nu G_\mu^a + g_s f^{abc} G_\mu^b G_\nu^c, \quad (2.31)$$

This merges into the final Lagrangian of the QCD:

$$\mathcal{L}_{\text{QCD}} = \sum_c \bar{q}_c (i\gamma^\mu \partial_\mu - m_c) q_c - g_s \sum_c \left(\bar{q}_c \gamma^\mu \frac{\lambda_a}{2} q_c \right) G_\mu^a - \frac{1}{4} G_{\mu\nu}^a G_a^{\mu\nu} \quad (2.32)$$

The first sum is already familiar from the Dirac equation, it describes the kinetic energy and mass (m_c) of the quark field q_c . The second sum represents the interaction

between quarks and the gluon fields. But the unique properties of the gluons are hidden in the last term. The expansion of the tensor product yields two different self-coupling terms for the gluons, but no mass term for the gluon fields.

The combination of massless force carriers and their self-interaction gives rise to the property known as *colour confinement*. There exist only colour-neutral bound states of quarks, and no singly colour-charged quarks are observed over large distances (> 1 fm) or small momentum transfer. The illustrative example is the separation of two quarks bound in a meson. The binding strength of the two quarks rises linearly with their spatial separation. Finally, if the continuous separation builds up more and more energy, the energy in the colour-connection is converted into a new quark-antiquark pair, which yields two mesons instead of two separated quarks. A further property of quarks and gluons exhibits at the other end of the interaction scale: the *asymptotic freedom*. Quarks act like quasi-free particles at large energies of the interaction scale between quarks and gluons (or at small length scales). In this case the coupling constant becomes small. The dependency of g_s on the interaction scale is also known as *running coupling*. When the coupling decreases, it is possible to approximate the calculation of the strong force via perturbation theory. Following the description from Sec. 2.1.2, it is legit, that an infinite number of terms is approximated accurately by a finite number of terms, if the coupling is reasonably small, which is true for g_s at small length scales. It is the driving technique to calculate observables in high energy physics and is referred to as *perturbative QCD*. If the length scale increases to the range of asymptotic freedom, the perturbative expansions fail to describe the QCD processes. The regime of low momentum transfer is therefore guided by experimental results and employs phenomenological models to describe QCD effects.

2.4 Probing Standard Model physics in proton-proton collisions

The LHC is the most powerful particle collider built by mankind until the present day. Its technical details are discussed in Sec. 3.1. This chapter sketches the theoretical approach to describe the particle collisions. The analysis in this thesis covers pure pp collision data. Therefore only pp interactions will be considered in the following.

2.4.1 General phenomenology of pp collisions

Protons are composite particles and own a complicated substructure. As a result, the signature of a pp collision is much more complex than e.g. an electron-positron collision. But measurements with hadron machines compensate with higher centre-of-mass energies and higher production rates for the heavy vector-bosons. Nevertheless, a good understanding of the proton itself is necessary to provide precision measurements. The proton substructure depends on how finely it is resolved. The coarse object is made of the three valence-quarks, two up- and one down-quark. These are tied together by exchanging gluons. Further virtual quark-antiquark pairs, the *sea* quarks, and gluons are contained in the proton. They become evident at smaller length scales and are subject to dynamic annihilation processes. The gluons split into quark-antiquark pairs, which either annihilate again or radiate additional gluons. The gluons couple to other gluons, which further complicates the substructure. All sub-particles of a proton are called *partons*. In general, the structure of a proton is driven by QCD processes at low-momentum transfer, which are described by phenomenological models, as they are not accessible via perturbative QCD.

A highly energetic pp collision at the LHC operates in the domain of asymptotic freedom. Some pp collisions at the LHC are energetic enough, that the colliding partons interact at small length scales and the corresponding coupling strength becomes small. Hence, perturbative QCD calculations are applicable to describe the parton-parton interaction. The corresponding process is termed as *hard scattering* and it is described with the momentum dependent cross-section. All other processes, which are involved in the collision, take place in a lower energetic and hence non-perturbative regime. They are described with the help of phenomenological models. These involve the progression of the proton remnants, i.e. the partons, which did not take part in the hard scattering. All partons are colour-charged and can radiate further gluons, which manifest subsequently in further quarks and finally hadrons. This cascade process is termed as *parton shower*. The parton shower and all colour-charged components of the collision terminate in the *hadronization*, i.e. the formation of new colour-neutral bound states.

All in all, a pp collision includes QCD processes at various interaction scales. In the theoretical description, these are disentangled in the different processes mentioned above. The factorization theorems [14, 15] allow to separate the calculation of the perturbatively-calculable parton cross-section from the long-distance processes. The calculation of the hard-scattering cross-section for the pp interaction ($\sigma_{pp \rightarrow X}$) splits then into the Parton Distribution Function (PDF), $f_i(x_i)$, and the cross-section of the hard subprocess ($\sigma_{ab \rightarrow X}$):

$$\sigma_{pp \rightarrow X} = \sum_{a,b} \int_0^1 dx_a dx_b f_a(x_a) f_b(x_b) \sigma_{ab \rightarrow X}(x_a, x_b) \quad (2.33)$$

a, b represent the colliding partons, i.e. quarks of different flavours or gluons, and the sum collects all possible combinations, which contribute to the process. All components depend on the momentum fractions $x_{a,b}$, which determine how much of the proton momentum the parton is carrying. The variable x is also known as the Bjorken scaling variable. The description treats the quarks as point-like particles. The integral in Eq. 2.33 summarizes all possible combinations of the distributed momentum. The determination of the corresponding PDF is explained in greater detail in Sec. 2.4.2. Section 2.4.3 discusses further details about the hard scattering and Sec. 2.4.6 outlines the soft contributions.

2.4.2 The proton structure captured in Parton Distribution Functions

The momentum of a proton is distributed among its partons. The parton momentum is therefore described as fraction x of the full proton momentum. The probability to find a parton carrying the momentum fraction x is summarized in the PDF ($f_i(x_i, Q^2)$ with $i = u, d, \dots, g$). These also depend on the momentum scale Q^2 of the corresponding process. The Q^2 dependence is captured in the DGLAP equation [16, 17, 18]. It provides the calculus for the PDF sets in combination with the Parisi-Altarelli splitting functions, but only for the perturbative regime. The state of the art are calculations at NNLO [19]. Fig. 2.4 presents the PDF predictions at two different momentum scales. The comparison of the figures highlights the increasing importance of the sea quark contributions at higher energy regimes.

However, PDF sets cannot be computed from first principles. They have to be extracted from the data, through a careful comparison of theoretical predictions and experimental results, because only the evolution but not the total numbers are captured in the theory. The most important input is up to the present day the Deep Inelastic Scattering (DIS) measurements conducted at HERA and recorded by H1 and ZEUS (a combination is presented in Reference [20]). Fixed target experiments are also

incorporated, in order to probe different regimes of x and Q^2 . Also the most recent LHC measurements like vector-boson asymmetries and differential cross-sections feedback the creation of PDF sets (see e.g. Reference [21])

The selection and method of combination varies among the different working groups, for instance the NNPDF collaboration applies neural networks for the combination. The choice and weighting of the different data sets play an important role, because some measurements contradict each other in their impact on the PDF sets (see for further details e.g. Ref.[22]). This illustrates the magnitude of theoretical uncertainty related to the choice of a PDF set.

The PDF of the proton is crucial to the final prediction of a parton scattering process, because the parton momentum affects the partonic cross-section and directly impacts the momentum of the final state.

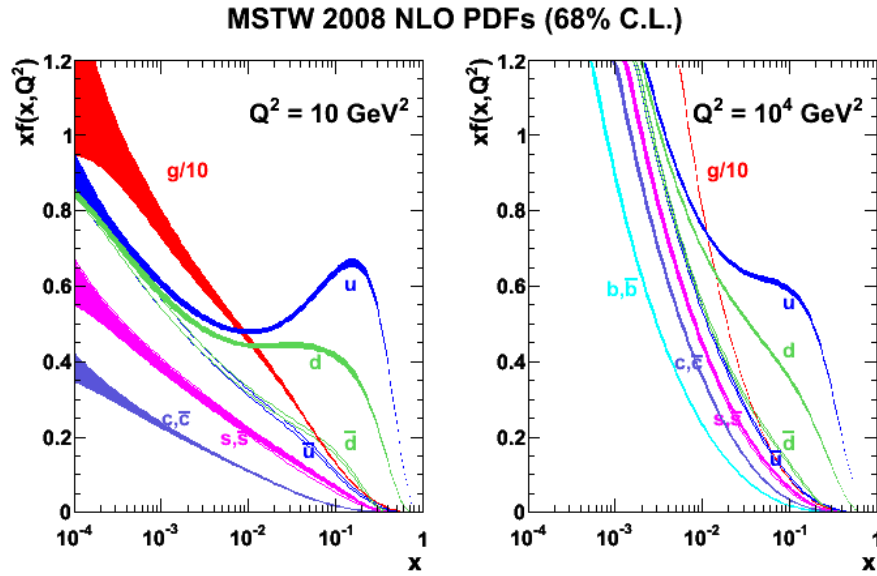


Figure 2.4: The PDF set MSTW 2008 NLOPDF provided by [23]. The form factor is presented in dependence of the Bjorken- x for different quark flavours and gluons. The left figure corresponds to $Q^2 = 10\text{GeV}^2$ and the right one to $Q^2 = 10^4\text{GeV}^2$.

2.4.3 The hard scattering process and vector boson production

The hard scattering process in a pp collision refers to the parton-parton interaction with the largest momentum transfer. Furthermore, the momentum transfer exceeds the scale of Λ_{QCD} , so that a perturbative calculation is possible. The partonic cross-section from Eq. 2.33 is then expressed in (infinite) orders of α_s :

$$\sigma_{ab \rightarrow X} = \sigma_0 + \alpha_s(\mu_R^2)\sigma_1 + \alpha_s^2(\mu_R^2)\sigma_2 + \dots \quad (2.34)$$

with μ_R being the renormalization scale of the running coupling.

It is not possible to unambiguously label the hard scattering process in the experiment, because it is rather an auxiliary term for the theory to separate the short and far range processes. Nevertheless, it is common to associate the most energetic collision product with the results of the hard scattering process. Here, the hard scattering process of interest is the creation (and subsequent decay) of a W or Z boson.

As a result the mass and transverse momentum serve as a reference for the initial momentum transfer.

The annihilation of a quark (q) and anti-quark (\bar{q}) dominates the production of the electroweak gauge bosons. Both quarks carry the same flavour in case of the Z boson creation, while the flavours are different and may also belong to different quark generations for the W boson creation. The anti-quark is always a sea-quark, while the second one belongs either to the valence or sea quarks. Their initial momenta, $x_q, x_{\bar{q}}$, determine the boost of the vector boson, which is exemplified in the following at lowest order in the centre-of-mass frame of the pp collision.

The lowest order of the partonic cross-section is:

$$\begin{aligned}\sigma_0^{q\bar{q}\rightarrow Z} &= \frac{\sqrt{2}\pi G_F m_Z^2}{3}(g^2 + g'^2) \\ \sigma_0^{q\bar{q}'\rightarrow W} &= \frac{\sqrt{2}\pi G_F m_W^2}{3}|V_{qq'}|^2\end{aligned}\quad (2.35)$$

with $V_{qq'}$ representing the corresponding entry of the Cabibbo-Kobayashi-Maskawa mixing matrix (CKM) matrix. The prime indicates a different quark flavour, but the notation is dropped in the following. The colliding partons are characterized with the four vectors (neglecting their rest mass):

$$\begin{aligned}p_q^\mu &= \frac{\sqrt{s}}{2}(x_q, 0, 0, x_q) \\ p_{\bar{q}}^\mu &= \frac{\sqrt{s}}{2}(x_{\bar{q}}, 0, 0, -x_{\bar{q}})\end{aligned}\quad (2.36)$$

The \sqrt{s} is the centre-of-mass energy and the relation between the pp and parton-parton collision energy is $\hat{s} = (p_1 + p_2)^2 = x_q x_{\bar{q}} s$. The rapidity y of the vector boson is constructed from its energy E and longitudinal momentum p_z . It can be related to the momentum fraction using four momenta of the partons ($V = W, Z$):

$$y = \frac{1}{2} \log \frac{E + p_z}{E - p_z} \Rightarrow x_q = \frac{m_V}{\sqrt{s}} e^y, \quad x_{\bar{q}} = \frac{m_V}{\sqrt{s}} e^{-y}\quad (2.37)$$

The final differential pp cross-section at lowest order is therefore:

$$\frac{d\sigma}{dy} = \frac{1}{s} \sum_{q,\bar{q}} \sigma_0^{q\bar{q}\rightarrow V} f_q(x_q, Q^2 = m_V^2) f_{\bar{q}}(x_{\bar{q}}, Q^2 = m_V^2)\quad (2.38)$$

The rapidity and invariant mass therefore probe different values of $x_{q,\bar{q}}$, because of the relation in Eq. 2.37. The relation reveals the possibility to constrain PDF sets by W and Z measurements. Or, the other way round, it highlights the sensitivity of the W measurement to the choice of the PDF set. Fig. 2.5 illustrates the case for two different PDF sets. It further underlines the difference of W^+ and W^- due to their creation with different valence quarks, u or d respectively.

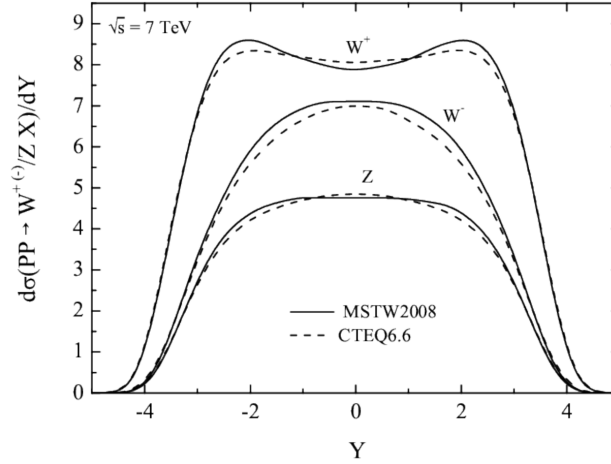


Figure 2.5: Rapidity Distribution for the leading-order production of Z and W bosons in $\sqrt{s} = 7$ TeV pp collisions. The differential cross-section is calculated with two different PDF sets.

2.4.4 Transverse momentum of vector bosons

The former illustration of the rapidity dependence neglects the transverse momentum of the vector bosons. In fact, if solely the leading order term would describe the physical case, the boson could not carry any transverse momentum due to momentum conservation. The higher order QCD and electroweak corrections provide additional particles, which recoil against the boson. This Initial State Radiation (ISR) induces a transverse momentum to the W and Z boson respectively. Exemplary processes are $q\bar{q} \rightarrow V + g$ or $qg \rightarrow V + q$, which are displayed as Feynman diagrams in Fig. 2.6. The colour-charged particles will hadronize and form *jets*, therefore the process is also referred to $V + n$ -*jets*, where n denotes the number of jets. The resummation of the leading logarithm terms in the perturbative calculations yields a differential p_T^V spectrum:

$$\frac{d\sigma}{d(p_T^V)^2} = \sigma \frac{d}{d(p_T^V)^2} \exp\left(-\frac{\alpha_S G_F}{2\pi} \log^2\left(\frac{m_V^2}{(p_T^V)^2}\right)\right) \quad (2.39)$$

However, it does not describe the lower p_T^V spectrum. The intrinsic parton momentum is of the order $k_T \approx 0.76$ GeV and it is not negligible in the lower regime of p_T^V . Moreover, the contributions from low energetic gluons is running into singularities for the calculation. The latter is handled with the parameter *infrared cut-off* and relies on tuning to experimental results. The corresponding details are specific to the different Monte-Carlo generators (see e.g. Sec. 5.4.2 Sec. 6.3.3).

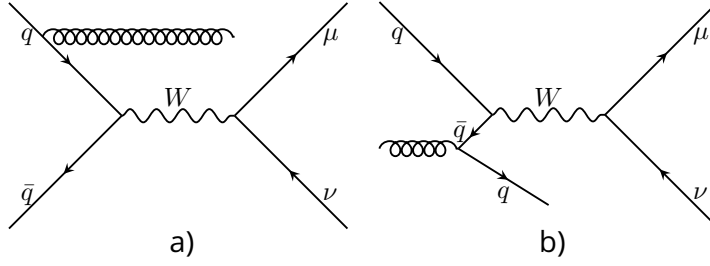


Figure 2.6: Production of the W at Next-to-Leading order (NLO) and its subsequent decay. The final state includes an additional (a) gluon or (b) quark, which manifest in jets within the detector. The recoil against the ISR initiates the transverse momentum of the vector-boson.

2.4.5 Decay kinematics of vector bosons

The properties of the vector bosons are derived from their decay products. The kinematic properties of these decay products are predominantly shaped by three effects: the initial momentum of the vector boson, its mass and spin correlations due to higher order effects.

The decay of a vector boson is a two-body decay, and the kinematics of the decay products depends on the available energy. Hence, the kinematics of the decay products are finally defined by the initial momentum and the mass of the boson. The initial momentum depends on the production via the colliding partons, but also the mass is subject to variations. The vector bosons are unstable and can be produced off-shell. The production cross-section (σ_W) is described by a Breit-Wigner distribution (here exemplarily for the W boson):

$$\sigma_W = \sigma_0 \frac{\hat{s} \Gamma_W^2}{(\hat{s} - m_W^2) + m_W^2 \Gamma_W^2} \quad (2.40)$$

The decay width Γ_W characterises the smearing of the possible off-shell mass values. It is the inverse of the lifetime ($\Gamma_W = 1/\tau_W$). The peak value of the production cross-section (σ_0) depends on the initial and final state, i.e. the production channel via fermion and anti-fermion ($((f\bar{f})_i)$), and the subsequent decay to fermion and anti-fermion ($((f\bar{f})_f)$):

$$\sigma_0 = \frac{12\pi}{m_W^2} \frac{\Gamma_W^{(f\bar{f})_i} \Gamma_W^{(f\bar{f})_f}}{\Gamma_W^2} \quad (2.41)$$

This thesis investigates solely the case for the decay into muon plus neutrino ($((f\bar{f})_f = \mu\nu)$), because the overwhelming multijet background rules out to reasonably investigate the hadronic decay channels of the W boson. The initial state of the W boson production is a combination of quark and anti-quark, here predominantly represented by $u\bar{d}$ and $d\bar{u}$ as outlined in the previous section. The partial decay width ($\Gamma_W^{(f\bar{f})}$) is defined as the product of the Branching ratio B and the total decay width Γ_W : $\Gamma_W^{(f\bar{f})} = B^{f\bar{f}} \cdot \Gamma_W$.

One could deduce the parameters Γ_W and m_W from the four momenta of the decay products, if the four momentum of the initial state (\hat{s}) is known. But the composite structure of protons complicates the reconstruction of the decay kinematics for the experiment. The initial momentum of the partons is unknown, so that the initial kinematics of the boson are not well defined in three dimensions. Nevertheless, one can assume zero initial momentum in the transverse plane of the beamline in case of a head-on pp collision.

In general, measurements at hadron colliders exploit the momentum conservation in the transverse plane. The ATLAS detector uses a (semi-)spherical coordinate system with the z-axis along the beamline (see for reference the sketch in Fig. 3.2 (b)). The polar angle θ presents the inclination angle with respect to the beam axis. The azimuthal angle Φ describes the rotation around the z-axis. The transverse momentum p_T of the measured decay products is then defined as:

$$p_T = |\vec{p}| \cdot \sin(\theta) \quad (2.42)$$

The angle θ is crucial to define the transverse properties. The adequate modelling of this angle is therefore important for the final measurement.

This orientation of the decay products is affected by polarisation effects. The transverse momentum of the vector boson is predominantly defined by the recoil off QCD and QED ISR. The higher order QCD corrections induce a transverse polarisation of the intermediate state due to the non-zero spin of the gluon. The polarisation manifests in the following differential cross-section for the decay products:

$$\begin{aligned} \frac{d\sigma}{d \cos \theta_{CS} d\varphi_{CS}} &\propto (1 + \cos^2 \theta_{CS}) + \frac{1}{2} A_0 (1 - 3 \cos^2 \theta_{CS}) + A_1 \sin(2\theta_{CS}) \cos \varphi_{CS} \\ &+ \frac{1}{2} A_2 \sin^2 \theta_{CS} \cos(2\varphi_{CS}) + A_3 \sin \theta_{CS} \cos \varphi_{CS} + A_4 \cos \theta_{CS} \\ &+ A_5 \sin \theta_{CS} \sin(2\varphi_{CS}) + A_6 \sin(2\theta_{CS}) \sin \varphi_{CS} + A_7 \sin \theta_{CS} \sin \varphi_{CS} \end{aligned} \quad (2.43)$$

The angles θ_{CS} and φ_{CS} are defined in the Collins-Soper frame and define the relative direction of the decay products. The factors A_i are termed as *angular coefficients*. Their validation for the m_W measurement is outlined in Sec. 5.6.2.

For the final measurement the dependence on φ_{CS} is negligible. The integration over φ_{CS} yields the one dimensional angular distribution:

$$\frac{d\sigma}{d \cos \theta_{CS}} \propto (1 + \cos^2 \theta_{CS}) + \frac{1}{2} A_0 (1 - 3 \cos^2 \theta_{CS}) + A_4 \cos \theta_{CS} \quad (2.44)$$

The following variable transformation provides the differential cross-section with respect to the transverse momentum³

$$\frac{d\sigma}{dp_T} = \frac{d\sigma}{d \cos \theta} \frac{d \cos \theta}{dp_T} \propto \frac{d\sigma}{d \cos \theta} \frac{2}{m_W} \frac{1}{\sqrt{m_W^2/4 - p_T^2}} \quad (2.45)$$

The last term is obtained from considering the boson decay in its restframe. The full shape is a *Jacobian peak*. The edge of this peak at $m_W/2$ is affected by the determination of the angular coefficients. The peak is on one hand broadened due to the possible off-shell production of the vector bosons, and on the other hand due to the initial momentum of the vector-boson.

2.4.6 The soft part of the collision - the underlying event

The hard scattering process involves usually only two partons. But many more partons and their corresponding interactions are part of the full pp collision. All these processes, excluding the hard scatter, are encapsulated in the so called *underlying*

³ The relation is presented in the lab frame. The laboratory frame is Lorentz boosted along the laboratory z axis into a frame where the z component of the lepton pair momentum vanishes. Then a boost along the transverse momentum of the lepton pair transforms into the Collins-Soper rest frame. At $p_T = 0$, the Collins-Soper and the laboratory coordinate systems are the equal.

event (UE). It is the activity accompanying the hard process. It is characterized by processes at low momentum scales, because most of the collision energy goes into the leading parton-parton interaction.

The UE includes the color-charged proton remnants, which hadronize to other stable particles. The UE receives the soft contributions from ISR and Final State Radiation (FSR). Moreover, additional parton-parton interactions can take place. These are called *multiple parton interactions* (MPI). All of these soft processes are not captured in the perturbative description. They are either approximated, such as the showering, or they rely on phenomenological modelling. Hence, the details are part of the Monte-Carlo generator implementation. The corresponding mechanisms are discussed in Sec. 4.2.

2.5 Limitations of the Standard Model

The SM of particle physics is in its current formulation one of the best established theories, which provides precise predictions for ongoing High Energy Physics experiments. It successfully predicted the existence of e.g. the top quark or the Higgs boson, which were discovered several decades after their first postulation. Although the SM is not yet proven to be wrong, it incorporates some conceptual problems or shortcomings. Several observed phenomena lack a description in terms of the SM mechanisms.

The first pressing example is the observation of the neutrino flavour oscillation [24]. As a consequence, neutrinos are required to be massive, which contradicts their current description in the SM. The SM does not provide a right handed spinor to describe neutrinos as Dirac particles as already mentioned in Sec. 2.2.2.

Further tremendous efforts of the particle physics community aim to incorporate Dark Matter and Dark Energy into the SM. The analysis of the rotation velocity of the luminous matter in galaxies [25] indicates the existence of a non-luminous matter halo. Other cosmological observations such as gravitational lensing or the Bullet Cluster [26] agree with the existence of some kind of matter, that does not interact via the strong or electromagnetic force. As a result, only the weak force is left to provide evidences on the scale of particle physics. Therefore, the neutrino is left as only suitable candidate in the SM, but it is ruled out by other experiments due to its lack of abundance.

The Dark Energy is needed to reason the observation, that the expansion of the universe is accelerating. So far no SM mechanism can explain the existence of the corresponding energy. To be precise, the SM describes about 5% of the energy present in the universe.

The observation of the matter-anti-matter-asymmetry is a rather striking observation, which does not conform with the SM. The big bang is expected to have created a balanced amount of both particle types. These should then annihilate almost completely, even when the CP violation of the SM is taken into account. Nevertheless, an excess of ordinary matter is obviously present.

Another kind of possible shortcomings of the SM follows rather aesthetic arguments. If the SM serves as a complete theory of everything, it needs to describe gravity as well. But so far, it is not possible to formulate gravity as a quantum field theory, which smoothly transfers from the elementary particle scales to the scales of General Relativity.

It is further self-evident to describe all forces as manifestation of one single force, if one follows the previous unifications of first the electric and magnetic and finally the weak force. These theories are termed as Great Unification Theories. Some available formulations predict the decay of the proton, which contradicts present observations from e.g. the Kamiokande experiment.

Last but not least, the SM itself is rather unsatisfactory in philosophical matters. It provides many free parameters, but does not reason their existence, e.g. the number of quark and lepton families. A possible interpretation depicts the SM an effective field theory, i.e. not a complete theory in this context. It describes phenomena up to a certain energy scale and breaks down for processes taking place above this energy. If the SM is valid up to a very high energy scale, it introduces very high corrections to the mass of the Higgs boson. These would be apparently larger than m_H itself. Hence it requires finely tuned quantum corrections, in order to cancel out and finally yield the measured value of m_H . These issues are termed as *naturalness* or the Hierarchy problem. They are a driving motivation to perform precision measurements on e.g. the Higgs particle properties.

Some of the described issues are answered, if the SM is extended with additional theory concepts. The corresponding theories are collected under the term Beyond Standard Model (BSM) theories. One prominent example is Super-Symmetry. Nevertheless, beyond the Standard Model (BSM) theories either predict signatures, which are hardly distinguishable from the SM background or not accessible at all with the currently available technologies. Precision measurements offer a rather straight forward approach to probe the consistency of the SM and therefore might point in a direction of valuable models.

2.6 Objectives of precision measurements

Precision measurements are a powerful tool to tackle some of the SM shortcomings mentioned in the previous section. They provide critical tests for the consistency of the SM and validate its limitations. Precision measurements are conducted at all orders of energies to be sensitive to various potential BSM phenomena. For example, the low energy frontier pushes the precision of the anomalous magnetic dipole moment of the muon, because a discrepancy with the theoretical prediction may reveal new particles in the quantum loop corrections. At the high energy frontier, the observables of the electroweak sector lay the foundations for consistency tests of the SM. The electroweak sector provides two relations [27], which are derived from Eq. 2.17 and Eq. 2.24. They are expressed in terms of the fine structure constant α , the Fermi coupling constant G_F , and the vector boson masses, m_Z and m_W :

$$m_W^2 = \frac{m_Z^2}{2} \left(1 + \sqrt{1 - \frac{\sqrt{8}\pi\alpha}{G_F m_Z^2} (1 + \Delta r)} \right) \quad (2.46)$$

$$\sin^2 \theta_{\text{eff}} = \kappa_Z \sin^2 \theta_W = \kappa_Z \left(1 - \frac{m_W^2}{m_Z^2} \right)$$

The factors Δr and κ_Z incorporate the effects of higher order corrections [28, 29], such as the examples presented in Fig. 2.7.

The one-loop corrections add a logarithmic dependence on the Higgs boson mass m_H to the relations. A dependence on all fermion masses is also encoded in the corrections, but it is dominated by the heaviest SM particle, the top quark with mass

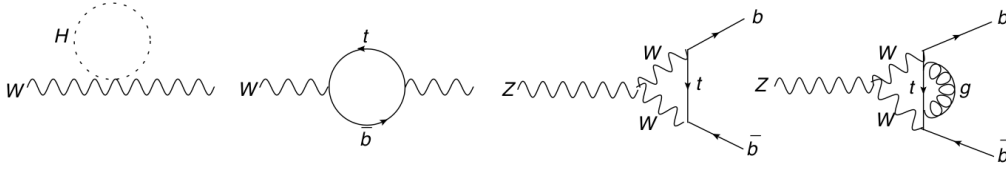


Figure 2.7: Feynman diagrams exemplifying loop corrections to the W boson propagator and the $Z \rightarrow b\bar{b}$ vertex, which affect the vector coupling. The figure is taken from [27].

m_t . This interconnection allows to indirectly determine one parameter, e.g. m_H , if all others are measured with sufficient precision and kept fixed within their constraints. This concept is realized with global electroweak fits. Such fits of the electroweak sector parameters provided guiding constraints on the mass of the Higgs boson before its discovery. The example of constraining m_H is visualized in Fig. 2.8 (a).

Following the discovery of the Higgs boson, measurements of all electroweak observables have been performed. Hence, this completeness is exploited to probe the consistency of the introduced SM relations, i.e. m_H is now fixed in the fit and other parameters can be evaluated. The mass of the W boson plays a key role among these parameters, because the prediction of the electroweak fit currently outperforms the precision of its experimentally measured value. Figure 2.8 (b) displays the corresponding comparison. The comparison of the electroweak fit results ($m_W^{EW} = 80.356 \pm 0.006$ GeV) with a combination of the available measurements ($m_W^{global} = 80.380 \pm 0.013$ GeV) results in a tension of about 1.6σ . It reveals, that improved m_W measurements are needed to determine, whether this tension persists with reduced experimental uncertainties. This thesis is part of the effort to further improve the precision on the m_W measurement with the ATLAS detector.

The electroweak fit employs further SM parameters, such as the decay width (Γ_W) of the W boson. The decay width has a special role in the fit environment, because its experimental precision is rather poor compared to the indirect fit constraints ($\Gamma_W^{global} = 2.085 \pm 0.042$ GeV vs. $\Gamma_W^{EW} = 2.091 \pm 0.001$ GeV). The measurement of Γ_W , which is presented in this thesis as well, therefore provides a further experimental opportunity to improve the consistency tests of the SM.

The significance of the consistency test is driven by the experimental and theoretical uncertainties. The precision of m_W and Γ_W measurements relies on an excellent understanding of the experiment. This thesis presents one contribution out of many crucial inputs to further boost the precision. It contributes with an improvement of the fit concept and the description of the UE activity. An overview of all recent measurements to reduce e.g. experimental or PDF related uncertainties is given in Ref. [30].

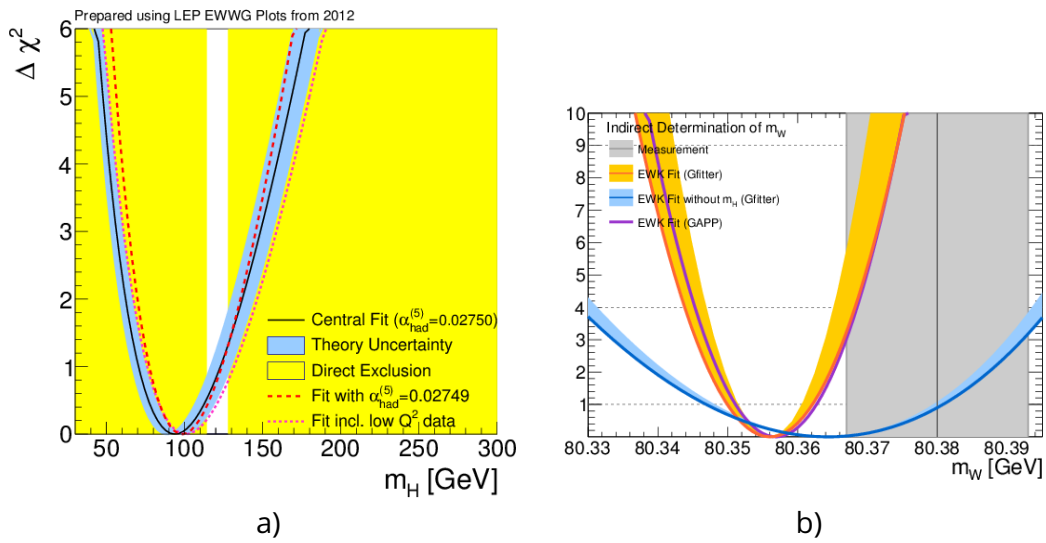


Figure 2.8: (a) illustrates the estimate of the Higgs Boson mass in the Standard Model from electroweak precision measurements. The excluded area by direct searches is shown in yellow, while the blue band illustrates the χ^2 distribution of the global electroweak fit. (b) illustrates a χ^2 distribution for m_W derived with (blue) and without (orange) including the Higgs boson mass using the Gfitter program. The filled blue and yellow areas indicate the theoretical uncertainties. The χ^2 distribution is also evaluated with an alternative software (GAPP). The grey band presents the current world average of the measurements with 1σ uncertainty. The plots are taken from [27] and are based on results from [31].

3.

Experimental Setup

3.1 The Large Hadron Collider

The Large Hadron Collider (LHC) is the largest scientific experiment ever built by mankind up to the present day. The dominating feature is a 27 km long storage ring, which is designed to accelerate protons (and other hadrons) to a centre-of-mass energy of $\sqrt{s} = 14$ TeV. This thesis covers measurements performed during the run periods RUN 1 and RUN 2 at $\sqrt{s} = 7$ TeV and $\sqrt{s} = 13$ TeV respectively.

The first one refers to the data taking period from early 2009 until the beginning of the year 2013. The second run period lasted from April 2015 until December 2018.

Several aspects motivate a highly energetic proton-proton collider. The particle physics community is striving for more and more powerful particle colliders, because the heavier the particle, which are to be produced, the higher must be the collision energy. And currently many BSM theories predict heavy particles. Moreover the Higgs boson was expected at a high mass regime (see exclusion limits in Sec. 2.6) during the design phase of the LHC. A circular pp collider is further able to provide a high rate of collisions, which increases the probability to detect processes of low cross-section, such as some BSM predictions.

The LHC collides two counter-rotating proton-beams head-on, so that the relative energy is much higher compared to a fixed target experiment. Of course a collider requires a much higher beam precision as a trade-off. The acceleration of hadrons is much cheaper compared to lighter stable elementary particles such as electrons. The latter suffer from a huge energy loss due to synchrotron radiation in case of a curved beam line. The loss is inversely proportional to the fourth power of the rest mass of the accelerated particle ($\Delta E_{\text{loss}} \propto \frac{1}{m^4}$). Therefore, electrons lose $1.13 \cdot 10^{13}$ more energy than protons due to synchrotron radiation. A linear accelerator would not suffer from these kind of energy losses, but a ring accelerator reuses the acceleration devices, saving material and space.

The following chapter briefly describes the techniques to accelerate the particles and to guide them to a controlled collision (Sec. 3.1.2). It also covers the proton beam characteristics, as they play a major role in the presented analysis.

3.1.1 The accelerator complex

The protons are guided through a large accelerator complex before they collide at the different interaction points, where the detectors collect their debris. The guiding principle is to accelerate the ionized hadrons with varying electromagnetic fields. Specialised cavities shape these fields and the momentum dependent frequency. Different magnet systems lead the direction of the proton beam.

The requirements in the cavities and magnets change with the increasing momentum of the protons. Hence, the beam is fed through a sequence of accelerator units. The structure further allows other experiments to extract protons at earlier stages and lower energies.

The beam itself starts as hydrogen gas induced into a stripper, which ionizes the hydrogen atoms, i.e. it strips off the electrons. The following first accelerator stage is

the LINear ACcelerator in CERN (LINAC2). It is a linear accelerator and releases the protons with an energy of 50 MeV into the Proton Synchrotron Booster (PSB). The latter accelerates the particles to 1.4 GeV, and is followed by the injection into the Proton Synchrotron (PS). The protons are then transferred to the next stage at an energy of 26 GeV. The Super Proton Synchrotron (SPS) further increases their energy to 450 GeV, before the particles are injected into the final accelerator stage, namely the LHC. The LHC works simultaneously as a storage ring and accelerator. It boosts the two counter-rotating proton beams to the final energy level, i.e. for the analysis presented here 3.5 TeV and 6.5 TeV per beam. The future run anticipates to reach the design energy with $\sqrt{s} = 14$ TeV.

The beams are brought to collision at the different interaction points. The full path of the protons is visualized in Fig. 3.1. The beam path is directed with superconducting dipole magnets. Quadrupole magnets focus the beam and further higher order multipole magnets shape the beam geometry.

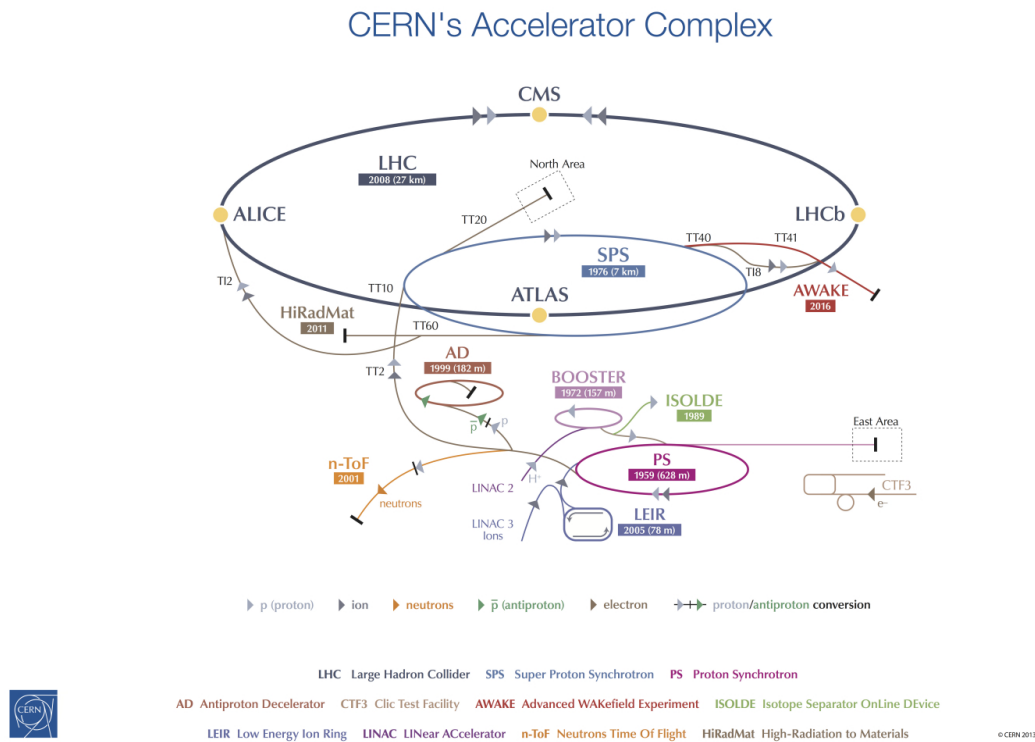


Figure 3.1: Schematic drawing of the accelerator complex at Conseil Européen pour la Recherche Nucléaire (CERN). The yellow dots refer to the experiments placed at the interaction points. The figure is courtesy of CERN [32]

3.1.2 Beam characteristics and luminosity

The LHC proton beam is divided into bunches. It is not a continuous proton current. The number of protons per bunch and the distance between the bunches provides a first handle for the collision rate at the experiments. The bunch-spacing time was 50 ns during RUN 1 and 50 ns or 25 ns during RUN 2.

The interaction rate is an important input for the experiments, because it is directly proportional to the expectation values of the investigated processes. The amount of

of collisions per time or over a run period is measured in luminosity (\mathcal{L}) and integrated luminosity ($\int \mathcal{L} dt$) respectively. In a head-on collision with Gaussian-shaped beam profiles the luminosity is derived from the following beam parameters:

$$\mathcal{L} = \frac{\dot{N}}{\sigma_{tot}} = \frac{N_1 N_2 f_{BC} N_b}{4\pi \sigma_x \sigma_y} \quad (3.1)$$

\dot{N} is the interaction rate and it is divided by the total pp interaction cross-section σ_{tot} . The latter is the sum of the cross-section for non-diffractive, single-diffractive and double diffractive pp scatterings. The final term calculates the luminosity for a collider operating at relativistic energies with $N_{1,2}$ particles in the colliding bunches. N_b is the number of bunches injected and f_{BC} denotes their revolution frequency in the collider. The denominator represents the geometrical beam cross-section for Gaussian-shaped beams. Both beams are expected to have the profile with the width $\sigma_{x,y}$. The different parameters are part of the designated run conditions. For example the LHC operated in 2018 during peak-luminosity with 2556 bunches per beam and $f = 400$ kHz. One bunch consisted of about $1.1 \cdot 10^{11}$ particles. At the focal point the beams are squeezed to a diameter in the order of several nm, while the longitudinal extension is about several cm. The final peak luminosity delivered to the experiments was up to $\mathcal{L} = 2.1 \cdot 10^{34} \text{ cm}^{-2} \text{ s}^{-1}$.

Naturally, there are several pp collisions taking place during one bunch-crossing. Only the most energetic collision is usually investigated in physics analysis. The corresponding collision point is referred to as the primary vertex. All others simultaneous collisions are termed as pile-up and mostly present low energetic processes, such as non-diffractive collisions. The average number of simultaneous pp per bunch-crossing average number of interactions per bunch crossing ($\langle \mu \rangle$) is directly proportional to the instantaneous luminosity and inversely proportional to the total inelastic cross-section for pp collisions (σ_{pp}):

$$\langle \mu \rangle = \frac{\mathcal{L} \cdot \sigma_{pp}}{f_{BC}} \quad (3.2)$$

The LHC operated with $\langle \mu \rangle \approx 34$ for the runs at $\sqrt{s} = 13$ TeV during the run period RUN 2, while during RUN 1 it delivered an average of about 9 and 21 interaction per bunch-crossing for the collisions with $\sqrt{s} = 7$ TeV and $\sqrt{s} = 8$ TeV.

The equations 3.1 and 3.2 include several simplifications compared to the real case at the LHC. The beams cross at an angle of about $300 \mu\text{rad}$ to avoid collisions outside of the design collision point. This slightly reduces the luminosity compared to a real head-on collision. Moreover, not all collisions take place within the beam focus. The geometrical cross-section diverges and the beam density reduces after the focal point, which reduces the collision rate in these areas. The betatron function (β) is the tuning parameter for the beam density and geometric shape of the focus. The LHC performs specialized runs for dedicated physics projects, which exploit exceptional values of β^* . The beam profile is further affected by dispersion due to the repellent forces among the protons. A discussion of these effects on the luminosity calculation is found in Ref.[33]. The luminosity delivered to the experiments is measured with special detectors, e.g. the LUCID-2 subdetector of ATLAS.

The final analysis exploits the integrated luminosity, which is simply the integral over time of the instantaneous luminosity. The critical aspect is, that the number of protons per bunch is time dependent, because protons are *burnt-off* in each collision. The run parameters for the analysis presented in this thesis are listed in Sec. 5.4.1 and Sec. 6.3.2.

3.2 ATLAS - the giant

The ATLAS (A Toroidal Lhc ApparatuS) detector is one of the four large experiments, which investigate the highly energetic hadron collisions at the LHC. The name refers to its unique characteristic: It is the largest experiment in size compared to the other LHC detectors.

It is cylindrically shaped with a length of 44 m and a diameter of 25 m (see Fig. 3.2 (a)). The collision point is placed at the very centre of the cylinder and the beam line runs along the symmetry axis. The shape is designed to provide almost full spatial coverage for the detection of the collision products. Solely the beamline itself is left out, as the beam would harm any detector parts. Special focus is set on the coverage in the transverse plane of the beam line, because it holds the most relevant information in case of hadron colliders.

In the following, all components are described with references to the ATLAS coordinate system, which is displayed in Fig. 3.2 (b). The origin of the Cartesian and spherical coordinates is the geometrical centre of the cylinder, which is the collision point by design. ATLAS defines right-handed Cartesian coordinates with the x-axis pointing toward the center of the LHC ring and the z-axis along the beam line. It is more suitable to refer to (semi-)spherical coordinates, in order to reflect the paths of the collision products. The azimuthal angle Φ is measured from the x-axis and rotates counter-clockwise around the z-axis. The polar angle θ describes the inclination relative to the z-axis. It is usually converted into pseudorapidity $\eta = -\log(\theta/2)$ in the context of particle trajectories. The radial component r denotes the distance to the z-axis measured in the transverse plane, namely the x-y-plane.

The ATLAS detector is a multi-purpose detector. It is able to reconstruct the debris of the different kinds of hadron collisions. Different layers are installed to probe different properties of the collision products. The combination of the information from different layers allows to identify individual particles and to define their kinematics and flavour.

The major components are outlined in detail in the following sections, starting from the innermost one, the Inner Detector (ID), which delivers tracking information of charged particles. It is embedded in a 2 T magnetic field, produced by the surrounding solenoid magnet. The subsequent detector layers are the calorimeters. These measure the energies of electrons and hadrons. The outermost and therefore largest detector part is the muon spectrometer. It is also suffused with a magnetic field of 0.5 T or 1 T. The muon spectrometer measures tracking and energy information of the highly penetrating muons.

There is a dedicated section about the trigger system after the technical details of the subsystems, as it receives input from several detector parts.

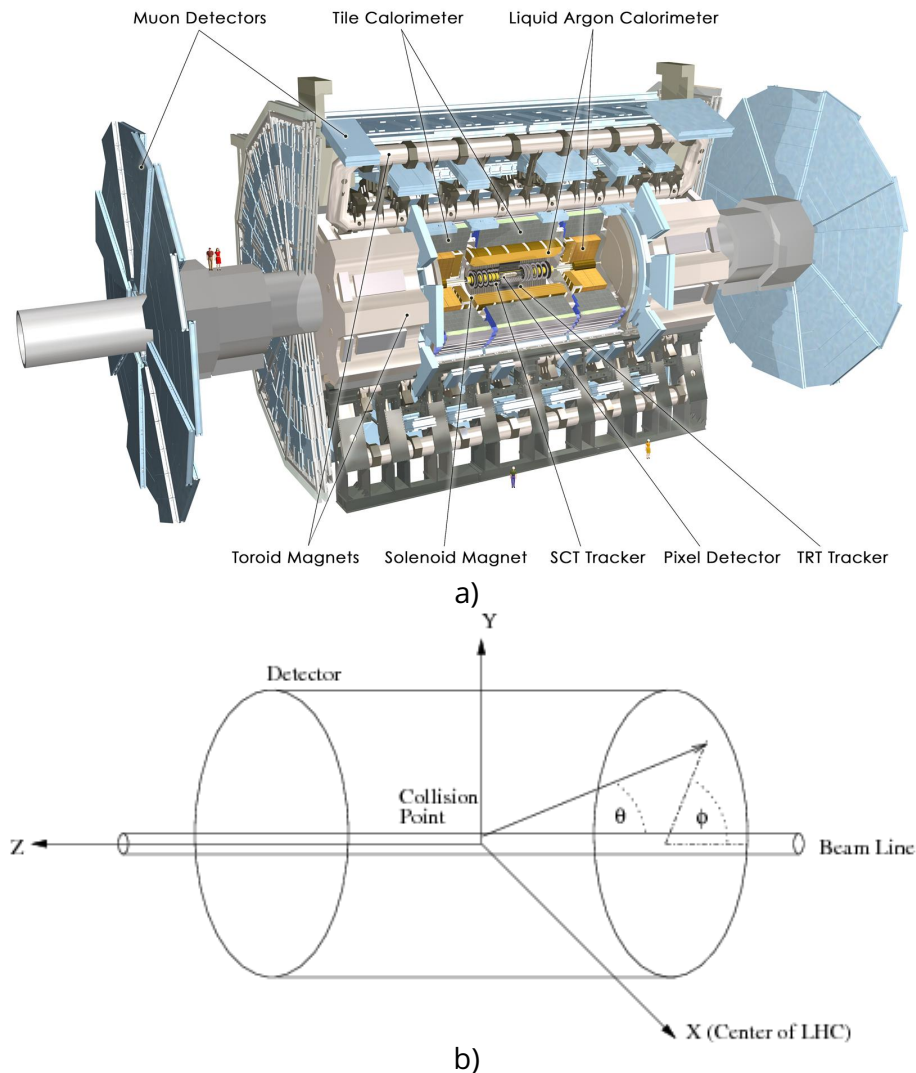


Figure 3.2: (a) is a cut-away view of the ATLAS detector. The figure highlights the three different detector regions: The central barrel region and the two endcap regions, which close up the cylinder top and bottom side. The figure is courtesy of CERN [34]. (b) illustrates the ATLAS coordinate system. The sketch is taken from [35].

3.2.1 The Inner Detector

The ID is the subdetector closest to the interaction point and therefore faces two important challenges: On one hand, it has to provide an excellent spatial resolution to allow precise track reconstruction and vertexing. On the other hand, it has to resist immense radiation, while in parallel it may not distract the particle trajectories due to too much material. The combination of three different detectors compromises these requirements, i.e. two silicon detectors and one gaseous detector. A detailed view of the ID parts is shown in Fig. 3.3.

The Pixel detector (Pixel) [37] is placed next to the beam pipe. It consisted of three layers of silicon sensors during RUN 1, which are inserted in the range of 5 cm to 1.15 m. The ID was extended with an additional layer, the Insertable b -layer (IBL) [38], for RUN 2. This fourth layer enables even more precise vertexing, because it is even closer to the collision at the radial distance of $r = 3.3$ cm. The pixel detector covers a rapidity range of $|\eta| < 2.5$.

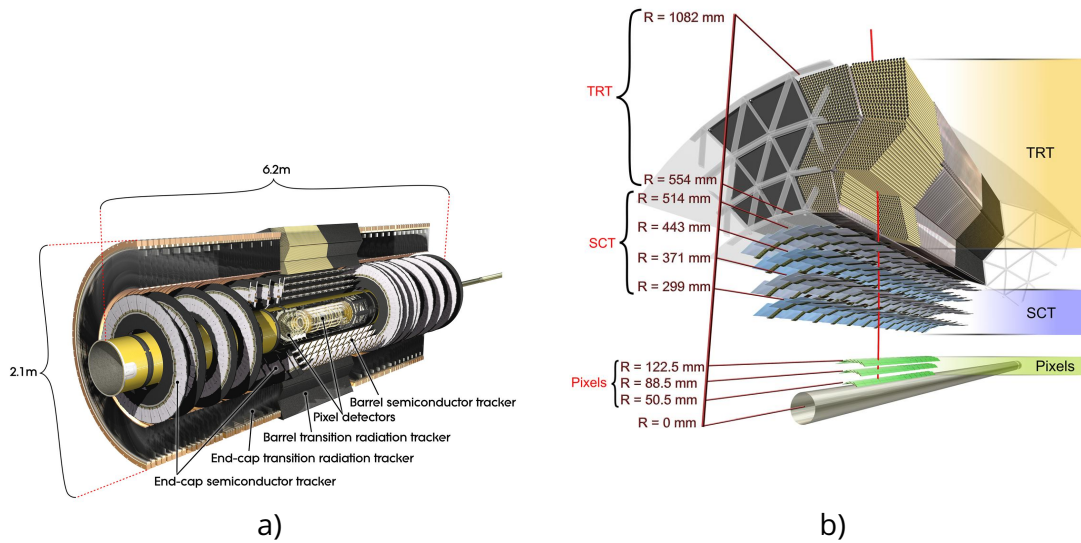


Figure 3.3: (a) is a cut-away view of the ID. The figures are courtesy of CERN [36].

The pixels of the IBL are of the size $50 \mu\text{m} \times 250 \mu\text{m}$. The three other layers consist of $50 \mu\text{m} \times 400 \mu\text{m}$ sized pixels. When a charged particle passes the silicon, it ionizes the material and induces a current. This current is converted into the final signal. If it is above a certain threshold, it is declared as a *hit*. The combination of all four layers provides a resolution of $10 \mu\text{m}$ in the r - Φ plane and of $115 \mu\text{m}$ in the z -direction. It has to be noted, that the performance of the Pixel is subject to the amount of radiation it received in total. The silicon lattice structure within the sensors is damaged by the radiation and the properties for ionization and electric current alter. The effects will become relevant for future extensions of the LHC with higher luminosities. A related study is highlighted in Sec. A.1.

The Pixel is surrounded by the Semiconductor Tracker (SCT) [39]. The SCT exploits a similar technology, but the active materials are long and narrow strips of the size $80 \mu\text{m} \times 12 \text{cm}$ instead of individual pixels. This design saves material, as it needs to cover a larger volume ($r = 29.9 \text{cm}$ to 51.4cm), but at the cost of precision in z -direction. There are four SCT layers in the barrel region and nine in the endcaps covering up to $|\eta| < 2.5$. The r - Φ resolution is $17 \mu\text{m}$ and $580 \mu\text{m}$ in z .

The final part of the ID is the Transition Radiation Tracker (TRT) [40]. It combines two gaseous detector techniques, namely a straw tracker and a transition radiation detector. It is placed at $r = 55.4 \text{cm}$ and covers $|\eta| < 2.0$.

The straw tracker part consists of 52 544 drift tubes, each with a diameter of 4mm and 144cm length. These are filled with a mixture of Xenon and Argon gas. If a charged particle traverses the tube, it ionizes the gas. The electrons drift to a wire in the centre of the tube, because a potential of 1.5kV is applied between the wire and the casing. The ions drift in the other direction to the walls of the tube. The timing difference of these two currents allows to determine the position of the hit with a resolution of $130 \mu\text{m}$.

The straws are interlaced with 3mm thick polypropylene-polyethylene fibres. The fibres provide a different refraction index compared to their surrounding. Traversing charged particles therefore emit transition radiation. The radiated energy depends on the total charge and the Lorentz factor of the particle. The latter fact yields the possibility to discriminate muons, electrons and pions, because the Lorentz factor

depends on the particle mass.

All in all, the ID is designed to provide charged particle momentum measurements with a precision of $\frac{\sigma_{pT}}{pT} \approx 0.5\% \oplus 1\%$.

3.2.2 The calorimeters

The calorimeter system surrounds the ID and the solenoid magnet. It is made of two individual calorimeters, the electromagnetic calorimeter and the hadronic calorimeter. Both are optimized to measure the energy of mainly electrons, positrons and photons or hadrons respectively. They are designed as sampling calorimeters, i.e. they consist of several alternating layers of active and passive material. The passive layers are made of dense material and force the traversing particles to interactions and the subsequent creation of particle showers. The active layers measure two aspects of these particle showers, namely their energy, which is determined by the amount of scintillation light, and the position or spread of the showers. The position is defined by the location of the scintillator tile.

It is a destructive measurement. The full shower must be contained within the calorimeter and the incoming particle must be stopped, in order to measure its complete energy. The calorimeters are designed sufficiently massive, so that only muons and neutrinos are able to pass through.

The electromagnetic calorimeter measures all electromagnetically interacting particles, in other words all charged particles and photons. But it is predominantly designed to determine the energy of photons, electrons and positrons. Photons and electrons can be distinguished based on their shower shape and matching tracking information. Their showers originate from the sequence of pair-production and Bremsstrahlung.

The active material of the electromagnetic calorimeter is liquid Argon, and the deposited energy is recorded with accordion-shaped Kapton electrodes. The passive material is lead and steel. There are three layers of active and passive material in the barrel region and four in the endcaps. The barrel region covers $|\eta| < 1.475$ and the endcaps $1.375 < |\eta| < 3.2$. The central region ($|\eta| < 1.8$) is introduced with a presampler to correct for energy losses in front of the calorimeter.

The middle layer is built with the highest tile granularity of $\Delta\eta \times \Delta\Phi = 0.003125 \times 0.1$, because the majority of the electromagnetic showers are contained in this depth of the calorimeter. All layers combine to a precision of 0.025 rad for the location of the deposited energy.

The subsequent hadronic calorimeter has to cover a much larger volume ($2.28 \text{ m} < r < 4.23 \text{ m}$), and exploits more cost-efficient technologies. The passive material is mostly iron, and the central region ($|\eta| < 1.7$) samples the showers with plastic scintillator tiles. The endcaps ($1.5 < |\eta| < 3.5$) and an additional very forward region exploits also liquid argon as scintillator and copper or tungsten as passive material, in order to better withstand the higher radiation dosage. The very forward part, or Forward Calorimeter, detects electrons and photons as well, because its pseudorapidity range is not covered by the electromagnetic calorimeter. The tiles of the hadronic calorimeter are much coarser with $\Delta\eta \times \Delta\Phi = 0.1 \times 0.1$. Therefore, the resolution is reduced to roughly 0.1 rad.

The hadronic calorimeter stops all strongly interacting particles, such as neutrons or protons.

3.2.3 The Muon spectrometer

The Muon spectrometer (MS) is similar to the ID designed as a tracking detector. It detects spatial hits of traversing charged particles. The magnetic field of the toroidal magnets bends their paths and the curvature yields the momentum information. Muons are the only charged particles, which are expected to pass the calorimeters, if they originate from the interaction point. It is also possible that tails of highly energetic particle showers in the calorimeter leak into the MS, but they are later suppressed, when matching them to the ID information. The MS is therefore the outermost detector systems and covers the largest area.

A suitable technology are gaseous detectors, which are either used for tracking information or for the triggers. The tracking information requires excellent spatial resolution, while the trigger chambers provide accurate time resolution.

The MS covers the volume from $r = (4.25 - 11) \text{ m}$ and down to $|\eta| < 2.7$. The four different kinds of tracking chambers are displayed in Fig. 3.4. The Mini Drift Tubes (MDT) provide tracking information in the barrel region and endcaps for $|\eta| < 2.7$. The Cathode Strip Chambers (CSC) deliver also hits, but at higher granularity in the region of $2.0 < |\eta| < 2.7$. The CSC are multiwire proportional chambers with cathodes segmented into strips. The Resistive Plate Chambers (RPC) provide trigger information for the barrel region of $|\eta| < 1.0$. And the Thin Gap Chambers (TGC) extend the trigger range in the endcaps for $1.0 < |\eta| < 2.4$. There are three layers of each chamber type, except the CSC, which measure in a segment of highest activity and are limited in space by the endcap toroid.

The long bending path path of the muons allows a measurement of the muon momentum with a 3% precision for muons of $|\vec{p}_\mu| \approx 100 \text{ GeV}$. The MS even manages a precision of about 10% for higher energetic muons with momenta above 1 TeV.

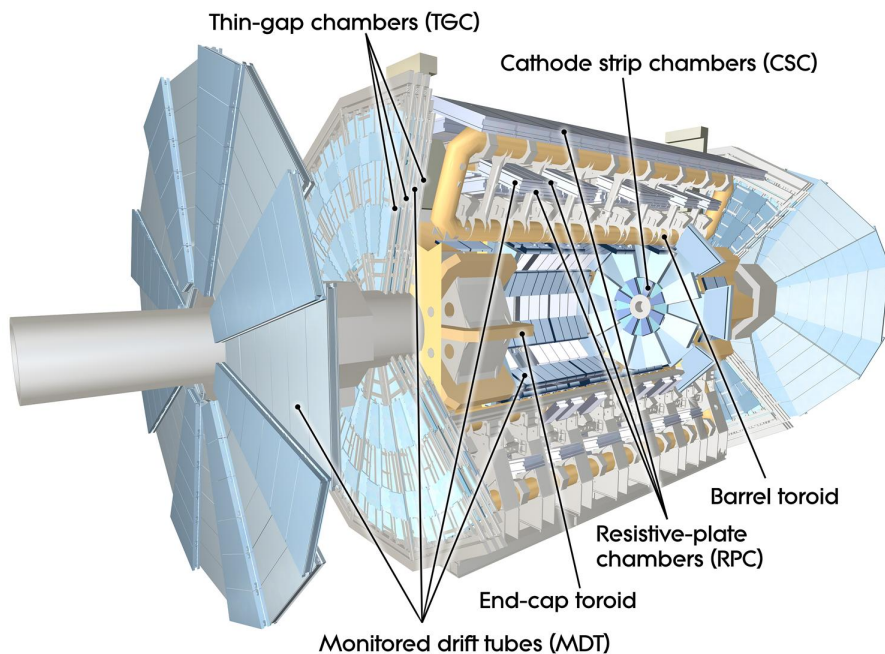


Figure 3.4: A cut-away view of the MS. The figure is courtesy of CERN [41].

3.2.4 Object reconstruction

After the raw data of an event has been stored, the individual physical objects are deduced offline from the detector signals. The detector response of a collision is too packed to simply spot the path of an individual particle. Therefore, algorithms are employed to cluster the detector information and to combine several signals in order to tag object candidates. There are numerous combinatorial possibilities to transform the detector response into its particle correspondence. As a result, some reconstructed particles might be misidentified or totally lack of a real correspondence, as they just originate from combinatorial background. These objects are further denoted as *fakes*.

However, the algorithms work at high reconstruction efficiency. Additional quality cuts allow to define the probability of misidentification and fakes. This choice is adapted for each analysis and is part of the event and object selection. The related cuts are outlined in Sec. 5.3.1 and Sec. 6.3.1.

The general object reconstruction is standardized for all ATLAS analysis. The m_W measurement in $W \rightarrow \mu\nu$ events requires the identification of muons and neutrinos. The latter are not detectable with ATLAS, but can be inferred from the full event information. The measurement of the activity of the UE in Z boson events relies on the measurement of charged particles and muons. Thus, the following sections focus on the reconstruction of charged particles, muons and neutrinos. The ATLAS detector is further capable to tag electrons, hadrons and jets, which originate from hadronized quarks or gluons. Their reconstruction is discussed briefly for completeness. Fig. 3.5 visualizes the combination of different signals to determine the particle origin.

Charged particle identification - Tracking with ATLAS

Tracking describes the reconstruction of the trajectories of charged particles. The potential path of a particle through the detector is denoted as a track. It is deduced from the combination of individual point-like hits in the different layers of the tracking detector. The tracking is a core feature of a multi-purpose detector, because it delivers an essential part of the kinematic information, namely the direction and momentum. The tracking information serves as input to more detailed identification techniques of e.g. the particle type. Furthermore, the tracks are retraced to determine the collision vertices. The following tracking procedure focuses on the ID data, but the algorithm is similarly applicable to the MS response.

During RUN 1 and RUN 2 ATLAS reconstructed tracks with an *inside-out* algorithm implemented in NEWT [43]. The reconstruction during RUN 2 took advantage from the additional IBL, which further improved the tracking precision.

The track finding algorithm is split into five steps. Each one is applied several times, as its results vary, when the hits are associated differently. The very first step accesses solely the spatial information of the detector. It bundles adjacent pixel cells, which detected energy deposits, and forms space points for the SCT and Pixel.

In the second step preliminary track candidates, so called seeds, are formed. The seeds are circles in the transverse plane, which are defined by the combination of three space points. Seeds are rejected, if they do not pass the momentum threshold or if they are not geometrically compatible with a physical collision point. The general recommendation is a threshold of $p_T > 400$ MeV, because less energetic charged particles might not pass the ID due to the strong deflection by the magnetic field.

The accepted seeds are further processed as track candidates in the third step. The track candidates exploit the full and more precise hits information. They are processed with the Kalman Filter [44] and the Global χ^2 Track Fitter algorithm [45]. The algorithms iteratively associate more and more hits from different layers to one

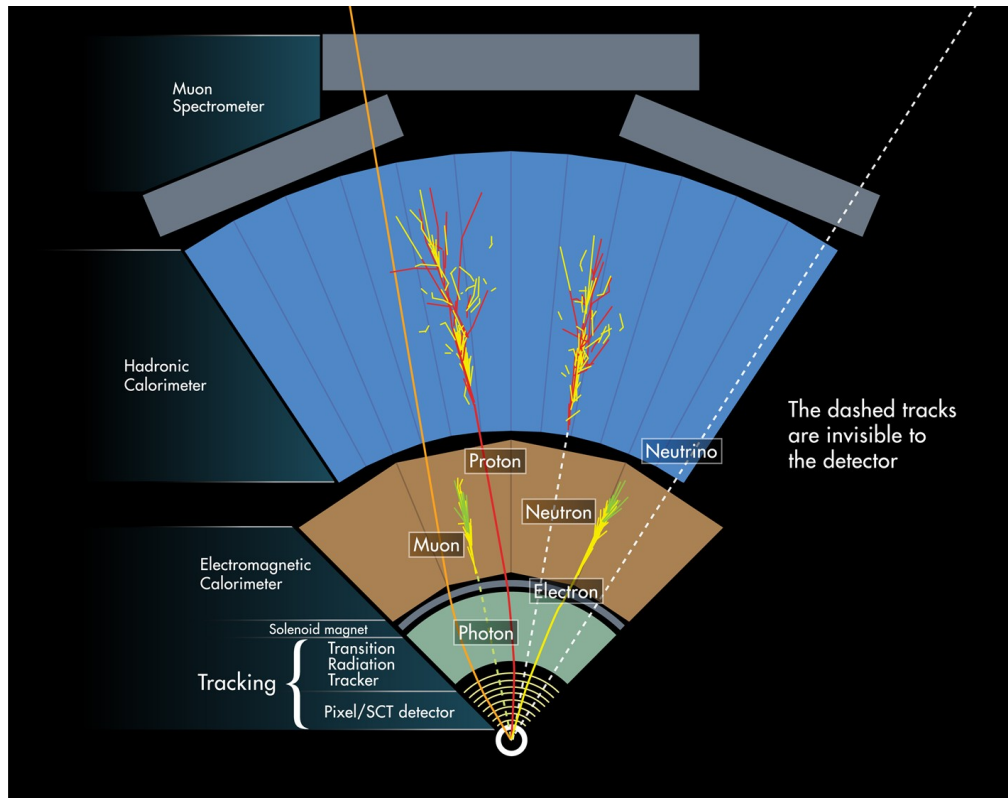


Figure 3.5: Schematic cross-section of an ATLAS detector segment. The paths of different particles are visualized. Solid lines correspond to reconstructable particle trajectories, while the dashed lines are invisible to the detector. Proton, Neutron, electron and photon shower in the corresponding calorimeters. The figure is courtesy of CERN [42].

track candidate.

Numerous ambiguities occur during this step, because of e.g. shared hits or combinatorial background. The ambiguities are removed in a simultaneous fourth step, which incorporates a weighting scheme into the Kalman Filter. The weights relate to the fit quality, the number of holes, i.e. layers on the track without a hit, and the energy deposit.

The final stage extends the remaining track candidates with hits from the TRT. The track candidates are re-evaluated with the additional TRT information, resulting in an improved momentum measurement. If the TRT and silicon detector information are compatible, the elongated track information will serve as final reference for the reconstructed tracks.

The track reconstruction is completed with an complementary outside-in algorithm. It extends the not associated TRT track segments back into the more inner detector parts. It allows to detect secondary vertices within the ID, which originate e.g. from long-lived particles.

A track is shaped like a helix and described with 5 parameters:

- The angles θ , Φ describe the initial direction of a track. They are defined according to the ATLAS coordinate system.
- The ratio of charge and momentum ($\frac{q}{p}$), which is obtained from the energy deposit, the Cherenkov light and the curvature of the track. The latter is directly

proportional to the radius (ρ) and magnetic field strength.

- The longitudinal and transverse impact parameters z_0 and d_0 , which are defined as the distance between the point of closest approach of the track relative to the associated collision.

Fig. 3.6 illustrates the different track parameters.

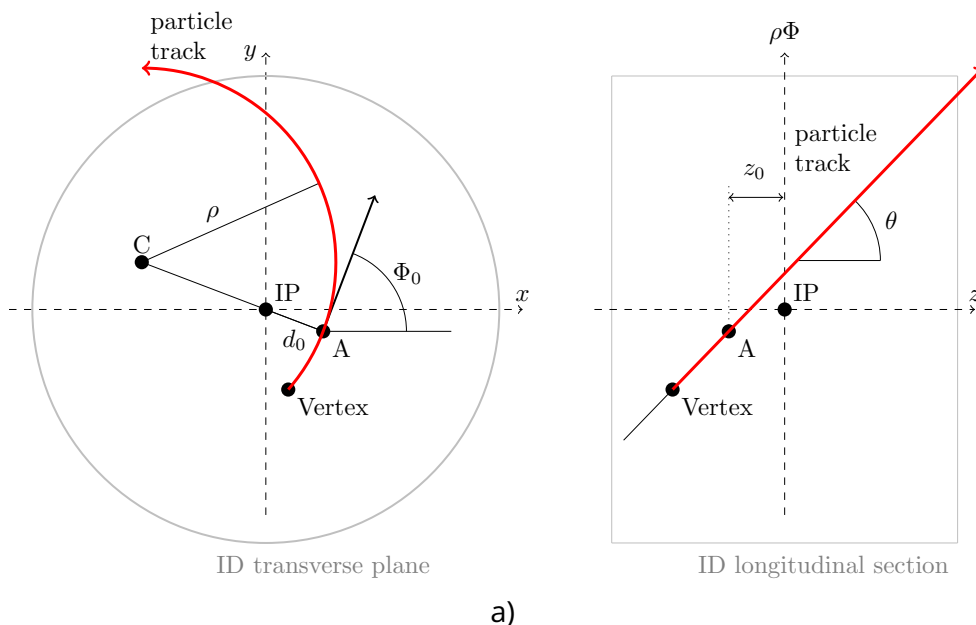


Figure 3.6: Illustration of the particle track parameters. The left hand side presents the definition of d_0 in the transverse plane of the detector. The right hand side visualizes the longitudinal impact parameter. IP is the design interaction point and C is the center of the track seed, i.e. a circle with radius ρ . The tangent is needed to define the angle Φ_0 .

Vertexing

The interaction vertices are the spatial correspondence of the pp collisions. They are inferred from the entirety of all reconstructed tracks. A vertex requires at least two associated tracks to be reconstructed.

A χ^2 -based algorithm is implemented to find the vertices. The starting seed for the algorithm is the z -coordinate or rather the longitudinal impact parameter, z_0 , from which the majority of tracks originates. The algorithm iteratively assigns tracks in the (longitudinal) vicinity to the corresponding vertex. Solely the z -coordinate of closest approach to the beamline is exploited in the first place, because the point-like origin of a track is not reconstructable and only the back-projected direction of the track serves as a reference. The transverse impact parameter allows to drop tracks, which are not close enough to the beamline, i.e. $d_0^{BL} < 4$ mm.

The vertex finding algorithm suffers from two pitfalls: A pp collision might be reconstructed as two vertices, if e.g. the associated track information is imprecise. This effect is later referred to as *split vertices*. Or the other way round, originally two vertices might be merged into one, if they are not (longitudinally) well separated. The latter issue is naturally correlated with the number of interactions per bunch crossing.

Nevertheless, it is crucial to physics analysis to distinguish vertices in order to deduce kinematic relations of the associated particles. The efficiency of the vertex reconstruction increases with the number of associated tracks and the vertex position

with respect to the tracking detector systems. Already four associated tracks are sufficient to reach a vertexing efficiency close to 100%.

In general, the vertex of interest is the one with the highest value of $\sum p_T^{\text{track}}$ associated. It is termed as *primary vertex* (PV) and obviously most likely to be associated with a hard scatter process of interest.

Muon reconstruction

Muons are identified with high efficiency, because they are the only kind of charged particles, which are able to penetrate the full detector volume. The signals in the MS are reconstructed as tracks. A muon track is simply distinguished from e.g. a particle shower leaking from the calorimeter, because the track is required to be associated to a vertex. The ATLAS community defines different classes to reconstruct muons:

- Combined muon - the track in the MS is matched to a track reconstructed in the ID and the kinematics are derived from a full refit of the combined tracking information. In the scope of this thesis, this kind of muons are later used for the reconstruction of Z bosons in the UE measurement.
- Segment-tagged muons - one track reconstructed in the ID is matched to (at least) one track reconstructed in the MS, but the kinematics are derived solely from the ID information. The measurement of m_W exploits this class of muons to tag W bosons.

It is also possible to tag muons with further information from the calorimeters or exceed the track acceptance of the ID by using MS tracks only. But these two classes are not further relevant.

A muon can be further distinguished with an isolation criterion to reject muons, which originate from jets. The isolation criteria measure either the $\sum p_T$ of tracks in the vicinity of the muon or the energy deposits in the EM around the muon path.

Neutrinos in ATLAS

Neutrinos are solely weakly interacting and escape the ATLAS detector without any trace. Their existence and kinematics are inferred from momentum conservation, or more precisely the momentum imbalance of an associated collision. The vectorial sum of all particle momenta in the transverse plane in one collision should add up to zero, because the colliding protons do not carry any transverse momentum. The missing amount from the sum of all reconstructed momenta in the transverse plane is termed as the missing momentum, \vec{p}_T^{miss} , and serves as reference for undetected particles. \vec{p}_T^{miss} or its magnitude E_T^{miss} approximate the momentum of the neutrino in the case of a W analysis. Usually tracking and calorimeter information is combined to construct \vec{p}_T^{miss} . It has to be noted, that the measurement of \vec{p}_T^{miss} is accompanied by several sources of uncertainties. For instance particles, which miss the detector acceptance, or the activity of the UE will contribute and blur the resolution of the \vec{p}_T^{miss} measurement. Further analysis specific details are listed in Sec. 5.2 and Sec. 5.3.1.

Further objects reconstructed by ATLAS

Electron reconstruction

Electrons leave a track in the ID and shower in the EM. Hence, the energy deposits in the EM are grouped in clusters and if a cluster is associated to an ID track, it yields an electron candidate.

Photon (γ) reconstruction

Photons behave similar in the EM as electrons. They can also be identified by clustered energy deposits in the EM. The reconstructed shower shape allows to partially

discriminate photons from electrons. Photons are distinguished in converted and unconverted photons. The latter do not appear in the ID, but the former ones converted into a pair of e.g. electrons, which left two close tracks in the ID.

Jet reconstruction

Jets are the detector correspondence of hadronized partons. The particle showers leave clustered energy deposits in the EM and hadronic calorimeter. The calorimeter cells are usually merged into topological clusters, which are then subsequently formed to *jets* by a specified algorithm. The ATLAS standard for jets is the *Anti- k_t* algorithm [46]. The jet energy and direction is corrected for dead material and the electromagnetic and hadronic response of the calorimeters. The jet reconstruction is further sensitive to pile-up. Some jets can be identified with a certain quark-flavour (bottom or charm), if they are associated to a displaced vertex.

3.2.5 The Trigger system

The stunning collision rate of 40 MHz challenges all aspects of the detector, either due to the immense radiation or the tons of information to be read out. The latter is crucial for the final physics analysis, because it is impossible to read out and store all collision events. Therefore a trigger system decides almost immediately, which collisions are read out and passed to the full event reprocessing. In general, the trigger is designed to pick events, which include interesting physics processes, such as the creation of vector bosons. These are very likely to be associated with a highly energetic object like a muon or electron, and therefore these leptons can serve as a signal to fire the trigger. So the trigger system is required to rapidly identify signatures of such objects, which requires the input and combination of several detector systems.

The trigger system of the ATLAS detector [47, 48] incorporates different decision stages. It has to be noted, that the trigger system underwent major upgrades between RUN 1 and RUN 2 due to the increasing centre-of-mass energy and luminosity. Nevertheless, the basic principle remains similar for both run periods, which are part of this thesis.

The first trigger level (First Level hardware trigger (L1)) is purely hardware based. The core part, the Central Trigger Processor (CTP), receives inputs from the trigger chambers of the MS (L1Muon) and the calorimeter (L1Calo). The information of the calorimeter is passed in a lowered granularity compared to its full capability. The L1 trigger is also linked to other subsystems such as the Minimum Bias Trigger Scintillators (MBTS) or the LUCID detector. These are incorporated to reduce the bias on the event selection, which is a natural cause of a trigger system. The CTP induces a dead-time to the detector, if it is triggered. L1 reduced the read out rate down to 100 kHz during RUN 2 and 75 kHz during RUN 1. It defines the Region of Interest (RoI) of the detector, which resembles the trigger object path. This information on the RoI is further processed on the next trigger level, the High Level Trigger (HLT).

The HLT is formed by the Fast software trigger (L2) and Event Filter - precise software trigger (EF). It is a software based trigger system. L2 accesses the information of the RoI at higher granularity, but does not exploit the full information, which is done by the EF. The resources for L2 and the EF were merged for RUN 2, while they operated on different hardware systems during RUN 1. The HLT reconstructs objects within the RoI in a similar fashion as the full event reconstruction. The output rate of the HLT was 400 Hz during RUN 1 and 1 kHz during RUN 2.

If an event passes the trigger decision, the full event info is fetched from the buffer and passed as raw data to the reprocessing. The transformation to an event with reconstructed physics objects is resource intensive and performed on a computing grid, provided by several institutes.

4.

Event Simulation

The very essence of most experiments is the comparison between the theoretical prediction of a process and the actually measured quantity. The bare SM theory describes the particle interactions at the so called *particle level*. This is not compatible to the measured *detector level* quantity, because many effects influence the properties of the interaction products before it is registered in the detector: Unstable particles decay, colour charged ones hadronize, some might shower in multiple ways, and finally they interact with the detector material, which is then turned into a signal.

The important link between the theory prediction and the measurement in High Energy Physics is the simulation with Monte-Carlo event generators. They translate the probabilities of the SM processes, which are deduced from the matrix elements, into discrete particle predictions. The calculation involves multidimensional integrals of partially non-analytic functions, which are evaluated with Monte Carlo integration techniques, i.e. numerical integration using random numbers. Therefore, the simulation programs are further referred to as Monte-Carlo event generators. The most prominent Monte-Carlo event generators for pp interactions are PYTHIA [49, 50], SHERPA [51] and HERWIG [52]. All three are incorporated in the analysis presented in this thesis. PYTHIA usually serves as the nominal generator choice, because it is the most flexible one to be tuned to data. Hence, the following section refers to the functionality provided by PYTHIA, but it is noted, if the other generators implement significantly different approaches. PYTHIA, SHERPA and HERWIG are multiple purpose generators. They interface the PDF sets to the calculation of the hard scatter process, simulate the parton showers and finally apply the hadronization to the decay products. Further details are outlined in Sec. 4.1. A special focus is set on the parameters for modelling the soft part of the pp interaction for the sake of the UE measurement (see Sec. 4.2). The stable final state particles are passed to a full simulation of the ATLAS detector. The GEANT4 programme simulates the detector response by modelling the microscopic interactions between the final state particles and the detector material. The details are revisited in Sec. 4.3. Despite the highly complex and detailed simulation not all aspects are realized in the simulation. E.g. the amount of dead material and the operation of electronics is accompanied by several uncertainties. A dedicated detector calibration and correction for such effects is therefore performed. The main techniques and the effects on the final analysis are presented in Sec. 4.4.

4.1 The hard process: Matrix Element and parton showers

The factorization theorem is the essential concept, which allows to separate the different processes. Figure 4.1 illustrates exemplarily these stages of particle evolution. The principle is already outlined in Sec. 2.4.2 to justify the factorization of PDF sets.

The Monte-Carlo generators interface the PDF sets to the calculation of the hard scattering. In general, the hard scattering is evaluated with a fixed order tree level matrix element, i.e. two incoming partons interact and result in n outgoing parton lines, so called (tree level) legs. PYTHIA allows to calculate the matrix element for an outgoing vector boson and up to one additional parton. SHERPA incorporates up to five outgoing partons. It is also common to transfer the matrix element calculation to other programs, such as MADGRAPH [53], which provide higher order calculations.

The phase space of the additional partons overlaps with the partons created in the subsequent parton showering. The removal of the overlap is not trivial. The simulation samples used in this thesis utilize the POWHEG generator [54]. It provides matrix element calculation at NLO with an automated matching to the parton shower. The inclusion of additional partons in the matrix element provides a better description of hard emissions compared with covering the same order only by the parton shower algorithm.

The general functionality of a parton shower algorithm is to further evolve the outgoing legs of the matrix element to an intermediate state with many more but low energetic partons. The lower energy limit, the infrared cut-off scale, is typically about 1 GeV, because the non-perturbative effects of colour-confinement take over in this regime.

The splitting functions iteratively determine the probability for a parton to radiate another one and form the parton shower. The emissions follow some ordering scheme, usually starting from the ones, which have the largest impact on the kinematics, ending in low energetic or collinear emissions. The Monte-Carlo generators implement either a p_T -ordered shower model, which starts with the hardest emission, or an angular order shower model, which begins with the widest emission angle. PYTHIA8 and SHERPA implement a momentum ordered parton shower based on a dipole approach, while HERWIG exploits an angular ordered parton shower model. Higher order effects and collinear or low energetic emissions, which would result in divergences, are taken into account with Sudakov form factors. Somewhat simplified, these determine the probability of a parton to have no emission in a certain energy range. This effect is related to the infrared cut-off parameter and needs to be adjusted to data.

The FSR is the showering of the outgoing partons of the hard subprocess and its implementation is straight forward in the picture of parton showers. A special procedure is applied for the ISR, namely backward evolution. The incoming partons of the hard scattering require sufficient energy to produce e.g. the vector bosons. Therefore, the Monte-Carlo generators start from the corresponding momentum fraction of the partons and evolve these backwards. They gain energy with each splitting. A non-trivial part is then to match the ISR of the Monte-Carlo generator to the order provided in the PDF set.

The different generators apply individual techniques, how to further evolve partons from ISR, e.g. with different cut-off parameters or coupling strengths. The parton showers connect the partons from the proton PDF to the hard scattering. The parton showers present basically higher order corrections to the hard process, but their exact calculation is not possible. Hence, the parton shower schemes provide only an approximation. The result is passed to the hadronization model to form bound states based on phenomenological models.

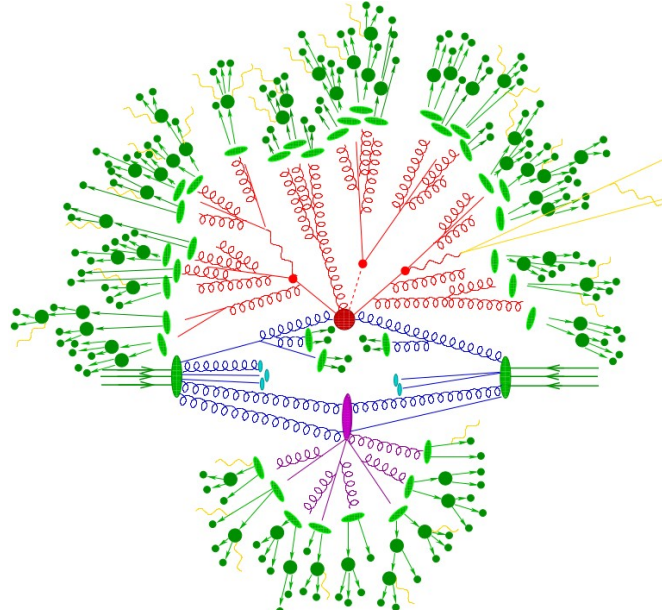


Figure 4.1: Pictorial representation of the event generation with a Monte-Carlo generator. The big red blob illustrates the hard interaction (here $t\bar{t}H$ production plus a QCD jet), the corresponding products decay subsequently. The purple blob visualizes an additional parton-parton interaction (MPI). The hadronization of the final state partons is initiated with the light green blobs, followed by hadron decays (dark green). The yellow lines represent photon emission. The figure is taken from Ref.[55].

4.2 The soft parts and its parameters

4.2.1 Hadronization models

The parton shower algorithms and the Matrix element calculations yield a list of coloured partons at the infrared cut-off. The coloured partons transform into colour-singlet primary hadrons as a consequence of colour confinement. The process is called hadronisation and is settled in the non-perturbative regime. Monte-Carlo generators realize it with semi-empirical models. PYTHIA implements an approach of string fragmentation, while HERWIG and SHERPA apply a cluster fragmentation model. Both models are briefly outlined in the following. The resulting hadrons decay further according to their measured lifetime and decay channels. The final outcomes are referred to as *final state particles*. The corresponding decay probabilities are usually referenced from the reviews of the *Particle Data Group*[56].

Lund String Model

The Lund string model [57] is motivated by the linear behaviour of the confinement. The corresponding force is imagined like a rubber band spanned between two colour-connected partons, that is pulled apart and eventually breaks into pieces. If the initial parton momentum is large enough to break the string a new $q\bar{q}$ pair is created, which is then subject to the same process. Otherwise, if the initial momentum does not break the rubber string, the partons are dragged towards each other and end in an state of oscillation. It is then interpreted as a meson.

The quarks obtain a mass and a transverse momentum in the breakup through a tunnelling mechanism. This feature suppresses heavy quarks. The formation of baryons is also included with the possibility of di-quark ($qq - \bar{q}\bar{q}$) breakups. The string

model delivers a very good energy-momentum picture. However, it does not reason hadron mass effects and includes many parameters, i.e. depending on the counting scheme 10 to 20 parameters.

Cluster model

The cluster model [58] exploits the *pre-confinement* of the QCD parton showers. Each gluon, that splits into a quark-anti-quark pair, determines a colour-connection between these two quarks. Further colour connections are formed along the subsequent splitting. The colour-singlet pairs, which end up close in phase space, form highly excited hadronic states, i.e. the clusters. The clusters are imagined as excited hadrons and undergo further decays into lighter well-known resonances and stable hadrons.

4.2.2 The MPI models

So far the Monte-Carlo generator functionality referred to only a single parton-parton interaction, namely the one with the largest momentum transfer, i.e. the hard scattering. However, it is highly likely, that several parton-parton interactions as well as multiple scattering of the very same parton might take place in one pp collision, due to the composite nature of protons. These additional scatterings are referred to as multiple parton interaction (MPI). They are characterized by much lower momentum transfer among the partons compared to the hard scattering. Therefore, MPI are settled in the transition regime between the perturbative and non-perturbative QCD models. They play an important role in the scope of this thesis, because they are considered as a part of the UE activity. Furthermore, they generally manifest in additional jets. And especially the hard perturbative tail of this jet spectrum, which follows $\frac{dp_T^2}{p_T^4}$, impacts the recoil measurement for the determination of m_W and Γ_W .

PYTHIA and SHERPA implement similar models to describe the ambivalent nature of MPI. Their model overlaps with the ideas for the MPI model of HERWIG++. Both models are summarized in Ref.[59] for the generator version included in this thesis. In the following only the major aspects are highlighted.

PYTHIA and SHERPA adopt the Sjöstrand–Zijl model [60] for MPI since several release iterations. It describes MPI as additional $2 \rightarrow 2$ scatterings, which are most likely introduced by the beam remnants. The possibility of the re-scattering of one parton, which is involved in the hard scattering, is also considered. The mean number of parton-parton interactions is assumed to be proportional to $\frac{\sigma_{2 \rightarrow 2}}{\sigma_{\text{ND}}}$, where σ_{ND} describes the non-diffractive and inelastic pp cross-section. $\sigma_{2 \rightarrow 2}$ is determined by perturbative QCD calculations similar to the hard scattering. In general, the MPI are processed with the same tools as the hard scattering. The MPI cross-section usually takes input from the same PDF sets and the interaction products underlie the same parton showering and hadronization algorithms. However, a rescaling of the PDF is implemented to consider the momentum fraction, which goes into other parton interactions as well as the correct colour flow.

The cross-section of MPI diverges for $p_T \rightarrow 0$ due to its proportionality to $\frac{dp_T^2}{p_T^4}$. The divergence is therefore fixed with a tunable cut-off parameter p_T^{min} , below which the perturbative cross section is either assumed completely vanishing or at least strongly damped. It is set phenomenologically in the order of 2 GeV with some energy dependence.

So far the individual parton-parton interaction MPI would be considered as independent and hence their number would follow a Poisson statistic. But the geometry

of the pp collision introduces some bias on the number of MPI: The smaller the impact parameter, the larger is the overlap of the protons and therefore it is more likely, that two incoming partons are close enough to interact. The resulting activity is proportional to the time-integrated overlap of the incoming hadrons. This overlap depends on one hand on the impact parameter, but on the other hand also on the matter distribution within the proton. PYTHIA assumes a double Gaussian matter distribution:

$$\rho(r) \propto \frac{1-\beta}{a_1^3} e^{-\frac{r^2}{a_1^2}} + \frac{\beta}{a_2^3} e^{-\frac{r^2}{a_2^2}} \quad (4.1)$$

The volume with radius a_2 contains the fraction β of the mass. It is embedded in the volume of radius a_1 containing the rest of the matter. The impact parameter dependence yields a suitable description of the *pedestal effect*, i.e. a more energetic hard scattering is correlated with a more central collision, which then leads to more UE activity or more MPI respectively.

HERWIG++ implements a formalism for MPI, which is complementary to the PYTHIA model. Additional semi-hard scatterings are also calculated with the standard QCD matrix element and rescaled PDF sets. The MPI are realized down to a cut-off $p_T > p_T^{\min}$. The first reference is a tuning to a Tevatron measurement [61], which yields $p_T^{\min} \approx 4$ GeV. Softer interactions are modelled with smooth non-perturbative modifications, which are complementary to the PYTHIA approach. However, HERWIG++ draws more stringent constraints on the MPI cross-section via the eikonal model [62]. The eikonal model couples the rate of MPI to the energy dependence of the total cross section.

The matter distribution is next to p_T^{\min} one of the most important tuning parameters. It is defined with the invariant beam particle radius μ and is described by the Fourier transform of the electromagnetic form factor. The distribution is similar to the double Gaussian implemented in PYTHIA. The default parameter is $\mu^2 = 1.5$ GeV and is also deduced from the Tevatron measurement. A detailed derivation is presented in Ref.[62].

4.3 Detector Simulation with GEANT4

The detector simulation proceeds the event simulation, after the hadronisation of the collision products. It is supposed to deliver a detector response as close as possible to the real world. Therefore, it is designed to simulate the interaction of the collision products with the detector material on a microscopic scale. It includes a variety of physical processes, such as multiple-scattering, nuclear reactions, decays and energy deposits.

The full design of the ATLAS detector is implemented in the GEANT4 [63] framework. It reproduces aspects like the magnetic field, the different materials used, as well as known defects and misalignments. GEANT4 realizes the passage of particles through the detector by a stepwise simulation. It propagates the particles iteratively and determines the possible interactions with Monte-Carlo methods. The list of (semi-)stable particles, so called final state particles, is interfaced into the GEANT4 framework from the Monte-Carlo generator.

The detail of simulation is designed to describe individual charges, which are deposited by the traversing ionizing particles and dragged to the read-out modules. This signal is defined as a *hit*, if it passes some threshold. The subsequent digitization simulates the response of the corresponding sub-detector. At this stage GEANT4 takes also into account noise signals such as cross-talk. The simulation further accounts

for the *aging* of the detector, i.e. the altering efficiency of the detector parts due to radiation damage. A special focus is set on the corresponding model for the ID, as it is exposed to the highest radiation dosage. Details about related studies are outlined in Sec. A.1. The signals are finally passed to the very same object reconstruction algorithms used for real data, in order to guarantee a high level of compatibility.

This highly detailed simulation is computing intensive. Hence, also simplified models are introduced, which use e.g. pre-defined shower shapes or simple maps to transfer the charge deposit into signals.

The accuracy of the presented simulations is validated by designated performance studies, which are described in the following Sec. 4.4.

4.4 Detector Corrections and Uncertainty Estimation

The measurement of m_W and Γ_W exploit the comparison between the real measurement and the simulation of the W decay. An adequate modelling of the detector response is crucial, because any bias in e.g. the measurement of p_T^μ would directly affect the result for m_W or Γ_W . The detector simulation is subject to high requirements to provide a measurement, which is precise enough to compete with the theoretical uncertainty on m_W and Γ_W .

Although the simulation contains an accurate description of the ATLAS detector, the level of detail is not enough to describe the resolution and efficiencies of the individual subdetectors down to the percent level. The remaining differences are covered with the application of scaling and correction factors to match the simulation to data. The Scaling Factor (SF) are obtained from the ratio of the measured observable in data and the observable measured with the same method in simulation. The correction factors are evaluated on benchmark distributions such as the p_T -resolution. These scaling and correction factors as well as remaining differences between data and simulation introduce sources of systematic uncertainties.

The following paragraphs briefly summarize the methodology to determine the detector performance and extract according correction factors or uncertainties, which are relevant within the scope of this thesis.

4.4.1 Inner Detector Tracking Performance and related Uncertainties for the 2015 dataset

The following performance studies and uncertainty estimates are taken from Reference [64]. These are performed on pp collision data from 2015 and provide the general recommendations from the ATLAS community to handle modelling uncertainties related to the ID for the data recorded during 2015. Reference [64] compares the data to Monte-Carlo simulations of PYTHIA8 and POWHEG+PYTHIA8. The methods are similar for RUN 1 parameters, solely the numbers change accordingly.

Track reconstruction efficiency and track-to-truth particle association

The track reconstruction efficiency is evaluated from simulation. The reconstructed tracks are associated to primary charged particles via a hit-based track-to-truth particle matching [65]. This method uses detector signals (clusters) which are located on a fitted reconstructed track, termed here as shared or common clusters. Each of the clusters is associated to the charged particle, which has the largest energy deposition in the GEANT4 simulation. The clusters are then weighted according to their importance in the track reconstruction, i.e. depending on their distance to the interaction point. The number of shared clusters within the Pixel detector (N_{Pixel}^{common})

receives the highest weight, SCT clusters are assigned with an intermediate weight and the TRT receives the minimal weight.

The weighted matching probability (P_{match}) is then defined by the ratio of the number of hits, which are common to a given track and the corresponding truth particle ($N_{Pixel,SCT,TRT}^{common}$), and the number of hits, which form the reconstructed track ($N_{Pixel,SCT,TRT}^{track}$):

$$P_{match} = \frac{10 \cdot N_{Pixel}^{common} + 5 \cdot N_{SCT}^{common} + 1 \cdot N_{TRT}^{common}}{10 \cdot N_{Pixel}^{track} + 5 \cdot N_{SCT}^{track} + 1 \cdot N_{TRT}^{track}} \quad (4.2)$$

A reconstructed track is linked to a charged particle if $P_{match} > 0.5$.

The track reconstruction efficiency ($\epsilon_{trk}(p_T, \eta)$) is then defined as the ratio of the number of reconstructed tracks, which are matched to truth charged particles ($N_{rec}^{matched}$), over the number of truth charged particles (N_{gen}) in the same (p_T, η) range:

$$\epsilon_{trk}(p_T, \eta) = \frac{N_{rec}^{matched}(p_T, \eta)}{N_{gen}(p_T, \eta)} \quad (4.3)$$

It ranges from about 90% for loose tracks in the central region to 70% for tight tracks in the peripheral parts ($|\eta| > 2$). In general, the track reconstruction efficiency lowers with increasing $|\eta|$, because the particles need to traverse a larger amount of material, which might deflect their path. The track reconstruction efficiency improves for higher values of p_T , as the tracks approximate a rather linear path, which simplifies the combination of hits.

Track reconstruction efficiency: systematic uncertainty

The track reconstruction efficiency is a crucial input for unfolding the data (see Sec. 6.4). But it is limited by the quality of the detector simulation. More precisely, the uncertainty on the track reconstruction efficiency is constrained by the knowledge of the ID material distribution. The simulation varies the amount of passive detector material, which might deflect the traversing particles, within its uncertainties in order to access the final impact on the track reconstruction efficiency.

There are four components to the uncertainty based on the ID material study described in Ref.[66]. An uncertainty of $\pm 5\%$ is assigned to the extra material uniformly distributed in the ID. It was already studied for RUN 1, which drives this level of precision. The amount of material in the Pixel services regions is varied by 25% in the central part and by 50% for $|\eta| > 1.5$. This is derived for example from the reconstruction of conversion vertices, where photons convert into electron pairs within the ID. The conversion probability is almost proportional to the amount of material the photon traverses. Hence, the multiplicity of vertices yields a direct measure of the material density. Another method is to extrapolate reconstructed tracks from one subdetector, e.g. SCT to another. Similar methods bring the uncertainty down to 10% for the extra material uniformly distributed in the IBL region.

Reference [64] states a total systematic uncertainty on the track reconstruction efficiency ranging from 0.4% for the central part with less service structure to 2.6% in the peripheral parts of the ID ($2.3 \leq |\eta| \leq 2.5$).

Fake rate

The immense number of hits measured in the ID yields several possibilities to combine these hits to tracks. Hence, not all reconstructed tracks correspond to a charged particle traversing the detector. The tracks from combinatorial background are called 'fake tracks' or 'fakes', as they are mimicking the signal of a charged particle. It is not possible to determine in real data, if a single track is a fake or not, but the amount

of fake tracks, the ‘fake rate’, rises linearly with the number of interactions during one bunch-crossing (μ). The modelling of the fake rate is tested by comparing the linear growth of the number of tracks as a function of μ for data and Monte-Carlo simulations. The size of the differences between data and MC is about 30% and serves as the recommended systematic uncertainty to be applied on the fake rate.

Track Impact Parameter Resolution

The transverse (d_0) and longitudinal (z_0) impact parameters are crucial to discriminate tracks originating from primary vertices from tracks originating from secondary vertices. The intrinsic track impact parameter resolution is measured as function of (p_T, η) of the tracks, because the curvature and the detector material affect the quality of the reconstruction. The track impact parameters are defined with respect to the position of the reconstructed primary vertex.

In data the resolution is defined as the width of a Gaussian function fitted to the impact parameters measured in one bin of (p_T, η) , after deconvolving the uncertainty on the position of the primary vertex. The simulation compares the reconstructed track impact parameters to the ones from the associated charged particles on generator level. In this case, the resolutions are calculated from difference of these two quantities. Additionally, the track impact parameter resolution is sensitive to the detector alignment and the number of not properly working modules of the pixel detector. The simulation is performed with different models for the detector alignment (cf. [67]) and with 5% (randomly) disabled modules of the pixel detectors in order to access these effects. The average resolution of d_0 is found to be in the order of 15 μm and about 50 μm for z_0 . The quadratic difference of the resolutions between the data and simulation ($\sqrt{\sigma_{Data}^2 - \sigma_{MC}^2}$) is defined to be the systematic uncertainty on the impact parameter resolutions.

Weak Modes

Weak modes are global distortions of the detector which cannot be easily removed by the ID alignment algorithms. The detector is deformed, but the track fits remain invariant. Three types of resulting biases on reconstructed track parameters are relevant for physics results: the impact parameters as well as the Sagitta for the charge over momentum ($\frac{q}{p}$) measurement. The size of the related uncertainties are studied in Reference [68].

4.4.2 Muon reconstruction performance and related systematic uncertainties

Reference [69] and [70] present measurements of the muon reconstruction and isolation efficiency, as well as of the muon momentum scale and resolution based on the 2015 dataset and the RUN 1 data respectively. The measurements are compared to Monte-Carlo simulations. The ratios of the individual efficiencies obtained in data and simulation represent the final SFs, while the resolution and scale corrections rely on a set of fitted parameters.

Derivation of SFs via a tag-and-probe method

The SFs are derived via a tag-and-probe method from $Z \rightarrow \mu\mu$ events.¹ These events are required to contain two muon candidates, whose invariant mass is close to the Z mass peak, i.e. $|m_Z - m_{\mu\mu}| \leq 10 \text{ GeV}$. If one muon candidate satisfies relatively tight selection criteria, it is depicted as the *tag*. In this case, it is highly probable that the second muon candidate, which passes looser selection criteria, is a true muon. It is called the *probe* and used to determine the different efficiencies.

¹The scale and correction factors are also derived from $J/\psi \rightarrow \mu\mu$ events. These serve for a lower p_T range, which is not relevant within the scope of the analysis presented here.

The efficiency measured in the data is corrected for the background contributions by subtracting the predicted probe yields from e.g. $t\bar{t}$ -events. It is defined as the ratio of the successfully reconstructed probes (N_R) and the total number of probes (N_P):

$$\epsilon = \frac{N_R^{Data} - N_R^{Bkg}}{N_P^{Data} - N_P^{Bkg}} \quad (4.4)$$

The selection criteria for the tags and probes vary for the individual efficiency measurements. There are three different categories of SFs applied to reconstructed muons in the simulation. The reconstruction scale factor adapts the efficiency of the reconstruction of a track in the muon system matching to an inner detector track. The isolation scale factor adjusts the probability of these muons to pass a detector-based isolation requirement. And the application of the trigger scale factor shapes the probability of a muon to have fired the trigger. These are referenced from Ref. [48]. The SFs are evaluated for the reconstruction, the isolation and the trigger efficiency individually.

The precision of the final SFs is limited by the size of the dataset from which they are deduced. Therefore, a statistical uncertainty accounts for this effect as a systematic uncertainty on the individual SFs. Furthermore, a systematic uncertainty comprises the effects of the theoretical and methodological uncertainty on the background yields. The interdependency of the different efficiencies is evaluated as well, but represents a minor source of a systematic uncertainty.

Muon momentum scale and resolution

The precise reconstruction of $Z \rightarrow \mu\mu$ events serves as a perfect environment to study the muon momentum scale and resolution. The detector simulation is not capable of fully reproducing the p_T -spectrum and the p_T -resolution of the muons observed in data. The comparison reveals deviations in the permille level for the muon momentum scale and in the percent level for the muon momentum resolution [69]. The discrepancies for p_T originate from a detector displacement, which causes a radial bias on the reconstructed muon track. The resolution is affected by inhomogeneities of the magnetic field, the distribution of passive material and the detector alignment.

The muon scale correction is parametrized as following: ²

$$p_T^{Cor} = p_T^{MC} (1 + \alpha(\eta, \phi)) (1 + \beta_{Mult}(\eta, \phi) G(0, 1) + \beta_{Curv}(\eta, \phi) G(0, 1) p_T^{MC}) \quad (4.5)$$

Here p_T^{MC} is the uncorrected transverse momentum in simulation, $G(0, 1)$ is a normally distributed random variable with mean 0 and width 1. The factor α corrects for the scale, while $\beta_{Curv, Mult}$ describes the momentum resolution smearing. It broadens the relative p_T resolution to describe the data. The terms with $\beta_{Curv, Mult}$ rely on the following empirical parametrization of the muon momentum resolution [71]

$$\frac{\sigma(p_T)}{p_T} = r_0/p_T \oplus r_1 \oplus r_2 \cdot p_T \quad (4.6)$$

The first term accounts for fluctuations of the energy loss in the traversed material, which is neglected in Eq. 4.5. The second one describes effects of multiple scattering, local magnetic field inhomogeneities and local radial displacements, which is included in β_{Mult} . The last term characterizes resolution effects caused by the spatial resolution of the hit measurements and by residual misalignment. This is depicted in β_{Curv} .

²Reference [69] presents an extended version of this parametrization, which distinguishes the different subdetectors involved in the muon reconstruction. The formula here is condensed to the parameters relevant to the analysis.

Additionally, a third correction, Sagitta bias, corrects the data for charge dependent local effects due to misalignments in the ID and smaller local effects due to local misalignments in the MS:

$$p_{\top}^{data,Cor} = \frac{p_{\top}^{data}}{1 + q \cdot \delta(\eta, \phi) \cdot p_{\top}^{data}} \quad (4.7)$$

The corrections factors are deduced in various regions of η and ϕ to account for the detector geometry. They are extracted from data using a binned maximum-likelihood fit with templates similar to the technique described in Sec. 5.9.1. The templates are derived from simulation. The invariant mass distributions for $Z \rightarrow \mu\mu$ events serve as the fit basis.

The uncertainties on the parameter estimates are propagated as systematic uncertainties. These are provided as up and down variations of the momentum scale α , as well as a variation of the smearing of the tracks reconstructed in the MS or in the ID. These emerge in variations of $\beta_{Curv,Mult}$. The Sagitta bias correction is provided with systematic uncertainties based on the residual charge-dependent bias after applying this correction and the dependency on the muon momentum scale.

Muon performance and uncertainties for the m_W measurement

In the original ATLAS measurement of m_W [72], the corrections are evaluated for the muon characteristics in dedicated analysis [73, 74] to further improve the compatibility between data and simulation. The studies exploit similar techniques (tag-and-probe with $Z \rightarrow \mu\mu$ events, template fits to $M_{Z \rightarrow \mu\mu}$), with a (η, ϕ) dependence optimised for the m_W measurement. They enhance the sensitivity by extrapolating the correction and scale factors from the scale of m_Z , where they are deduced, to the scale of m_W .

4.4.3 Pile Up correction

The number of interactions per bunch crossing (μ) is a function of the instantaneous luminosity (\mathcal{L}), which itself depends on the recent run conditions, such as the beam geometry (spatial extension and focal point) and the filling (number of protons per bunch). The simulation cannot map these parameters as they are also time dependent e.g. due to the burning rate (loss of protons) during collisions. Hence, the simulation events are provided only for discrete pile-up conditions and are later reweighted to the conditions of the data set of interest. The full reweighting procedure is performed with the pile-up reweighting tool provided by the ATLAS community [75].

The benchmark for the reweighting process is the $\langle \mu \rangle$, which is defined per Lumi-block, i.e. a period of constant beam conditions. It is connected to the instantaneous luminosity via the total inelastic cross-section for pp collisions (σ_{pp}) and the average bunch crossing rate (f_{BC}), as outlined in Eq. 3.2. It is directly correlated to the actual number of vertices per collision, but is likely higher due to vertex reconstruction effects. The relation is illustrated exemplarily in Fig. 4.2. Therefore, $\langle \mu \rangle$ is a first measure for pile-up contamination to the events. The correct description by the simulation is of great importance to the measurement of the UE and the hadronic recoil, which is essential for the measurement of m_W .

The uncertainty on the instantaneous luminosity and the bunch crossing frequency is negligible for the determination of $\langle \mu \rangle$. But a systematic uncertainty on the pile-up reweighting is introduced to take into account the uncertainty on σ_{pp} . It covers the uncertainty from the ratio between the predicted and measured inelastic cross-section in the fiducial volume defined by $M_X > 13 \text{ GeV}$, where M_X is the mass of the hadronic system [76]. The value of $\langle \mu \rangle$ assumed in the Monte-Carlo simulations is varied by $\pm 9\%$ from the nominal value. In other words, the amount of pile-up in the simulation

is increased or decreased to estimate this systematic uncertainty.

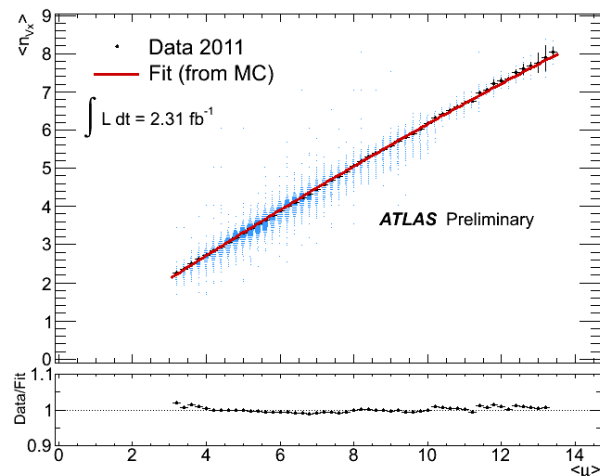


Figure 4.2: Distribution of the average number of reconstructed vertices as function of the average number of interactions per bunch crossing. The azure boxes show the mean number of reconstructed vertices per minute of data taking. The plot is taken from Ref. [77].

4.4.4 Beam spot size (primary vertex reconstruction)

The modelling of the beam geometry affects also the position of the reconstructed vertices. Usually, the beam spot size is wider in the Monte-Carlo simulations than in the actual beam setup. This way it is possible to reweight the Monte-Carlo simulation to match the data of interest. This correction is applied solely to the longitudinal parameter, because the transversal beam spread is usually not varied during the runs, because it is naturally limited by the size of the beam pipe. The correction factors adjust the distribution of the longitudinal position of the primary pp collision vertex [77] to the one observed in the data.

The correction factors are constructed from a comparison of data and Monte-Carlo distributions of the position of the primary vertex along the z -axis. (z^{PV}) The bin-wise ratio of data over Monte-Carlo serves as correction factor for a Monte-Carlo generated event reconstructed in the according bin of z^{PV} . The longitudinal position and resolution of the primary vertex plays an important role for the overall pile-up rejection.

Part II

On the road to precision with the ATLAS experiment



5.

Reanalysis of the W boson mass and a first measurement of its width with the ATLAS detector

5.1 Motivation to re-analyze the m_W measurement

The properties of the W boson take on a key role in consistency tests of the SM. The global electroweak fit is able to probe the SM relations for possible BSM contributions, if the parameters are known to sufficient precision. The corresponding detail are already outlined in Sec. 2.6. The mass of the W boson is of special importance and is therefore measured with ever improving precision. A selection of measurements is displayed in Fig. 5.1. The latest measurement of m_W at a centre-of-mass energy

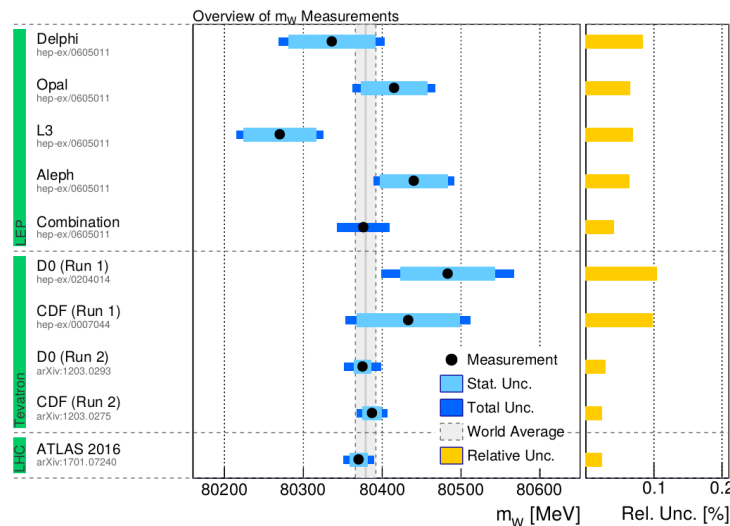


Figure 5.1: Overview of selected measurements of m_W , including the most precise measurements from Large Electron-Positron collider (LEP) [78], Tevatron [79] and the LHC [72]. The grey area presents the world average of $m_W = 80380 \pm 13$ MeV. The figure is taken from Ref. [27].

of $\sqrt{s} = 7$ TeV by the ATLAS collaboration achieved the remarkable result of $m_W = (80370 \pm 19)$ MeV [72]. However, it was previously estimated, that an ultimate precision of $\delta m_W = 7$ MeV is achievable with the LHC data [80]. The latest developments of ancillary measurements provide new inputs to reach this precision. An advanced fit approach is the key to the full potential of all these improvements. This thesis presents the new fitting strategy and evaluates it on the original samples of the previously mentioned legacy ATLAS measurement. ¹

¹The original measurement by ATLAS at $\sqrt{s} = 7$ TeV, which is published in Ref.[72], will from now on referred to as *legacy* measurement for simplicity.

The mass of the W boson is determined from the measurement of the energy of its decay products ($W \rightarrow e\nu, W \rightarrow \mu\nu$). The new fit approach employs a template fit of the corresponding distributions similar to the legacy analysis. But the new fit strategy profits from a Profile Likelihood Ratio estimate (PLH), while the legacy measurement relies on a χ^2 -minimization. This thesis evaluates the new approach and validates it against the legacy one. The advantage of the PLH approach is, that it incorporates the systematic uncertainties directly into the fit as nuisance parameter (NP). These are then further constrained by the fit itself. The specific details are introduced in Sec. 5.9. The incorporation of the PLH ratio enhances the sensitivity to the shape differences of the theory modelling, namely the PDF sets, and reduces the impact of the related uncertainties. The enhanced sensitivity to the uncertainties related to the theory modelling is a key point for the improvement, because they dominated the total uncertainty of the legacy measurement. Moreover, recent LHC measurements of e.g. W/Z -cross-sections in association with heavy quark flavours (cf. exemplarily [81]) constrain the modern PDF sets and further reduce the accompanying uncertainties [21]. A driving role of the improvement is for instance the improved estimate of the contribution of heavy quarks [82] to the production of the W boson at the LHC. It is anticipated to include the newly constrained PDF sets at the final stage of the analysis, which further highlights the potential for an improved precision.

Furthermore, the knowledge of the detector and hence the detector modelling improved since the $\sqrt{s} = 7$ TeV data taking period. With the end of RUN 2 a huge amount of data is available to reduce the uncertainties related to the detector response. This significantly reduces the uncertainties on the lepton momentum corrections, which were originally deduced from the $\sqrt{s} = 7$ TeV dataset only [73]. Hence, a reanalysis of the $\sqrt{s} = 7$ TeV dataset, which includes these reduced uncertainties, will further minimize the uncertainty on m_W .

The implementation of the new fit approach with its enhanced shape sensitivity enables the measurement of a further parameter of the W boson, namely its decay width (Γ_W) as introduced in Sec. 2.4.5. It is interlaced with the mass of the W boson and predicted to be equal to the sum of the partial widths of the decay channels, i.e. all three lepton generations and two quark doublet generations. The partial widths are expressed as following:

$$\begin{aligned}\Gamma_{W \rightarrow f\bar{f}'} &= \frac{|M_{f\bar{f}'}| N_C G_\mu m_W^3}{6\pi\sqrt{2}} \left[1 + \delta_f^{rad}(m_t, M_H, \dots) \right] \\ \Gamma_{W \rightarrow \mu\bar{\nu}} &= \frac{G_\mu m_W^3}{6\pi\sqrt{2}} \left[1 + \delta_l^{rad} \right]\end{aligned}\tag{5.1}$$

The first line is the more general expression for any of the possible decay fermions f , with the colour factor N_C and $M_{f\bar{f}'}$ representing the CKM matrix elements. Both vanish in the second line, which expresses the width for the muonic decay channel. δ^{rad} summarizes electroweak radiative corrections including corrections to α_s [83, 84] and is found to be $\delta_l^{rad} \approx -0.34\%$ [85].

The measurement of Γ_W introduces on one hand an additional consistency test of the SM, and on the other hand it constrains predictions for new particles, which could open an additional decay channel of the W boson. The latter one would alter Γ_W .

The measurement strategy for Γ_W is almost congruent to measuring m_W at hadron colliders, comparing for instance the measurements of the CDF Collaboration as published in Ref.[86] and Ref.[87]. The ongoing reanalysis effort of m_W at $\sqrt{s} = 7$ TeV with the ATLAS detector therefore exploits this synergy and performs the measurement of

Γ_W on the very same dataset including all considerations on the related uncertainties. But the fit for Γ_W is performed blinded, i.e. an unknown offset is added to the measured values of Γ_W , to avoid any bias towards former measurements, while the measurement of m_W is unblinded in this thesis, in order to validate the reanalysis effort with the legacy values. The blinding of Γ_W is required, because the analysis is still reviewed by the ATLAS collaboration and will be published afterwards.

Once again, the new fit procedure plays a crucial role for the measurement of Γ_W , because the sensitivity of the observables to the width is much more subtle than the sensitivity to the mass of the W boson. The establishment of the PLH in the scope of a template fit approach delivers the sensitivity for a competitive measurement of Γ_W with the ATLAS detector. The precision of the global average value, $\Gamma_W^{global} = 2.085 \pm 0.042$ GeV [56], sets a natural target for the precision of the measurement of Γ_W , in order to be relevant for precision tests. This thesis presents the first competitive results for the muon decay channel.

5.2 Overview and measurement strategy

The W boson decays almost instantly after its production. The boson itself is therefore not detectable, but its decay products can be traced with the ATLAS detector. The mass and the decay width of the W boson manifest in the kinematics of these decay products, the corresponding details are outlined in Sec. 2.4.5. The most profitable measurement of the W mass and width are the kinematics in the transverse plane of the leptonic decay channels. This thesis focuses on the muon channel only, because the studies serve as a proof of principle. The final measurement anticipates a combination with the electron channel results.

There are three relevant observables, which are sensitive to m_W and Γ_W :

- p_T^ℓ , the transverse momentum of the decay lepton (in the scope of the thesis a muon: p_T^μ).
- $\vec{E}_T^{miss} = \vec{p}_T^\nu = -\vec{p}_T^\ell + \vec{p}_T^W$, the missing transverse momentum or energy. It is an approximation for the transverse momentum of the second, undetectable, decay product, the neutrino. The transverse momentum of the W boson, p_T^W , is experimentally estimated with the hadronic recoil (u_T), which is defined as the vectorial sum of the reconstructed energy clusters in the calorimeters ($u_T = \sum \vec{E}_T$). The geometrical relation is illustrated in Fig. 5.2.

- The transverse mass: $m_T = \sqrt{2p_T^\ell \vec{E}_T^{miss} (1 - \cos \Delta\Phi (p_T^\ell, \vec{E}_T^{miss}))}$

$\Delta\Phi$ is the opening angle between \vec{E}_T^{miss} and \vec{p}_T^ℓ in the transverse plane. m_T corresponds to the invariant mass of the dilepton system, when the W boson decays fully in the transverse plane.

This thesis follows the strategy of the legacy publication [72] and considers only p_T^μ and m_T for the measurements. The measurement of \vec{E}_T^{miss} is of significantly lower precision and is solely exploited for consistency checks in the original analysis. The precision of the \vec{E}_T^{miss} and m_T measurements, respectively, suffers mainly from the uncertainties on the calorimeter response parameters and is highly sensitive to pile-up as well as the UE activity. In contrast, p_T^μ is measured with very high precision and almost unaffected by pile-up. But the distributions of p_T^μ are more sensitive to the uncertainties of the physics and detector-modelling than m_T .

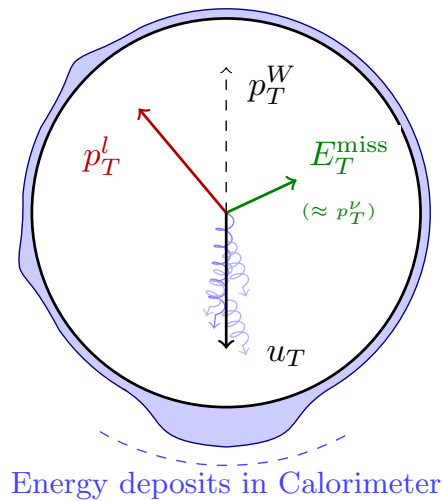


Figure 5.2: Illustration of the geometrical relations between the hadronic recoil, u_T , which serves as reference for p_T^W , the lepton momentum, p_T^l , and the missing transverse energy, \vec{E}_T^{miss} . The latter approximates the momentum of the undetected neutrino and is inferred from the imbalance of measured vectorial energies. The blue area symbolizes energy deposits in the calorimeters.

Detector effects, such as the finite resolution, smear the spectra of p_T^μ and m_T and prevent the direct access to the mass and width of the W boson. The application of forward folding [88] takes these effects into account. It applies detector effects via simulation to the theory predictions of the Monte-Carlo generators. The forward-folded distributions of the generator-level distributions then become compatible to the reconstructed data distributions.

The preparation of the simulation samples and the estimates of the related systematic uncertainties are a major focus of the legacy W mass analysis. The corresponding corrections are adopted for the reanalysis in this thesis. The sections 5.5 to 5.8 summarize the variety of modifications, in order to explain the impact on the final total uncertainty. The corrections to the modelling of the detector are presented in Sec. 5.7 and Sec. 5.8. The physics modelling, such as the boson transverse momentum, is solely available at finite order, and requires to be modified as well. This is the focus of Sec. 5.6.

The mass and width are extracted from the comparison of the measured data distributions and the forward-folded Monte-Carlo generator predictions. The technique is known as *template-fit* approach and is also used in former measurements of m_W and Γ_W by the CDF or DØ collaborations [86, 87, 89]. The Monte-Carlo simulation produces distributions of m_T and p_T^μ based on different values for m_W or Γ_W , respectively. These distributions are referred to as *templates*. Fig. 5.3 shows an example for three different m_W -templates. The compatibility of the different templates to data is evaluated. The legacy analysis employs a χ^2 -test to measure the compatibility. The one template corresponding to the minimal χ^2 value serves as the final estimate for the parameter of interest, i.e. m_W or Γ_W . The procedure is presented in detail for m_W in Sec. 5.9.1 to validate the successful resurrection of the $\sqrt{s} = 7$ TeV samples. The newly introduced PLH approach is discussed in Sec. 5.9.2.

The final measurements of m_W and Γ_W are performed in different channels. They

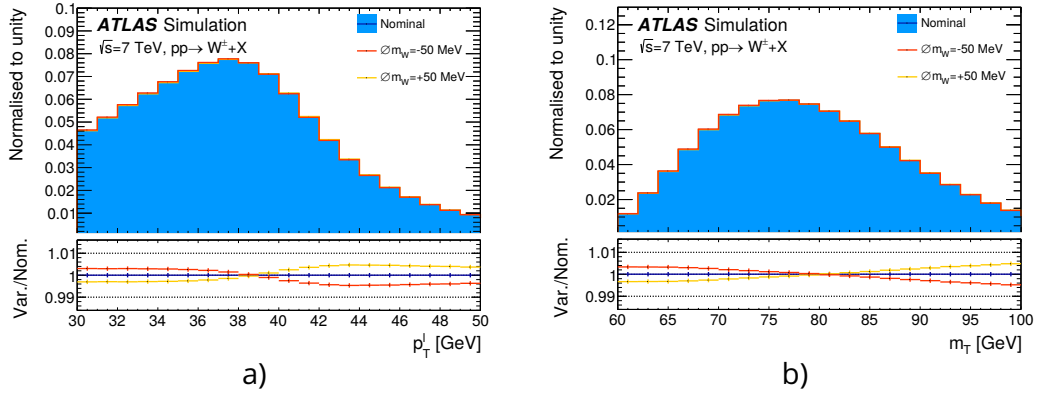


Figure 5.3: Templates of the p_T^μ (a) and m_T (b) distributions for three different values of m_W . The templates are forward-folded with the response of the ATLAS detector. Both are taken from [72].

Table 5.1: Summary of categories and kinematic distributions used in the m_W and Γ_W measurements.

Channels	Distinction
Kinematic distribution	p_T^μ, m_T
Charge categories	W^-, W^+
$ \eta^\mu $ categories	$[0,0.8],[0.8,1.4],[1.4,2.0],[2.0,2.4]$

are split in categories of the distributions of the lepton charge and the lepton pseudorapidity ($|\eta^\mu|$). The discrimination allows to compare and decorrelate the impact of e.g. the charge dependence in different systematic uncertainties. Furthermore, the distinction in η -regions enhances the sensitivity to the effects of PDF uncertainties, which are themselves η dependent. All categories and the pseudorapidity boundaries are listed in Tab. 5.1. The choice of the pseudorapidity regions is driven by experimental and statistical constraints.

The most powerful measurement is the combination of these different channels. This thesis presents the combination for all channels in p_T^μ and m_T .

In general, the full analysis procedure is similar for measuring m_W or Γ_W . But the two parameters are correlated, so that they either need to be considered in parallel with a two dimensional fit or by performing iterative fits in one dimension. The latter approach foresees to firstly measure m_W , and then to fix the measured value of m_W in the Monte-Carlo simulations. The second step will measure Γ_W with these newly produced templates. This procedure could be repeated, i.e. measuring m_W again with the newly measured value of Γ_W , but one iteration should be sufficient, because m_W is affected η maximally by 3 MeV, when Γ_W is varied within its current uncertainty of 42 MeV.

Nevertheless, this dependent evaluation exceeds the scope of this thesis. Hence, it is anticipated for the corresponding publication. Here, the width and the mass of the W boson are determined separately. One of the two parameters, m_W or Γ_W , is kept fixed at the nominal value, i.e. the world average, while the other is altered for the template production.

5.3 Signal process selection

The process of interest here is the production of W bosons, which subsequently decay into a muon-neutrino pair, $W \rightarrow \mu\nu$. Only the muon is detectable with the ATLAS detector in this final state, while the neutrino is generally linked to significant values of \vec{E}_T^{miss} and hadronic recoil, u_T , respectively. The event selection focuses on signatures related to these objects. The following section summarizes the event and object selection from Reference [72]. It is applied to the data and simulation samples introduced in the subsequent Sec. 5.4.

The legacy samples are only available without the final selection. However, the $W \rightarrow \mu\nu$ event candidate selection is re-performed in the scope of the re-analysis to allow an extended fitting range in m_T and p_T^μ . The selection process is validated with a brief comparison of the resurrected cutflow with the legacy one in Sec. 5.4.4.

5.3.1 Event selection

The event and object selection is standardized within the ATLAS community and is guided by the technical event reconstruction. The recommended procedure for most ATLAS analysis follows these selection steps:

1. Requirements on the data quality
2. Trigger conditions
3. Requirements single reconstructed objects (here one muon, hadronic recoil and \vec{E}_T^{miss})
4. Combined conditions for W boson candidates

If an event passes the final selection step, the corresponding objects are used to construct the observables p_T^ℓ and m_T . The following selection requirements extend the regular recommendations of the ATLAS community for $W \rightarrow \mu\nu$ events. The criteria are optimised to reduce the contribution from multijet background and to minimise model uncertainties from W bosons produced at high transverse momentum.

The first step requires, that the ATLAS detector is running on nominal conditions, such as high voltage ramped up and no major defects are recorded during data taking. The trigger condition for this analysis is one muon candidate carrying transverse momentum larger than 18 GeV. All events need to contain at least one reconstructed collision vertex subsequent to the trigger condition. A vertex requires at least two associated tracks with $p_T > 400$ MeV due to the vertex-reconstruction algorithm. The reconstructed vertex with the highest $\sum p_T^2$ of the associated tracks in the event is defined to be the primary vertex and represents the pp collision under investigation.

The collision products coming from the primary vertex are further investigated, if they are compatible with the final state of $W \rightarrow \mu\nu$. This determines the conditions on the muon and the hadronic recoil u_T .

5.3.2 Muon selection

The muon candidates are identified with the combined information of the MS and ID as described in Sec. 3.2. Only the ID hits are used to derive the kinematic properties of the muon, which simplifies the calibration process. The accompanying loss of 10-14 % of the momentum resolution is negligible in the investigated measurement range. The reconstructed transverse momentum p_T^μ is required to be larger than

20 GeV. It supersedes the trigger threshold and safeguards against efficiency losses close to the trigger-edge. Furthermore, the cut on $p_T^\mu > 20$ GeV guarantees a peak efficiency of the muon trigger and resolution [48]. The muon candidate must equal the trigger-object, which restricts the muon candidate to be within the geometric trigger range of $|\eta| < 2.4$.

Furthermore the muon candidates are cleaned from contributions from cosmic muons or muons created in pile-up collisions. In other words, the muon candidates must be associated to the primary vertex. This requires that the longitudinal impact parameter ($|z_0 \sin \theta|$) is less than 10 mm with z_0 measured relative to the primary vertex.

It is crucial to suppress muon candidates originating from multi-jet background. Hence, the activity in vicinity of the muon is limited for the selection. In detail, the measured $\sum p_T$ of the tracks within a $\Delta R < 0.2$ cone around the muon must be below 10% of the muon transverse momentum.

5.3.3 Hadronic recoil reconstruction

The second decay product, the neutrino, is not detectable with the ATLAS detector. But the hadronic recoil in the transverse plane, u_T , gives an estimate for the momentum of the vector boson and therefore indirectly of the neutrino, respectively, as illustrated in Fig. 5.2. The hadronic recoil consists of the hadronized ISR recoiling against the vector-boson. Most of its energy is deposited in the calorimeters, but a certain fraction is lost undetected in the dead material. Therefore, it serves solely as an estimate. However, u_T is constructed in three steps:

1. The measurement is based on a cluster-based approach: The vector sum of all topological-clusters (see for details Sec. 3.2) is calculated as a first estimate for u_T .
2. The showering signal muons also deposit energy in the calorimeters. When p_T^μ is combined with u_T from the previous step, this energy would be double counted. Hence, parts of the energy clusters are excluded from the vectorial sum, if they are within a $\Delta R < 0.2$ cone around the muon.
3. The previous step removes also the energy contribution coming from the UE, which degrades the resolution. It is compensated by replacing the removed energy cone with an energy cone measured in the same pseudo-rapidity region. Furthermore, the replacement cone is required to be sufficiently far away in the transverse plane ($\Delta\Phi > 0.6$) to avoid overlap with the showers.

The hadronic recoil u_T is included in the event selection and the construction of m_T , after the correction for the UE activity.

A sufficiently well modelled simulation of the activity of the UE yields a further possibility to improve the measurement of u_T . A first step in this direction is the analysis presented in Chapter 6. Nonetheless, future measurements at higher collision energies anticipate a more complex algorithm to construct u_T , because of the rising pile-up and UE activity. Both carry the same signature and smear the resolution of the u_T measurement.

5.3.4 W boson candidate selection

The combination of the two reconstructed quantities, the muon and the hadronic recoil, gives access to the kinematics of the W boson candidate. Of course, there are other processes, which create a similar signature, e.g. if a muon is created within a jet, there is also one muon and some hadronic recoil measured due to the hadronic collision environment. In order to further clean the W boson candidate events especially from multijet background, the following requirements are introduced:

- the event contains exactly one muon with $p_T^\mu > 30 \text{ GeV}$
- $|\vec{E}_T^{miss}| = |\vec{u}_T - \vec{p}_T^\ell| > 30 \text{ GeV}$
- $u_T < 30 \text{ GeV}$
- $m_T > 60 \text{ GeV}$

All conditions are optimized to reduce the multijet contribution. Especially, the lower tail of m_T is dominated by this background. The upper limit for u_T sets an indirect restriction on W bosons produced with high transverse momentum. These are suppressed, because they suffer from larger model uncertainties due to the larger amount of ISR.

If a data or Monte-Carlo simulation event passes all requirements from above, it enters the distributions for the template fit.

5.4 Data and Monte-Carlo simulation samples

5.4.1 The 2011 pp collision data

In 2011 the LHC delivered pp collisions at $\sqrt{s} = 7 \text{ TeV}$ corresponding to an integrated luminosity of $\int \mathcal{L} dt = 5.46 \text{ fb}^{-1}$. The ATLAS detector recorded an amount of $\int \mathcal{L} dt = 5.08 \text{ fb}^{-1}$, of which 4.57 fb^{-1} meet the quality requirements for entering physics analysis (see also Fig. 5.4). Only $\int \mathcal{L} dt = 4.1 \text{ fb}^{-1}$ of these recorded high quality collision events are included in the measurement of m_W and Γ_W via the muonic decay channel, because a part of the data was discarded. The reason is a timing problem in the resistive plate chambers, which affected the muon trigger efficiency. The relative uncertainty on the integrated luminosity is 1.8% [90]. The amount of pp collisions yields about $7.84 \cdot 10^6$ events passing the selection criteria presented in Sec. 5.3.1. These represent the $W \rightarrow \mu\nu$ event candidates displayed in the final distributions.

There were $\langle \mu \rangle = 9.1$ pp interactions in average taking place per bunch crossing during the 2011 data taking. This reflects a rather low contribution coming from parallel pp collisions (pile-up) in comparison to the pp runs of the year 2012 at $\sqrt{s} = 8 \text{ TeV}$ (see Fig. 5.4 (b)). It distinguishes the dataset to be suitable for precision measurements.

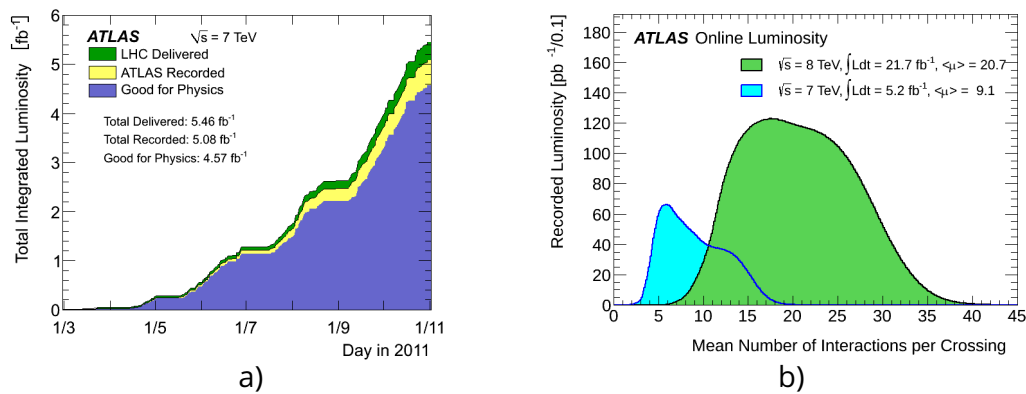


Figure 5.4: (a) Cumulative luminosity versus time delivered to (green), recorded by ATLAS (yellow), and certified to be good quality data (blue) during stable beams and for pp collisions at $\sqrt{s} = 7 \text{ TeV}$ in 2011. (b) Luminosity-weighted distribution of the mean number of interactions per crossing for the 2011 and 2012 data. Both plots are made publicly available by the ATLAS collaboration.

5.4.2 Simulation setup for the signal process

The correct simulation of the signal process is the main key to measuring m_W and Γ_W with the template fit approach. Both parameters are derived from the Monte-Carlo generator setup, when the simulation matches the data. Several aspects are not perfectly modelled, but can be corrected based on the reference measurement of the Z boson. Details on the corrections follow in Sec. 5.6. The basic simulation setup is introduced below. It serves as a reference sample for the template production, which is summarized in the subsequent paragraph.

The initial hard scattering process, which produces the W (Z) boson from the colliding partons, is simulated with the next-to-leading-order POWHEG(V1/R1556) [54, 91] event generator. The parton contributions are derived from the CT10 set of PDFs [92]. The result of the hard scattering process is interfaced to the PYTHIA 8.170 event generator [49, 50] to simulate the parton shower, hadronization and UE with the CTEQ6L1 PDF set and the AZNLO set of tuned parameters. The latter option tunes the event generator to the p_T^Z measurement at $\sqrt{s} = 7$ TeV [93]. The final-state electromagnetic radiation is simulated with PHOTOS [94].

The simulated hard-scattering process is overlaid with Monte-Carlo-generated minimum-bias events [95] to simulate the effect of multiple interactions in the same bunch crossing (pile-up). These minimum-bias samples are also produced with PYTHIA 8 using the A2 tune set [96] in combination with the MSTW2008LO PDF set. The A2 tune set was matched to the ATLAS minimum-bias measurement at $\sqrt{s} = 7$ TeV [97]. The simulated number of interactions per bunch-crossing is adapted to the data taking conditions via reweighting.

The nominal setup sets $m_W = 80.399$ GeV and $\Gamma_W = 2.085$ GeV for the resonance, which is described by a Breit-Wigner function in the event generation. The simulated W sample is normalized according to its measured production cross-section [98]. The extraction of m_W and Γ_W relies on the shape of the distributions and is not affected by the overall normalization. But it is applied to account correctly for the relative fractions of the background contributions.

An alternative set of samples for the vector boson production was produced for the legacy measurement, but it is not of further interest here. The ATLAS measurement relies on the pure leading-order parton shower modelling based on PYTHIA8, which incorporates heavy quark mass effects. In contrast, the Tevatron measurements employ re-summed calculations with Drell-Yan Monte-Carlo generator using resummation calculation (RESBOS), but event generators based on re-summation techniques or next-to-leading order generators with parton shower approaches fail to describe p_T^W/p_T^Z ratio measured at the LHC.

Template creation via reweighting

It would be computationally too intensive to produce Monte-Carlo events for each template value of m_W or Γ_W . Hence, only one nominal sample ($m_W = 80.399$ GeV, $\Gamma_W = 2.085$ GeV) is produced and reweighted to other template values of m_W and Γ_W respectively.

This approach assumes the Breit-Wigner running-width scheme propagator [99]. It interlaces the mass and width of vector-boson as following:

$$\frac{d\sigma}{dm} \propto \frac{m^2}{(m^2 - m_V^2)^2 + m^4 \Gamma_V^2 / m_V^2} \quad (5.2)$$

The index V refers to the general application for the vector-bosons W and Z . m_V and Γ_V represent their corresponding rest mass and decay width, while m is the invariant mass of the decay products of W or Z .

The reweighting includes a scaling according to the SM relation presented in Eq. 5.1, $\Gamma_W \propto m_W^3$. The full reweighting process is provided as an official software tool by the ATLAS community (LINESHAPE TOOL).

The template production includes the blinding process to prevent a possible bias towards previous measurements. A fixed, but unknown shift s applied to the value of the parameter of interest, i.e. either m_W or Γ_W . In case of the m_W measurement, the shift is known ($b = -18\text{MeV}$) to allow the validation with the legacy results. Nevertheless, the blinding value for Γ_W remains undisclosed within in the scope of this thesis.

5.4.3 Simulation setup for the background processes

The background contributions are simulated in the same manner as the signal Monte-Carlo simulation of $W \rightarrow \mu\nu$, if they are sufficiently well described by the Monte-Carlo generators. It is not feasible to simulate multijet background at a hadron collider due to the variety of possible origins. A dedicated data-driven estimate is introduced in Sec. 5.5. All other background processes are described below and summarized in Tab. 5.2.

The various leptonic decay channels of the vector bosons (W, Z) are simulated with the same setup as presented in Sec. 5.4.2. The mass and width reweighting as well as the blinding are applied to all W simulation samples ($W \rightarrow \mu\nu, W \rightarrow \tau\nu$). In case of $W \rightarrow \tau\nu$, the τ lepton can further decay into a final state of a muon and two neutrinos, which is not distinguishable to the detector from $W \rightarrow \mu\nu$. Most of the $W \rightarrow \tau\nu$ background is suppressed due to the displaced vertex of the τ decay, hence the resulting muon is not compatible with the primary vertex. This process contributes about 1% to the finally selected events.

The other vector boson process, $Z \rightarrow \mu\mu$, contributes about 4.8% (W^+) and 6.3% (W^-) to the final selection. It mimics the signal process, when one of the muons is not detected, e.g. due to blind spots or reconstruction inefficiencies. About 0.12% of the finally selected events are attributed to $Z \rightarrow \tau\tau$, which also resembles the signal process, if one τ decays into a muon plus neutrinos.

The production of top-quarks can also fake the $W \rightarrow \mu\nu$ signature. $t\bar{t}$ pairs and single top quark processes may decay to a W boson, which subsequently decays to a muon-neutrino pair. In total these contributions add up to 0.1%.

Furthermore, the hard-scattering can produce two Gauge bosons at once (WW, WZ, ZZ). If one of the bosons decays leptonically and the other one hadronically, the diboson process equals the final state of $W \rightarrow \mu\nu$ plus jets. The small cross-section and kinematic constraints reduce this background to an estimated contribution of 0.07%.

All simulated background samples are overlaid with simulated pile-up vertices as described in Sec. 5.4.2. They are also normalized to their production cross-section. The accompanying uncertainties of the cross-sections are also listed in Tab. 5.2.

Table 5.2: Summary of the simulated background samples. The contribution is stated as relative fraction of the template sample in percent. The uncertainty on the cross-section relative to the signal sample is also given in percent.

Background process	$Z \rightarrow \mu\mu$	$W \rightarrow \tau\nu$	$Z \rightarrow \tau\tau$	Top quark	Di-boson
Relative fraction of full sample [%]	4.8 (W^+)/6.3 (W^-)	1.00	0.12	0.10	0.07
Uncertainty on cross-section fraction [%]	1.8 (W^+)/2.3 (W^-)	2	2	7	10

5.4.4 Validation of the re-analysis selection criteria

The reanalysis is validated against the legacy analysis at several benchmarks to track down possible differences. The very first benchmark is the cutflow for the simulation and data. It is presented in Tab. 5.3. The numbers for the legacy analysis are taken from the internal documentation [100]. The cut steps correspond to the following criteria:

- *No cut*: The numbers correspond to the initial reprocessed event files. They are already pre-selected and slimmed. The parent file sets contain only information sufficient for a standard W/Z selection within ATLAS. It already requires e.g. at least one identified lepton per event.
- *GRL*: The GoodRunList guarantees the nominal condition of the detector for the recorded events.
- *GoodPV*: Selects events with a reconstructed primary vertex
- *Trigger*: The corresponding trigger needs to have fired.
- *MuonSel*: Applies muon selection from Sec. 5.3.1, excluding subsequent cut levels
- *Muon/LAr veto*: If the lepton trajectory passes a malfunctioning module, the event is dropped.
- *Jet cleaning*: If there are jets formed from calorimeter information, which do not originate from the hard scatter but interfere with the construction of \vec{E}_T^{miss} , the event is rejected.

The cutflow for the data is fully resurrected at all levels. The simulation samples reveal a deviation at the permille level, which is reasonable for the reanalysis. Minor deviations are expected from e.g. choices in random seeds or rounding errors. This kind of deviations are expected to affect rather the simulation samples, because they rely on a complex dependence of different scaling factors.

Cut	Data			$W \rightarrow \mu^+\nu$			$W \rightarrow \mu^-\nu$			$W \rightarrow \tau\nu$		
	Legacy Analysis	Reprocessing	Agreement[%]	Legacy Analysis	Reprocessing	Agreement[%]	Legacy Analysis	Reprocessing	Agreement[%]	Legacy Analysis	Reprocessing	Agreement[%]
No cut	154532753	154532753	100.0000	29129499	29129499	100.0000	20092555	20092555	100.0000	7041098	7041098	100.0000
GRL	14097611	14097611	100.0000	29129499	29129499	100.0000	20092555	20092555	100.0000	7041098	7041098	100.0000
Good PV	139003866	139003866	100.0000	28956395	28956386	100.0000	19991586	19991572	99.9999	7003914	7003846	99.9990
Trigger	116109480	116109480	100.0000	1483771	14837129	99.9889	9035835	9034912	99.9898	1319622	1318512	99.9159
Muon Sel.	43803081	43803081	100.0000	12775948	12775350	99.9875	7934334	7933339	99.9875	930906	930123	99.9159
$p_T^{\mu} > 20$ GeV	42951700	42951700	100.0000	12713212	12711615	99.9874	7903333	7902343	99.9875	912106	911341	99.9161
Muon veto	41153751	41153751	100.0000	12713068	12711471	99.9874	7903195	7902205	99.9875	912084	911319	99.9161
Trigger Matching	41044423	41044423	100.0000	12710370	12708772	99.9874	7901520	7900531	99.9875	911863	911098	99.9161
Jet Cleaning	40996618	40996618	100.0000	12705864	12704266	99.9874	7898825	7897836	99.9875	911546	910781	99.9161
LAr simple veto	40915645	40915645	100.0000	12694963	12693363	99.9874	7891061	7890071	99.9875	910452	909688	99.9161
LAr noise bursts	40801743	40801743	100.0000	12694963	12693363	99.9874	7891061	7890071	99.9875	910452	909688	99.9161
$p_T^{\mu} > 30$ GeV AND remove periods L3+L4	16077674	16077674	100.0000	7670767	7669244	99.9801	5181689	5181049	99.9876	242669	242470	99.9180
$p_T^{\nu} < 30$ GeV	10811788	10811788	100.0000	5814759	5813597	99.9800	3894645	3894166	99.9877	142062	141944	99.9169
$m_{\mu\nu}^W > 60$ GeV	8851402	8851402	100.0000	4885304	4884327	99.9800	3322739	3322331	99.9877	90351	90276	99.9170
$E_{\tau}^{\text{miss}} > 30$ GeV	7844778	7844778	100.0000	4342572	4341705	99.9800	2950049	2949683	99.9876	78674	78609	99.9174
				top			Diboson (W,W, W,Z, ZZ)			Z $\rightarrow \tau\tau$		
Cut	Legacy Analysis	Reprocessing	Agreement[%]	Legacy Analysis	Reprocessing	Agreement[%]	Legacy Analysis	Reprocessing	Agreement[%]	Legacy Analysis	Reprocessing	Agreement[%]
No cut	4546477	4546477	100.0000	632302	632302	100.0000	110722	110722	100.0000	1195589	1195589	100.0000
GRL	4546477	4546477	100.0000	632302	632302	100.0000	110722	110722	100.0000	1195589	1195589	100.0000
Good PV	4519068	4519065	99.9999	632027	632026	99.9998	110505	110505	100.0000	1191224	1191220	99.9997
Trigger	3304329	3304386	100.0017	168595	168511	99.9502	37262	37235	99.9275	249997	249983	99.9944
Muon Sel.	3109210	3109268	100.0019	132693	132622	99.9465	32140	32117	99.9284	183105	183095	99.9945
$p_T^{\mu} > 20$ GeV	3102010	3102069	100.0019	132256	132185	99.9463	32024	32001	99.9282	179908	179898	99.9944
Muon veto	1423848	1423925	100.0054	126006	125939	99.9468	28652	28630	99.9232	175628	175619	99.9949
Trigger Matching	1369356	1369429	100.0053	124299	124233	99.9469	28516	28494	99.9229	175123	175114	99.9949
Jet Cleaning	1365933	1366006	100.0053	124148	124082	99.9468	28482	28460	99.9228	174768	174759	99.9949
LAr simple veto	1364188	1364262	100.0054	122172	122107	99.9468	28311	28289	99.9223	174181	174172	99.9948
LAr noise bursts	1364188	1364262	100.0054	122172	122107	99.9468	28311	28289	99.9223	174181	174172	99.9948
$p_T^{\mu} > 30$ GeV AND remove periods L3+L4	839816	839860	100.0052	86257	86211	99.9467	19235	19220	99.9220	54751	54748	99.9945
$p_T^{\nu} < 30$ GeV	577069	577100	100.0054	10041	10036	99.9502	6331	6326	99.9210	22405	22404	99.9955
$m_{\mu\nu}^W > 60$ GeV	476111	476137	100.0055	8639	8635	99.9537	5478	5474	99.9270	10715	10715	100.0000
$E_{\tau}^{\text{miss}} > 30$ GeV	420111	420133	100.0052	7771	7767	99.9485	4916	4912	99.9186	8721	8721	100.0000

Table 5.3: Cutflow comparison for the process $W \rightarrow \mu\nu$. The simulation samples are normalized to the corresponding cross-section. Data taking periods L3 and L4 are discarded due to a timing problem in the RPC.

5.5 Data-based background estimation for Multi-Jet contribution

MJ events deserve a special consideration as background source. The production cross-section is relatively large at hadron-machines and the involved processes are manifold. MJ events can mimic the W boson signal, if they contain semi-leptonic decays of a heavy b or c quark. Also the decays of Pions or Kaons within the tracking region contribute to this background. Or other long-lived particles might traverse the detector and fake a muon signal. This resembles the signature of $W \rightarrow \mu\nu$, if it occurs in combination with a \vec{E}_T^{miss} signal. The latter might result from jets escaping the detector coverage or activity lost in the dead material. Furthermore, the low-momentum processes, such as the hadronization of heavy quarks, are not sufficiently well described by theory in order to provide accurate simulations.

As a consequence, it is necessary to estimate the MJ background with a data-driven technique. It is based on template fits and is split into two parts: The first one is to determine the cross-section, i.e. the event yield in the signal region. And the second part derives the shape of the MJ background.

The MJ background estimate is resurrected in the scope of the reanalysis of m_W in order to extend the observable intervals and possibly optimize the binning. Nevertheless, the studies presented here copy the original estimate from the legacy measurement [72] to provide the proof-of-principle.

5.5.1 Event yield of the MJ background

Muons, which originate from jets, are surrounded by higher activity than the ones from a W decay, because of other hadronization products of e.g. a b quark decay. The requirement on the isolation parameter (I_μ) of a muon track ² gives a handle for the fraction of multijet events of the selected data sample. In the following, if a muon passes the regular event selection of $I_\mu < 0.1$ (see Sec. 5.3.1), it is declared as *isolated* muon and rather unlikely to originate from jets. While all selections with $I_\mu > 0.1$ are declared as *anti-isolated* and are highly likely to be produced within a jet. Nevertheless, muons from MJ events can pass the isolation criterion and vice versa.

The MJ estimate derives the fraction of isolated MJ muons in the signal region from the amount of anti-isolated MJ muons. The proportionality is expected, because both types of muons perform equally with respect to the other kinematic selection criteria. The event yield from other background sources, such as top quark decays, is subtracted using Monte-Carlo simulations. The MJ event yield is evaluated in 10 intervals in I_μ of size 0.03 from 0.1 to 0.4 and extrapolated to $I_\mu = 0$. The information is combined from three discriminating variables: $\vec{E}_T^{miss}, m_T, p_T^\ell/m_T$.

The model uncertainties limit the estimate of the MJ yield, if it is measured solely in the signal region (SR), which is defined by the kinematic cuts in Sec. 5.3.1. Therefore, the proportionality is derived via a fit in two MJ enriched fit regions, FR1 and FR2. The cuts on \vec{E}_T^{miss} and m_T are removed to define FR1. FR2 drops additionally the requirement on u_T from the nominal event selection. The multijet background in the signal region is determined by correcting the multijet fraction fitted in FR1 and FR2 for the different efficiencies of the selection requirements of the signal region. Fig. 5.5 (a) to Fig. 5.5 (c) present the final fit result and illustrate that the loosened cuts allow a much higher contribution from MJ events.

²The isolation of a muon track is defined as the ratio of the activity within a cone of $\Delta R < 0.2$ around the muon ID track of the muon over the transverse momentum of the muon, i.e. $I_\mu = \sum p_T^{cone} / p_T^\mu$

The full MJ yield is evaluated as following exemplarily for FR1, but it is also applicable to FR2. All steps are repeated for each interval of anti-isolated muons and discriminating variable:

1. Select the distributions of the discriminating variables (denoted with N in the following) from data and all background Monte-Carlo samples, once requiring the muons to be isolated and for the anti-isolated category. The distributions are constructed in SR and FR1.
2. Create a pure MJ data template by subtracting the background fraction from the anti-isolated data distributions. The background fraction is estimated via signal and background Monte-Carlo simulations.

$$N_{jet}^{FR1-anti-iso} = N_{data}^{FR1-anti-iso} \cdot \left(1 - \frac{N_{MC(bkg)}^{FR1-anti-iso}}{N_{MC(W \rightarrow \mu\nu)}^{FR1-anti-iso} + N_{MC(bkg)}^{FR1-anti-iso}} \right) \quad (5.3)$$

3. The shape of the pure MJ distributions is assumed to be equal for the isolated and anti-isolated muons, as the isolation does not affect the kinematics. Nevertheless, the total event count is different and to be defined in the following binned likelihood fit. It scales the anti-isolated MJ template to match the data distributions with isolated muons ($N_{data}^{FR1-iso}$):

$$T \cdot N_{jet}^{FR1-anti-iso} + \alpha \cdot N_{MC(bkg)}^{FR1-iso} = N_{MC}^{FR1-iso} \quad (5.4)$$

α is treated as a nuisance parameter and is found to be $\alpha \approx 1$, which reflects the correct modelling of the Monte-Carlo background. T is the parameter of interest and is varied to resemble the data distribution on the right hand side of the equation. Fig. 5.5 (a) to Fig. 5.5 (c) show the fit results for FR1.

4. T is the proportionality factor to transform the MJ event yield with anti-isolated muons to the one with isolated muons. It is applied to the SR to obtain the MJ event yield entering the nominal event selection:

$$N_{jet}^{SR-iso} = T \cdot N_{jet}^{SRanti-iso} \quad (5.5)$$

The final MJ event yield, which passes the isolation requirement, N_{jet}^{SR-iso} , is evaluated for all 10 intervals in I_μ . It is back-projected to $I_\mu = 0$ to obtain the final event yield. The linear extrapolation accounts for the dependence of T on the muon isolation. The results evaluated in FR1 and FR2 are combined to derive an estimate for the uncertainty of this MJ estimate. Fig. 5.5 (d) presents the process for both regions and all variables. It illustrates, that the method converges for the different variations in the region of the signal selection ($I_\mu < 0.1$). The uncertainty assigned to this method is estimated as half of the largest difference of all extrapolations.

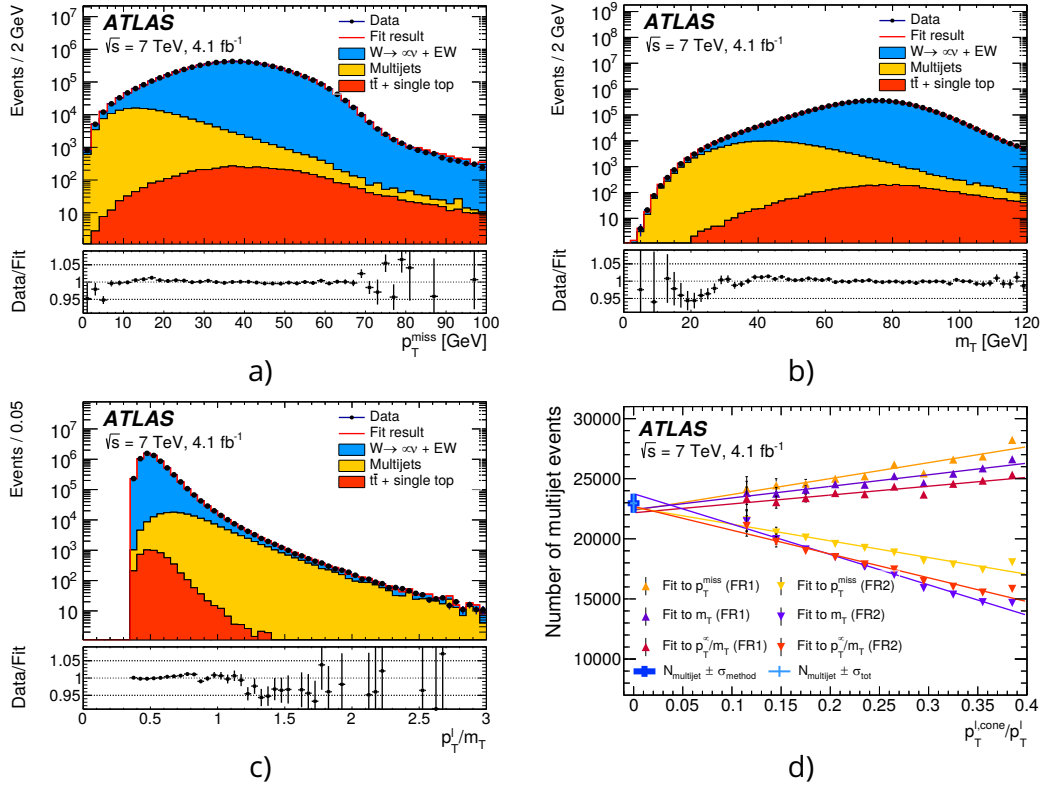


Figure 5.5: Example template fits to the p_T^{miss} (a), m_T (b), and p_T^l/m_T (c) distributions in the FR1 kinematic region, in the muon decay channels. Multijet templates are derived from the data requiring $0.2 < I_\mu < 0.4$. The data are compared to the simulation including signal and background contributions. (d) And the extrapolation to estimate the number of multijet-background events for both fit regions and the three variables. The linear extrapolations are indicated by the solid lines. The thick crosses show the results of the linear extrapolation of the background estimate to the signal region, including uncertainties from the extrapolation only. The thin crosses also include the uncertainty induced by the contamination of the control regions by electroweak and top-quark processes. All figures are taken from [72].

5.5.2 Shape construction of the MJ background

The method presented in Sec. 5.5.1 estimates the MJ background yield without an exact knowledge of the shape of the MJ distribution in the signal region. However, the final fits of m_W and Γ_W , especially in the case of the newly introduced profile likelihood fit, are sensitive to the shape as well. The method to extract the MJ shape is similar to the method to obtain the event yield. It describes the evolution of the shape as function of the muon isolation criteria.

The corresponding dependence is extracted from two control regions (CR): CR1 with $0.1 < I_\mu < 0.25$ and CR2 with $0.25 < I_\mu < 0.4$. The observables m_T and p_T^μ are constructed in these two regions. The extrapolation is extracted from the bin-wise ratio of the distributions in these two control regions. The correction factors are then scaled to match the extrapolation to the signal region, $I_\mu = 0$. The corrected multijet distributions are obtained by multiplying the distributions observed in CR1 with the scaled correction factors.

The uncertainty assigned to this method is estimated with the Monte-Carlo toy

method, because it is dominated by the statistical uncertainty on the distributions. The histogram bin contents are fluctuated within their statistical uncertainties, the extrapolation method is repeated and the standard-deviation of all 500 toys is defined as final uncertainty for the MJ background shape.

5.6 Physics modelling corrections

The template fit approach compares the measured kinematics of the W decay products against the theoretical predictions. Two aspects are crucial for the analysis, in order to provide a measurement of m_W and Γ_W at highest precision: On one hand, this requires an accurate modelling of the detector response, which is discussed in Sec. 5.7. On the other hand, a precise theoretical description is crucial for the W boson production, its decay and subsequently the kinematics of the decay products. The following section summarizes the physics modelling and points to the major uncertainties related to this topic.

The nominal simulation samples created with POWHEG+PYTHIA8 are reweighted to improve the compatibility to the lepton kinematics observed in data. The reweighting procedure accounts for QCD and electroweak higher order calculations and adapts the simulations to match with related measured distributions. The corrections rely on the factorization of the differential cross-section of the vector bosons:

$$\frac{d\sigma}{dp_1 dp_2} = \left[\frac{d\sigma(m_{\ell\ell})}{dm_{\ell\ell}} \right] \left[\frac{d\sigma(y_{\ell\ell})}{dy_{\ell\ell}} \right] \left[\frac{d\sigma(p_T(\ell\ell), y_{\ell\ell})}{dp_T(\ell\ell) dy_{\ell\ell}} \left(\frac{d\sigma(y_{\ell\ell})}{dy_{\ell\ell}} \right)^{-1} \right] \left[(1 + \cos^2(\theta)) + \sum_{i=0}^7 A_i(p_T(\ell\ell), y_{\ell\ell}) P_i(\cos\theta, \Phi) \right] \quad (5.6)$$

p_1 and p_2 represent the four momenta of the decay products, the lepton and anti-lepton. The invariant mass $m_{\ell\ell}$, the transverse momentum $p_T(\ell\ell)$ and the rapidity $y_{\ell\ell}$ characterize the kinematics of the di-lepton system. The polar angle θ and the azimuthal angle Φ describe the relative direction of the two leptons within their restframe (Colins-Soper frame). The last term includes the impact of the helicity and polarization effects on the decay kinematics. A_i are eight numerical coefficients linked to the spherical harmonics P_i of the order zero, one and two [101].

The following subsections group the corrections to the terms of Eq. 5.6 into categories of their origin. The final reweighting process is subsequently described in Sec. 5.6.4.

5.6.1 Electroweak Corrections

The major sources of corrections due to electroweak theory effects include QED FSR affecting the kinematics of the decay leptons, and electroweak loop corrections to the mass term of Eq. 5.6 [102].

The first effect is evaluated by comparing the QED FSR results of the nominal setup with PHOTOS [94] and the QED ISR produced with the parton showering algorithm of PYTHIA8 with higher order Monte-Carlo generators and alternatives to PHOTOS. The

differences to SANC [103] and other generators is found to be negligible with respect to measuring m_W .

However, systematic uncertainties are assigned for the interference of ISR and FSR, as well as possible lepton pair production within the FSR ($\gamma \rightarrow \ell\ell$). These affect predominantly the transverse momentum of the W boson and are propagated to the p_T^W distribution.

5.6.2 Rapidity and angular coefficient corrections

The ISR, which manifests in jets, introduce azimuthal asymmetries in the angular distribution of the decay leptons of the W (Z) boson due to spin correlations as outlined in Sec. 2.4.5. Eight spherical harmonics (P_i) in combination with the numerical coefficients (A_i) describe the impact of these helicity and polarization effects on the decay kinematics.

The angular coefficients depend on p_T , rapidity y and the invariant mass of the dilepton system. Fixed-order perturbative QCD models at $\mathcal{O}(\alpha_s^2)$ predict the differential cross section as a function of boson rapidity (the second term of Eq. 5.6, $d\sigma/dy$) and the coefficients A_i . The predictions rely on the CT10NNLO PDF set [104]. An optimized version of DYNNLO [105, 106] provides the calculations at NNLO.

The nominal coefficients predicted by POWHEG+PYTHIA8 are compared to NNLO predictions. A_5 , A_6 and A_7 are non-zero only at orders of $\mathcal{O}(\alpha_s^2)$ and above. While the contributions of A_5 - A_7 are negligible in the range of p_T^W relevant in this analysis [107], a significant impact is observed for A_0 , A_1 and A_2 . The remaining two coefficients A_3 and A_4 are sensitive to the coupling between the Z boson. These are derived from the measurement of the weak mixing angle [101].

The corrections of A_i relevant to the m_W and Γ_W measurement are applied via the reweighting as presented in Sec. 5.6.4.

5.6.3 Boson transverse momentum corrections

Any inaccuracies in modelling the transverse momentum of the W boson affect the description of p_T^μ and hence directly affect the measurement of m_W and Γ_W . The equivalent to modelling p_T^W is the third term of Eq. 5.6, the cross-section as function of p_T^V and rapidity.

The theoretical description of the vector boson transverse momentum is challenging at both ends: Non-perturbative effects gain importance in the low momentum range ($p_T^W < 30\text{GeV}$) as well as the need to resum large logarithmic terms of the type $\log(m_W/p_T^W)$ [107, 108, 109, 110]. The other end of the p_T^W spectrum is driven by multiple gluon emissions of the initial state partons [105]. The latter effect is incorporated to large extend in the PDFs and discussed in the following section Sec. 5.6.5.

The uncertainties on modelling p_T^W are dominated by various approximations and the choice of free parameters for e.g. parton shower models or the vector boson production. However, the direct measurement of p_T^Z constrains the uncertainties for modelling p_T^W . The QCD parameters incorporated in PYTHIA8 are fitted to the results of the p_T^Z measurement at $\sqrt{s} = 7\text{ TeV}$ [93]. The corresponding simulations are denoted as PYTHIA8 AZ tune. They provide a satisfactory agreement of the vector boson production cross section in several ranges of rapidity [111, 112]. All other tested Monte-Carlo generator alternatives predict a harder p_T^W spectrum for a given p_T^Z spectrum, when compared to PYTHIA8 AZ.

5.6.4 Reweighting procedure

The corrections discussed in Sec. 5.6.2 and Sec. 5.6.3 are applied to the nominal Monte-Carlo generator predictions of POWHEG+PYTHIA8 in three reweighting steps. The method exploits, that each correction affects only one term of Eq. 5.6. Therefore, they can be treated independently through the event-by-event reweighting. The transformation is applied first to the vector boson production phase space, defined by m_T, p_T^W and rapidity y . Subsequently, the decay phase space spanned by (θ, Φ) is transformed.

The individual steps are:

1. Reweight the inclusive rapidity y distribution to the QCD calculations at NNLO (DYNNLO, see Sec. 5.6.2).
2. Reweight the p_T^W distribution in intervals of rapidity to the predictions of PYTHIA8 AZ (see Sec. 5.6.3)
3. The angular coefficients are reweighted in bins of p_T^W and y with the following weights to match calculations at $\mathcal{O}(\alpha_s^2)$:

$$w(\cos\theta, \Phi, p_T, y) = \frac{1 + \cos^2\theta + \sum_i A_i' P_i}{1 + \cos^2\theta + \sum_i A_i P_i} \quad (5.7)$$

with A_i evaluated with POWHEG+PYTHIA8 and A_i' at $\mathcal{O}(\alpha_s^2)$.

The result is compared to the related ATLAS measurements [98, 113] and presented in Fig. 5.6.

The reweighting is performed with Various PDF sets. The plots correspond to the predictions drawn from the CT10NNLO PDF set, which show the best description of the data. Only MMHT2014 [114] and CT14 [115] yield predictions of compatible quality. Detailed studies are presented Ref. [98]. As a result, the CT10NNLO PDF set defines the nominal setup for this analysis. The corresponding uncertainties are described in Sec. 5.6.5. They are propagated to the final distributions following the same reweighting procedure as presented above.

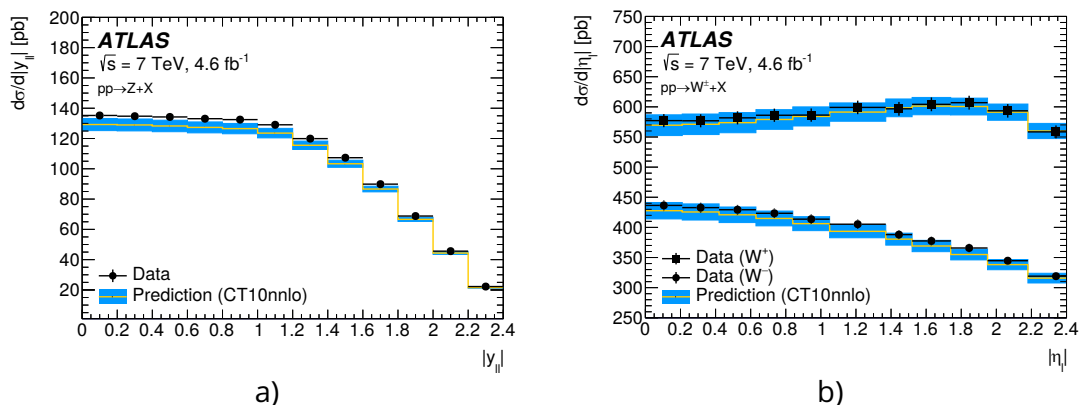


Figure 5.6: (a) Differential Z boson cross section as a function boson rapidity, and (b) differential W^+ and W^- cross sections as a function of charged decay-lepton pseudorapidity at $\sqrt{s} = 7$ TeV [98]. The measured cross sections are compared to the POWHEG+PYTHIA8 predictions, corrected to NNLO using DYNLLO with the CT10NNLO PDF set. The error bars show the total experimental uncertainties, including luminosity uncertainty, and the bands show the PDF uncertainties of the predictions. The plots are taken from [72].

5.6.5 Uncertainties in the QCD modelling

The modelling of the strong force involves perturbative and non-perturbative processes. The uncertainties on the perturbative ones are accessible via the incorporation of higher order effects, while the uncertainty on the non-perturbative modelling relies on the comparison of different phenomenological approaches implemented in the Monte-Carlo generators. The related variations are processed likewise to the QED modelling via the reweighting procedure presented in Sec. 5.6.4. The associated uncertainties are estimated with the comparison to the nominal setup. In the following, special focus is set on the PDF uncertainties, because they dominate the physics modelling uncertainties of the legacy measurement. Other sources of QCD related uncertainties contribute a negligible fraction and are summarized at the end of the section.

The imperfect knowledge of the PDFs dominates the physics modelling uncertainties, because it affects the differential cross section as function of boson rapidity, the angular coefficients, and the p_T^W distribution. The total PDF related uncertainty results in about 14MeV averaged over all fit categories for the legacy measurement.

These uncertainties are strongly anti-correlated in the different charge categories. The average uncertainty is almost halved (≈ 7.4 MeV) when combining opposite charge categories. The correlation originates from the measurement constraints on the PDFs: The total light quark sea PDF is well constrained by deep inelastic scattering experiments [20]. The fraction of the different flavours can vary, but the variations depend on each other due to the constraint on the total amount. E.g., if the contribution from \bar{u} in the production of W^- bosons is altered, it directly compensates in the contribution from \bar{d} quarks changing the W^+ production. The huge impact of PDF variations is a major motivation for the reanalysis of m_W , because they are accompanied with significant shape variations of the p_T^μ and m_T distributions, and hold great potential for further constraints from the PLH fit approach. Hence, the analysis presented here implements the legacy PDF uncertainties to focus on improvements based on the new fit approach. A future publication is anticipated to extend this approach with the recently improved the uncertainties on the proton structure [82, 21].

Here, the PDF contribution to the modelling uncertainty is estimated with the CT10NNLO PDF set by using the Hessian method[116]. The Hessian matrix of the second derivatives at the global minimum of the PDF fit is calculated and the eigenvectors are extracted. The uncertainties of the CT10NNLO PDF are described by 25 eigenvectors. A positive and negative excursion along each eigenvector estimate the 90% confidence limit. The mean value of both variations is defined as the corresponding uncertainty. The overall uncertainty is scaled to the 68% confidence limit similar to all other uncertainties.

The legacy measurement considers the usage of alternative PDF sets with an general uncertainty of 3.8 MeV. The value corresponds to the envelope values of m_W using MMHT2014 and CT14 NNLO PDF sets. Alternative PDF sets are not considered here, because they do not contribute to the proof-of-principle for the PLH fit approach. But they will be profiled individually in future studies.

The legacy analysis includes further uncertainties on the QCD modelling. The corresponding uncertainties are simply with the total modelling uncertainty in the scope of the legacy analysis. Hence, no corresponding distributions are available for the profiling. The associated uncertainties are either subtracted from the legacy uncertainty or added to the PLH uncertainty for the purpose of validation.

One of these uncertainties on the QCD modelling arises from the parameters of the parton shower models determined in the AZ tune of PYTHIA8. They are originally estimated with the experimental uncertainties of the tuned measurement [93] and propagated to p_T^W . Also the uncertainties on the angular coefficients are driven by the experimental uncertainties on the corresponding measurement. These are propagated with toy variations of pseudo-data.

Additional parameters of the simulation are inspected, which are not retrieved from the tune. E.g. the masses of the charm and bottom quark defined in PYTHIA8 are varied within their uncertainties and propagated to the final distributions. Nevertheless, it contributes a minor fraction to the overall physics modelling uncertainty compared to the impact of the PDF description.

5.7 Detector calibrations for the muon reconstruction

The kinematic properties of the decay muon are the key to access information about the W boson. Any imperfect calibration of the detector response affects the measured p_T^μ and m_T distributions and finally results in a mismeasurement of m_W and Γ_W , respectively. Hence, it is crucial to provide agreement between the data and simulated Monte-Carlo distributions to the per-mille level. It is impossible to describe all aspects, especially the malfunctions, of a detector in the simulation. The simulation has to be calibrated against data for this purpose. The ATLAS community provides corresponding studies with recommendations for the calibration process [70].

But these calibration studies are superseded by dedicated analysis in Ref.[73] and Ref.[74] in order to meet the high requirements of the m_W measurement. The calibration itself is usually in agreement with the official recommendations, but the important aspect is to precisely determine the systematic uncertainties of the detector calibration. The techniques of the calibration studies are already introduced in Sec. 4.4.2.

However, the calibration studies are briefly summarized in the following section for a better overview. And the relevant systematic uncertainties are outlined.

5.7.1 Muon momentum scale calibration

The kinematic properties of the muon candidates in this analysis are derived from the associated ID tracks. The momenta of the muon candidates are calculated based on the curvature of the corresponding muon tracks in the magnetic field. The accuracy of this measurement is limited by the coarse description of the detector alignment and resolution. The limited knowledge of the magnetic field, and of the amount of passive material in the detector further limit the accuracy.

The different kinds of distortions to the ID track result in radial or Sagitta biases. The correction factors are applied to the measured value of p_T in the simulation and data as well. The detailed application is presented in equation Eq. 4.5 and Eq. 4.7 in Sec. 4.4.2.

The correction factors are deduced from $Z \rightarrow \mu\mu$ event candidates, which serve as standard candles, because they are already well understood from other experiments. A binned maximum-likelihood fit compares Monte-Carlo templates to the data distributions in order to derive the calibration parameters for the momentum scale. The method is described in detail in Ref.[70].

The uncertainties arise from the fitting range, methodological biases, background contributions, theoretical modelling of the Z boson and the material distribution in the ID. The measurement of m_W and Γ_W applied the correction factors in the momentum range of $W \rightarrow \mu\nu$ candidates, although they are deduced in the range of $Z \rightarrow \mu\mu$ events. Therefore, an additional systematic uncertainty is introduced to take this extrapolation into account. The correction to the momentum scale ($\delta\alpha$) is parametrized as a function of the average transverse momentum of the muon in W boson events $\langle p_T^\mu(W) \rangle$ in order to reveal a possible dependency:

$$\delta\alpha = p_0 + \frac{p_1}{\langle p_T^\mu(W) \rangle} \quad (5.8)$$

The fit is performed in various regions of pseudorapidity with p_0 and p_1 as free parameters. A possible momentum dependence of $\delta\alpha$ would manifest in $p_1 \neq 0$. The results of the fits are presented in Fig. 5.7(a). The deviations of p_1 from zero are assigned as systematics uncertainty to the extrapolation. These dominate the systematic uncertainties of the muon calibration.

The determination of the Sagitta bias also exploits $Z \rightarrow \mu\mu$ events. The mass peak of the Z boson is determined in the di-muon invariant mass distribution for data and Monte-Carlo simulations. The distributions are distinguished in categories of charge and pseudorapidity of the muons. The Sagitta bias is derived from the comparison of data to simulated distributions. This method is statistically limited by the sample size.

An alternative method incorporates a comparison of the ID information to the measurement in the electromagnetic calorimeters to determine the Sagitta bias. The results are compatible to the first method. Both are combined for the final corrections. The results are presented in Fig. 5.7(b). The variations in dependence of the pseudorapidity reveal the detector distortions.

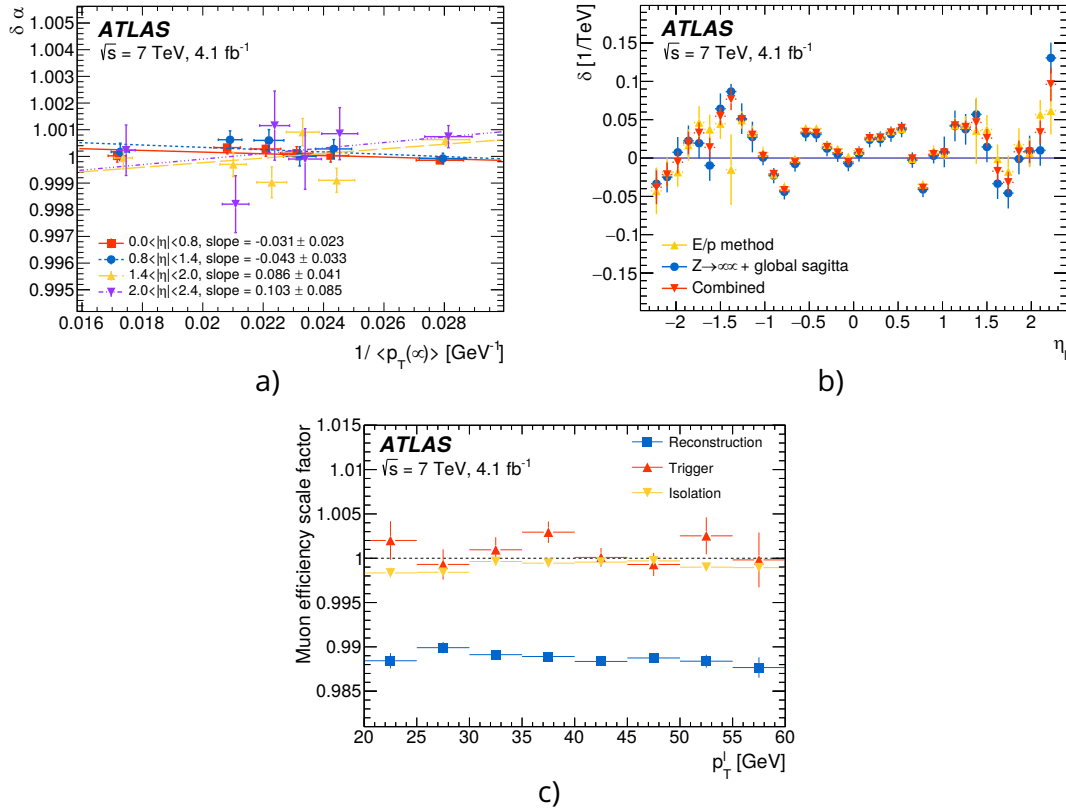


Figure 5.7: (a) Residual muon momentum scale corrections as a function of muon $1/\langle p_T \rangle$ in four pseudorapidity regions. The extrapolation applies linear fits. (b) Sagitta bias as a function of pseudorapidity and averaged over the azimuthal angle. (c) Scale factors for the muon reconstruction, trigger and isolation efficiency obtained with the tag and probe method as a function of p_T^μ . All three plots show statistical uncertainties only. The plots are taken from [72].

5.7.2 Muon selection efficiency

The selection requirements (Sec. 5.3.1) are optimized to guarantee peak performance of the detector to identify muon candidates. While the selection efficiency usually operates close to the saturation at 100 % efficiency, it is crucial to model the very same selection efficiency in the Monte-Carlo simulation. Any p_T^μ dependent mismodelling of the selection efficiency would introduce a shift in the measurement of m_W and Γ_W . The efficiency scale factors, which are explained in detail in Sec. 4.4.2, correct the efficiencies in the simulation to match the efficiencies obtained in data.

The muon selection relies on the modelling of three different categories of efficiencies: The reconstruction efficiency, which describes the probability to identify a muon measured in the ID also with the MS. The trigger efficiency describing how often a measured muon also fired the corresponding trigger. And lastly the isolation efficiency, which is the efficiency of a signal muon to pass a detector-based isolation requirement. The latter one is of special interest, because the isolation criterion is p_T^μ dependent by definition.

The efficiencies are determined with the *tag-and-probe* method [70] applied to $Z \rightarrow \mu\mu$ events. One of the muons is defined as the *tag* and required to pass rather tight selection criteria. The other muon is the *probe*, which passes looser criteria, i.e. the selection requirement for which the efficiency is determined is removed. If the

combination of both muons is consistent with a $Z \rightarrow \mu\mu$ event candidate, the probe muon is most likely a real muon and the corresponding efficiencies can be derived from its properties. The correction factors for the Monte-Carlo simulation are derived from the ratio between simulation and data efficiencies (see also Eq. 4.4).

The corrections are evaluated as a function of p_T^μ , η_μ , Φ_μ and the charge. No significant p_T^μ -dependence of the corrections is observed in any of the detector regions, as exemplarily presented in Fig. 5.7 (c).

The accuracy of the method suffers from statistical limitations. Further systematic uncertainties are assigned to the contribution of MJ background and the momentum scale.

5.8 Detector calibrations for the hadronic recoil

The hadronic recoil (u_T) is, besides the transverse momentum of the muon, the essential parameter to access the $W \rightarrow \mu\nu$ process, because it is directly linked to the transverse momentum of the vector boson. As a brief reminder:

The recoil in the transverse plane is defined as the vector sum of the transverse energy of all clusters reconstructed in the calorimeters: $\vec{u}_T = \sum \vec{E}_T$ [117]. It is corrected for the contributions associated with the decay muon and the opposite orientation ($-\vec{u}_T$) provides an estimate for p_T^W (compare Fig. 5.2).

The compatibility of the simulated and the measured u_T is crucial for the m_T distribution, from which m_W and Γ_W are derived. Additionally, a mismodelling would affect the p_T^μ distribution, because a selection cut on u_T is included to suppress MJ background. The following corrections applied to u_T are evaluated in detail in Ref.[118].

The theoretical description of the hadronic recoil is challenging, because many processes of low momentum transfer are involved. Processes, such as the underlying event ³ and the contributions from other pp interactions (pile-up), cannot be fully calculated perturbatively. A dedicated correction of the simulation to data is presented in Sec. 5.8.1.

A slight discrepancy between data and simulation is remaining despite the former corrections. It is associated to the geometrical modelling of the pp collision. A corresponding set of corrections is summarized in Sec. 5.8.2.

Both correction categories rely on $Z \rightarrow \mu\mu$ events to deduce correction factors. In case of Z boson events, p_T^Z is measured with a resolution of about 2 GeV due to the combination of the decay muons. This precision fairly exceeds the resolution of the recoil energy. It is therefore exploited as a reference for the hadronic recoil of the Z boson. Here, u_{\parallel}^Z and u_{\perp}^Z represents the projections of the recoil onto the axes parallel or perpendicular to the direction of p_T^Z , determined with the decay muons.

5.8.1 Modelling of the event activity

Particles, that pass the selection criteria, but originate from additional pp collisions or the UE enter the calculation of u_T and broaden the resolution. The signature of this additional activity is not distinguishable from the hadronized recoil of the vector-bosons. Their contribution needs to be controlled by an accurate description in the event simulation. All simulated events are overlaid with Monte-Carlo-generated

³An adequate modelling of the underlying event activity is essential to improve the resolution of the hadronic recoil. This motivates the corresponding measurement at $\sqrt{s} = 13$ TeV presented in Chapter 6. It will further improve the measurement of m_W at $\sqrt{s} = 13$ TeV.

minimum-bias events [95] to simulate the effect of pile-up (see Sec. 5.4.2). The simulation is reweighted to the data taking conditions, because the average number of interaction per bunch-crossing ($\langle\mu\rangle$) depends e.g. on the beam-geometry. The reweighting process and further details are discussed in Sec. 4.4.3 as it follows the recommendations of the ATLAS community. The modelling of the UE activity is based on the tuning of the Monte-Carlo generator prediction to data.

The value of $\langle\mu\rangle$ is scaled by a factor α to optimise the modelling of observed data distributions, which are relevant to the modelling of u_T . The scaling factor is found to be $\alpha = 1.10 \pm 0.04$. The errors are treated as a systematic uncertainty on the pile-up reweighting.

After the correction for pile-up contributions, minor discrepancies between data and simulation remain. These are attributed to imperfect modelling of the subprocesses involved in the primary pp collision, namely the underlying event and the hadronization of unstable particles. The total reconstructed transverse energy, which is corrected by the magnitude of u_T , is highly sensitive to such effects, while being less correlated to u_T itself:

$$\sum E_T^* = \sum E_T - |\vec{u}_T| \quad (5.9)$$

It is therefore corrected to data to cover the remaining mismodelling.

The correction utilizes the means of a Smirnov transform[119] to map the distribution of $\sum E_T^*$ measured in Monte-Carlo events to the one measured in data. This correction is derived for Z boson events in bins of $p_T^{\mu\mu}$, because the comprised processes depend on the transverse momentum of the vector boson. The correspondence for the W boson is to include a dependence on u_T , which is rather coarse compared to $p_T^{\mu\mu}$. The p_T dependence of the correction is assumed to be equal for Z and W bosons. As a result, u_T is bypassed in such a way, that the dependence on $p_T^{\mu\mu}$ scaled scaled to W boson events. Fig. 5.8 (a) illustrates the improved agreement for $\sum E_T^*$ after the correction.

The assumption for the p_T dependence of the correction is covered by a systematic uncertainty. The full correction is compared to the results without the p_T dependence. The difference is included in the final uncertainty.

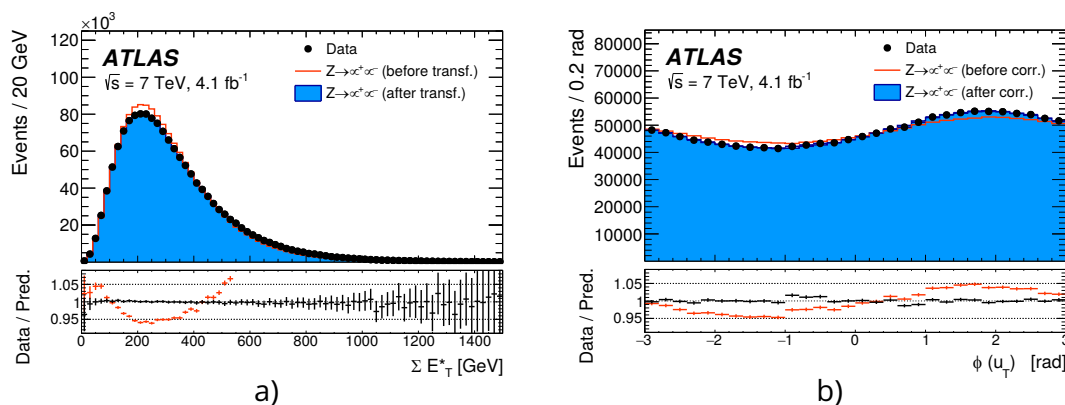


Figure 5.8: Distributions of (a) $\sum E_T^*$ and (b) the azimuth direction Φ of the recoil in data and simulation for $Z \rightarrow \mu\mu$ events. Both plots illustrates the effect of the transformation and correction respectively. The lower ratio plots show statistical uncertainties only.

5.8.2 Response corrections

There is no favoured transversal direction for physics processes, if one deals with the ideal case of a head-on pp collision and an isotropic detector response. However, Fig. 5.8(b) illustrates, that the Φ -direction of \vec{u}_T is biased. The effect is partially expected from the crossing angle of the proton beams. Additionally, the non-uniformities of the calorimeter response affect the reconstruction of the Φ direction. These are not included in Monte-Carlo simulation and are corrected for based on Z events from data. The projections of \vec{u}_T, u_x and u_y , are shifted by the difference of the average values in data and the simulation.

The recoil scale and resolution also needs to be calibrated, similar to the muon detector response presented in Sec. 5.7.1. The calibration is derived from $Z \rightarrow \mu\mu$ events in bins of $p_T^{\mu\mu}$ and $\sum E_T^*$. The recoil energy scale is evaluated with the difference between data and simulation for the average value of $u_{\parallel}^Z + p_T^{\mu\mu}$. The resolution correction utilizes the ratio of data and simulation distributions for the standard deviation of u_{\perp}^Z . The corrections are applied to the simulation values of $u_{\parallel}^{W,Z}$ and $u_{\perp}^{W,Z}$ according to the vector-boson transverse momentum on particle-level. The resolution of u_T depends on the amount pile-up contributions. The correction is therefore further distinguished in three bins of $\langle\mu\rangle$.

The correction relies once again on the extrapolation from the Z kinematics to the momentum scale of the W boson. The systematic uncertainty related to this extrapolation is estimated by transferring the event activity from Z events to W events. As a result, the energy resolution correction varies by 6%. This variation is included as the final systematic uncertainty related to the extrapolation.

A further systematic uncertainty is included for the limited size of the reference samples. The impact of the binning in $p_T^{\mu\mu}$ and $\sum E_T^*$ is evaluated for the scale and resolution correction. A smooth interpolation of the correction values between the bins is performed instead of using a binned correction. The difference between these approaches is taken as systematic uncertainty.

In general, all uncertainties related to the hadronic recoil calibration affect mainly the parameters extracted from the m_T distributions. The effect on p_T^{μ} remains rather low, because it varies predominantly the event count. The largest uncertainties are induced by the correction of the event activity and the extrapolation of the recoil scale and resolution. All corrections are cross checked with simulation provided by the POWHEG+HERWIG6 Monte-Carlo generator. It implements a different model for the UE and hadronization as well as the parton showering. The corrections are compatible to the ones deduced with the POWHEG+PYTHIA8 generator.

5.9 The template fits

The final values of m_W and Γ_W are obtained from the comparison between data and simulation, as already outlined in Sec. 5.2. For this purpose, the extensive studies summarized in Sec. 5.6, Sec. 5.7 and Sec. 5.8 guarantee, that the theoretical description of the W boson production and decay is sufficiently accurate, and that a precise modelling of the detector response is provided.

Henceforth, the template fit can be applied: The parameters m_W and Γ_W are varied in the simulation and the best agreement to data reveals the appropriate estimate of these parameters. The new approach implements a profiled binned Likelihood fit. It is introduced in Sec. 5.9.2. Its advantage is, that the profiling is highly sensitive to the

shape of distributions and allows to profile systematic uncertainties. This way, it is possible to further constrain the dominating PDF related uncertainties, which control the shape dependence on the pseudorapidity.

The legacy fit approach is re-performed as well to validate the correct resurrection of the data and simulation samples. The legacy fit approach is outlined in Sec. 5.9.1. The validation is presented in Sec. 5.9.5.

The ATLAS community provides a well advanced framework for profile likelihood fits, called TREXFITTER. Details about the software package are listed in Sec. 5.9.3. The realisation of a template fit in this framework is explained in the subsequent Sec. 5.9.4. Section 5.9.6 presents the handling of systematic uncertainties in a PLH fit, because not all uncertainties can be directly transformed from the former χ^2 -minimization to the PLH. The final fit results are presented in Sec. 5.10 and Sec. 5.11 for m_W and Γ_W , respectively.

5.9.1 The legacy χ^2 -fit approach

The template fit approach relies on the comparison between data and simulated distributions. It is therefore crucial to include all processes into the templates, in case they contribute to the selected samples in data. The simulation templates are built by adding up all background samples and the signal Monte-Carlo simulation sample. All distributions retrieved from Monte-Carlo simulations are normalized according to their production cross-section. The dependence of the cross-section on m_W or Γ_W is taken into account for the $W \rightarrow \mu\nu$ and $W \rightarrow \tau\nu$ samples, when altering the corresponding parameters. The MJ background is scaled according to the procedure from Sec. 5.5.1.

The different scaling preserves the proportions among the contributing processes. However, the fit compares solely the shape between data and simulation. The integral of the full template distribution is therefore scaled to the integral of the corresponding distribution in data.

The measurement for the compatibility between the templates (tmp) and the data is defined by the χ^2 value:

$$\chi^2 = \sum_{i=1}^N \frac{(b_{\text{tmp},i} - b_{\text{data},i})^2}{(\Delta b_{\text{tmp},i})^2 + (\Delta b_{\text{data},i})^2} \quad (5.10)$$

It is the sum over all bins N of the corresponding distribution, with the bin content b_i and the corresponding uncertainty on the bin content, Δb_i . Only the statistical uncertainty is taken into account. It corresponds to the square root of the number of bin entries assuming that the filling of each bin obeys a Poisson distribution.

The availability of templates is restricted to discrete values. The computational expense further limits the number of available templates. However, this is overcome with an interpolation. The templates are treated as probability density functions with m_W as a nuisance parameter. If the shape of the templates is a linear function of m_W , it is possible to apply the following approximation as described in Ref.[120]. The dependency of the χ^2 values are approximated by a parabola, when plotted as function of the varied parameter m_W :

$$\chi^2 \approx \chi_{\text{min}}^2 + U_{11}(m_W - m_W^{\text{min}})^2 \quad (5.11)$$

χ_{min}^2 denotes the minimum value of χ^2 from the fit and m_W^{min} the value of m_W , where the minimum is reached. The coefficient U_{11} is the entry of the inverse of the

covariance matrix of all nuisance parameters. Its value stretches the shape of the parabola. m_W^{\min} yields the best estimate for the real value of m_W . The curvature of the parabola allows to determine the statistical uncertainty of the estimated parameter. It corresponds to the deviation from m_W^{\min} , which fulfils: $\chi^2(m_W^{\min} \pm \Delta m_W^{\text{stat}}) = \chi_{\min}^2 + 1$.

Figure 5.9 illustrates the template fit and the corresponding parabola interpolation. The method is similar to the approach used by the CDF or DØ collaborations [87, 89].

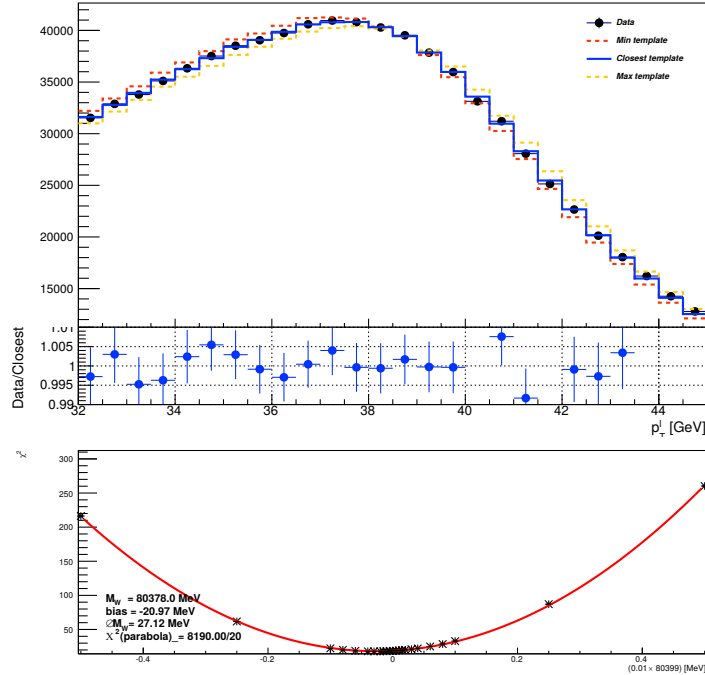


Figure 5.9: The top plot presents the p_T^l distribution in data (black) compared to different templates. The blue line corresponds to the highest template value of m_W , red to the lowest and purple to the best one with the lowest value of χ^2 . The lower plot presents the χ^2 values as function of the template values of m_W relative to the nominal mass value. The red curve illustrates the parabola fit.

Technical details

The fit is performed on distributions of p_T^μ and m_T , because they are most sensitive to the kinematics of the $W \rightarrow \mu\nu$ decay. The fits are further differentiated in different categories to test the consistency of the experimental and physical modelling corrections. The distributions are fitted separately for negatively and positively charged W bosons in four bins of pseudorapidity (see Tab. 5.1). This yields 16 different categories to measure m_W in the $W \rightarrow \mu\nu$ channel. The differentiation allows to verify the consistency of the PDF modelling, if results in different charges or η -regions are in agreement. The comparison of p_T and m_T can reveal possible inaccuracies in the hadronic recoil calibration or the modelling of p_T^W . All categories are consistent within the uncertainties of the legacy measurement.

The lower and upper bounds of the fit ranges are optimized in p_T^μ and m_T . The initial ranges of $30 \text{ GeV} < p_T^\mu < 50 \text{ GeV}$ and $60 \text{ GeV} < m_T < 100 \text{ GeV}$ are altered to minimize the total uncertainty of the combined fit result. The following ranges yield the minimal uncertainty:

- $32 \text{ GeV} < p_T^\mu < 45 \text{ GeV}$

- $66\text{GeV} < m_T < 99\text{GeV}$

The corresponding bin size is 500 MeV for both distributions.

The final fit is performed with 35 templates. The values of m_W vary in steps of 1 MeV to 10 MeV, centred around the simulation reference value ($m_W^{\text{PDG}} = 80.399\text{ GeV}$). They cover a range of $\pm 400\text{ MeV}$ relative to the reference value. The granularity of templates is reduced in the extremes of the fitted m_W range.

The choice of the template density affects the χ^2 minimization by less than 1 MeV. This is tested with different sets of templates within the legacy measurement.

Estimation of uncertainties

The systematic uncertainties are assessed by varying the simulation sampled within the corresponding error estimates of a simulation parameter. The legacy analysis exploits the construction of pseudo-data distributions to estimate the effect of the systematic uncertainties on the final fit of m_W . The pseudo-data is constructed in the same manner as the simulation templates: The signal and background samples are added up after being scaled to their production cross-sections. The important difference is, that the samples are produced with a variation in the Monte-Carlo simulation parameters, such as the up or down variation of the muon reconstruction scale factors presented in Sec. 5.7.2. The nominal templates are fitted to the pseudo-data and the difference to the nominal pseudo-data fit without parameter variation is defined as the corresponding uncertainty.

This approach is purely based on Monte-Carlo simulations and therefore independent of statistical fluctuations in the data sample. On the other hand, it relies on the precise description of the data by the simulation.

The analysis presented here distinguishes three types of systematic uncertainties, which are combined in different ways:

- *Paired uncertainties:* Most of the systematic uncertainties are provided as a paired uncertainty, i.e. one simulation parameter is varied (symmetrically) within its uncertainties to propagate the effect to the fit of m_W . E.g. the eigenvector variations of the PDF uncertainties are presented as *down*- and an *up* variation of the eigenvector. The resulting uncertainty is the mean difference:

$$\delta m_W^{\text{syst}} = \frac{1}{2} \sqrt{\left(m_W^{\text{syst-up}} - m_W^{\text{syst-down}}\right)^2} \quad (5.12)$$

- *Shifts:* If the uncertainty is estimated with a single variation of the nominal setup, the final uncertainty is symmetrized based on the difference to the baseline fit. An example is the uncertainty related to the binning of the hadronic recoil calibration, which is validated by the comparison to an interpolation approach.

$$\delta m_W^{\text{syst}} = \frac{1}{2} \sqrt{\left(m_W^{\text{syst-shift}} - m_W^{\text{syst-baseline}}\right)^2} \quad (5.13)$$

- *Toy Monte-Carlo samples:* If the bin-to-bin correlation between several parameters is complicated to be modelled, toy Monte-Carlo simulations are used to estimate the impact of the uncertainty on m_W . This is the case for all statistical uncertainties on calibration factors, such as the muon reconstruction scale factors. There are N sets of toy Monte-Carlo simulation samples produced to contract the pseudo-data. The varied parameter is smeared for each set within its uncertainties with a Gaussian function. The final uncertainty is the standard deviation of all N values of m_W :

$$\delta m_W^{\text{syst-toys}} = \sqrt{\frac{1}{N-1} \sum \left(m_W^{\text{toy},i} - \bar{m}_W^{\text{toys}}\right)^2} \quad (5.14)$$

All uncertainty estimates are constructed to be uncorrelated to each other. If several uncertainties belong into one category, such as the 25 eigenvector variations of the PDF uncertainties, they are added in quadrature to estimate the combined impact.

5.9.2 General aspects of the Profile Likelihood fit

The PLH technique is used, when fitting models with more than one floating parameter. In the scope of this thesis, there is one parameter of interest (p.o.i.) (also denoted as μ in the literature) either m_W or Γ_W , and several NPs (denoted with θ). The NPs are related to simulation and modelling parameters such as cross-sections, which are associated with uncertainties, but are of no further interest to the actual result. The PLH is commonly used in searches for exotic particles or rare SM processes. Hence, the p.o.i. μ usually refers to the overall signal strength factor, which acts as a scaling to the total rate of signal events ($\mu \cdot N^{sig}$). The p.o.i. μ can be imagined as the scaling of the simulation reference value for m_W or Γ_W in the scope of this analysis. The actual translation from the normalisation factor to the usage of templates exploits a *morphing* approach. It is presented in detail in the following Sec. 5.9.4.

The global likelihood function provides a measure to estimate the compatibility of two distributions. In other words, it measures the goodness of fit of a statistical model to a sample of data for given values of the unknown parameters. Here, the statistical models are the templates of m_W or Γ_W . The general likelihood function is a product of Poisson measurements, which represent the binned entries of the distribution. This is linked to a probability density function for the systematic uncertainties. The general representation of the likelihood in Eq. 5.15 is subsequently broken down into the analysis related parts:

$$L(\mu, \theta | N^{obs}) = \prod_{j=1}^{channels} \prod_{i=1}^{n_j^{bins}} \text{Pois}(n_{ji}^{obs} | S_{ji}(\mu, \theta) + B_{ji}(\mu, \theta)) \cdot C(\theta) \quad (5.15)$$

Here, N^{obs} is the observed distribution in data. n_{ji} is the number of events observed in data in bin i of the distribution in channel j . It is the input to the Poisson measurement with the expectation of S_{ji} events from the signal sample and B_{ji} events from the background contributions.

The different channels are presented by the different distributions of the different measurement categories, i.e. the two charges and the different regions in η . The first product vanishes, if only one channels is investigated. Also the distributions of p_T^μ and m_T can be combined on a global likelihood function, but this requires to determine the correlations as the included events are identical. This scenario is not covered here. The last term ($C(\theta)$) is the constrain or penalty term, which takes the variation of the NPs into account.

The different terms can be explained as following:

- The first term simplifies to a counting experiment in a limit of $n_{bins} = 1$. The Poisson distribution is defined as (for only one channel, $j = 1$):

$$\text{Pois}(n_i^{obs} | \mu, \theta) = \exp(-(S_i + B_i)) \frac{(S_i + B_i)^{n_i^{obs}}}{n_i^{obs}!} \quad (5.16)$$

The sum $S_i + B_i$ represents the number of events in bin i of the corresponding template. These numbers depend on μ ($= m_W$ or Γ_W) and θ .

- The constraint term *penalises* a deviation of the NP from their nominal value. It applies a Gaussian prior by default. The constrain term resembles the NP denoted with t to:

$$C(\theta) = \prod_{t=1}^{n^{NP}} \frac{1}{\sigma_t \sqrt{2\pi}} \exp\left(-\frac{(\theta_t^{nom} - \theta_t)^2}{2\sigma_t^2}\right) \quad (5.17)$$

with σ_t being the standard deviation of the NP t .

The maximization of Eq. 5.15 yields the best estimate for $\mu(\equiv m_W, \Gamma_W)$ for a fixed dataset N^{obs} . Equivalently, it is typical to minimize the negative log-likelihood ($-\log L(\mu, \theta)$), because the logarithm tames excessive numerical values and minimization algorithms are more common for historical reasons. The functionality of the PLH allows the implementation of control regions, which can further constrain some of the NPs. A possible use case is the MJ event-yield, which already exploits MJ enriched control regions. Nevertheless, this functionality is neglected for the simplicity of this proof of principle here.

The novelty of the PLH in comparison to the former χ^2 minimization is, that the systematic uncertainties, represented by θ , are effectively considered in the fit. The legacy χ^2 minimization takes only statistical errors into account within the fitting process. The systematic uncertainties are propagated via pseudo-data. But some systematics vary the shape of the template distribution in a way, which is incompatible with the shape observed in data. Hence, these NP can be further constrained. Or the other way round, if a feature of the data shape is better described by a θ_t far off the nominal value, it could indicate modelling inconsistencies. The latter fact is visualized in the so called *pull* and *ranking* representation.

However, the negative log-likelihood approaches a χ^2 distribution in the asymptotic regime of large statistics data samples. As a results, the values of the negative log-likelihood also resemble a parabola as function of the p.o.i., i.e. m_W or Γ_W .

5.9.3 Implementation of the PLH-fit

The reanalysis profits from the advanced TREXFITTER project, i.e. a framework for binned template profile likelihood fits. It is an ATLAS internal software package, which utilized the functionality of HistFactory [121]. The latter one is a tool for creating statistical models. These are finally integrated in the C++ particle physics data analysis package ROOT [122].

The TREXFITTER framework builds a model, which represents the likelihood function introduced in Eq. 5.15, based on the input of ROOT histograms. The different systematic uncertainties are provided as variations of these histograms or as scaling factors. The model is a parametrised probability density function in RooFit/ROOSTATS, an extension to the ROOT framework. The tools exploit a modular approach to add complexity to the probability density function, such as systematic constraints. The core of the model is stored in a RooWorkspace, a persistable container for RooFit projects.

Once the model is defined, the parameters are optimised based on the input data. The minimisation of the negative log-likelihood is exploits the MINUIT algorithm [123]. There are alternative implementations available, but Minuit has proven to be most stable for such high-dimensional optimisation problems.

The details on the computation of systematic uncertainties are sketched in Sec. 5.9.6, and the incorporation of the templates is explained in Sec. 5.9.4.

5.9.4 Template fits with a PLH: Morphing

TREXFITTER controls the NPs θ_t with the help of inter- and extrapolation. Three histograms are provided for each systematic uncertainty, which correspond to the nominal reference ($\theta_t = 0$) of the NP and the up ($\theta_t = +1$) and down ($\theta_t = -1$) variations of the simulation parameters.

The inter- and extrapolation controls how a variation of the NP θ_t varies the predicted yields, in terms of Eq. 5.15, namely $S_i(\theta_t), B_i(\theta_t)$. Various interpolation methods are available in TREXFITTER. Here only the default setting of a piecewise linear interpolation is used. A one-bin example is illustrated in Fig. 5.10(a).

The TREXFITTER framework extends this common template functionality from NPs to p.o.i. . Additionally, it allows the incorporation of more than three templates, because some dependencies are not well modelled by far range interpolation. A technique known as *morphing* transfers the usual parameter for the signal strength (μ) to represent a sequence of templates. It is inspired by the Effective-Field-Theory morphing applied in Higgs boson analysis [124].

The morphing interpolates between the templates and assigns a weight $w^k(\mu)$ to each template k . The weight is a function of the p.o.i., in general μ or in the scope of this analysis m_W or Γ_W . The default setup is a piecewise linear interpolation between the templates, which combines templates to model intermediate values of the p.o.i.. If S_i is the total number of events in bin i of the sample, which is to be constructed, and T_i^k is the number of events in bin i of template k , the creation of the sample is summarized with:

$$S_i = \sum_k w^k(m_W) \cdot T_i^k, \quad (5.18)$$

In the default case the sum over k is presented by two neighbouring templates. Hence, the weight w^k of template k , which is assigned to the p.o.i. value of m_W^k , is implemented as following:

$$w_i^k(m_W) = \begin{cases} 0, & \text{if } m_W < m_W^{k-1} \\ 1 - \frac{m_W^k - m_W}{m_W^k - m_W^{k-1}}, & \text{if } m_W^{k-1} < m_W < m_W^k \\ 1 - \frac{m_W - m_W^k}{m_W^{k+1} - m_W^k}, & \text{if } m_W^k < m_W < m_W^{k+1} \\ 0, & \text{if } m_W > m_W^{k+1} \end{cases}$$

Also more complex variations are available, which combine more than two templates for modelling interpolation steps. The default method is illustrated in Fig. 5.11(a). It presents the case of providing two templates corresponding to $m_W^{k=1} = 79999 \text{ MeV} (= 80399 - 400 \text{ MeV} = m_W^{\text{nom}} - 0.5\%)$ and $m_W^{k=2} = 80799 \text{ MeV} (= 80399 + 400 \text{ MeV} = m_W^{\text{nom}} + 0.5\%)$, which are interpolated for the fit. If the fit would converge at e.g. m_W^{nom} , the corresponding template would be built by scaling both templates by 0.5 and then adding them together. The comparison of this interpolated template with the original template for m_W^{nom} reflects the stability of this approach.

It has to be noted, that the morphing relies on a smooth transition between the templates, which is approximated with a linear behaviour in the default case. The default linear interpolation of bin contents is only applicable, if the bin contents behave linearly as function of the p.o.i. in the inspected range. The templates have to be provided in sufficient granularity to allow the linear approximation between the available templates. 5.11(b) and Fig. 5.12(a) present the bin content as function of Δm_W or $\Delta \Gamma_W$ for one exemplary bin in p_T^μ . The investigated template shifts are

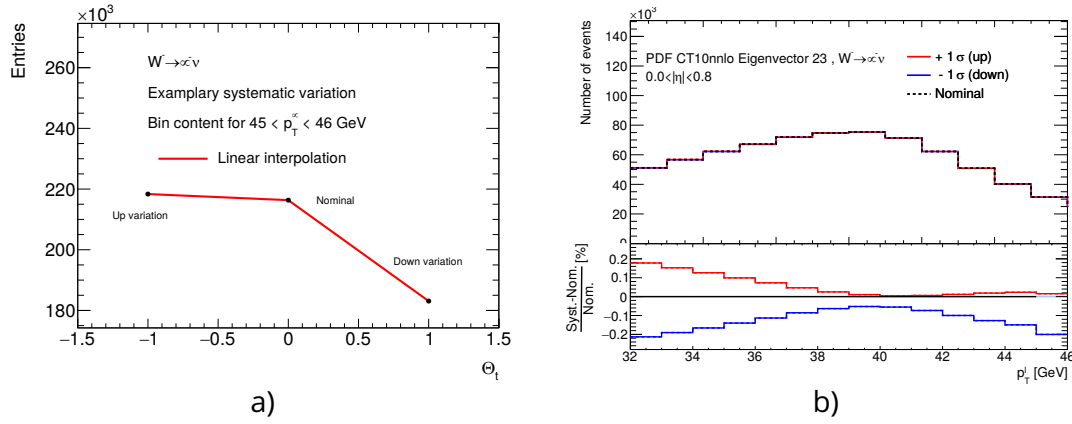


Figure 5.10: (a) Example for linear interpolation of bin content. The parameter Θ_t controls the pull of the NP. (b) The full distribution in p_T^μ for an exemplary systematic uncertainty.

much smaller than the nominal value of the p.o.i. for m_W ($\frac{\Delta m_W^{\max}}{m_W^{\text{nom}}} = \frac{400 \text{ MeV}}{80399 \text{ MeV}} \approx 0.5\%$). The linear approximation for the template transformation is therefore suitable in the investigated range. However, the inspected p.o.i. range is relatively large for Γ_W ($\frac{\Delta \Gamma_W^{\max}}{\Gamma_W^{\text{nom}}} = \frac{400 \text{ MeV}}{2085 \text{ MeV}} \approx 20\%$). Hence, the granularity of templates has to be high to approximate the change of the bin content as piecewise-linear. 5.12 (a) illustrates, that the bin content is not linear in $\Delta \Gamma_W$ in a range of about 400 MeV, but the zoom in Fig. 5.12 (b) justifies the linear approximation for a template spacing below 100 MeV. The template value selection employed here is

- relative to $m_W^{\text{nom}} = 80\,399 \text{ MeV}$:
 $\Delta m_W [\text{MeV}] = [0, \pm 4, \pm 12, \pm 16, \pm 24, \pm 32, \pm 48, \pm 64, \pm 80, \pm 200, \pm 400]$,
for the cross-check with the legacy fit approach.
And for the final results: $\Delta m_W [\text{MeV}] = [0, \pm 400]$
The results for the reduced set of templates are equivalent in the case of m_W . A smaller number of templates reduces the computation time significantly.
- relative to $\Gamma_W^{\text{nom}} = 2085 \text{ MeV}$:
 $\Delta \Gamma_W [\text{MeV}] = [0, \pm 10, \pm 20, \pm 60, \pm 110, \pm 160, \pm 220, \pm 270, \pm 320, \pm 360, \pm 400]$

The original setup of a PLH fit with TREXFITTER draws a further constrain from the comparison between the event count in data and the provided templates. The setup applied in this thesis discards the sensitivity to the normalization with the inclusion of a free floating normalization parameter for the Monte-Carlo simulation samples. The normalization factor is an additional free parameter similar to a NP, but without the Gaussian penalty term. The resulting fit strategy is then compatible to the legacy setup. The constraint via normalization will be re-included for the final publication.

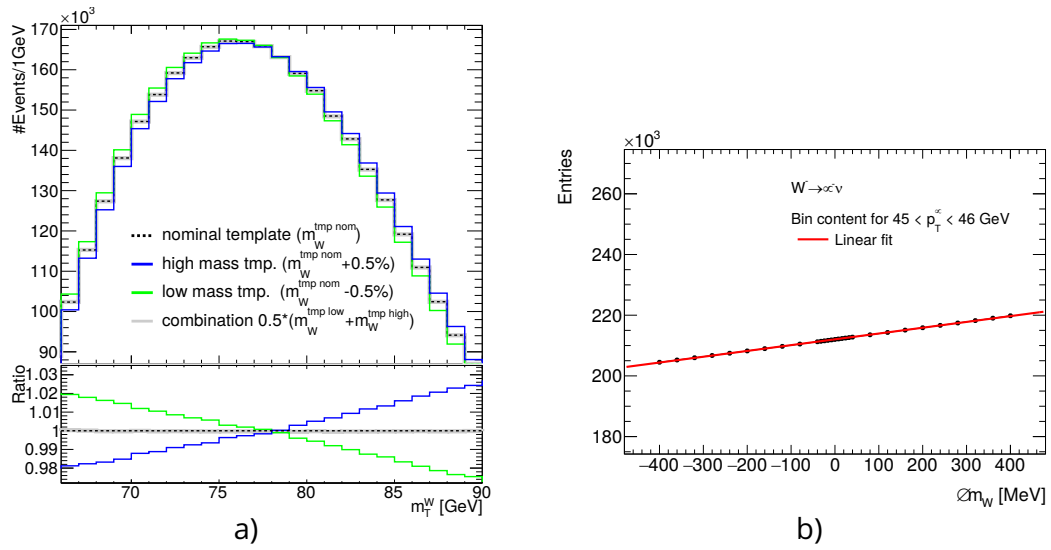


Figure 5.11: (a) Green corresponds to a template of lower mass value of m_W , blue to a higher one. Grey presents the linear combination of both templates and reproduces here the template of the central nominal value. (b) Bin content for an exemplary bin as function of the template shift of m_W . The linear approximation is suitable over the full range presented for m_W .

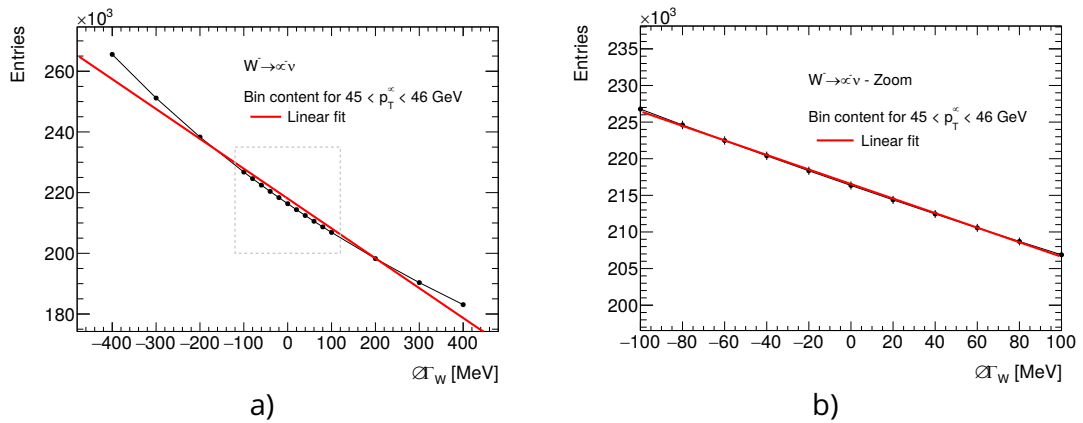


Figure 5.12: Bin content for an exemplary bin as function of the template shift of Γ_W . (a) The linear approximation is not suitable over the full range presented Γ_W . (b) The zoom reveals, that the linear approximation is sufficient for a template separation of about $\Delta \Gamma_W = 100$ MeV.

5.9.5 Validation of the reanalysis process

The core part of the validation is the closure of the central fit results for the individual channels and their combination. Fig. 5.13 presents the comparison between the legacy and reanalysis results. The central values agree within roughly 2 MeV. The largest deviation occurs for p_T^μ of positively charged muons in the most outer rapidity region ($W^+, p_T^\mu, 2.0 < |\eta| < 2.4$). The regions of high rapidity suffer from large statistical uncertainties, hence a larger difference is reasonable. The error bars in Fig. 5.13 indicate the statistical uncertainties. The reanalysis estimates the statistical uncertainties systematically too large, which could also reason the small shifts of the central fit values. The discrepancies might point to minimal differences in the fit setup, but are still reasonably small to confirm the agreement.

The plot includes the results for the PLH approach applied to the very same data set. Only statistical uncertainties are profiled. The differences between the reanalysis χ^2 fit and the PLH fit are also in the order of about 2 MeV and are covered by the statistical uncertainties. Minor deviations are expected for this comparison, because of the differences in the fit approach and the slightly increased statistical uncertainties. The statistical uncertainties, which are cited in Fig. 5.13 for the PLH approach, are all constantly smaller than the χ^2 counterpart, because they only incorporate the statistical uncertainty related to the measured data, while the χ^2 fit includes the Monte-Carlo statistical uncertainties as well. The individual fit results are also provided in Tab. B.1 in the appendix.

The validation is summarized in greater detail in Tab. 5.4. It compares the different uncertainty categories. Sec. 5.9.1 presents the details on the uncertainty estimation with the χ^2 approach. The agreement with the legacy results is of the same order as the closure of the central fit results. It shows also a tendency for larger discrepancies in outer pseudorapidity regions.

The statistical uncertainties are in good agreement. They diverge at most by 0.3 MeV, most channels agree even within 0.1 MeV. All other uncertainty categories close within 1 MeV, which agrees with the tolerance of the fit setup. For instance, the choice of the template values or the range of the parabola fit to the χ^2 distribution affect the results in the same order. And these detail of the setup could not be resurrected, hence this order of difference is expected.

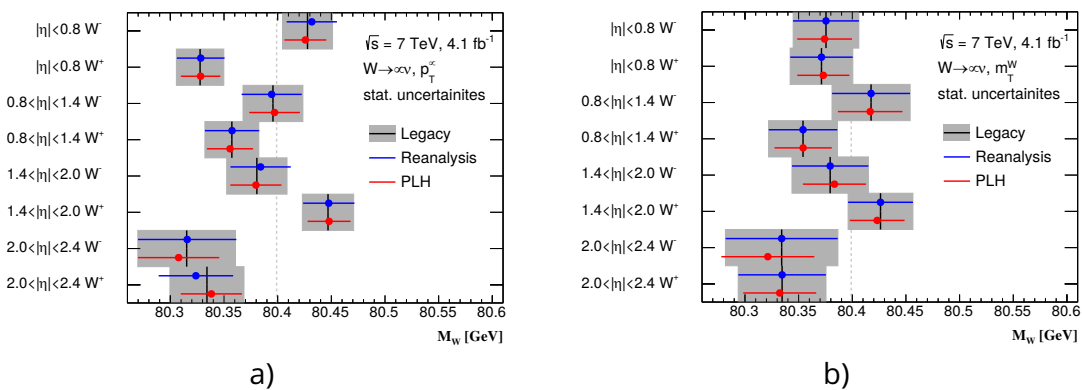


Figure 5.13: Comparison between the central fits of the legacy analysis (grey), the resurrected χ^2 fit for the reanalysis (blue) and the PLH fit (PLH) on the very same data set. (a) are the results for the fits in p_T^μ and (b) in m_T . All fits are shown with statistical uncertainties only.

Unc. category [MeV]	Stat. Unc.		Muon Unc.		Recoil Unc.		PDF Unc.	
	Legacy	Reanalysis	Legacy	Reanalysis	Legacy	Reanalysis	Legacy	Reanalysis
$m_T W^- \eta < 0.8$	30.6	30.7	11.6	12.7	13.1	11.8	30.6	30.2
$m_T W^- 0.8 < \eta < 1.4$	36.4	36.3	18.5	20.8	12.2	11.1	22.2	21.3
$m_T W^- 1.4 < \eta < 2.0$	35.6	35.6	33.9	32.9	10.5	10.9	23.1	22.4
$m_T W^- 2.0 < \eta < 2.4$	52.4	52.2	123.7	115.7	11.6	11.6	34.1	33.5
$m_T W^+ \eta < 0.8$	29.2	29.1	12.4	11.9	15.2	14.5	28.4	28
$m_T W^+ 0.8 < \eta < 1.4$	32.1	31.9	19.3	19.8	13	13	23.3	22.3
$m_T W^+ 1.4 < \eta < 2.0$	30.2	30.2	35.1	33.4	14.3	13.5	27.2	26.4
$m_T W^+ 2.0 < \eta < 2.4$	40.9	40.8	112.4	101.7	14.4	12.1	32.8	32.6
$p_T^\mu W^- \eta < 0.8$	23.3	23.4	11.6	12.1	2.6	2.6	26.4	25.3
$p_T^\mu W^- 0.8 < \eta < 1.4$	27.9	28	18.3	19.3	2.5	2.5	19.8	18.9
$p_T^\mu W^- 1.4 < \eta < 2.0$	28.1	28.1	35.2	32.2	2.6	2.6	20.6	19.9
$p_T^\mu W^- 2.0 < \eta < 2.4$	45.5	45.8	116.1	111.7	2.6	2.6	32.7	31.3
$p_T^\mu W^+ \eta < 0.8$	22.1	22.2	12.2	12.8	2.6	2.6	24.7	23.3
$p_T^\mu W^+ 0.8 < \eta < 1.4$	25.1	25.3	19.1	19.2	2.5	2.5	20.6	19.8
$p_T^\mu W^+ 1.4 < \eta < 2.0$	23.9	23.9	33.1	31.2	2.5	2.5	25.2	23.9
$p_T^\mu W^+ 2.0 < \eta < 2.4$	34.5	34.7	110.1	109.5	2.5	2.5	31.8	31.3

Table 5.4: Validation of the different uncertainty categories. The values for the legacy analysis are taken from [72], while the reanalysis reevaluates the uncertainties based on pseudo experiments.

5.9.6 Migration of the legacy uncertainties to the PLH fit approach

The uncertainties of the legacy χ^2 fit are transformed to NPs in the context of the PLH approach as defined before in Eq. 5.15. A parameter θ_i is assigned to each systematic and floats within the provided up and down variation following interpolation technique presented in Sec. 5.9.4. The samples, which are employed in this thesis, are all tailored to the different types of uncertainties presented in Sec. 5.9.1. The migration of the paired (or up-down type) uncertainties is straight-forward. They are directly incorporated into the PLH framework. For instance, all uncertainties related to the muon momentum calibration are provided as up- and down-variations. The muon momentum calibration is further decorrelated among the pseudorapidity regions, which define the different fit channels (see Tab. 5.1). Therefore a unique NP is assigned to each region in pseudorapidity for each muon reconstruction related uncertainty.

However, the other types of systematic uncertainties are not well defined in a PLH fit. The uncertainties, which represent a single shift, are artificially translated into the shape of a up-down type variation, as an only one-sided systematic uncertainty would introduce instabilities in the fit and contradicts the Gaussian shaped approximation. The given shift is simply defined as the up variation, while the down variation is created by mirroring the shift with respect to the nominal distribution. This extension with an artificial down variation tends to a higher estimation of the related uncertainty compared to the χ^2 evaluation. The enlarged estimate is justified, as the one-sided systematic itself presents only rough estimate. Usually it refers to the comparison of two setups, in order to assess the size of the effect.

The migration of systematic uncertainties, which are based on toy Monte-Carlo samples, are estimated with a first approximation, as there is no distinct correspondence for an up or down type variation in this case. It will be further improved for the future publication. The aim of the proof of principle remains valid, because the corresponding uncertainties contributed marginally to the overall uncertainty and are hence not expected to dominate the profiling.

Two more uncertainty categories, which are related to the physics modelling, are

Systematic Name	Source of the uncertainty	Reference
	Physics Modeling	
PDF	The CT10NNLO PDF uncertainties are described by 25 eigenvectors with up- and down variation each.	Sec. 5.6.5
cross-section	Cross section uncertainty of the simulated background contributions (diboson, top, $Z \rightarrow \mu\mu$, $W \rightarrow \tau\nu$) as well as the MJ background.	Sec. 5.4.3
	Hadronic Recoil Uncertainty	
HR VAR_RESO, HR VAR_SUMET	Uncertainty from the extrapolation of the hadronic recoil from the kinematic range of the Z boson decay to the W decay due to the dependence of the hadronic recoil resolution on the sum of the missing transverse energy.	Sec. 5.8
	Muon reconstruction Uncertainties (decorrelated in η)	
MUON EXTRAP	Uncertainty related to the extrapolation of the muon transverse momentum calibration of the Z to the W boson decay.	Sec. 5.7.1
MUON METHOD	Uncertainty from the non closure of the two methods used for the sagitta bias calibration.	
MUON RESOL	Uncertainty on the estimation of the muon momentum resolution smearing the transverse momentum dependent calibration procedure.	
MUON STAT	Propagation of the uncertainty due to the limited statistics of the Z boson sample used for the muon momentum calibration.	
MUON SAGITTA	Uncertainty on the sagitta bias estimation.	
MUON SF TRIGGER	Uncertainty on the estimation of the muon trigger scale factor.	Sec. 5.7.2
MUON SF ISO	Uncertainty on the estimation of the muon isolation scale factor.	
MUON SF RECO	Uncertainty on the estimation of the muon reconstruction scale factor.	

Table 5.5: Summary of the systematic uncertainties, which are profiled in the PLH fit. A similar summary is found in [125], which employs the same set of simulation samples.

to be migrated. The systematic uncertainties on the QCD modelling, except the PDF uncertainties, are not available for profiling, as well as the uncertainties assigned to the electroweak corrections, like scale variations, parton shower and angular coefficients. The legacy analysis added in square the corresponding uncertainty estimates as constant offset to the total uncertainty. But the individual distributions are still to be resurrected. Therefore, these are never included in the PLH fits in the following, but usually part of full uncertainty for legacy measurement unless stated differently.

The systematic uncertainties, which are profiled in the fit of m_W and Γ_W are summarized in Tab. 5.5.

5.10 First results for m_W using a PLH fit

The PLH fit approach develops its full potential, when all NP are considered simultaneously. The measurements of m_W are performed with the PLH framework including all NP discussed in Sec. 5.9.6. The fits are applied on the p_T^μ and m_T distributions for negatively and positively charged muons and separately in four bins of muon pseudorapidity (η). The most powerful fit setup presented here is the combination for all channels in p_T^μ or m_T , because the correlated NPs are constraint by all channels simultaneously. In the following, there are 18 different determinations of m_W in total.

Figure 5.14 illustrates all results in comparison to the legacy analysis. The table 5.6 states the corresponding numbers. The contribution of the uncertainties, which are neglected in the PLH approach, is about 2-3 MeV to the total legacy uncertainty of the individual channels.

A more precise comparison is provided in Tab. 5.7. The total uncertainty of the legacy analysis is cleaned from these contributions, i.e. the corresponding uncertainty categories are subtracted in quadrature.

In general, all measurements of m_W are consistent with the legacy analysis. The larger discrepancies in the regions of higher pseudorapidity are covered by the uncertainties. The uncertainties in the individual η -bins are smaller than the legacy values. There are a few outliers, which will be discussed at the end of this section, when focussing on the individual NP. The important results are the combinations in p_T^μ and m_T :

$$\begin{aligned} m_W(p_T^\mu) &= 80\,372.6 \pm 15.8 \text{ MeV} = 80\,372.6 \pm 13.1(\text{syst.}) \pm 8.9(\text{stat.}) \text{ MeV} \\ m_W(m_T) &= 80\,365.6 \pm 19.3 \text{ MeV} = 80\,365.6 \pm 15.5(\text{syst.}) \pm 11.5(\text{stat.}) \text{ MeV} \end{aligned} \quad (5.19)$$

The implementation of the PLH fit approach narrows the uncertainties by 2.6 MeV in the combination for p_T^μ and by 5 MeV for m_T compared to the (modified) legacy values as shown in the first column of Tab. 5.7. Overall, the improvement results from a reduced PDF uncertainty for p_T^μ , while m_T benefits mostly from the reduction of the uncertainty related to the hadronic recoil.

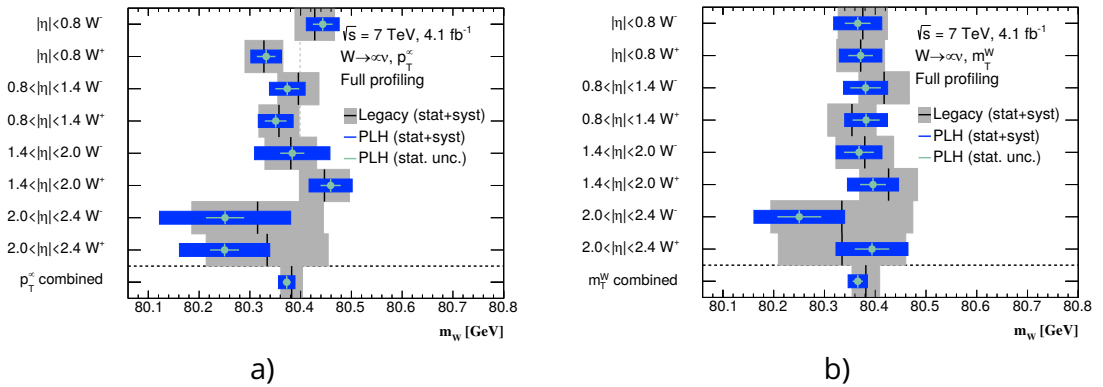


Figure 5.14: Results of the m_W fit using a PLH approach on the distributions in (a) p_T^μ and (b) m_T . The fits profiled all uncertainties listed in Tab. 5.5. The grey shades correspond to the fit results of the χ^2 fit applied in the legacy analysis including all uncertainties. The corresponding central values are already presented in Fig. 5.13.

Table 5.7 displays the impact of the different uncertainty categories in greater detail. The first column, *Full Profiling*, is compatible to Tab. 5.6. It represents the inclusion of all available NPs. It lists the corresponding full uncertainty for the PLH fit in the column *PLH* and for the legacy χ^2 fit in column *Leg.*. The statistical uncertainty related to the data is not profiled here in contrast to Tab. 5.6, but it is simply added in quadrature. Hence, possible correlations are neglected and the total uncertainty (*Full Profiling* - *PLH*) is slightly larger in Tab. 5.7 than in Tab. 5.6. Also the legacy values (*Leg.*) are modified. The contribution from the uncertainties, which are not available for profiling yet, are subtracted. It yields therefore the best benchmark to evaluate the PLH fit uncertainty.

Channel	Central value[MeV]		Difference	Full uncertainty [MeV]	
p_T^μ -fit	PLH	Legacy	(PLH-Legacy)	PLH	Legacy
$W^- \eta < 0.8$	80443.6	80427.8	-15.8	33.4	39
$W^+ \eta < 0.8$	80332.1	80327.7	-4.3	30.5	37.3
$W^- 0.8 < \eta < 1.4$	80373.7	80395.6	21.9	35.7	40.5
$W^+ 0.8 < \eta < 1.4$	80350.9	80357.3	6.4	34.6	39.5
$W^- 1.4 < \eta < 2.0$	80383.5	80380.6	-2.8	60.7	50.9
$W^+ 1.4 < \eta < 2.0$	80459.1	80446.9	-12.1	41.7	49.3
$W^- 2.0 < \eta < 2.4$	80251.1	80315.2	64.1	116.3	129.6
$W^+ 2.0 < \eta < 2.4$	80250.2	80334.1	83.9	92.4	120.2
p_T^μ combined	80372.6	80382.3	9.6	15.8	21.4
m_T -fit					
$W^- \eta < 0.8$	80365.5	80375.5	10	47.8	48.5
$W^+ \eta < 0.8$	80371.2	80371.3	0.1	43.6	47.1
$W^- 0.8 < \eta < 1.4$	80381	80417.5	36.5	55.4	49.7
$W^+ 0.8 < \eta < 1.4$	80382	80354.1	-27.8	41.4	47.6
$W^- 1.4 < \eta < 2.0$	80368.1	80379.4	11.3	45.6	56.9
$W^+ 1.4 < \eta < 2.0$	80395.6	80426.3	30.6	50.2	56.9
$W^- 2.0 < \eta < 2.4$	80250.4	80334.2	83.8	87.1	139.9
$W^+ 2.0 < \eta < 2.4$	80393.6	80334.6	-59	73.5	125.5
m_T^W combined	80365.6	80381.5	15.8	19.3	27.2

Table 5.6: Summary of the results from the legacy analysis (χ^2 fit) with the uncertainties compared to the results of the profile likelihood approach. The latter profiled all available uncertainties. The toy based ones and the uncertainty on the MJ shape are excluded by now. The legacy numbers are unmodified and quoted from Ref.[72]. Tab. 5.7 provides the legacy uncertainty cleaned from the contributions, which are not included in the profile likelihood fit.

The column *Shift* presents the difference of the results for m_W between profiling only statistical uncertainties (see Fig. 5.13) and profiling only the declared NP category plus statistical ones. It is a measure for the impact of the corresponding NPs on m_W .

The uncertainty on m_W due to a group of NPs (column *PLH*) is evaluated slightly differently: Here, the full uncertainty is firstly evaluated using all NP. Then all NPs, which belong to the category of interest, e.g. PDF, are removed from the fit and the full uncertainty is evaluated again. The quadratic difference between the uncertainties for profiling all NPs and a reduced group of NPs defines the impact of the removed category on the uncertainty of m_W .⁴

The dominating uncertainties are still the PDF related uncertainties, which range from 18 MeV to 36 MeV among the different channels. However, especially the lowest pseudorapidity region ($|\eta| < 0.8$) is able to improve the corresponding uncertainty compared to the legacy measurement. Other regions of η remain in the same order with respect to this uncertainty.

The muon calibration uncertainties are the largest experimental systematic uncertainty group ranging from 10 MeV to 40 MeV in $|\eta| < 2.0$, and they reach about 90 MeV in the outer pseudorapidity regions. This behaviour is parallel to the legacy analysis. The PLH fit approach lowers the corresponding uncertainty only in the outer pseudorapidity regions, but it does not affect the combination.

The background category (*Bkg.*) summarizes the impact of the NPs, which describe the uncertainty on the cross-section for simulated backgrounds. These are of the same order as the legacy analysis. Only the regions of high pseudorapidity reveal an increased impact compared to the legacy values. The relative background contribution rises in these regions, an increased impact and a larger effect due to the shape sensitivity are therefore reasonable.

The *recoil* category sums up the impact of the uncertainties on the measurement of the hadronic recoil. The increased impact for the PLH approach can be attributed to the artificial symmetrization of the NP *VAR_SUMET*, which is originally provided as a single shift. Hence, it is expected, that the impact is overestimated. Moreover, the shape sensitivity is able to reduce the uncertainty for m_T despite of this modification.

So far the presented impacts highlighted the validity of the reanalysis, but gave only a hint to its actual potential. The ranking plots in Fig. 5.15 allow a more detailed inspection of the individual NPs and give evidence for the future prospects of the reanalysis effort.

The impact Δm_W of a NP (Θ) on m_W is given by the shift in m_W between the nominal fit and another fit, where the NP is fixed to a value $\hat{\Theta} \pm x$. The value $\hat{\Theta}$ is the maximum likelihood estimator of the nuisance parameter, also termed as *post-fit value*. The nominal shift, $\hat{\Theta} \pm 1$, represents the *pre-fit value* with its original constraints. A ranking plot summarizes the pre- and post-fit impact of the NPs, listed in the order of their impact on m_W . Only ten NPs with the largest impact are listed here for better visibility. The figure presents solely results for the combination for the same reason.

The ranking plots resemble similar effects as Tab. 5.7, i.e. the fits are most sensitive to NPs related to the muon calibration and the PDF uncertainties. One of the largest impacts on m_W is assigned to *MUON_STAT*. This is exactly the NP, which will be tailored with the planned inclusion of further datasets to determine the muon momentum calibration.

The listed PDF NPs, for example *PDF ev. 8*, *PDF ev. 12*, show two different aspects in the ranking plot. On one hand, the PLH approach could already trim down the corresponding uncertainties. It is visualized in the smaller post-fit impact compared to the pre-fit impact (non-filled vs. filled blue blocks). This is already reflected in the

⁴The corresponding feature of the TREXFITTER software is called *Grouped Impact*.

Channel p_T^μ -fit	Full Profiling [MeV]			Muon impact			Recoil impact			Bkg. impact			PDF impact			MC Stat. impact		Full Stat. Unc.	
	Shift	PLH	Leg.	Shift	PLH	Leg.	Shift	PLH	Leg.	Shift	PLH	Leg.	Shift	PLH	Leg.	Shift	PLH	PLH	Leg.
$W^- \eta < 0.8$	-19.6	31.9	37.5	9.2	13.7	11.6	-0.1	1.7	2.6	1.3	3.1	5.8	10.5	18.3	26.4	-0.1	7.7	20.7	23.3
$W^+ \eta < 0.8$	-30.4	32.5	35.3	3.5	10.3	12.2	-0.9	1.2	2.5	0.8	4.1	5.1	10.1	18.6	24.7	0.2	7.2	24.2	22.1
$W^- 0.8 < \eta < 1.4$	-59.3	34.8	38.7	-10.2	17.8	18.3	0.1	0.7	2.6	-3.3	4.9	5.6	-12.2	17.9	19.8	0.2	9.8	25.2	27.9
$W^+ 0.8 < \eta < 1.4$	-40.7	45.9	37.5	0.5	17.3	19.1	-0.5	2.4	2.6	-0.4	2	4.7	-2.8	20	20.6	0	8.9	39	25.1
$W^- 1.4 < \eta < 2.0$	-33.5	44.7	49.8	-11.5	40	35.2	0	15.8	2.6	0	5.3	5.6	9.9	24.7	20.6	-0.7	20.7	27.7	28.1
$W^+ 1.4 < \eta < 2.0$	-25	40.4	47.7	4.1	27.3	33.1	0.2	3.8	2.5	0.8	4.9	4.9	5.4	22.6	25.2	0	9.5	23	23.9
$W^- 2.0 < \eta < 2.4$	-92.3	94.3	129.1	-67	88.4	116.1	-0.7	1.8	2.5	-1.1	15.5	7.6	15.4	36.6	32.7	-0.1	25.6	32.4	45.5
$W^+ 2.0 < \eta < 2.4$	-124.5	98.1	119.8	-89.3	85.2	110.1	-0.7	0	2.5	-2.3	12.6	6.4	4.6	35.2	31.8	-0.3	24.4	37.7	34.5
p_T^μ combined	-37.5	16	18.6	3.3	10.7	10.7	-1.3	1.4	2.5	19.1	5.1	3.9	3.9	8.6	10.7	0	4	8.9	10.1
m_T -fit																			
$W^- \eta < 0.8$	-44.4	45.8	47.2	11.7	11.7	11.6	-9.9	4.3	13.1	-2.9	14.2	8.5	-5.7	26.3	30.6	-0.1	10.2	27.3	30.6
$W^+ \eta < 0.8$	-38	46.5	45.7	-1.2	8.3	12.4	3.6	17.5	12.2	-0.4	10.3	8.1	-3.4	27.5	28.4	-0.1	10.7	31.8	29.2
$W^- 0.8 < \eta < 1.4$	-70.1	52.3	48.4	21.3	18.9	18.5	-26.9	13.4	10.5	-0.6	2.5	7.7	-0.4	21.1	22.2	0	13.4	32.1	36.4
$W^+ 0.8 < \eta < 1.4$	-8.3	52.3	46.2	-0.7	11.6	19.3	26.5	15.9	11.6	0.3	6.8	6.8	2.6	23.9	23.3	-0.1	16.5	46	32.1
$W^- 1.4 < \eta < 2.0$	-49.1	41.2	55.8	-12.1	19.7	33.9	3.7	13	15.2	-0.2	9.5	8.1	-1.2	22.4	23.1	1.7	13.5	27.7	35.6
$W^+ 1.4 < \eta < 2.0$	-63.2	50.6	55.7	-24.5	26.7	35.1	-5	13.1	13	0.1	6.6	7.2	-5.3	28.6	27.2	-0.1	13	29.6	30.2
$W^- 2.0 < \eta < 2.4$	-107.4	72.8	139.4	-74.8	58	123.7	-10.5	6.8	14.3	-2.6	25	10.2	5.5	33.5	34.1	-0.2	27.4	37.1	52.4
$W^+ 2.0 < \eta < 2.4$	25.3	67.9	125.1	33.2	41.9	112.4	17.8	19.1	14.4	-0.7	11.6	9	5.5	31.4	32.8	-0.6	17.9	38.6	40.9
m_T^W combined	-38.5	19.5	25	2	11	11.6	-12.7	6	13	23.6	9.7	6	5.1	12.3	11.2	-0.6	5.7	11.5	13

Table 5.7: Summary of the impact of different NP categories on the profile likelihood fit compared to the corresponding uncertainty from the legacy analysis (Leg.). Shift states the difference between profiling the NP category and profiling only statistical uncertainties. PLH lists the uncertainty on m_W related to this category of NP. The first category, Full Profiling, profiled only systematic uncertainties. The statistical uncertainties are not profiled in this case, but added afterwards. This results in a slightly higher total uncertainty for PLH than it is stated in Tab. 5.6. The total uncertainty of the legacy analysis is cleaned from the contributions, which are not profiled, in order to guarantee compatibility of the results.

reduction presented in Tab. 5.7. On the other hand, a few PDF NPs encounter large pulls ($\geq 2 - 3$), which indicates, that the nominal PDF setup describes the data not adequately. The future, improved PDF sets for the final profiling, which will include recent LHC measurements, hold therefore great potential for further reduction of the corresponding uncertainty. They might reduce the observed pulls with a better description of the data and in parallel decrease this dominant source of uncertainties.

All in all, the PLH approach offers a great opportunity to reduce the systematic uncertainties on m_W , already the reprocessing of the legacy samples is able to improve it visibly. The presented results further announce an even greater potential for the anticipated improvements on the uncertainties of the muon calibration and the PDF sets. Hence, a significant reduction of the legacy uncertainty on m_W is made accessible with the presented PLH approach.

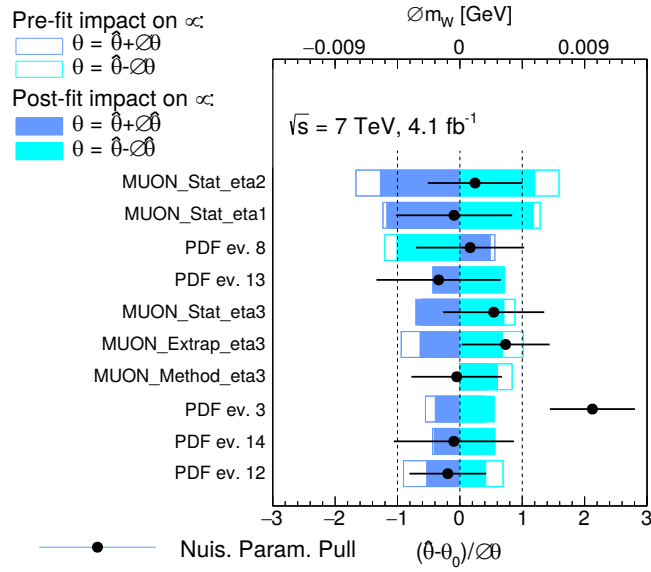


Figure 5.15: Ranking plot for profiling the combination fit of p_T^μ . It lists the ten NPs with the largest impact for a better overview. An overview of all NPs for p_T^μ and m_T are displayed in Fig. B.1. The blue blocks indicate the pre- and post-fit impact and belong to the top x-axis. The black dots indicate the pulls and refer to the bottom axis. Only the ten most impacting NPs are listed.

5.11 Measuring Γ_W using a PLH fit

5.11.1 Adaptions for the Γ_W fit setup

In general, the measurements of Γ_W are performed in the same manner as the measurements of m_W , i.e. performing a template fit to the kinematic distributions. But the fit of Γ_W gains in complexity compared to the measurement of m_W , although the very same data set and simulation samples are used.

Firstly, the morphing of Γ_W templates requires a careful choice of template samples, because the linear approximation is applicable only to a sub-range of the investigated range of Γ_W as outlined in Sec. 5.9.4. Secondly, the investigated distributions are less sensitive to changes in Γ_W compared to similar variations in m_W . Former measurements of Γ_W , such as the one in Ref. [86], demonstrated, that the kinematic distribution of m_T becomes sensitive to Γ_W in the range of $m_T > m_W$. This thesis presents the measurement of Γ_W in synergy with the legacy measurement of m_W .

So only the range of $60 \text{ GeV} < m_T < 100 \text{ GeV}$ is available, which overlaps minorly with the most sensitive region. The current scope lacks the considerations of the corresponding lepton scale factors and systematic uncertainties, in order to investigate m_T far above the m_W value. The results for the fit of Γ_W using m_T templates are therefore not sufficiently robust and are not cited in the following results section 5.11.2. Nevertheless, they are listed in the Appendix Sec. B.3 for completeness. They still serve as a basis to estimate the future potential of the analysis, when the fit range will be extended.

The results for Γ_W are sufficiently robust for the fits using p_T^μ templates. Three different fit ranges are investigated:

- $30 \text{ GeV} < p_T^\mu < 50 \text{ GeV}$
- $35 \text{ GeV} < p_T^\mu < 50 \text{ GeV}$
- $30 \text{ GeV} < p_T^\mu < 45 \text{ GeV}$

Results from all three intervals are found to be compatible within the related uncertainties. The largest fit range yields the smallest uncertainties, which is expected for a PLH fit, as the constraining power grows with the number of bins. This range is chosen for the final results.

A further peculiarity of the W boson width in comparison to the W mass should be noted: Γ_W is highly correlated with the production cross-section for the W boson, which becomes evident in the corresponding relation presented in Eq. 2.40. Preliminary Monte-Carlo generator studies revealed, that the cross-section alters by about 2%, when the value of Γ_W is varied within the uncertainties of the world average, 42 MeV. This dependence offers the possibility to further constrain Γ_W by fitting the event yield in addition to the template shape. However, the scope of this thesis applies solely a shape sensitive fit and therefore drops the normalization sensitivity, but it will be integrated for the anticipated publication.

5.11.2 First results for Γ_W using a PLH fit

The following results focus on the effectiveness of the PLH fit approach and take over the general setup of the previously presented m_W fit using p_T^μ templates. The fit range is adapted to the originally investigated range as outlined in Sec. 5.9.1, i.e. $30 \text{ GeV} < p_T^\mu < 50 \text{ GeV}$. There are eight measurements performed separately in muon pseudorapidity and charge categories plus the corresponding combination.

The following results are still blinded, i.e. an unknown constant offset is added to the nominal width to produce template distributions. The results for the individual channels and the corresponding combinations are summarized in Fig. 5.16 displaying the full uncertainty. It further provides a comparison to the profiling results using statistical uncertainties only and the results from the application of the legacy χ^2 -minimization fit. The table 5.8 presents a more detailed differentiation of the individual uncertainty categories and lists the impact of the different NPs. The combined and blinded result is:

$$\begin{aligned} \Gamma_W(p_T^\mu) &= 2165.5(+blinding) \pm 29.3 \text{ MeV} \\ &= 2165.5(+blinding) \pm 26.6(syst.) \pm 12.2(stat.) \text{ MeV} \end{aligned} \quad (5.20)$$

The blinding offset does not allow any statement, whether the global average or the electroweak fit value is favoured. The presentation in Fig. 5.16 exposes a tension for the measurements of W^- in $|0.8| < \eta < |1.4|$ and $|1.4| < \eta < |2.0|$ compared to

all other channels. There is no comparable behaviour visible for the measurement of m_W (Fig. 5.14), which suggests, that possible discrepancies in the PDF set or the lepton calibrations are not causing this tension. But the impact of the background contribution varies, when comparing the measurement of m_W and Γ_W , and could cause such an imbalance.

Nevertheless, it is remarkable, that already these preliminary results yield an uncertainty, which is about 25% smaller than the world average uncertainty ($\Gamma_W^{global} = 2.085 \pm 0.042$ GeV [56]). Even the uncertainty on individual channels is already in the order of the world average uncertainty. Contributions from electroweak and QCD corrections are not taken into account yet. These can be estimated by referencing the corresponding uncertainties from the comparable measurement by the DØ collaboration [126], namely 7 MeV. It further provides a first reference for the impact of the uncertainty on m_W for the measurement of Γ_W . The DØ collaboration estimates the corresponding uncertainty on Γ_W to be 5 MeV. It is not evaluated particularly in the scope of this thesis, but the related uncertainty on Γ_W is expected to be smaller than the value for the DØ measurement due to the improved measurement of m_W . However, the presented total uncertainty remains below the uncertainty of the world average, even with the consideration of the referenced uncertainties. And the sensitivity of the presented results will further improve, when combined with results from m_T fits and the electron channel. Hence, the final measurement is anticipated to significantly impact the global average.

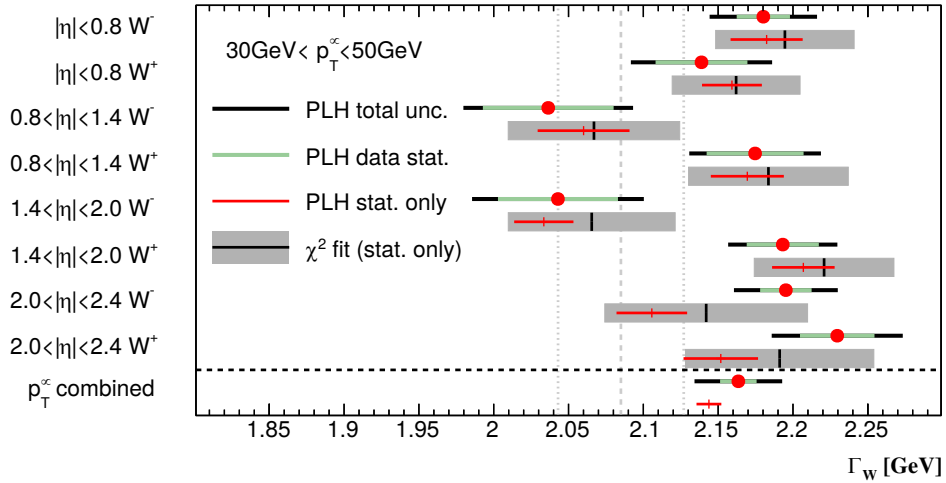


Figure 5.16: Results of the Γ_W fit using a PLH approach on the distributions in p_T^μ . The fits presented with green and black bars profiled all uncertainties listed in Tab. 5.5, but exclude the Monte-Carlo statistical uncertainties. The red bars illustrate the results for profiling only data statistical uncertainties. These are put in direct comparison to the χ^2 -minimization results (grey squares), which include only statistical uncertainties. The vertical dotted lines reference the world average and its uncertainties ($\Gamma_W^{global} = 2.085 \pm 0.042$ GeV). But all results for the central values of Γ_W are still blinded, so the world average serves only for the comparison of the uncertainties.

The split of the impact of the various NP categories is different to the measurement of m_W , despite the usage of similar simulation and data sets. The impact of the uncertainties on the background yields is comparable to the impact related to the

Channel p_T^μ -fit	Full Profiling [MeV]			Muon NPs		Recoil NPs		Bkg. NPs		PDF NPs		Stat. Unc.
	Central Value	Full Unc.	Shift	Shift	Impact	Shift	Impact	Shift	Impact	Shift	Impact	Impact
$W^- \eta < 0.8$	2179.9	35.9	-2.5	-8.7	17.6	0.2	26.6	0.5	7	3.1	24.1	17.8
$W^+ \eta < 0.8$	2138.4	47.2	-20.8	-17.4	22.2	-7.5	18.2	4.1	17.1	5.2	25.3	30.7
$W^- 0.8 < \eta < 1.4$	2036.4	56.7	-23.6	-15.2	12.5	-7.4	18.1	1.4	10.2	0.3	25	43.7
$W^+ 0.8 < \eta < 1.4$	2174.7	44	5.2	-1.8	13.4	5.2	29.1	-0.1	21.1	-0.1	21.5	32.4
$W^- 1.4 < \eta < 2.0$	2045	57.4	11.5	24	25.1	-5.5	15.7	0.7	11.7	3	20.4	40.1
$W^+ 1.4 < \eta < 2.0$	2193.8	36.5	-13.2	-9.4	0.9	-0.1	6.6	-0.9	13.5	-10	16.9	24.1
$W^- 2.0 < \eta < 2.4$	2195.3	34.7	89.7	90.8	2	-4.6	11.9	22.8	1.6	51.8	22.4	17.2
$W^+ 2.0 < \eta < 2.4$	2222.5	43.8	70.7	77.6	11.1	-7.1	8.1	20.6	25.7	65.5	17.7	24.9
p_T^μ combined	2164.5	29.3	20.7	36.1	8.6	-36.4	9.8	11.5	12.3	2.6	12.3	12.2

Table 5.8: Summary of the impact of different NP categories on the profile likelihood fit of Γ_W . Shift states the difference between profiling the NP category and profiling only (data) statistical uncertainties. Impact lists the uncertainty on Γ_W related to this category of NP. The first category, Full Profiling, profiled all available uncertainties and presents the blinded results for the central values of Γ_W .

PDF modelling. Both categories have a larger impact than the NPs, which represent the uncertainty on the muon calibrations or the hadronic recoil.

The decay width of the W boson is directly connected with its production cross-section, which is displayed in Eq. 2.40. The measurement of Γ_W is therefore particularly sensitive to variations of the predicted or measured event yield, although the fit is predominantly sensitive to the distribution shape in its current setup. This dependence manifests itself in relatively large contributions from the statistical and the background related uncertainties. Therefore, an extension of the fit range to higher values of m_T and p_T^μ will not only improve the sensitivity to Γ_W due to kinematic reasons, but it will also reduce the statistical uncertainty.

Furthermore, the inspection of the different NP categories reveals, that the measurement of Γ_W will also profit from improved uncertainties on the PDF sets. The PDF related NPs and the muon calibration related NPs induce a large shift for the fits of the outer pseudorapidity region ($2.0 < |\eta| < 2.4$) in p_T^μ , which further indicates the need for a revision of the corresponding NP modelling. The improvement on the muon related systematics might be of less importance, when comparing the impact values.

Nonetheless, the current analysis points to a measurement sensitivity of Γ_W , which will be able to compete with previous measurements regardless of the anticipated improvements.

5.12 Conclusion for the measurements of m_W and Γ_W

This thesis presents the re-evaluation of the measurement of the W boson mass with the ATLAS detector. The studies are based on the legacy analysis presented in Ref.[72]. The value of m_W is obtained with template fits to the kinematic distributions of the decay muons, namely m_T and p_T^μ . The first stage of the measurement is the successful resurrection of the legacy samples and fit techniques, which are incorporated into the validation steps and outlined in Sec. 5.4.4 and Sec. 5.9.5.

The presented analysis replaces the former χ^2 based fit with a PLH approach. The latter is especially sensitive to shape variations, which result from systematic uncertainties. It is therefore able to improve the modelling uncertainties related to the choice of the PDF set by about 2 MeV to 5 MeV compared to the legacy measurement.

The results of the PLH fit are:

$$\begin{aligned} m_W(p_T^\mu) &= 80\,372.6 \pm 19.1 \text{ MeV} \quad [\text{legacy} : 80\,382.3 \pm 21.4 \text{ MeV}] \\ m_W(m_T) &= 80\,365.6 \pm 22.1 \text{ MeV} \quad [\text{legacy} : 80\,361.5 \pm 27.2 \text{ MeV}] \end{aligned} \quad (5.21)$$

The presented numbers correspond to the total uncertainties. The missing systematic uncertainties for the PLH fit on the QCD and electroweak modelling are taken from the legacy measurement and added in quadrature for a simplified comparison. The combination for p_T^μ tends towards a lower value of m_W compared to the legacy measurement, which is favoured by the electroweak fit presented in Sec. 2.6. The value for the combination in m_T rises in parallel and supports the compatibility of the combination results in p_T^μ and m_T .

The very same framework is further exploited to measure the decay width of the W boson, Γ_W , using the distributions of p_T^μ . The kinematic distributions depend more subtly on Γ_W compared to m_W . Hence, the newly introduced PLH approach presents the mean of choice in order to exploit the shape sensitivity. The blinded result with a preliminary set of profiled systematic uncertainties is:

$$\Gamma_W(p_T^\mu) = 2\,165.5(+\text{blinding}) \pm 29.3 \text{ MeV} \quad (5.22)$$

The presented approach is able to measure Γ_W with the preliminary setup to a precision, which is compatible to the current world average ($\Gamma_W^{\text{global}} = 2.085 \pm 0.042 \text{ GeV}$ [56]). The results point to a possible precision, which is below the currently leading measurements by DØ [127] ($\Gamma_W^{DØ} = 2028 \pm 72 \text{ MeV}$) and CDF [86] ($\Gamma_W^{CDF} = 2032 \pm 72 \text{ MeV}$), even without the final combinations of results from p_T^μ and m_T fits, and the electron channel.

Both results are currently under review within the ATLAS Collaboration. Given the various possible improvements previously discussed, it is expected that two new world leading precision measurements on the properties of the W boson will be published within the coming months.

A few sources of systematic uncertainties are not reduced with the PLH approach. For example, the uncertainties related to the hadronic recoil calibration remain in the same order for the measurement of m_W . But they could be further reduced with an improved modelling of the UE, which blurs the measurement of the hadronic recoil. This approach is tackled for the measurement at $\sqrt{s} = 13 \text{ TeV}$ in the following second part of this thesis.

6.

Measurement of the activity of the Underlying Event

6.1 Motivation and Outline

Disclaimer: Parts of the following were previously published in [3] and form the basis of an internal ATLAS note [128] within the context of this work.

The complex environment of a pp collision can be split into two components in different energetic regimes: the hard-scattering, i.e. the parton-parton interaction with the largest momentum transfer, and all other event activity, which is summarized as the *Underlying Event* (UE). The UE activity is an irreducible background to most hadron collider observables and its appropriate modelling is crucial for precision measurements and the understanding of soft-QCD processes. For example, the measurement of the mass of the W boson relies on the modelling of the UE, because the activity of the UE overlaps with the hadronic recoil u_T , which was introduced in Sec. 5.8. The dependency is illustrated in Fig. 6.1. The corresponding UE activity needs to be subtracted to determine u_T correctly. The accuracy of this correction heavily depends on the quality of the UE modelling.

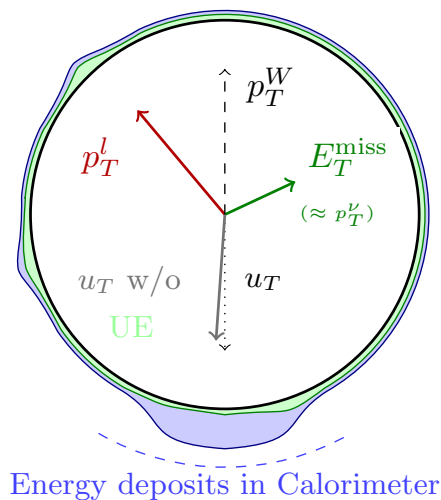


Figure 6.1: The activity of the UE (green) contributes to the overall energy deposit in the calorimeters (blue). Its contribution needs to be subtracted to properly determine the hadronic recoil u_T .

The driving mechanisms for the production of the UE are connected to relatively low momentum scales. These mechanisms include the fragmentation of partons not participating in the hard-scattering process, e.g. beam remnants, radiation processes and additional hard and semi-hard scatters in the same pp collision, termed MPI. Phenomenological models are required to describe these processes using several free parameters determined from experiment. The main features of these models are described in Sec. 4.2.

The activity of the UE depends on the centre-of-mass energy and can overlap with that of the hard-scattering, therefore its measurements are conducted at different energies and with different tags for the hard scattering. The first measurements of observables sensitive to the UE, which is comparable to the one presented in this thesis, were performed by the CDF Collaboration in proton–antiproton ($p\bar{p}$) collisions at a centre-of-mass energy of 1.8 TeV [129]. The predecessors of the analysis presented here are the measurements of distributions sensitive to the properties of the UE in Drell–Yan events in pp collisions at a centre-of-mass energy of 7 TeV by the ATLAS [130] and Compact Muon Solenoid (CMS) [131] Collaborations. There is also another measurement at a centre-of-mass energy of 13 TeV by the CMS Collaboration [132].

The studies presented in this thesis are also partially documented in an ATLAS internal note [128] and are published in Ref. [3], which makes the results of this measurement available to the High Energy Physics community. The measurement provides important input for Monte-Carlo generator authors to adapt the model parameters, in order to improve their compatibility with the measurement. This process is usually referred to as tuning. The major challenge of measuring the UE activity is, that the UE is not distinguishable from the hard scattering on an event-by-event basis. However, there are observables which are sensitive to the UE properties, as first introduced by the CDF Collaboration [129]. Further details on the observables will be given in the following Sec. 6.2.

Section 6.3 introduces the data and Monte-Carlo samples included in the analysis. Several aspects of the setup for the different Monte-Carlo generators will be discussed, because they are crucial for interpreting the comparison between measurement results and generator predictions. Furthermore, Sec. 6.3.1 lists the criteria to select events and tracks to build the UE event observables.

The measured observables are smeared by the detector response. The unfolding process explained in Sec. 6.4 corrects the observables for detector effects, which allows to compare the resulting particle-level distributions to the Monte-Carlo generator predictions. The method chosen for the unfolding is a Bayesian Iterative approach and the details are listed in Sec. 6.4.2. A dedicated validation follows in the next subsections.

This analysis relies on the removal of pile-up contributions via the unfolding. The approach is simulation-based and hence cross-checked with a data-based unfolding alternative, the Hit-backspace-once-more (HBOM) algorithm introduced in Sec. 6.5.2. Pile-up has the same signature as the UE activity and is hard to mitigate. It mostly consists of soft particles without any preferred orientation, which originate predominantly from non-diffractive or soft pp collisions. Hence, an additional method described in Sec. 6.5.1 is used to test the consistency of the simulation based pile-up removal.

The unfolding process and the detector reconstruction introduce several uncertainty components on the final results on particle level. The origin and magnitude of these will be discussed in Sec. 6.6.

Finally, a general overview of the characteristics of the UE at $\sqrt{s} = 13$ TeV is presented in Sec. 6.7.1. It is followed by a detailed discussion of the findings in Sec. 6.7.2, which traces them back to the different subprocesses of the UE. The Monte-Carlo model predictions qualitatively describe the data, but significant discrepancies in some phase-space regions highlight the need for improved generator tunes. Those based on this measurement will have the potential to improve e.g. the future measurements of the mass of the W boson. Furthermore, a comparison to previous measurements is provided. The reference is e.g. the UE measurement at $\sqrt{s} = 7$ TeV by ATLAS [130].

6.2 Measurement strategy for the UE activity

The measurement strategy, which is introduced here to access the properties of the UE, was first suggested by Rick Field in Ref. [129]). The differentiation between UE and hard-scattering process is inspired by the QCD Monte-Carlo generator realization of a highly energetic pp collision. It starts with the perturbative 2-to-2 parton-parton (hard) scattering, i.e. two incoming partons interact and produce two objects balancing each other. The resulting object of this hard-scattering carries the largest momentum of all collision products. Its transverse momentum and mass serves as a scale for the momentum transfer in the hard interaction. It also correlates with the centrality of the collision and the amount of UE activity.

Originally, the jet with the largest p_T was used to represent the leading object, because there was a sufficiently high number of events available in minimum-bias data. The analysis presented here employs the production of a Z boson recoiling against ISR jets in order to tag the hard-scattering. The choice of this process is manifold: Firstly, the Z boson is similar to the W boson for a various properties and therefore serves as a suitable and well detectable reference process. The same argument reasons the calibration measurements in Sec. 5.7. The momentum transfer among the partons is compatible for both productions and subsequently the correlation with the accompanying UE activity. Thus, the UE activity measured in Z events is transferable to W events. The great advantage of Z events with leptonic final states is the precise reconstruction of the direction in the transverse plane of the detector. This feature is further exploited, when focusing only on the decay of the Z boson into a muon-antimuon pair. The muons leave an extremely clean signal and precise kinematic information, when combining ID and MS tracks. The reconstruction details are listed in Sec. 3.2.3. Additionally, the muons are less likely to produce Bremsstrahlung compared to electrons. Hence, there is no FSR expected in the $Z \rightarrow \mu\mu$ events, which could overlap with the UE activity.

In general, processes with leptonic final states like Drell-Yan events are experimentally clean and theoretically well understood. The leptons are easily removed from the event information to carve out the particles from the UE. It should be noted, that the choice of the muon decay channel does not bias the UE measurement itself, because the observables exclude signal leptons explicitly.

Events containing two muons originating from the decay of a singly produced Z boson form a particularly interesting sample for studying the UE. The final-state Z boson is well-identified and colour neutral, so that interaction between the final-state leading particle and the UE is minimal. It permits a study of different kinematic regions with varying transverse momenta of the Z boson due to harder or softer ISR. Further topological considerations are introduced to enhance the sensitivity to the MPI component of the UE.

The Tab. 6.1 presents an overview over all event characteristics and observables.

6.2.1 Becoming sensitive to the UE: UE regions

It is impossible to determine from which process a single particle originated in a pp collision. But one can exploit the event topology to extract a clean signal of the UE activity on average over many collision events. The Z boson, which is created in the hard-scattering process, recoils against jets, also termed as hadronic recoil. The boson and the hadronic recoil balance each other in the transverse plane perpendicular to the beam-beam axis. They are orientated roughly back-to-back, while the activity of the UE does not imply any favoured orientation. Therefore, the hard-scattering activity will dominate in direction of the Z boson, manifesting itself in the two decay muons, and in the opposite direction by the jets. The regions perpendicular to the

direction of the Z boson remain mostly free from the hard-scattering contributions. UE observables are therefore measured in different regions of the transverse plane, which are defined relative to the direction of the Z boson as illustrated in Fig. 6.2.

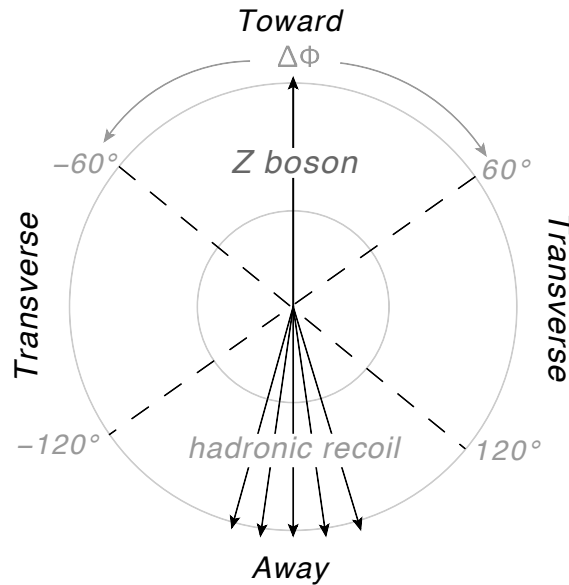


Figure 6.2: Illustration of away, transverse, and toward regions in the transverse plane defined relative to the direction of the Z boson.

A charged particle lies in the *away* region if its azimuthal angle relative to the Z boson direction $|\Delta\phi|$ is greater than 120° . This region is heavily dominated by the hadronic recoil against the Z boson from initial state quark/gluon radiation and is therefore not particularly sensitive to the UE. The *toward* ($|\Delta\phi| \leq 60^\circ$) and *transverse* ($60^\circ < |\Delta\phi| \leq 120^\circ$) regions contain less contamination from the hard process after subtraction of the two muons from the Z boson. The contamination with FSR, which is attributed to the hard-scattering process, is negligible for the muonic final-state. The transverse region is sensitive to the UE because, by construction, it is perpendicular to the direction of the Z boson and hence is expected to have a lower level of activity from the hard-scattering process than the away region. Nevertheless, the higher the transverse momentum of the Z boson, the higher will be the activity of the hadronic recoil and the probability rises, that particles from the hard-scattering process leak into the transverse region.

The two *transverse* regions are differentiated on an event-by-event basis by their scalar sum of the charged-particle transverse momenta (Σp_T). The one with the larger sum is labelled *trans-max* and the other *trans-min* [133, 134]. This distinction enforces, that the trans-max region will contain more contribution from the ISR, while the trans-min region is more sensitive to the beam-beam remnants component of the UE.

6.2.2 Observables sensitive to the activity of the UE

This thesis focus mainly on two aspects of *activity* in the context of particles: How many particles are created and how much energy or momentum respectively do they carry.

The measurement takes into account only charged particles, because these can be precisely measured by the ID. Measuring the electrically neutral component of the UE activity is accompanied by further uncertainties due to e.g. the energy scale of the

calorimeter information. The neutral particles were measured in e.g. [135], but will be disregarded in the measurement presented here.

Four distributions are studied to understand the UE activity. The first is the charged-particle transverse momentum (p_T) distribution inclusive over all selected particles. The final spectrum for this variable is accumulated over all events and then normalized.

The next three are evaluated on an event-by-event basis: The charged-particle multiplicity (N_{ch}) simply counts the number of charged particles. The binning of N_{ch} allows to be sensitive to individual particles. The scalar sum of the transverse momentum of those particles (Σp_T) is highly correlated to N_{ch} , because it sums up the corresponding momenta. This observable is of high interest to the measurement of the mass of the W boson, because of its similarities to measure the momentum of the hadronic recoil of the W . The mean transverse momentum ($\text{mean } p_T$) is a combination of the previous two observables. Mean p_T is the quotient of Σp_T over N_{ch} , provided $N_{\text{ch}} > 0$ in the corresponding region. Additionally, the arithmetic mean of all three observables is investigated as function of transverse momentum of the Z boson (p_T^Z).

The distributions of these variables are produced separately for charged particles lying in each of the regions described in Sec. 6.2.1. The charged-particle multiplicity and the scalar sum of transverse momenta are transformed to densities, when normalized relative to the area of the corresponding region in the η - ϕ space. The bin contents are divided by $\frac{10\pi}{3}$ ($= 2 \cdot 2.5 \cdot \frac{2\pi}{3} = \Delta\eta \cdot \Delta\Phi$) (away, transverse, towards) or $\frac{5\pi}{3}$ (trans-min, trans-max) respectively. The interval in η correspond to the size of the ID and the extension in ϕ to the size of the region defined in the previous section. The usage of densities simplifies the comparison of the activity in different regions. The detailed transformation into a density is illustrated in Sec. C.1 to clarify the intermediate steps.

6.2.3 Enhancing MPI sensitivity: Transverse Thrust

The measurement becomes sensitive to the properties of the UE by the selection in different transversal regions as presented in Sec. 6.2.1. Nevertheless, the UE comprises different processes, such as the hadronization of the beam remnants and additional interactions of colliding partons (MPI). General purpose Monte-Carlo generators aim to adequately model all these subprocesses, and the prediction needs to be validated against the actual measurement. But it is impossible to unambiguously separate the UE from the hard-scatter process on an event-by-event basis and the same is true for the subprocesses of the UE.

However, one can once again exploit the event topology to become sensitive to particular subprocesses. The analysis here follows the recommendations of Ref. [136] and employs a selection on transverse thrust (T_{\perp}) to enhance the sensitivity to MPI.

Transverse thrust describes, whether an event is isotropic in the transverse plane (low value of thrust, see left Fig. 6.3 (a)), or rather pencil-shaped, i.e. back-to-back (high value of thrust, see right Fig. 6.3 (a)). The low thrust events are more likely to contain activity coming from MPI. Figure 6.3 (b) gives an intuitive explanation for this. If there are more parton-parton interactions in addition to the hard-scattering process, these will produce mainly back-to-back jets. But the orientation of the MPI products is independent of the hard-scattering process. They are most probably not parallel to the hard-scattering and therefore add activity to the transverse region. As a result, the final event shape is rather isotropic in the transverse plane.

Event characteristics	UE regions		observables
p_T^Z $\in (0, 10, 20, 40, 60, 80, 120, 200, 500)$ GeV $T_\perp \in (\frac{2}{\pi}, 0.75, 1)$, inclusive	toward	$ \Delta\phi \leq 60^\circ$	p_T
	transverse	$60^\circ < \Delta\phi \leq 120^\circ$	$\Sigma p_T(\langle \Sigma p_T \rangle)$
	(trans-min, -max)		$N_{\text{ch}}(\langle N_{\text{ch}} \rangle)$
	away	$ \Delta\phi > 120^\circ$	mean $p_T(\langle \text{mean } p_T \rangle)$

Table 6.1: Summary on observable reconstruction. The event characteristics target the sensitivity to the general UE components. The regions distinguish UE activity and hard-scattering. The observables are measured in all combinations of these categories.

The transverse thrust of a given event is defined as proposed in [137]:

$$T_\perp = \max_{\hat{n}} \frac{\sum_i |\vec{p}_{T,i}| \cdot \hat{n}}{\sum_i |\vec{p}_{T,i}|} \quad (6.1)$$

Where the sum is performed over the transverse momenta p_T of all charged particles in the event. The thrust axis \hat{n}_T is the unit vector \hat{n} that maximizes the ratio in Eq. 6.1. It is determined numerically following the algorithm in [49]. The transverse thrust ranges from $T = 1$ for a perfectly balanced, pencil-like, Dijet topology to $T = \frac{2}{\pi} \approx 0.63$ for a circularly symmetric distribution of particles in the transverse plane.

Reference [136] suggests the value of $T_\perp = 0.75$ to distinguish between events of low and high thrust. The measurement presented here examines all observables in all regions inclusively in thrust and additionally for $T_\perp \leq 0.75$ and $T_\perp > 0.75$. The latter two categories are optimized to distinguish extra jet activity from the actual UE activity. A compatible measurement of transverse thrust in combination with the UE activity was performed at $\sqrt{s} = 7$ TeV [138], but it does not distinguish the transverse regions.

The analysis distinguishes only these two rather large bins in transverse thrust to guarantee statistical stability despite the additional cut. Furthermore, the coarse binning avoids a bias from bin-migration, which then simplifies the unfolding procedure. The unfolding routine corrects for first order effects of bin migration in thrust, for details see Sec. 6.4.2.

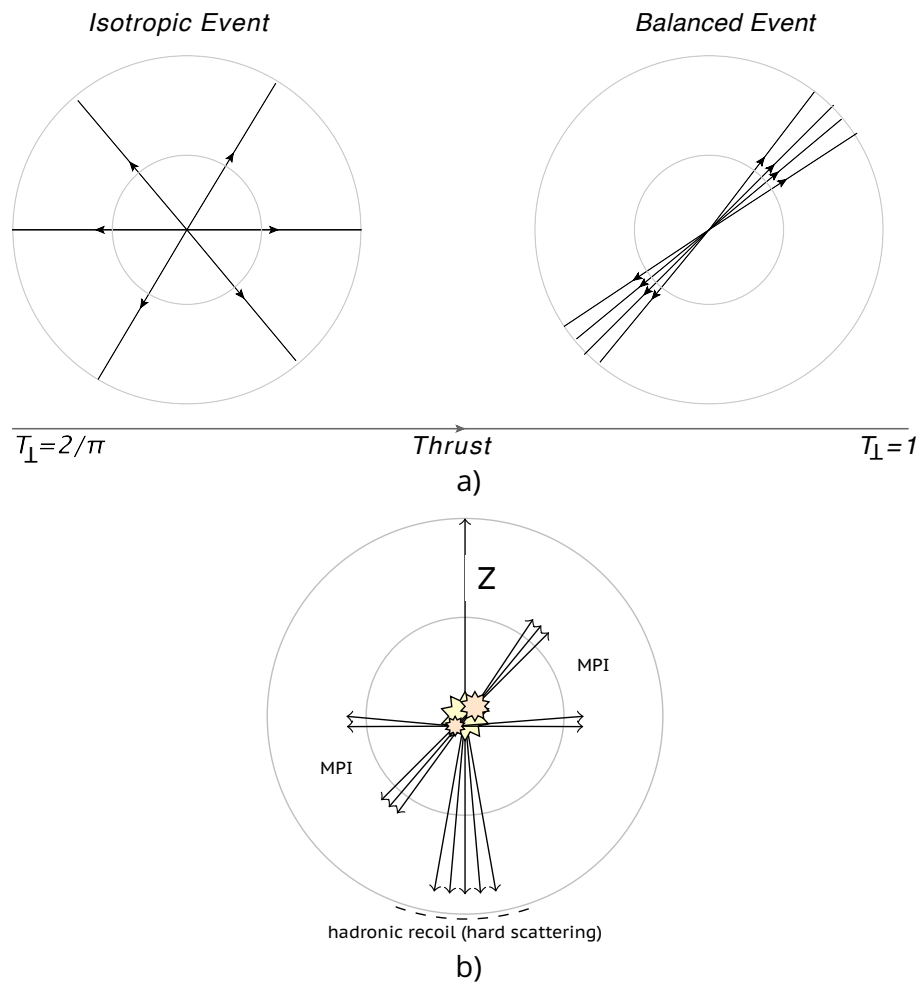


Figure 6.3: (a) Illustration of an isotropic and a balanced event topology in the transverse plane with their corresponding values of thrust T_{\perp} . In these figures, the beams are travelling perpendicular to the plane of the page. (b) The picture exemplifies, that MPI activity is likely to produce an event topology of low thrust.

6.3 Data and Monte-Carlo simulation samples

The Z boson itself cannot be measured with the ATLAS detector, because of its almost immediate decay after creation. The decay-signature of $Z \rightarrow \mu\mu$ events is not unique, hence selection criteria are introduced to obtain samples containing a high amount of possible Z decays while rejecting as many background events as possible.

The following section describes the selection criteria, which are used to study observables sensitive to the UE in Z boson events. The choices follow mainly the previous UE analysis at $\sqrt{s} = 7$ TeV [130] to preserve compatibility. Of course, a few properties are updated to adapt the needs to the collision environment at $\sqrt{s} = 13$ TeV and to exploit improvements of the detector such as the IBL. The selection of the $Z \rightarrow \mu\mu$ event candidates is well established in the ATLAS community (compare e.g. [139]). The details are listed in Sec. 6.3.1.

The data results are compared to the generator predictions. The data taking conditions are explained in Sec. 6.3.2 and the details on the setup of the generators is presented in Sec. 6.3.3. It is possible that other interaction processes produce a similar final state as the $Z \rightarrow \mu\mu$ process. These will enter the finally selected data events. Their contribution is discussed in Sec. 6.3.4.

6.3.1 Event and object selection

The event and object selection serves two purposes, which apply to all cut-based analysis: The selected events should represent the signal process of interest as purely as possible. And in parallel, it is crucial to include a sufficiently large number of events to ensure a statistically robust sample. Both is achievable with the $Z \rightarrow \mu\mu$ process, as its production cross section at the LHC is sufficiently large and the final state of two muons provides a distinct signature.

This chapter describes the selection of $Z \rightarrow \mu\mu$ event candidates from the 2015 dataset and the corresponding Monte-Carlo simulation samples. The selection is based on reconstructed objects in both cases. The recommended procedure for most ATLAS analysis follows these selection steps:

1. requirements on the data quality
2. Trigger conditions
3. requirements on the single reconstructed objects (here the muons)
4. combined conditions for Z boson candidates

The tracks recorded in these events are used to build the final observables on reconstruction level.

The status of the data quality is recorded live during the data taking, and later additionally reviewed in the offline reprocessing. The Good-Runs-List (GRL) reports all Lumi-blocks, which are recorded during nominal detector conditions. This GRL could be updated, if e.g. minor defects can be cleared in post-processing. The requirement on an adequate data quality safeguards against corrupted measurements due to e.g. malfunctions of the magnets affecting the magnetic field or the MS not operating at the nominal voltage.

If the investigated Lumi-block is listed in the GRL, each event is required to have fired at least one out of two single-muon triggers. It is either a low-threshold trigger requiring $p_{\text{T}}^{\mu} > 20$ GeV and the muon to be isolated from additional nearby tracks, or a high-threshold trigger, which requires one muon to have $p_{\text{T}}^{\mu} > 40$ GeV without any conditions on the isolation.

In detail, the low-threshold trigger requirement comprises a passing of L1 muon trigger system with $p_{\text{T}}^{\mu} > 15$ GeV and a HLT logic. The latter one is seeded by the L1 trigger and demands a threshold of 20 GeV and the muon candidate to be isolated from ID tracks, which are reconstructed online by the HLT. The additional high-threshold muon trigger recovers any possible efficiency losses at high momenta ¹.

All events need to contain at least one reconstructed collision vertex subsequent to the trigger condition. A vertex requires at least two associated tracks with $p_{\text{T}} > 400$ MeV due to the vertex-reconstruction algorithm. The reconstructed vertex with the highest Σp_{T} of the associated tracks in the event is defined to be the primary vertex and represents the pp collision under investigation. All other interaction vertices are referred to as pile-up and their contribution needs to be suppressed.

If an event fulfils the criteria from above the individual reconstructed objects are filtered for Z boson candidates. The Z boson candidates are reconstructed from muon pairs, which itself serve certain requirements listed in the following section.

Muon selection

The final state of $Z \rightarrow \mu\mu$ consists of two oppositely charged muons. These muon objects need to pass the following criteria:

- A combined muon is required, i.e. the track reconstructed in the MS needs to match an ID track [69].
- The reconstructed muons are required to fulfil $p_{\text{T}}^{\mu} > 25$ GeV to operate at the efficiency plateau of the trigger system.
- The muon track is restricted to be within the MS or more precisely the geometric range of the muon trigger, i.e. $|\eta| < 2.4$.
- The muon candidate is required to be isolated using a p_{T} - and η -dependent 'gradient' isolation criterion [69] based on track and calorimeter information.
- Muon candidates are rejected if the significance of the transverse impact parameter ($|d_0/\sigma(d_0)|$, with d_0 representing the transverse impact parameter and $\sigma(d_0)$ the related uncertainty) is above three.
- The muon candidates must be associated to the primary vertex. This requires that the longitudinal ($|z_0 \sin \theta|$) impact parameter is less than 0.5 mm. The variables d_0 and z_0 are measured relative to the primary vertex.

The isolation and impact parameter requirement suppress muon signals from light mesons and b or c quark semi-leptonic decays. Other requirements are due to the detector geometry and performance, e.g. combined muons provide a better momentum resolution than muons solely reconstructed in the MS.

Z boson selection

Events are considered to contain a Z candidate if the following holds true for the muon signals:

- The event contains exactly two opposite-charged muons satisfying the selection criteria above.
- The invariant mass of the dimuon system is consistent with $66\text{GeV} < m_{\mu\mu} < 116\text{GeV}$.

¹The ATLAS internal technical term for the trigger condition is HLT_MU20_LOOSE_L1MU15 or MU50.

The invariant mass $m_{\mu\mu}$ of the Z boson candidate is calculated by adding the reconstructed four vectors of the two muons. The muon-pair invariant mass region is chosen, because the lepton-pair backgrounds coming from events with multi-jets or events with a W boson and jets are negligible within this window. Nevertheless, the remaining background contribution is discussed in Sec. 6.3.4. If an event fulfils all selection criteria, it is designated to be a Z boson candidate event and the UE observables are investigated.

Track selection criteria for the UE observables

Tracks reconstructed in the ID from the passage of charged particles are used to form the UE observables. The acceptance of tracks in η is limited by the size of the ID. Further quality requirements on the reconstructed tracks are kept compatible to the UE at lower centre-of-mass energy and are recommended by the ATLAS community. Each track needs to fulfil the following criteria to enter the UE observables:

- $p_t > 0.5$ GeV and $|\eta| < 2.5$
- 1 hit in innermost pixel layer
- at least 1 pixel hit
- at least 6 SCT hits
- for tracks with $p_t > 10$ GeV a goodness of fit probability greater than 0.1 ($\frac{\chi^2}{n_{Dof}} > 0.1$)
- transverse and longitudinal impact parameters with respect to the primary vertex: $|d_0| < 1.5$ mm & $|z_0 \cdot \sin(\theta)| < 1.5$ mm

Charged particles far below the p_T threshold might not leave the ID due to the strong curvature. The ID of ATLAS is able to reliably reconstruct tracks of charged particles down to a momentum of 400 MeV, but the higher cut marks a plateau of track reconstruction efficiency and complies with the UE analysis at $\sqrt{s} = 7$ TeV. The innermost layer hit rejects secondary particles originating from interactions with the detector material. The other conditions on the hit numbers are mainly required by the track reconstruction algorithms [64]. The additional requirement on the quality of the fit of the track to the hits in the detector suppresses falsely measured tracks at high p_T . The mismeasurement can occur due to mis-alignment or nuclear interactions. But this criterion affects mainly the tracks associated with the muon candidates and has little impact on the predominantly low- p_T tracks of the UE activity. The d_0 and z_0 cuts extinguish tracks which are associated to charged particles coming from other pp interactions within the same bunch-crossing.

The muon tracks associated with the Z boson are excluded during the construction of the observables by removing all tracks measured in the vicinity of the muons ($\Delta R_{\mu-track} < 0.01$). Due to the isolation requirement on the muons, this erases exactly two tracks per event. The potential bias due to the isolation requirement of the signal muons has been tested by comparing the results using the 'gradient' isolation requirement to a selection without any isolation requirement on the signal muons. The difference was found to be negligible compared to other systematic uncertainties and will be therefore neglected in the following.

Exemplary distributions based on the selected objects are presented in Sec. 6.3.5. Nevertheless, the final results of this analysis are presented on particle level. The unfolding procedure (see Sec. 6.4) which transforms the results on construction level to particle level distributions, requires the input of the selected objects on particle level as predicted by the Monte-Carlo generators. The following section lists the according selections on particle level.

Particle level object selection

The kinematics of the Z boson and of the charged particles in the event define the phase space of the fiducial region (particle level). This closely reflects the selection made on measured detector quantities outlined before. Simulated events are required to have two opposite-charge prompt muons that satisfy $p_T > 25$ GeV and $|\eta| < 2.4$ with each muon defined at the ‘bare’ level (after final-state QED radiation). Hereby, it is automatically ensured that the muons originate from the decay of the Z boson in the signal sample. The mass window for $m_{Z/\mu\mu}$ is kept identical to the reconstruction level selection.

Charged particles must be stable, i.e. have a proper lifetime with $c\tau > 10$ mm, with $p_T > 0.5$ GeV and $|\eta| < 2.5$. Stable charged particles are excluded on detector level, if they associated to the muons from the Z . Stable charged particles are also vetoed if they originate from the decay of charged-strange particles. The latter ones are dropped due to their poor reconstruction efficiency, as they typically decay within the tracker.

6.3.2 The 2015 pp collision data

The analysis of observables sensitive to the activity of the UE investigates the data collected by ATLAS from August to November 2015. During this period the LHC circulated the proton beams with an energy of 6.5 TeV each, resulting in a centre-of-mass energy of $\sqrt{s} = 13$ TeV. The bunches were brought to collision every 25 ns. In this way the LHC delivered a total amount of 4.2 fb^{-1} of which 3.2 fb^{-1} were record by ATLAS and met the quality conditions to enter the physics analysis. This requires for example that all subdetectors were running on their nominal conditions. The dataset here exploits the full 3.2 fb^{-1} of collision data.

The peak delivered instantaneous luminosity was $\mathcal{L} = 5 \cdot 10^{33} \text{ cm}^{-2}\text{s}^{-1}$ during 2015 and the mean number of pp interactions per bunch crossing (hard scattering and pile-up events) was $\langle\mu\rangle = 13$. The 2015 dataset is the one with the lowest contribution of pile-up available at the time of conduction of this analysis. Particles coming from pile-up vertices can mimic the signature of the UE activity. The datasets from the year 2016 with $\langle\mu\rangle = 24.9$ are neglected, in order to keep this background as low as possible (see for reference Fig. 6.4 (b))

The 2015 dataset yields about $2 \cdot 10^6$ Z candidates, which is sufficient to avoid major limitations from statistical uncertainties in this analysis. A detailed overview how many data events fulfil the individual cut levels is listed in Tab. 6.3.

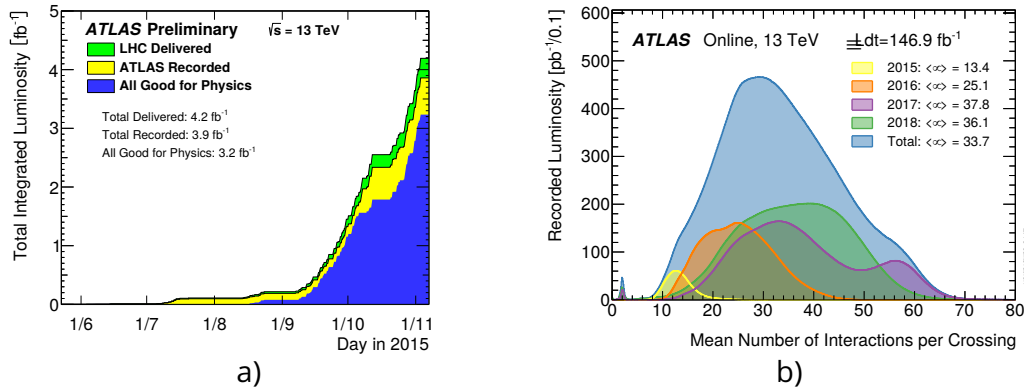


Figure 6.4: (a) Total Integrated Luminosity and Data Quality in 2015 Cumulative luminosity versus time delivered to ATLAS (green), recorded by ATLAS (yellow), and certified to be good quality data (blue) during stable beams for pp collisions at $\sqrt{s} = 13$ TeV centre-of-mass energy in 2015. (b) The luminosity-weighted distribution of the mean number of interactions per crossing ($\langle \mu \rangle$).

6.3.3 Setup of the Monte-Carlo generators

This analysis compares its results to the Monte-Carlo generator predictions. The feedback will allow to tune the generators to improve their description of the UE activity. It is crucial to know about the individual compositions to identify possible tuning approaches. The Chapter 4 lists further details about the general functionality of Monte-Carlo generators.

Three different setups of Monte-Carlo generators enter the analysis for the signal process and serve as a reference for the final results. All three are established in the field of particle physics and represent the state-of-the-art for simulation of SM processes. An overview is presented in Tab. 6.2.

The first one applied to simulate the $Z \rightarrow \mu\mu$ signal process is the next-to-leading-order POWHEG [54, 91] event generator with the CT10 set of PDFs [92]. It is interfaced to the PYTHIA 8.170 event generator [49, 50] to simulate the parton shower, hadronization and UE with the CTEQ6L1 PDF set and the AZNLO set of tuned parameters. The latter option is of great interest to this analysis, because it tunes the event generator to the p_T^Z measurement at $\sqrt{s} = 7$ TeV [93]. Hence, it retunes the overall UE activity by adjusting the PYTHIA MPI cut-off parameter to the UE activity of the previous measurement [130] in the lowest p_T^Z bin (0 to 5 GeV). In other words, this Monte-Carlo generator setup is adjusted to correctly describe the UE activity at $\sqrt{s} = 7$ TeV in the lower regime of p_T^Z . The final-state electromagnetic radiation is simulated with PHOTOS [94]. The simulation of the parton-showers with the PYTHIA generator exploits a dipole showering approach and it implements a hadronization model based on the fragmentation of colour strings. The MPI model interleaves the ISR and FSR emissions with MPI scatters. This full combination is later referred to as just POWHEG+PYTHIA8, *nominal* or *baseline* Monte-Carlo generator set, as it serves for the data unfolding (see Sec. 6.4).

An alternative signal sample is used for cross-checks and systematic uncertainty evaluations. It was simulated using SHERPA 2.2.0 [51], which has an independent implementation of the parton shower, hadronization, UE and FSR. This makes it a suitable counterpart to the usage of POWHEG+PYTHIA8. The SHERPA samples are produced with the NNPDF3NNLO PDF set [140]. The nominal tune set of SHERPA version 2.2.0 was kept for this analysis. The SHERPA generator uses leading-order matrix elements

Generator	Type	Version	PDF	Tune
POWHEG	NLO	v1_r2856	CTEQ6L1	AZNLO
+PYTHIA8	+ Parton Shower	8.186		
+PHOTOS		1.2.0		
SHERPA	LO multi-leg matrix-element + Parton Shower	2.2.0	NNPDF3.0 (NNLO)	
HERWIG++	Parton Shower	2.7.1	CTEQ6L1	UE-EE-5

Table 6.2: Overview of the Monte-Carlo generator setup used for the simulation of the signal process $Z \rightarrow \mu\mu$.

with a model for MPI similar to that of PYTHIA. But as a major difference it does not interleave the MPI scatters with the FSR. Moreover, the hadronization model is different to PYTHIA. SHERPA implements a cluster hadronization model. SHERPA and PYTHIA both impose the infrared cut-off for MPI as a smooth function.

The SHERPA sample and the previously described POWHEG+PYTHIA8 sample are both overlaid with Monte-Carlo-generated minimum-bias events [95] to simulate the effect of multiple interactions in the same bunch crossing (pile-up). These minimum-bias samples were produced with PYTHIA 8 using the A2 tune set [96] in combination with the MSTW2008LO PDF set. The A2 tune set was matched to the ATLAS minimum-bias measurement at $\sqrt{s} = 7$ TeV [97]. The simulated samples are reweighted to reproduce the distribution of the number of interactions per bunch crossing observed in the data (see Sec. 4.4.3).

This analysis incorporates the *baseline* (POWHEG+PYTHIA8) sample with and without the overlaid pile-up events. The two variations are used to verify the pile-up simulation based on a data-driven approach (see for details Sec. 6.5.2).

The third generator used to produce the signal process is HERWIG++ [52]. The simulation included the UE-EE-5 tune [141] provided by the generator authors and the corresponding CTEQ6L1 PDF set. This tuning uses energy extrapolation and was developed to describe the UE and the double parton interaction effective cross-section, which makes it highly relevant for the scope of this thesis. HERWIG++ uses, similarly to PYTHIA, a leading-logarithm parton shower model matched to leading-order matrix element calculations, but it implements a cluster hadronization scheme with parton showering ordered by emission angle. In contrast to SHERPA and PYTHIA it realises the infrared cut-off as a step function. The hadronization model of HERWIG++ is similar to the one implemented in SHERPA.

The $Z \rightarrow \mu\mu$ sample produced with HERWIG++ was not available with the simulation of the detector response. Therefore, it is only compared on particle level to the unfolded data and could not be exploited to e.g. cross-check the unfolding procedure.

The estimation of three major background sources is based on Monte-Carlo samples. These are the production of $Z \rightarrow \tau\tau$ and $WW \rightarrow \mu\nu\mu\nu$ events as well as the $t\bar{t}$ process. All three are simulated with POWHEG interfaced to PYTHIA8 or PYTHIA6 for $t\bar{t}$ respectively. PYTHIA was tuned with the AZNLO set for the two electroweak processes, which is similar to the signal process. The simulation of the $t\bar{t}$ process applied the PERUGIA 2012 [142] tune set.

The different Monte-Carlo generators predict the events on particle level. These predictions are passed to the GEANT4 [63] program to simulate the passage of particles through the ATLAS detector. For all Monte-Carlo samples except the HERWIG++ production this simulation is provided. In Sec. 6.3.5 several control distributions are listed in order to validate the performance of the Monte-Carlo generator to describe the $Z \rightarrow \mu\mu$ process including the detector simulation.

6.3.4 Background processes

This analysis includes two different methods to estimate the background contributions to the signal process. If the background process is well described by the SM and captured in the Monte-Carlo generators, its contribution is estimated via simulation. The description of the generator setup is mentioned in Sec. 6.3.3 and the event yields are summarized in Tab. 6.3.

The simulation-based estimation of the electroweak (Diboson), $Z \rightarrow \tau\tau$, and top background yields less than 1% contribution to the Z boson events when scaled with respect to their cross section (10.631 pb, 1901.2 pb, and 696.110 pb respectively) and data luminosity. The main background processes are $WW \rightarrow \mu\nu\mu\nu$ and $Z \rightarrow \tau\tau, t\bar{t}$.

Nevertheless, the multijet background cannot be tackled by the theory description as the production channels are too various at a Hadron collider. For example, jets can originate from the proton-remnants or the sea-quarks and form muons within the hadronization process. Hence, the multijet background estimation is data-driven using a *same-sign* approach. All selection cuts are applied to data, but instead of requiring an opposite-charge muon pair, a pair of same-sign muons is requested. Assuming that the number of muons produced within hadronic jets is independent of their charge, this yields roughly the number of MJ background events. In this way the contribution of the multijet background is found to be 66 events, which corresponds to less than 0.1% with respect to the full data sample. The total numbers are summarized in Tab. 6.3. Additionally, Figure 6.5 presents a selection of observables on detector-level with highlighted background contamination.

The handling of the background contributions is straight forward for the final observables. In the following, the background estimates are subtracted on detector-level from the observables constructed from data. This yields an estimation for a data based observable, which contains solely the signal process.

The simple subtraction of background events brings along one major source of uncertainty for the final results: the mismodelling of the count of background events. It therefore needs to be evaluated and propagated for the individual background channels (for details on the propagation see section 6.6.2). The error on the number of background events is depicted as the uncertainty on the corresponding cross-section for the simulation based background channels. Thus, the electroweak background normalization is varied by $\pm 5\%$ and the $t\bar{t}$ background normalization by $\pm 15\%$, which corresponds approximately to their theoretical uncertainties stated e.g. in [143, 144]. The full effect of including the multijet background or not is taken as an uncertainty. This conservative estimate covers a possible misestimation with the *same-sign* method due to implicit isolation requirements. This way the multijet uncertainty is of the same magnitude as the corresponding background contribution evaluated in the related analysis of the p_T^Z spectrum at $\sqrt{s} = 13$ TeV [145].

	Data ($\int \mathcal{L} dt = 3.2 \text{ fb}^{-1}$)	$Z \rightarrow \mu\mu$ (Powheg) ($\sigma = 1901.2 \text{ pb}$)	WW ($\sigma = 10.631 \text{ pb}$)	$Z \rightarrow \tau\tau$ ($\sigma = 1901.2 \text{ pb}$)	top ($\sigma = 696.110 \text{ pb}$)	multijet
All events	62204212.0	6054889.00	93884.00	1812620.00	6083404.00	
Good events	55048920.0					
Trigger events	19377432.0					
exactly 2 muons	2159260.00	2065470.62	982.03	15679.16	3446.10	
$66 \text{ GeV} < m_{\mu\mu} < 116 \text{ GeV}$	2046608.00	2035417.88	383.05	5546.61	1615.64	same sign
opposite charge	2046461.00	2035414.38 ($\pm 2\%$)	383.05 ($\pm 5\%$)	4966.58 ($\pm 5\%$)	1615.64 ($\pm 15\%$)	66 ($\pm 100\%$)

Table 6.3: The table lists the total number of events passing the different cut-levels listed in Sec. 6.3.1. The simulation based samples are simulated equivalent to the trigger stage and scaled with respect to their cross-section and the data luminosity (3.2 fb^{-1}). The last line states the relative uncertainty on the background estimation and cross-section respectively. 'All events' refers to the number of events provided as datasets, hence the data already passed low quality criteria to be recorded.

6.3.5 Control distributions

The measurements are all reported in bins of p_T^Z , the results presented in this paper are not sensitive to the predicted shape of the p_T^Z spectrum, even though they are sensitive to jet activity in the event. The following selection of plots is representative for the different background contributions to the observables. The plots are shown on detector level. The bins in the following Fig. 6.5 represent the absolute number of events measured within this observable range. This is in contrast to the final results in Sec. 6.7.2, which are normalized for the shape comparison. The electroweak background combines the Diboson and $Z \rightarrow \tau\tau$ samples. The multijet background corresponds to a same-signed muon selection applied to the data set.

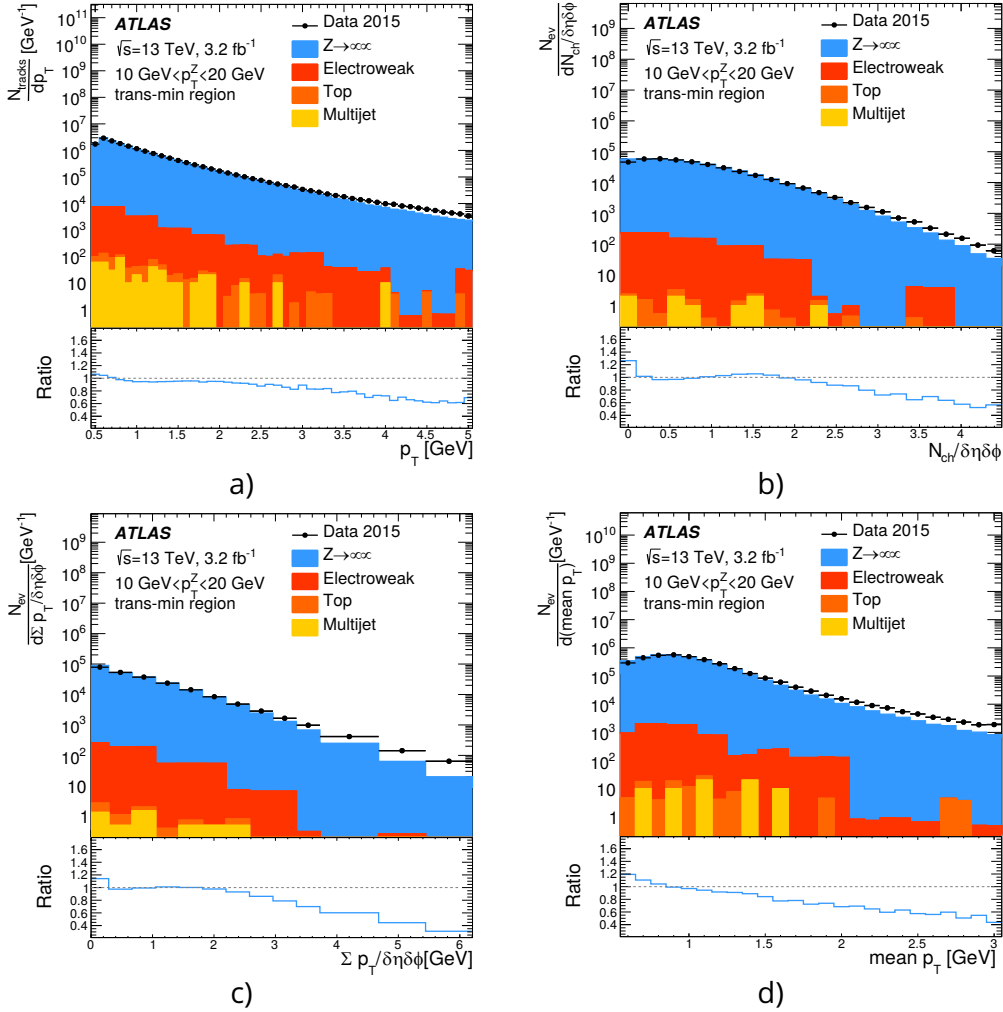


Figure 6.5: Detector level distributions of (a) the spectra of p_T , (b) the charged-particle multiplicity N_{ch} , (c) the scalar sum of the transverse momentum of those particles Σp_T , and (d) the mean transverse momentum $\text{mean } p_T$ in the trans-min region, inclusively in T_\perp for events with $10 < p_T^Z < 20$ GeV. The data are presented before the unfolding step and the background and signal samples are presented as a stack. The multijet background is statistically limited.

6.4 Correction to particle level: Unfolding

The SM theory calculations, which are realized in the Monte-Carlo generator predictions, provide particle descriptions on the so-called particle-level. In the first place, these are completely independent of any detector or measurement strategy. Hence, the experimental results need to be cleaned from detector effects and, as far as possible, from any bias incorporated in the model assumptions, in order to provide a valuable comparison. This purification process is termed as ‘unfolding’² in the following and in the literature [146].

The analysis presented here applies the method of Bayesian Iterative Unfolding to correct the data for detector inefficiencies and resolution [147, 148]. It will be explained in the following sections alongside the prerequisites (Sec. 6.4.1) and different validation approaches (Sec. 6.4.5 and Sec. 6.5). The Bayesian iterative unfolding follows well established examples from previous ATLAS analysis such as reference [111].

6.4.1 Unfolding preparations: Monte-Carlo corrections

The unfolding process relies on the correct simulation of detector effects. The effects coming from e.g. a limited detector resolution should be inverted on the measured data. It is crucial for the unfolding process, that they are modelled sufficiently well in the first place. But not all quantities are described to the percent level, which is needed for precision measurements. Thus, corrections are applied to the Monte-Carlo simulations in order to match the simulation to data. The corrections, which are relevant to this analysis, are described in Sec. 4.4. All corrections are listed here again for completeness:

- muon momentum scale and resolution
- muon isolation and trigger efficiency
- track reconstruction efficiency
- track fake rate
- track impact parameter resolution
- pile-up reweighting
- correction of the beamspot size

It has to be noted, that all corrections are applied to improve the detector simulation and not to rearrange the Monte-Carlo generator predictions.

6.4.2 Bayesian iterative unfolding

The unfolding process transforms the data distribution, which is naturally obtained on detector-level (R^{data}), to the particle-level equivalent (T^{data}) to allow the comparison with general Monte-Carlo generator predictions (T^{MC}). Distributions representing the particle-level will be denoted with $T^{data|MC}$ and particle-level distributions with $R^{data|MC}$ in the following, because the terms *truth-level* (T) and *reconstruction level* (R) respectively are used as synonyms in the High Energy Physics community. The particle level spectrum is defined in Section 6.3.1 and summarized below in Tab. 6.4 for reasons of clarity. The Bayesian Iterative unfolding is visualized exemplarily for the charged particle multiplicity (N_{ch}) in the fiducial volume of $10 < p_T^Z < 20$ GeV inclusive

²The process of predicting the expected reconstructed spectrum from a spectrum of particle-level values is called *folding*, because each particle level value is convoluted, or folded, with the detector resolution.

in T_{\perp} (see Fig. 6.6). The unfolding is applied to all differential observables ($dN_{\text{ch}}/dp_{\text{T}}^{\text{ch}}$, $dN_{\text{ev}}/d(N_{\text{ch}}/\delta\eta\delta\phi)$, $dN_{\text{ev}}/d(\Sigma p_{\text{T}}/\delta\eta\delta\phi)$, $dN_{\text{ev}}/d(\text{mean } p_{\text{T}})$) individually in the different bins of p_{T}^Z and T_{\perp} . The evaluation of the mean value of each observable in a bin of p_{T}^Z and thrust occurs after unfolding.

The Bayesian iterative unfolding allows to take into account the migration between different bins and provides the bin-by-bin correlation information of the results. In terms of the example chosen here, the unfolding assigns, how likely it is, that events with $N_{\text{ch}}^{\text{det}} = 0, 1, 2, 3, \dots$ measured tracks contribute to e.g. the bin representing $N_{\text{ch}} = 5$ charged particles on particle-level.

Generally speaking, Bayes iterative unfolding gives access to the probability, that an event was generated in bin i of the particle-level distribution T , under the condition that it is found in bin j of the reconstructed distribution R . Expressed in a formula: $\mathcal{P}(T_i | R_j)$. This probability is retrieved from Monte-Carlo simulation and calculated via Bayes theorem [149]:

$$\begin{aligned} \mathcal{P}(T_i^{MC} | R_j^{MC}) &= \frac{\mathcal{P}(R_j^{MC} | T_i^{MC}) \mathcal{P}_0(T_i^{MC})}{\mathcal{P}(R_j^{MC})} \\ &= \frac{\mathcal{P}(R_j^{MC} | T_i^{MC}) \mathcal{P}_0(T_i^{MC})}{\sum_i \mathcal{P}(R_j^{MC} | T_i^{MC}) \mathcal{P}_0(T_i^{MC})} \end{aligned} \quad (6.2)$$

Here, $\mathcal{P}(R_j^{MC} | T_i^{MC})$ gives the conditional probability of the event generated in bin i to be reconstructed in bin j and $\mathcal{P}_0(T_i^{MC})$ is the probability of the event to be generated in bin i . The second line of Eq. 6.2 applies the law of total probability to the denominator of the previous equation.

$\mathcal{P}(T_i^{MC} | R_j^{MC})$ is represented by the response matrix, which itself is obtained from the *transfer-matrix*. Its creation is discussed in detail in Sec. 6.4.4. A crucial input is $\mathcal{P}_0(T_i^{MC})$, because it implies a precisely determined initial spectrum, a priori a flat one. This is a very strong prior statement, that would bias the result, if no additional information was used. It motivates the choice of an iterative approach, which is also discussed with the transfer-matrix.

Nevertheless, the best estimate of the data distribution on particle-level, i.e. the number of events in data in each bin i of the data distribution (T_i^{data}), is given by:

$$T_i^{\text{data}} = \frac{1}{\epsilon_i^{\text{part}}} \sum_j (R_j^{\text{data}} \epsilon_j^{\text{det}}) \cdot \mathcal{P}(T_i^{MC} | R_j^{MC}) \quad (6.3)$$

Where R_j^{data} is a number of events measured in bin j , ϵ_i^{part} and ϵ_j^{det} are the event efficiency correction and the non-fiducial signal correction in a given bin i or j . The latter two corrections are calculated in Monte-Carlo simulation as described in Sec. 6.4.3.

The unfolding procedure proceeds in the following steps, when Eq. 6.3 is broken down for the computation:

1. apply non-fiducial signal correction ($\epsilon_j^{\text{det}} \cdot R_j^{\text{data}}$)
2. multiply the response matrix ($\sum_j [\dots] \cdot \mathcal{P}(T_i^{MC} | R_j^{MC})$)
3. apply event efficiency correction ($\frac{1}{\epsilon_i^{\text{part}}} \cdot [\dots]$)

Fiducial volume (for muon selection)	$p_T^\mu > 25 \text{ GeV}$, $ \eta < 2.4$, $66 \text{ GeV} < m^{\mu\mu/Z} < 116 \text{ GeV}$, $p_T^{\mu\mu/Z} = (0, 10, 20, 40, 60, 80, 120, 200, 500) \text{ GeV}$ $(T_\perp \text{ inclusive}, T_\perp < 0.75, 0.75 \leq T_\perp)$
Particle-level definition	$p_T > 0.5 \text{ GeV}$, $ \eta < 2.5$, charge $\neq 0$, stable (i.e. a proper lifetime of $c\tau > 10 \text{ mm}$)

Table 6.4: A summary of the fiducial volume definition of the measurement, the particle-level definition, and the main observables. The first row lists selection criteria for the signal muons (indicated with an μ as superscript) limited by the detector geometry, while the cut on the dimuon invariant mass $m^{\mu\mu}$ yields a low background contamination.

Here, the unfolding step 2 considers bin migration only for the UE observables. This is realized with the creation of the transfer matrix, which relates the track-based measurements to particle-level quantities. The bin migration can be applied only to matched events, i.e. events which are found to be in the same fiducial volume on detector- and particle-level. The fiducial volume is defined here by the bins of p_T^Z and transverse thrust. Unmatched events are a priori not accounted for in the transfer matrix and have to be treated separately.

The simplest approach is a bin-by-bin correction to account for unmatched events and is implemented in step 1 and 3. Basically, it is summarized by multiplying the (background-subtracted) data with the fraction of matched events at detector-level (before the migration correction) and dividing by the fraction of matched events at particle level (after the migration correction). The migration in p_T^Z (and in T_\perp , if applicable) is also corrected for in first order with this non-fiducial signal correction and the event efficiency correction.

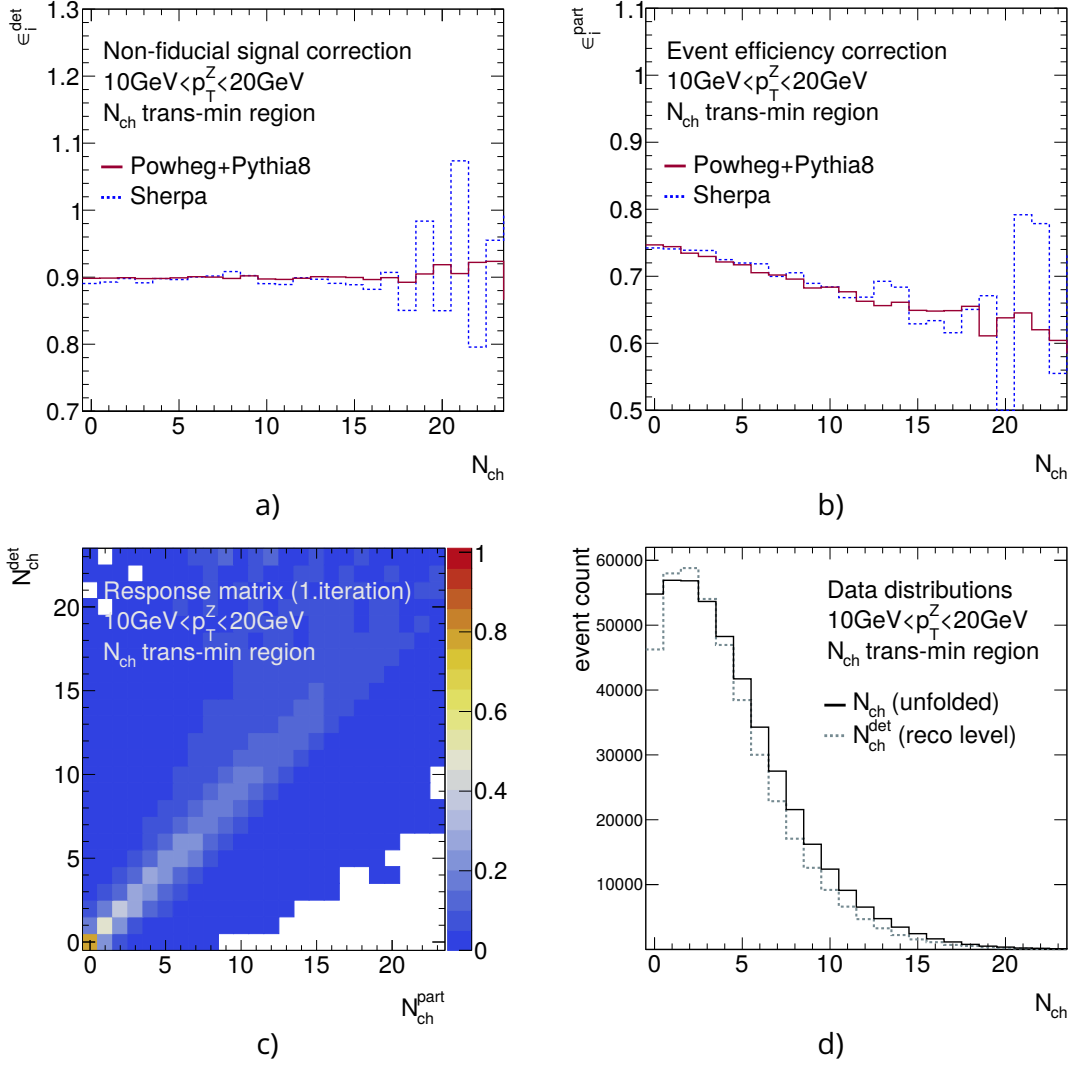


Figure 6.6: The non-fiducial signal correction (a) and event efficiency correction (b) according to Eq. 6.4. The values are evaluated on the two main Monte-Carlo generators. The response matrix (c) completes the inputs for Eq. 6.3. And (d) presents the result of unfolding real data.

6.4.3 Non-fiducial signal correction and event efficiency correction

The bin-migration accounts for detector effects, only if the event is recorded in the fiducial volume for detector- and particle-level. The non-fiducial signal correction and event efficiency correction correct for the unmatched events. The first one is a scale factor (ϵ_i^{det}) for events, that are identified as a Z boson candidate on detector level, but do not have a counterpart in the fiducial volume on particle-level. This happens e.g. if a fake-muon, which originated from a jet, is reconstructed or if the transverse momentum of one muon (p_T^μ) is smeared by the measurement so that p_T^Z is recorded in different bins on detector- and particle-level.

The event efficiency correction provides scale factors (ϵ_i^{part}) for the opposite case, if an event is in the fiducial volume on particle- but not on detector-level. This scenario applies to events, when for example the trigger missed to fire or when the muon leaked outside the fiducial volume due to multiple scattering.

The correction factors are constructed for each bin i of the different UE observables for each bin of the fiducial volume (i.e. p_{\perp}^Z and T_{\perp} intervals). They are defined as:

$$\begin{aligned}\epsilon_i^{reco} &= \frac{N_i^{reco-matched}}{N_i^{all-reco}} \\ \epsilon_i^{part} &= \frac{N_i^{part-matched}}{N_i^{all-part}}\end{aligned}\tag{6.4}$$

Here $N_i^{reco-matched}$ is the number of events in bin i of the UE observable, where the p_{\perp}^Z -bin on detector-level matches the same p_{\perp}^Z -bin on particle-level. $N_i^{all-reco}$ is the number of all events reconstructed in this bin i and this bin of p_{\perp}^Z , regardless of a match on particle-level. Similarly, $N_i^{part-matched}$ counts the events with a p_{\perp}^Z -bin match on particle- and detector-level. While $N_i^{all-part}$ is the number of all events in this p_{\perp}^Z range on particle-level.

Figures 6.6 (a) and (b) show the correction factors for N_{ch} in $10 < p_{\perp}^Z < 20$ GeV for the two Monte-Carlo generators SHERPA and POWHEG+PYTHIA8. The generators agree well, although SHERPA suffers from some statistical fluctuations in the tails. This is one reason to pick POWHEG+PYTHIA8 as the nominal reference for the unfolding process. Furthermore, the distributions follow the expected detector performance. For rising particle multiplicity the event efficiency reduces, as the trigger and reconstruction efficiency of muons deteriorate in a busy detector environment. In contrast, the non-fiducial signal correction, which illustrates the presence of fakes or a smeared p_{\perp}^{μ} , is independent of the charged particle multiplicity.

6.4.4 The response matrix and number of iterations

The unfolding or response matrix is the heart of the unfolding process. Here, it accounts for bin migration within the UE observables. It gives the probability for a value of the reconstructed physical quantity to be originating at another value ($\mathcal{P}(T_i | R_j)$). The response matrix is based on the transfer matrix, which represents the reconstructed physical quantity versus the particle-level physical quantity. This matrix is in general obtained from the Monte-Carlo simulation. It is filled for each matched event, i.e. the value for p_{\perp}^Z is within the same p_{\perp}^Z -bin on detector and particle-level. The event-weight is filled for the bin connecting e.g. the number of measured tracks (N_{ch}^{det}) to the number of originally generated charged particles (N_{ch}). For N_{ch} , Σp_{\perp} and $\text{mean } p_{\perp}$ the matched variables are defined by the simple numbers of objects, which are either all tracks or all charged particles. It becomes more complex, if one individual charged particle needs to be assigned to a reconstructed track. The reconstructed tracks are associated to primary charged particles via a hit-based track-to-truth particle matching [65] for the transfer-matrix of dN_{ch}/dp_{\perp}^{ch} . The matching algorithm is explained in detail in Sec. 4.4.1.

Initially, the response matrix is obtained from the transfer matrix. The conversion simply normalizes the sum of the entries in a bin of the reconstructed physical quantity to unity. Figure 6.6 (c) shows the response matrix for N_{ch} for the fiducial volume of $10 < p_{\perp}^Z < 20$ GeV. It is constructed using the POWHEG+PYTHIA8 signal Monte-Carlo sample which is overlaid with pile-up events at detector level. The migration effects between the reconstructed and simulated observable bins, here e.g. N_{ch}^{det} and N_{ch} , are represented with the non-diagonal elements of the matrix. For N_{ch} , Σp_{\perp} and $\text{mean } p_{\perp}$ the unfolding matrix is skewed to the reconstruction side (in Fig. 6.6 (c) the y-axis). In other words, the reconstructed observable tends to a higher activity than originally generated on particle level. The direct comparison to a transfer-matrix obtained from the Monte-Carlo sample without pile-up overlay reveals that the main reason for the

asymmetry is the impact of pile-up contributions. An additional contribution comes from fake-tracks. These add activity to the detector level observables and are more likely to occur in busy collision environments, i.e. the tails of N_{ch} and Σp_{T} . In general, the bin migration becomes more likely for higher values of all observables. There is no visible difference apart from statistical fluctuations between the transfer-matrix constructed with the SHERPA or the POWHEG+PYTHIA8 Monte-Carlo sample. Therefore, only the first iteration of the response matrix based on POWHEG+PYTHIA8 is presented in Fig. 6.6(c).

The MC generator level distribution (T^{MC}) is used to represent the initial Bayesian prior probability $\mathcal{P}_0(T_i^{MC})$ for the very first iteration of the unfolding algorithm. This assumption introduces a high model dependence, which is set by the choice of the Monte-Carlo generator. In the first place, there is no other estimation available than the generator prediction. But the subsequent iterations have access to a less biased estimation of $\mathcal{P}_0(T_i^{MC})$: The unfolded distribution from the previous iteration (T^{data}) is used as the prior, in order to reduce the dependence of the final result on the simulation model. In fact, the vertical bins of the transfer-matrix, which represent the bins of the particle level distribution, are reweighted to match the unfolded data distribution from the previous iteration. Then the response matrix is derived again and the full unfolding process represented by Eq. 6.3 is performed with the updated matrix.

Finally, the agreement between the measured unfolded distribution T^{data} and the Monte-Carlo generator level distribution T^{MC} depends on their consistency. In general, the unfolded distribution T^{data} lies between T^{MC} and the true (particle-level) data spectrum. The consistency of the prior and the unfolded data is improved with each iteration. Hence, the results of the iterations converge to the true data spectrum.

However, the statistical bin-by-bin fluctuations in the unfolded spectrum increase with the number of iterations. As a result, a trade-off needs to be defined between this uncertainty and the mitigation of the prior dependence. In general, the iteration is continued until the solution is considered stable. The ATLAS community suggests different strategies to optimize the number of iterations, e.g. the previous ATLAS UE analysis suggests, that two iterations are sufficient to remove the prior dependence while keeping the fluctuations low. The analysis presented here implements an optimization following the idea of D'Agostini [148]. If the unfolded distribution is in agreement with the previous iteration within the statistical uncertainties, there is no possibility to gain better precision with more iterations. As soon as this agreement is accomplished, the iteration is fixed at this point.

For the observable $dN_{\text{ch}}/dp_{\text{T}}^{\text{ch}}$, two unfolding iterations are sufficient for convergence of the unfolding results. This number is high enough to mitigate the prior dependence and it reflects the reasonable agreement between the generator prediction and the unfolded data distribution, while all other observables require eight iterations to converge. Fig. 6.7 shows an example of the unfolded data for different numbers of iterations. Especially the bins of low activity reveal high fluctuations among the first iterations.

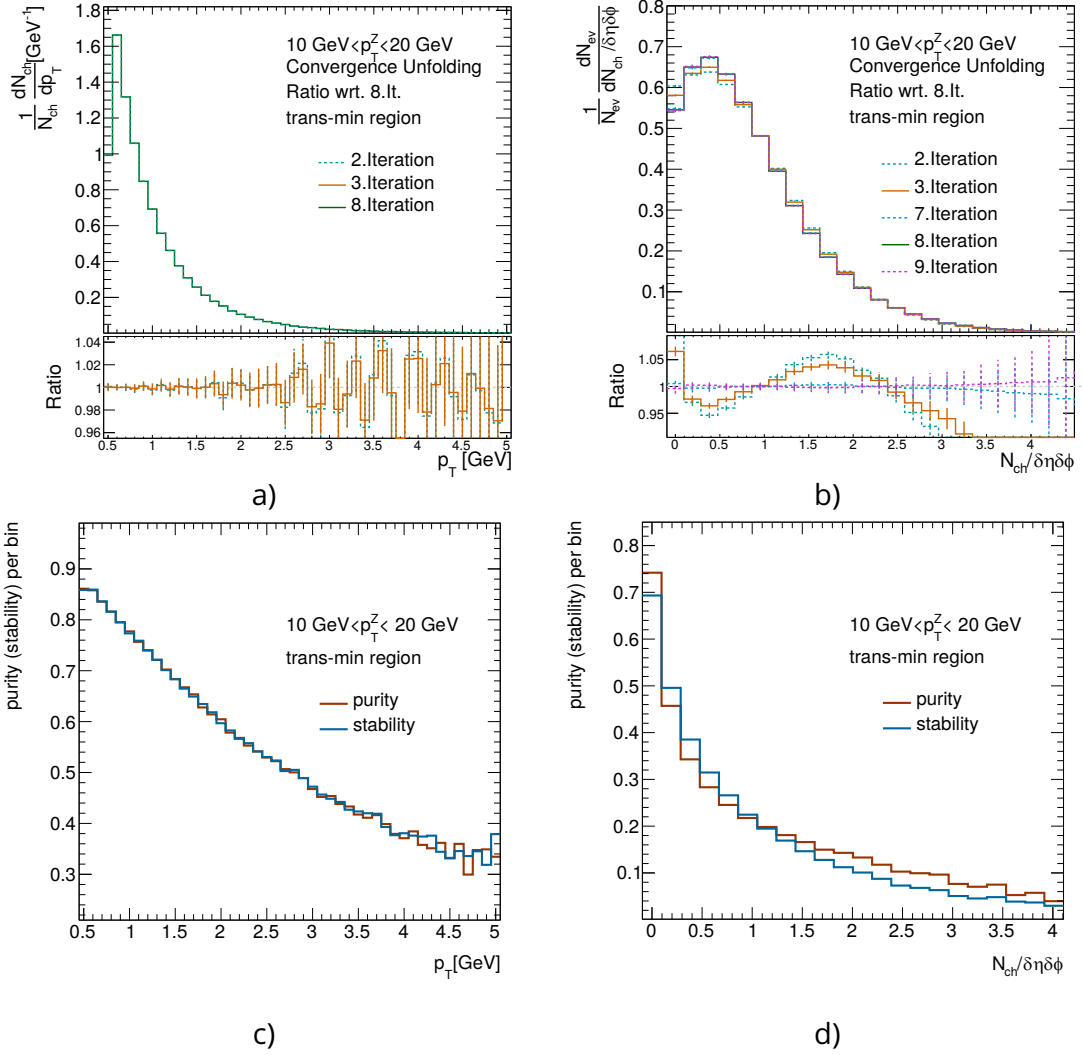


Figure 6.7: The different iteration steps for unfolding dN_{ch}/dp_T^{ch} (a) and $dN_{ev}/d(N_{ch}/\delta\eta\delta\phi)$ (b) exemplarily in $10 < p_T^Z < 20 \text{ GeV}$. The errors indicate the statistical uncertainty evaluated for the iteration. The ratio is calculated with respect to iteration step 8. The second and third iteration are almost similar for (a), while in (b) the convergence is visible for iteration 7 and 8. The values of the corresponding purity and stability indicate (c,d), that the convergence of $dN_{ev}/d(N_{ch}/\delta\eta\delta\phi)$ requires a higher number of iterations than dN_{ch}/dp_T^{ch} .

6.4.5 Unfolding validation

The unfolding process is complex and any inconsistency in the setup will be directly propagated to the final results. This section presents different validations of the unfolding technique to guarantee its robustness and functionality.

Benchmark: Purity and stability

The effect of bin migrations between bins is described by purity (P_i) and stability (S_i). Both benchmarks are calculated for each bin i as following:

$$\begin{aligned} P_i &= \frac{N_i^{det\&part}}{N_i^{det}} \\ S_i &= \frac{N_i^{det\&part}}{N_i^{part}} \end{aligned} \quad (6.5)$$

$N_i^{det(part)}$ is the number of matched events in bin i of the UE observable on detector level or particle level respectively. And $N_i^{det\&part}$ is the number of events, that are reconstructed and generated in the same bin i . The formulas show similarities to Eq. 6.4 for the event efficiency and non-fiducial signal correction, but the crucial difference is that purity and stability are derived for matched events only, while Eq. 6.4 handles the counterpart of unmatched events.

Fig. 6.7 (c) and Fig. 6.7 (d) show an example of purity and stability for dN_{ch}/dp_T^{ch} and N_{ch} in $10 < p_T^Z < 20$ GeV. The distributions for N_{ch} match the description of the response matrix in Sec. 6.4.4: The values decrease with rising activity, i.e. bins representing higher values of N_{ch} . This indicates a higher probability of bin migration for those bins. Peaks are visible, if the bin-width is enlarged. The same is true for the purity and stability distributions for Σp_T and $\text{mean } p_T$. The purity and stability are higher for the bins of dN_{ch}/dp_T^{ch} and the slope of the distributions is flatter compared to e.g. N_{ch} . So less bin migration is expected for the bins of dN_{ch}/dp_T^{ch} . In general, the binning of the UE observables presented here yield a purity and stability below 0.7. In other words, bin i retrieves more than 30 % of its content from events, which migrated from another bin. Hence, the Bayes iterative unfolding is the mean of choice in order to keep accompanying errors low.

Nevertheless, the analysis includes further binning for the fiducial volume, i.e. the bins in p_T^Z and transverse thrust. The bin intervals in p_T^Z and thrust are chosen to yield high purities (> 0.9 for the bins in p_T^Z and > 0.85 for the two bins in T_\perp). Therefore, it is sufficient to correct the associated bin migration with the per-bin corrections, as described in steps 1 and 3 of Sec. 6.4.2.

Closure tests

Self-driven closure

The simplest closure test is to unfold the detector level distributions of a Monte-Carlo sample with the response matrix and corrections obtained from the very same sample. This test yields perfect agreement for the POWHEG+PYTHIA8 sample comparing the unfolded detector-level distributions to the corresponding particle-level distributions. The successful closure attests the correct operation for the first iteration of the unfolding method. Any further iterations are pointless due to the perfect closure.

Data-driven closure test

Mismodelling of the Monte-Carlo particle-level distribution (T^{MC}) as well as residual dependencies of the response matrix on physics quantities can lead to biases in

the unfolded spectrum. Residual biases due to assumptions on the particle-level spectrum can be estimated by the data-driven closure test. This test serves as an estimate for the corresponding systematic uncertainty on the unfolding process. It is described in detail in the dedicated section 6.6.2.

In summary, the idea is to transfer the shape of the data distribution on detector-level to the corresponding Monte-Carlo distribution. The particle-level distribution of the Monte-Carlo sample is adapted in parallel. The uncertainty due to the model bias is defined to be the remaining discrepancy between the unfolded reweighted Monte-Carlo detector-level and the adapted particle-level distribution. This uncertainty dominates in the bins representing rather low UE activities. It is consistent with the fluctuations within these bins among the first iterations of the unfolding procedure.

Model variations using SHERPA

The UE observables are constructed from the SHERPA detector-level information and unfolded using the response matrix and correction factors derived from the baseline POWHEG+PYTHIA8 sample. The results are compared to the particle-level distributions derived from SHERPA as well. The remaining difference serves as a feedback for the accuracy of the unfolding procedure similar to the data-driven closure test. Both Monte-Carlo samples are produced with an equivalent detector simulation, so that the unfolding with POWHEG+PYTHIA8 is capable of correcting all detector effects on the SHERPA sample.

Nevertheless, there are a few deviations, which exceed the disagreement observed in the data-driven closure test. In these cases, the systematic uncertainty is raised to cover the outliers. The combination of data and an alternative Monte-Carlo model give a handle for the remaining prior dependence. Further details on the uncertainty assigned are listed in section 6.6.2.

Alternative unfolding methods

Bin-by-bin unfolding

An additional validation approach is the comparison to a different unfolding technique, the bin-by-bin unfolding [146]. This procedure implies multiplying the observed number of events in data in a given bin by scale factors obtained from Monte-Carlo simulation. The scale factors (also called c -factors) are calculated from the ratio of the number of events on particle-level over the number of reconstructed events in the given bin. Hence, the procedure is much simpler than the Bayesian iterative unfolding, because there is only one scale factor per bin. But the method fully relies on the shape of the Monte-Carlo distribution and results in a dominating dependence on this prior assumption. Usually, it can only be applied when migrations between bins are not very large, such as the bins of p_T^Z or T_\perp presented here.

The c -factors are obtained from the POWHEG+PYTHIA8 sample and applied to the SHERPA detector-level distributions for the cross-check. Once again, the SHERPA particle-level distributions are compared to unfolded detector-level distributions. The discrepancies overshoot the ones observed in the Monte-Carlo based closure-test presented in the previous paragraph. As a conclusion the Bayesian iterative unfolding is more appropriate to correct for detector effects.

'Dressed' leptons for particle-level

The choice of the fiducial-volume or the particle-level definition impacts the unfolded results. The default generator level definition of this analysis includes 'bare' level muons (see Sec.6.3.1). The previous UE measurement in Z events [130] unfolded to

the ‘dressed’ level (i.e. collinear QED FSR is added to the ‘bare’ level muons). The difference between these two generator level definitions affects only the kinematics of the final-state muons and therefore the migration in bins of p_{T}^Z . The choice of rather large bins in p_{T}^Z safeguards against according bin migrations independent of the particle-level definition. The observables are constructed as defined in Sec. 6.3.1, but the muons are unfolded to the ‘dressed’ level to provide a cross-check. The difference between the results after unfolding to different generator levels is below the percent level and is less than the uncertainty related to the unfolding procedure. Therefore, the unfolded results remain compatible with the previous UE analysis in Z boson events.

6.5 Pile-up correction via unfolding

Analogous studies of the UE in Z boson events [130] indicate that particles coming from additional proton-proton collisions during the same bunch-crossing are one of the major background sources. These particles are termed in general as pile-up and they show a similar signature as charged particles, which are originally attributed to the UE of the central collision. They carry low transverse momentum without any preferred orientation in the ϕ -plane. The Bayesian iterative unfolding corrects the detector-level distributions for the pile-up contributions. It relies on the correct modelling of the pile-up contribution in the simulation. As reminder, the Monte-Carlo samples are overlaid with Monte-Carlo-generated minimum-bias events [95] to simulate the effect of multiple interactions in the same bunch crossing. The simulation of minimum-bias events faces two major challenges, namely the modelling of the inelastic scattering of protons and the associated number of interactions per bunch crossing (μ). The first one is limited by the theory calculations, which assess the low-momentum transfer in the (semi-)inelastic scatterings. The comparison with measurements is limited, as the number of interactions per bunch-crossing is not directly accessible with the detector. It is interconnected with the measurement of the luminosity and the number of reconstructed vertices. Hence, it is advisable to cross-check the pile-up simulation or in particular the pile-up removal based on the unfolding process. This section introduces two data-driven cross-checks to validate the pile-up correction via simulated pile-up contributions.

The first one splits the full analysis in three regions based on the amount of pile-up and finally compares the unfolded data. The second approach implements the HBOM algorithm [150], which relies on a purely data-driven pile-up estimation. Both methods reveal that pile-up mainly affects the observables in regions of low activity. Moreover, the results obtained using the different methods are consistent with the baseline procedure, and no additional uncertainty needs to be assigned.

6.5.1 Consistency validation: Pile-up intervals

The first approach splits the full analysis in three samples, which are affected by pile-up by different degrees. The unfolding procedure for all observables in all measurement bins is repeated for three intervals of $\langle\mu\rangle$, namely [8,10], [11,13] and [14,16]. The differentiation in $\langle\mu\rangle$ is applied to data and Monte-Carlo simulation samples. A mismodelling of pile-up in Monte-Carlo simulations would manifest itself less in the interval of $8 \leq \langle\mu\rangle \leq 10$ and more in the interval of $14 \leq \langle\mu\rangle \leq 16$. The difference between the regions in $\langle\mu\rangle$ is clearly visible on detector-level (see Fig. 6.8 (a)), because the more pile-up the larger the measured activity. Nevertheless, after the unfolding the differences vanish (see Fig. 6.8 (b)). The bins of low activity are still varying among the different $\langle\mu\rangle$ regions, but it is within the statistical uncertainty. In general, the unfolded results for the three intervals are found to be fully compatible within their associated statistical uncertainties. Thus, the consistency is confirmed for the handling of pile-up in the unfolding process.

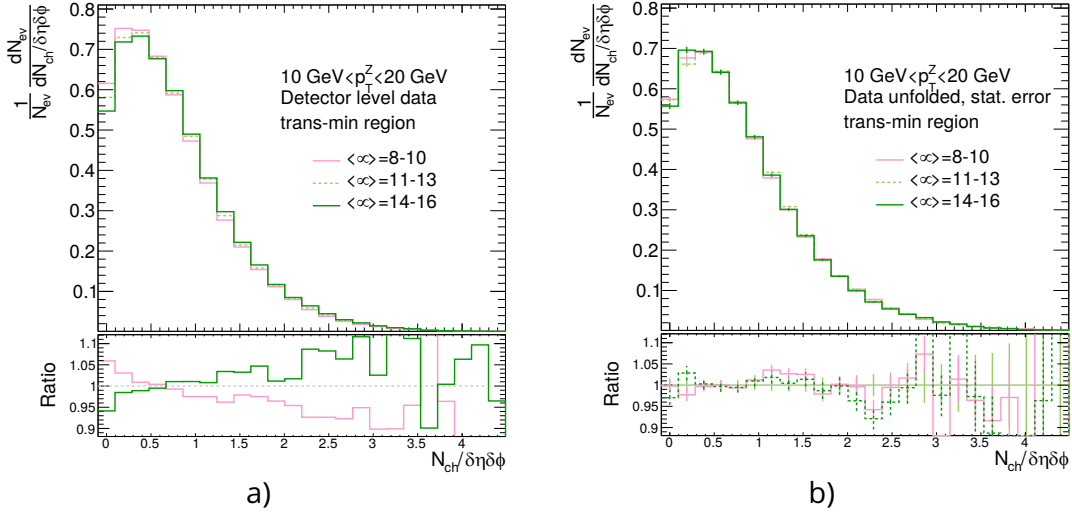


Figure 6.8: Data distributions of $dN_{ev}/d(N_{ch}/\delta\eta\delta\phi)$ split in different regions of $\langle \mu \rangle$ before the unfolding (a) and after the unfolding procedure (b). (b) displays the unfolded data with the statistical uncertainties. The different $\langle \mu \rangle$ regions are in agreement within these uncertainties after unfolding. The ratio is calculated with respect to the middle region [11,13].

6.5.2 Data-driven pile-up correction: The HBOM algorithm

The following approach removes the pile-up contamination from the observables already on detector-level. Hence, the unfolding corrects only detector effects based on Monte-Carlo simulations, while the removal of pile-up relies on a complementary data-driven algorithm. It is the *Hit Backspace Once More* (HBOM) method adapted from reference [150]. It serves as a cross-check for the baseline pile-up removal via Monte-Carlo simulation, because it is independent of any simulation model. Furthermore, it is applied individually to each observable, so that it accounts for the different sensitivities to pile-up contamination. First, the idea of the algorithm is sketched and the details are explained in the following sections. The results and interpretation regarding this analysis are discussed in the last paragraph of this section.

The principle of the HBOM algorithm is to overlay a given data sample multiple times with a well defined amount of additional pile-up tracks. The additional pile-up is derived from the data sample itself. More precisely, the final cross-check collects pile-up tracks from the data sample and adds these in a controlled manner to the observables constructed from the very same data set. The Monte-Carlo sample is overlaid with pile-up tracks from the simulation sample for the validation of the algorithm.

The crucial step of the algorithm is to go from the observable with additional pile-up tracks to a distribution cleaned from pile-up tracks. The dependence between the observable and the amount of pile-up contribution is averaged over the multiple overlays with additional pile-up tracks. The regular distribution is naturally contaminated with pile-up tracks and referred to as D_1 . The indices indicate the amount of pile-up tracks in this distribution measured in multiples of the natural contribution. Thus, one is the amount of the natural contamination. The algorithm adds pile-up tracks to D_1 emulating the natural pile-up contamination. The result is called D_2 . This process is repeated to construct D_3 , D_4 and so on. An example is shown in Fig. 6.9 (a) for N_{ch} in $10 < p_T^Z < 20 \text{ GeV}$. The validation confirmed that running up to D_6 is sufficient to grasp the effects of pile-up on the observables in the scope of this analysis.

The removal of pile-up is then realized in the extrapolation from D_1, D_2, \dots, D_6 back to D_0 , the distribution without pile-up contamination. The name of the algorithm, *Hit Backspace Once More*, refers to this process of removing one contamination more than actually added. This step relies on the assumption, that the dependence on pile-up contamination is quantifiable over the iterations D_1, D_2, \dots , and hence can be inverted by the extrapolation. Here, the extrapolation is applied bin-wisely for each observable using a polynomial of third order. Fig. 6.9(b) exemplifies the extrapolation for one bin of N_{ch} .

D_0 is then unfolded using a Monte-Carlo sample, that does not include pile-up by definition. In detail, it is the very same POWHEG+PYTHIA8 sample as it is used for the baseline unfolding, but without the overlay with simulated pile-up events (see Sec. 6.3.3). The result is a particle-level distribution, that is cleaned from pile-up contaminations not by the simulation based unfolding, but a data-driven procedure.

The full HBOM algorithm relies on three steps:

1. the choice of pile-up track representatives
2. the way these are added to the distribution
3. the extrapolation to D_0

These steps can be realized in different ways, as presented in e.g. [151] or [150]. The following sections give details about the setup employed here. Different variations of the corresponding parameters are investigated as well. The variations and the full validation of the algorithm are presented in the Appendix Sec. C.2. If the variations significantly affect the results, the difference is assigned as an uncertainty on the HBOM algorithm.

Selection of pile-up track representatives

The HBOM algorithm intends to reproduce pile-up contaminations as realistically as possible for a given sample. The pile-up conditions depend again on the data taking conditions, such as the number of protons in the beam or the beam shape. The event selection can affect the pile-up contamination as well, e.g. by certain trigger requirements. Therefore, the most realistic copy of pile-up contaminations is based on the data set of interest itself. The pile-up characteristics of this sample are summarized in the so called *pile-up library*. It holds information about any suitable pile-up track and is unique to each dataset. It is created by scanning through all events of the sample, which are selected through the regular event selection. The analysis presented here is affected only by track based pile-up. Hence, the pile-up library needs to characterize the number of pile-up interactions, where they take place, and how many or which kind of pile-up tracks do these additional interactions contribute. The pile-up library stores this pile-up information for each event. These are:

- the number of reconstructed pile-up vertices (n_{vtx}),
- z-position along the beamline of each pile-up vertex (z_{vtx}),
- for each pile-up vertex the associated tracks with their kinematic (p_{T}, ϕ, η) and spatial ($|z_{\text{track}} - z_{\text{vtx}}|$) properties.

The pile-up vertices, which are stored with their associated tracks, are required to have a minimum distance along the beam line of more than 60 mm from any other vertex. This safeguards against split vertices, i.e. single vertices falsely reconstructed as two vertices. The rather large spacing takes into account the projection of the track trajectories on the beam axis, which is manifested in the cut on $|z_0 \cdot \sin(\theta)|$. The tracks

are required to pass the general quality cuts (see track selection, section Sec. 6.3.1), except for the cut on $|z_0 \cdot \sin(\theta)|$. This criterion is loosened to allow for modelling of non-exactly overlapping vertices. Tracks are associated to a PU vertex and stored in the pile-up library, if they fall into a selection window of $|(z_0^{PUvx} - z_{trk}) \cdot \sin(\theta_{trk})| < 3 \text{ mm}$.

Addition of pile-up tracks

The pile-up library from the previous section characterizes the natural pile-up conditions. The following procedure replicates the pile-up contamination event-by-event. The contamination over all events reproduces the distributions from the pile-up library. The process of contamination is performed once per event to add the equivalent of the natural amount of pile-up. The results corresponds to D_2 . If further iterations are needed, the procedure is repeated accordingly.

The additional pile-up contamination is performed, when the event passes the selection criteria (see Sec. 6.3.1) and before the observables ($dN_{ch}/dp_T^{ch}, N_{ch}, \Sigma p_T, \text{mean } p_T$) have been constructed. Then the following steps are

- Determine how many additional pile-up vertices will be added, i.e. draw this random number from the frequency distribution of n_{vtx} from the pile-up library.
- Determine where these additional vertices are placed, i.e. draw for each of these vertices a random z-position (z_{randm}). The z-position follows the distribution recorded for this sample (z_{vtx}).
- Retrieve which tracks are associated to each additional pile-up vertex, i.e. draw randomly a collection of tracks from the pile-up library for each of these artificial vertices.
- Finally, add all of the pile-up tracks from the previous step to original collection of tracks or observables respectively, if they can be associated to the primary vertex. This is true for the analysis presented here, if $|(z_{PV} + z_{randm} + (z_0^{PUvx} - z_{trk})) \cdot \sin(\theta_{trk})| < 1.5 \text{ mm}$.

These steps will basically add more and more tracks to the observables with higher iterations. The consequent shift to higher multiplicities is clearly visible in Fig. 6.9 (a). The implementation based on random variables guarantees, that these additional tracks copy the random nature of real pile-up tracks.

Pile-up track removal via extrapolation - Hit Backspace

The final step removes the pile-up contamination by extrapolating to D_0 from the pile-up enriched samples (D_1, D_2, \dots, D_6). The extrapolation is performed bin-wise for each distribution individually. The bin contents of the contaminated distributions are plotted as a function of the number of pile-up contaminations (see Fig. 6.9 (b)), and a polynomial of third order is fitted to the resulting distribution (i.e. bin content vs. iterations). The bin content of the pile-up free distribution (D_0) is defined as the fit value at zero.

Results of the cross-check of the regular unfolding and HBOM

The HBOM algorithm serves as a cross-check for the baseline unfolding, which relies on the simulation of pile-up contributions. The results of the HBOM algorithm and the baseline unfolding are in agreement on particle-level within the uncertainties. An example is presented in Fig. 6.10 for $dN_{ev}/d(N_{ch}/\delta\eta\delta\phi)$ and dN_{ch}/dp_T^{ch} in $10 < p_T^Z < 20 \text{ GeV}$.

The comparison considers only uncertainties related to the two methods. Any other uncertainties, such as the ones assigned to the track reconstruction, are correlated, because both methods use the POWHEG+PYTHIA8 generator and the same

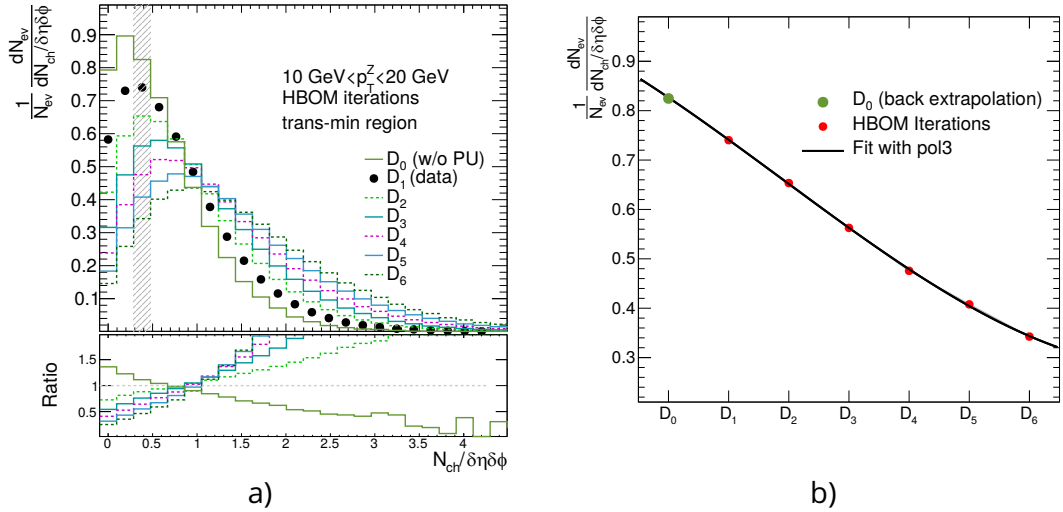


Figure 6.9: (a) Example of the HBOM iterations. D_1 is the actual data distribution on detector level, and D_0 is the same distribution, but cleaned from pile-up. The back-extrapolation step from D_1, \dots, D_6 to D_0 is presented in (b) for the gray shaded bin in plot (a).

detector simulation. The uncertainties assigned to the baseline unfolding are the ones attributed to the simulation of pile-up and the prior dependence of the unfolding. On the other hand, the HBOM algorithm itself is affected by the following uncertainties: One uncertainty accounts for the parameter choice for assembling the pile-up library and another one for the extrapolation method. Both are estimated by running the algorithm with different settings and comparing it to the nominal choice. Their size is compatible to the uncertainty of the pile-up simulation.

The HBOM algorithm itself is validated with the Monte-Carlo generator samples including simulated pile-up. It has to be noted, that the algorithm is not consistent for the pile-up removal in bins of low activity, i.e. bins representing no or only a few charged particles (for further details see Sec. C.2). The behaviour is similar to the baseline unfolding process, which required a higher number of iterations to converge within these bins. However, these bins are assigned with a relatively large Monte-Carlo prior uncertainty, which covers the differences.

All in all, the cross-check is found to be successful and no further uncertainty is assigned to the baseline unfolding process.

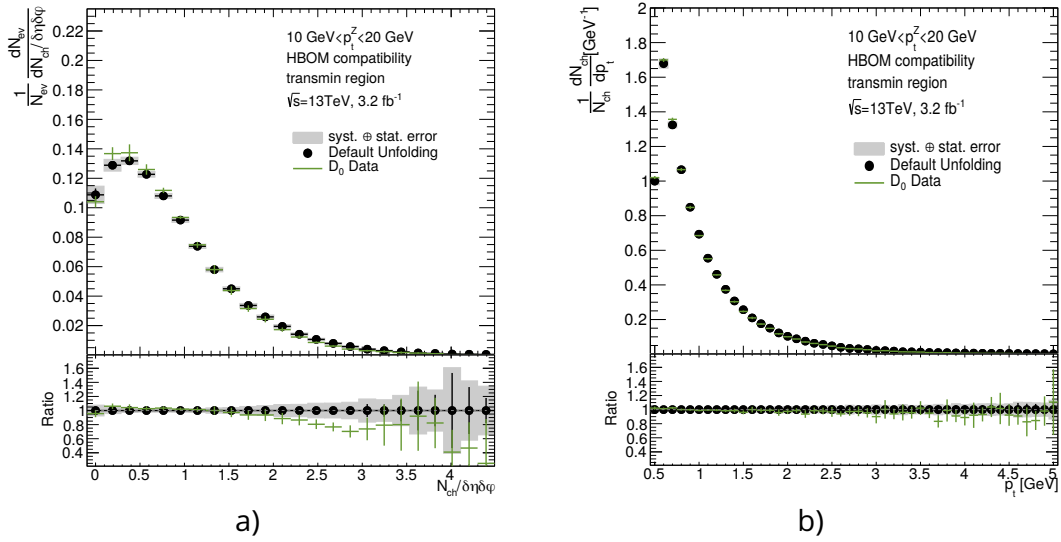


Figure 6.10: Example of the result of the HBOM algorithm (D_0) compared to the nominal unfolding for (a) $dN_{ev}/d(N_{ch}/\delta\eta\delta\phi)$ and (b) dN_{ch}/dp_T^{ch} . The error bars correspond to unfolding and pile-up related uncertainties.

6.6 Uncertainties

This analysis distinguishes the uncertainties in the two common categories of statistical and systematic uncertainties. The first one is constrained by the number of events selected to enter the analysis. In contrast, the systematic uncertainties cannot be reduced by enlarging the dataset³. Here, these are further grouped in detector related and theory related uncertainties. The systematic detector uncertainties arise from the limited resolution and reconstruction techniques of the detector and inaccuracies in the simulation model of the detector. The following Section Sec. 6.6.2 lists the individual contributions relevant for this analysis. Sec. 4.4 provides further details on the estimation of detector related systematic uncertainties.

The theoretical uncertainties include the errors on the cross sections of the background samples and the unfolding procedure. Their estimates are also included in Sec. 6.6.2.

Sec. 6.6.3 discusses the individual contributions to the overall uncertainty and presents a brief comparison.

6.6.1 Statistical Uncertainties

Within this measurement the evaluation of statistical uncertainties includes the unfolding effects following guidelines of the ATLAS community. The statistical uncertainties can be propagated through the unfolding including all corresponding iterations using pseudo-experiments, i.e. all observables measured are fluctuated with a Poisson distribution. The number of entries on reconstruction level corresponds to the expectation value. Then the iterative unfolding is performed with the fluctuated input. This process is repeated 1000 times and the resulting mean error of each bin is taken as the statistical uncertainty. The statistical uncertainty rises with a lower number of events within one bin, e.g. with rising p_T^Z or higher activity.

6.6.2 Systematic Uncertainties

Treatment of Systematic Errors

The full analysis process is re-performed for each source of uncertainty with the adapted simulation parameters of e.g. the track and muon parameters. The selection criteria remain the same as for the regular analysis. The data sample on detector-level is then unfolded with the results of the systematically varied Monte-Carlo sample. The assigned systematic uncertainty is the difference to the nominally unfolded result. The systematic uncertainties, which are directly correlated, i.e. provided with two variations ('down', 'up'), have to be merged in order to obtain the correct estimate for the corresponding systematic. The corresponding systematic uncertainty (σ_{syst}) is simply the average of both variations:

$$\sigma_{syst} = \left(\frac{\sigma_{up}}{2} + \frac{\sigma_{down}}{2} \right)$$

In general, all other systematic variations are assumed to be uncorrelated. Therefore, a rather conservative approach is chosen to estimate the total systematic uncertainty. All systematic errors are added in quadrature. The statistical uncertainty is added in quadrature as well for the final total error.

Detector related systematic uncertainties

³ A few systematic uncertainties are limited by the dataset they were originally evaluated on, e.g. trigger efficiency uncertainties. But these are neither directly affected by the choice of the data inspected nor limiting the results of this analysis to investigate a possible reduction.

Track Reconstruction Efficiency

The track selection is performed on different simulation models for the passive material distributions in order to access the systematic uncertainty on the track reconstruction efficiency. The observables created in this analysis alter by maximally 0.5% with the different variations. The requirement of $p_T > 0.5$ GeV safeguards against considerable effects from missing deflected charged particles.

Fake Rate

The systematic uncertainty on the modelling of the fake rate is 30 % (for details see Sec. 4.4). The variation to a lower fake rate is propagated to the final distributions by randomly removing an appropriate fraction of the tracks during the selection. Since it is impossible to add tracks of non-reconstructed particles, the method is asymmetric. However, it is assumed that the effect is symmetric. The comparisons with the nominally reconstructed observables yields a deviation of about 0.4 % independent of the p_T^Z regime and regions.

Track Impact Parameter Resolution

The transverse (d_0) and longitudinal (z_0) impact parameters of the tracks are smeared out to propagate the systematic uncertainty of the track impact parameter resolution. The width of the Gaussian depends on the track kinematics. The resulting systematic effect for d_0 is negligible, a relative deviation of less than 0.01 % in comparison to the nominal values is calculated. Whereas the systematic uncertainty for z_0 peaks at a deviation of 0.1 % for the distributions which rely on the number of reconstructed tracks, i.e. the charged particle multiplicity and the sum of transverse momenta. This also reflects the sensitivity of the selection on z_0 to discriminate pile-up while d_0 is of minor importance.

Weak Modes

The uncertainties originating from deformations of the detector are handled by applying bias corrections to tracks as a function of their angular position. The variations of all three affected parameters ($z_0 + \delta_{z_0}$, $d_0 + \delta_{d_0}$, $Q/p + \delta_{sagitta}$) yield a negligible effect on the final results. The relative deviation from the nominal observables is in the order of magnitude of $1 \cdot 10^{-5}$.

Muon Scale Factors

The analysis includes SFs for the muon isolation, trigger and reconstruction efficiencies. For each one, the systematic and statistical error is varied individually, once by $+\sigma$ and once by $-\sigma$. The variation of the systematic uncertainty corresponds to the combination of uncertainties on the SFs named in Sec. 4.4. All systematic SF variations result in deviations less than 0.1 % for the final observables.

Muon momentum scale and resolution

The differences are negligible when comparing the nominal observables and the ones deduced with varied Muon momentum scales. Also the variation of the resolution and the Sagitta Bias shows almost zero effect.

Pile Up correction

The unfolding procedure corrects for effects coming from pile-up activity. Therefore, the correct description of $\langle \mu \rangle$, which serves as a measure for the pile-up activity, is essential for the final unfolded results. The value of $\langle \mu \rangle$ is varied according to the uncertainty on the inelastic pp collision cross-section resulting in more (less) pile-up activity modelled in the simulation (see also Sec. 4.4.3). These variations represent one of the largest systematic uncertainties for all distributions. Especially the tails of the distributions of dN_{ch}/dp_T^{ch} and Σp_T are sensitive to the variation of the pile-up

activity, because objects with higher p_T are more likely to originate from pile-up than from the actual UE.

Two additional cross-checks validate the pile-up modelling and the consistency of removing the pile-up effects via the unfolding technique. These are presented in Sec. 6.5. The results are consistent with the nominal procedure within the unfolding and pile-up correction uncertainty. Therefore, the variation of $\langle\mu\rangle$ is the only uncertainty assigned to the pile-up modelling and correction.

Theory Model related systematic uncertainties

Uncertainty on the background contamination

The background processes retrieved from Monte-Carlo simulations are scaled according to their cross-sections. This parameter is deduced only to a certain order by the theory calculations. Hence, the electroweak background normalization is varied by $\pm 5\%$ and the $t\bar{t}$ background normalization by $\pm 15\%$, which corresponds approximately to the theoretical uncertainties [143, 144].

The multijet background estimation is data driven. It represents only a minor fraction of all events (see Sec. 6.3.4). Conservatively, the full effect of including the multijet background or not is taken as an uncertainty. The uncertainties on the final results are evaluated for each background process individually. But for a better overview all background uncertainties are summed in quadrature for the presentation in Fig. 6.12 and Fig. 6.11. This combined background uncertainty forms a negligible fraction of the total systematic uncertainty. The dependence of the background uncertainty on p_T^Z is negligible for this measurement.

Uncertainty on the unfolding procedure

The unfolding method (see Sec. 6.4.2) depends on the precise knowledge of the underlying particle-level distribution. Mismodelling of such a distribution can lead to biases in the unfolded spectrum. The uncertainties on the shape of the unfolded spectrum is determined in two ways by using a data-driven and a simulation based closure test. Both employ the same idea: An alternative distribution on detector-level is unfolded using the nominal unfolding method. The result of the unfolding is compared to the original particle-level distribution corresponding to the alternative sample. This approach requires, that the alternative distributions differ from the nominal Monte-Carlo simulation, which is used to build the response matrix and correction factors.

The data-driven closure test derives the shape of the distributions from data. It creates a Monte-Carlo simulated distribution on detector level, which resembles data. This is then unfolded and compared to its reweighted particle-level counterpart.

In detail, one assumes that the shape difference on detector-level between data and the Monte-Carlo simulation originates from the improper modelling on particle-level. The particle-level distribution is reweighted with a smooth function such that the simulation and data are in better agreement on detector-level. In this analysis the *smooth function* corresponds to a polynomial of third order, which approximates the ratio of data and simulation at detector-level.

The reweighted detector-level distribution is then unfolded using the regular response matrix, i.e. the one which is used for the actual data unfolding. Finally, the systematic uncertainty of the unfolding method is given by the relative difference between the unfolded reweighted Monte-Carlo simulation and the reweighted particle-level distributions.

This dependence on the prior knowledge is evaluated for the bin-by-bin unfolding and the Bayesian iterative unfolding with various iterations. The final value, which is assigned to the results, corresponds then to the eight and two iterations respectively.

It is the dominant systematic uncertainty in most distributions at lower values of p_{T}^Z .

The second method of estimating the uncertainty related to the unfolding is to unfold the detector-level Monte-Carlo distributions generated with SHERPA using the unfolding matrices based on the POWHEG+PYTHIA8 sample. The results are compared with the particle-level quantities predicted by SHERPA. After taking the uncertainty due to the Monte-Carlo prior into account, a slight discrepancy between the unfolded SHERPA sample and the particle-level distributions remains.

Therefore, an additional contribution to the MC prior uncertainty is introduced to cover this remaining non-closure of the unfolded results and the SHERPA generator level. In general, it does not exceed the 2–4% level and is smoothed over the full range of the observable. In a few cases, this non-closure component dominates the Monte-Carlo prior uncertainty.

These two separate unfolding uncertainties are added in quadrature in Fig. 6.12 and Fig. 6.11.

6.6.3 Relative uncertainties and discussion

The breakdown of the individual sources of uncertainties for the four observables, p_{T} , N_{ch} , Σp_{T} , and $\text{mean } p_{\text{T}}$ is illustrated in Fig. 6.12 for the example of events with $10 < p_{\text{T}}^Z < 20$ GeV in the trans-min region (the region most sensitive to the UE), inclusively in T_{\perp} . Figure Fig. 6.11 shows the systematic uncertainties in the arithmetic mean of the N_{ch} , Σp_{T} and $\text{mean } p_{\text{T}}$ spectra in the trans-min region as a function of p_{T}^Z also inclusively in T_{\perp} . The detector related uncertainties are combined in *Detector* for better visibility. These include the uncertainties of the lepton and track selection performance and the pile-up reweighting.

The uncertainty depicted as *Prior* is the combination of the two uncertainties related to the model dependence of the unfolding technique. All sources of systematic uncertainty are considered uncorrelated and are combined in quadrature. The squared sum with the statistical uncertainty yields the *overall* (total) uncertainty.

Naturally, the statistical uncertainty of the data rises with increasing p_{T}^Z , and for bins presenting high multiplicity or high charged particle p_{T} . In these cases, a low event or particle count is expected. The statistical uncertainty of the data dominates the systematic uncertainties for p_{T}^Z greater than around 200 GeV (see e.g. Fig. 6.11 (b)). Nevertheless, it does not limit the significance for distributions in bins of lower p_{T}^Z , which are most important for measuring the UE activity. Concluding, the size of the dataset is sufficiently large.

The Monte-Carlo prior uncertainty is one of the largest contributors of the systematic uncertainties at all values of p_{T} and in each p_{T}^Z region. The uncertainty is in the same order for the other differential distributions, but the effect on the mean values is marginal. The shape of the prior uncertainty correlates with the discrepancy between the Monte-Carlo particle level and the unfolded data distributions (this is discussed in detail in Sec. 6.7). POWHEG+PYTHIA8 misjudges particularly the first bins of the differential distributions, which leads to an imbalance of the unfolding matrices. And this results in the rather large bias and corresponding uncertainty in first bins. Especially, the first bins of $\text{mean } p_{\text{T}}$ reveal an exorbitant sensitivity on the Monte-Carlo prior. But in this case one has to take into account, that these bins reflect a tiny fraction of the full $\text{mean } p_{\text{T}}$ distribution (see Fig. 6.16 (e)). The effect on the final significance is therefore uncritical.

The detector related uncertainties represent a similar fraction as the Monte-Carlo prior uncertainty. The contributions are mainly twofold: In the ranges of low p_{T} and low charged particle multiplicity the uncertainties on the track reconstruction performance

drive the *Detector* uncertainty. In this regime the p_T resolution is lower and e.g. the modelling of the fake rate can affect a relatively large fraction of the charged particles. The uncertainty on the pile-up reweighting exceeds these uncertainties in the tails of the distributions of p_T , N_{ch} , Σp_T , and $\text{mean } p_T$. With increasing p_T it is more likely that the reconstructed charged particles originate from other pp collisions during the same bunch crossing. Hence, these are more sensitive to the variation of the pile-up contribution.

The uncertainties on the tracking performance and the pile-up reweighting are independent of p_T^Z . Their contribution is constant for the different bins of the mean distributions as function of p_T^Z . The uncertainties on the lepton efficiencies shape the *Detector* uncertainty for the mean values, because these vary with p_T^Z .

Nevertheless, the lepton related uncertainties are negligible for the differential distributions. The muons are removed from the final state selection. And small shifts of the reconstructed direction or momentum of the Z boson introduce almost no changes to e.g. the number of charged particles in a certain region. Last but not least, the uncertainty on the background contribution is listed for completeness. It is negligible in any distribution and any region. The clean selection channel $Z \rightarrow \mu\mu$ guarantees a small background contamination. The same holds true for the related uncertainty. Additionally, the measurement of the activity of the UE is based on shape comparisons. As a consequence, minor changes of the event count are suppressed in the final results.

In summary, the uncertainties associated to the pile-up modelling and the unfolding dominate the measurement of the UE observables, but do not limit its significance. The overall total uncertainty is rather small compared to the discrepancy of the Monte-Carlo generator prediction to data as it is presented in the following Sec. 6.7.

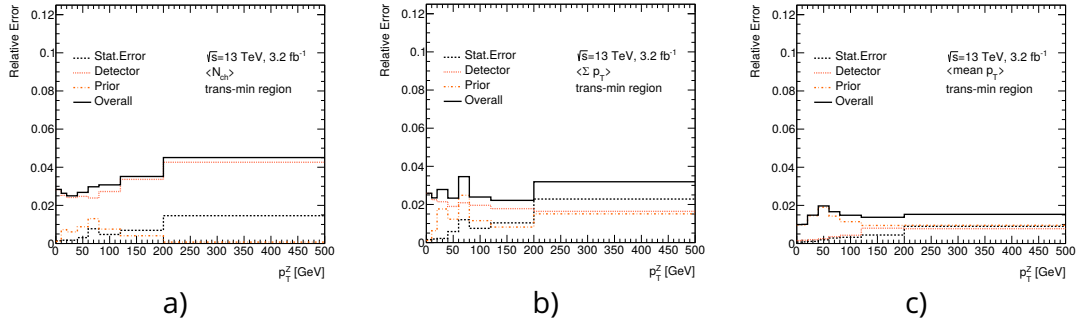


Figure 6.11: A summary of the systematic uncertainties in the arithmetic mean of the N_{ch} and Σp_T spectra in the trans-min region as a function of p_T^Z . Here ‘Prior’ combines the two approaches to estimate the unfolding-related uncertainties. ‘Detector’ includes the modelling of the detector and the pile-up conditions.

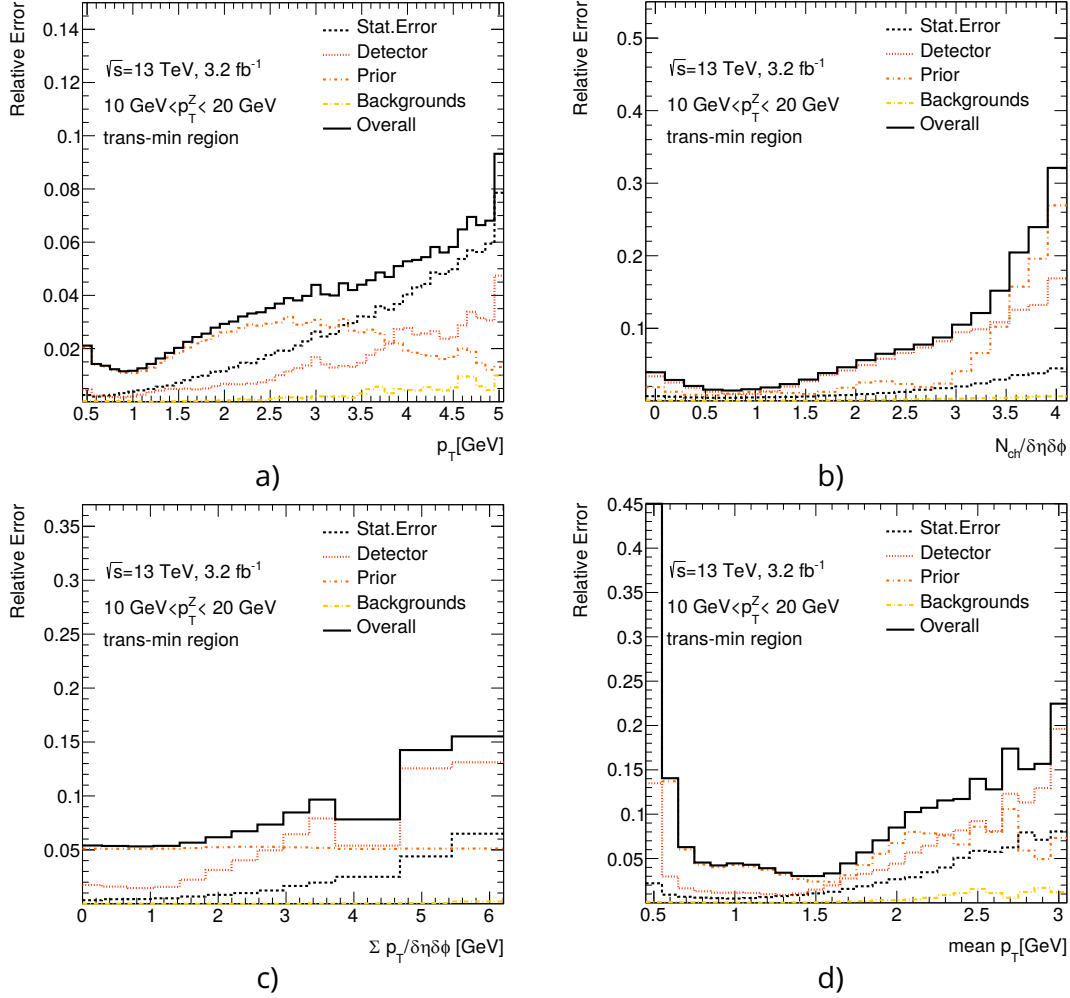


Figure 6.12: Breakdown of systematic uncertainties in the p_T spectrum (a), the charged-particle multiplicity (N_{ch} , (b)), the scalar sum of the transverse momenta (Σp_T , (c)) and the mean transverse momentum ($mean p_T$, (d)) for events with $10 < p_T^Z < 20$ GeV in the trans-min region inclusively in T_\perp . Here ‘Prior’ combines the two approaches to estimate the unfolding-related uncertainties. ‘Detector’ includes the modelling of the detector and the pile-up conditions.

6.7 Unfolded observables and comparison with model predictions

Distributions of p_T , N_{ch} , Σp_T , and $\text{mean } p_T$ are obtained in slices of p_T^Z for the different regions defined in the transverse plane and different regions of T_\perp . The arithmetic means of N_{ch} , Σp_T , and $\text{mean } p_T$ ($\langle N_{\text{ch}} \rangle$, $\langle \Sigma p_T \rangle$, and $\langle \text{mean } p_T \rangle$) are measured as a function of p_T^Z in addition to the measurements in slices of p_T^Z . The results for N_{ch} and Σp_T are presented as a density, i.e. the observables are divided by the size of the according region in the η - ϕ -plane. The axis labels indicate the presentation as a density with $\delta\eta\delta\phi$ in the denominator. The densities allow to compare the activity of different regions more easily. Section C.1 explains the convention, how to transform the measured quantities into the presented densities.

The results are selected to be sensitive to certain subprocesses of the UE. This is illustrated in the dependence on p_T^Z described in Sec. 6.7.1. The discussion of the results in individual p_T^Z -bins starts with the trans-min region with emphasis on the MPI enhanced selection. The results of the trans-max regions follow in the subsequent section and present insights into the effects of ISR and FSR. The transverse and toward regions represent the full collection of the UE processes, because both regions are well separated from the hard scattering. The away region is dominated by the recoiling jets off the Z boson, but it gives an impression of the general generator performance for the hard scattering simulation. The final results compare the mean activity to previous measurements at lower collision energies.

6.7.1 Underlying-event activity as a function of p_T^Z

General characteristics of the UE regions

Figures 6.13 and 6.14 show the mean of the scalar sum of the transverse momenta of charged particles ($\langle \Sigma p_T \rangle$) and the mean number of charged particles ($\langle N_{\text{ch}} \rangle$) both illustrated per unit η - ϕ space. The lower plot presents the ratio, $\langle \frac{\Sigma p_T}{N_{\text{ch}}} \rangle$, namely the arithmetic mean of $\text{mean } p_T$ ($\langle \text{mean } p_T \rangle$). All three observables are illustrated as a function of p_T^Z . The left hand figures compare these observables in the away, toward and transverse regions and the right hand ones in in the transverse, trans-min and trans-max regions. The results presented in Fig. 6.13 are measured inclusively in T_\perp , while Fig. 6.14 distinguished in MPI enriched ($T_\perp < 0.75$) and rather pencil-shaped events ($0.75 \leq T_\perp$).

The three observables behave similarly in their dependence on p_T^Z in the different regions, because they are all based on the same charged particles. Generally, the activity of the UE grows with the transverse momentum of the Z boson in any azimuthal region. A higher value of p_T^Z indicates a more central collision. And a larger overlap of the colliding protons involves a higher momentum transfer among the partons, which finally yields an overall higher event activity. The growth in dependence of p_T^Z is characteristic for the individual azimuthal regions.

The away region stands out due to the strongest correlation with p_T^Z . $\langle \Sigma p_T \rangle$ rises linearly with p_T^Z as the away region is dominated by the recoil of the Z boson. The transverse and toward region contain an equal amount of activity in the lowest bins of p_T^Z , but the activity in the transverse region grows faster with the momentum of the Z boson. It is more likely with higher p_T^Z that recoil jets from the Z boson leak into the transverse region, while the toward region is less affected due to the larger distance in the azimuthal plane. The toward region receives minor contributions from the ISR and the remaining parts associated with the hard scatter process, namely the muons, are efficiently removed. As a result, the slope with p_T^Z is smaller compared to the transverse region.

The plots in the right hand column of Fig. 6.13 show the same observables also

measured in the transverse region but compared to its segments, the trans-min and trans-max region. The construction assigns the higher activity to the trans-max region and makes the trans-min region more sensitive to the UE. The latter argument is reflected by the fact, that the distributions flatten out for lower values of p_T^Z in the trans-min regions. They represent the lowest plateaus for all regions. The difference between the trans-min and the trans-max region is a measure for the recoil activity leaking from the away region into the transverse region. Therefore, $\langle \Sigma p_T \rangle$ scales proportionally with p_T^Z in the trans-max region and exceeds the measured activity densities in the transverse region.

The gap between the trans-min and trans-max region grows almost linearly for $\langle \text{mean } p_T \rangle$ and $\langle \Sigma p_T \rangle$ with p_T^Z (Fig. 6.13 (b) and Fig. 6.13 (f)), but remains static for $\langle N_{\text{ch}} \rangle$ when comparing all three transverse regions in Fig. 6.13 (d). This behaviour is an artefact due to the number of charged particles being an integer value. The trans-max region contains on average two more particles than the trans-min region. The differences of the densities in the trans-min and trans-max region is about $0.4 (\approx 2 / (\delta\eta\delta\phi)_{\text{trans-min}})$ for $\langle N_{\text{ch}} \rangle^4$. Hence it corresponds to a difference of two particles in absolute numbers. The transverse region represents the average of the trans-min and trans-max region and therefore shows a difference corresponding to one charged particle (≈ 0.2) when compared to its subregions.

⁴The normalisation to η - ϕ space depends on the fiducial volume of the different regions, i.e. $\delta\eta = 5$ for all regions while the toward, away and transverse region cover twice the area in the azimuthal plane as the trans-min and trans-max regions $\delta\phi_{\text{trans-min,max}} = 2\pi / (3 \cdot 2)$, see also Sec. 6.2.1.

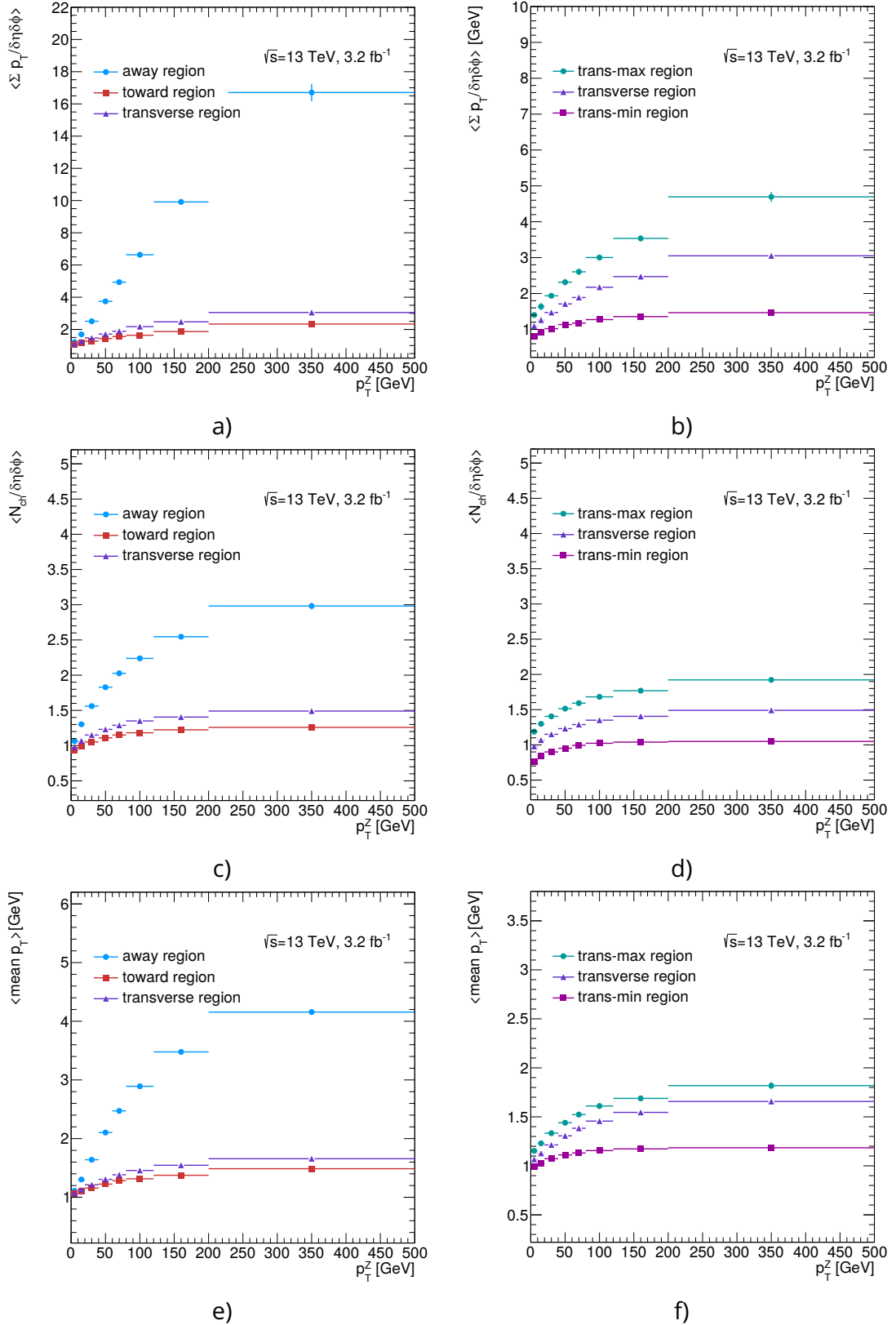


Figure 6.13: Comparison of the activities in the different regions of the transverse plane as a function of p_T^Z . From top to bottom: arithmetic mean of the scalar sum of the transverse momenta, mean number of charged particles both presented per unit $\eta-\phi$ and the mean of mean p_T .

The UE regions selected in transverse thrust (T_{\perp})

The activity in the trans-min region rises slowly with increasing Z boson transverse momentum, but it is not possible to distinguish which fraction is coming from recoil jets or due to an overall rising event activity. The additional selection on the transverse thrust enhances the sensitivity to MPI as explained in section Sec. 6.2.3 and Reference [136]. The order of Fig. 6.14 is the same as for Fig. 6.13. The difference is that the lighter colours present the MPI enriched results (lower values of thrust: $T_{\perp} < 0.75$) and the darker colours represent the results, which are more likely to be contaminated by activity from the recoil jets (higher values of thrust: $0.75 \leq T_{\perp}$).

The distinction in transverse thrust shows two major effects within the transverse, trans-min and trans-max regions (right hand column of Fig. 6.14, the transverse regions is not displayed for better visibility). The most prominent effect is the rise in activity when focussing on the MPI enriched events. The selection of spherically balanced events ($T_{\perp} < 0.75$) implies a higher activity in the transverse region. The second effect is that the dependence on p_{T}^Z changes, when the results are distinguished in thrust. The low and high thrust results diverge for higher p_{T}^Z , because the spherical balanced (low thrust) events create a stronger correlation with p_{T}^Z . The event topology is spherically balanced only if higher activity in the transverse region compensates the high p_{T} recoil of the Z boson. So the selection on low thrust implies a stronger dependence on the hard scatter for increasing values of p_{T}^Z . Nevertheless, this bias is negligible for lower values of p_{T}^Z and the additional activity in low thrust events is more likely to come from a higher amount of MPI.

The selection on thrust does not affect the $\langle \text{mean } p_{\text{T}} \rangle$ for $p_{\text{T}}^Z < 50\text{GeV}$ in the trans-max and trans-min region (see Fig. 6.14 (f)), because the UE activity already dominates the low p_{T}^Z transverse region. The enhanced sensitivity to MPI increases mostly the total amount of activity, which is clearly manifested in $\langle \Sigma p_{\text{T}} \rangle$ and $\langle N_{\text{ch}} \rangle$.

The observations change, when focussing on the regions, which are topologically parallel to the hard scattering. Firstly, the dependence on thrust is similar for the away and toward region for $\langle N_{\text{ch}} \rangle$, when it is compared to the transverse regions (see Fig. 6.14 (c) and Fig. 6.14 (d)). The MPI enriched (low thrust) events contain more particles than the recoil dominated (high thrust) ones, because naturally there are more particles required to balance the event topology.

But the away and toward regions reveal an inverted behaviour for $\langle \Sigma p_{\text{T}} \rangle$ and $\langle \text{mean } p_{\text{T}} \rangle$, i.e. the total activity is higher for events of high thrust and also rises faster with p_{T}^Z . The reason is, that a rather pencil shaped event ($0.75 \leq T_{\perp}$) requires, that the bulk of the activity is concentrated in the away and toward regions. It enhances the correlation of $\langle \Sigma p_{\text{T}} \rangle$ and $\langle \text{mean } p_{\text{T}} \rangle$ with p_{T}^Z . In general, there are less particles in the toward and away region for the selection on high thrust, but these particles are more energetic. This fact highlights, that the selection $0.75 \leq T_{\perp}$ captures rather the hard scattering activity, which is characterized by objects of high momentum.

The values of $\langle \Sigma p_{\text{T}} \rangle$ and subsequently $\langle \text{mean } p_{\text{T}} \rangle$ are lower for the MPI enriched (low thrust) events in the toward and away region, because, if there is more energy deposited in the transverse region due to MPI, a lower fraction of the collision energy is available for the toward and away region. This causes the difference between the low and high thrust events in the toward and away regions.

The toward region is only sensitive to the enhanced MPI activity for a certain range of p_{T}^Z , as it is seen in Fig. 6.14 (a). $\langle \Sigma p_{\text{T}} \rangle$ is higher for $p_{\text{T}}^Z < 100\text{GeV}$ for events on low thrust, which indicates more contributions from MPI. Nevertheless, the related effects are better visible in the trans-min region.

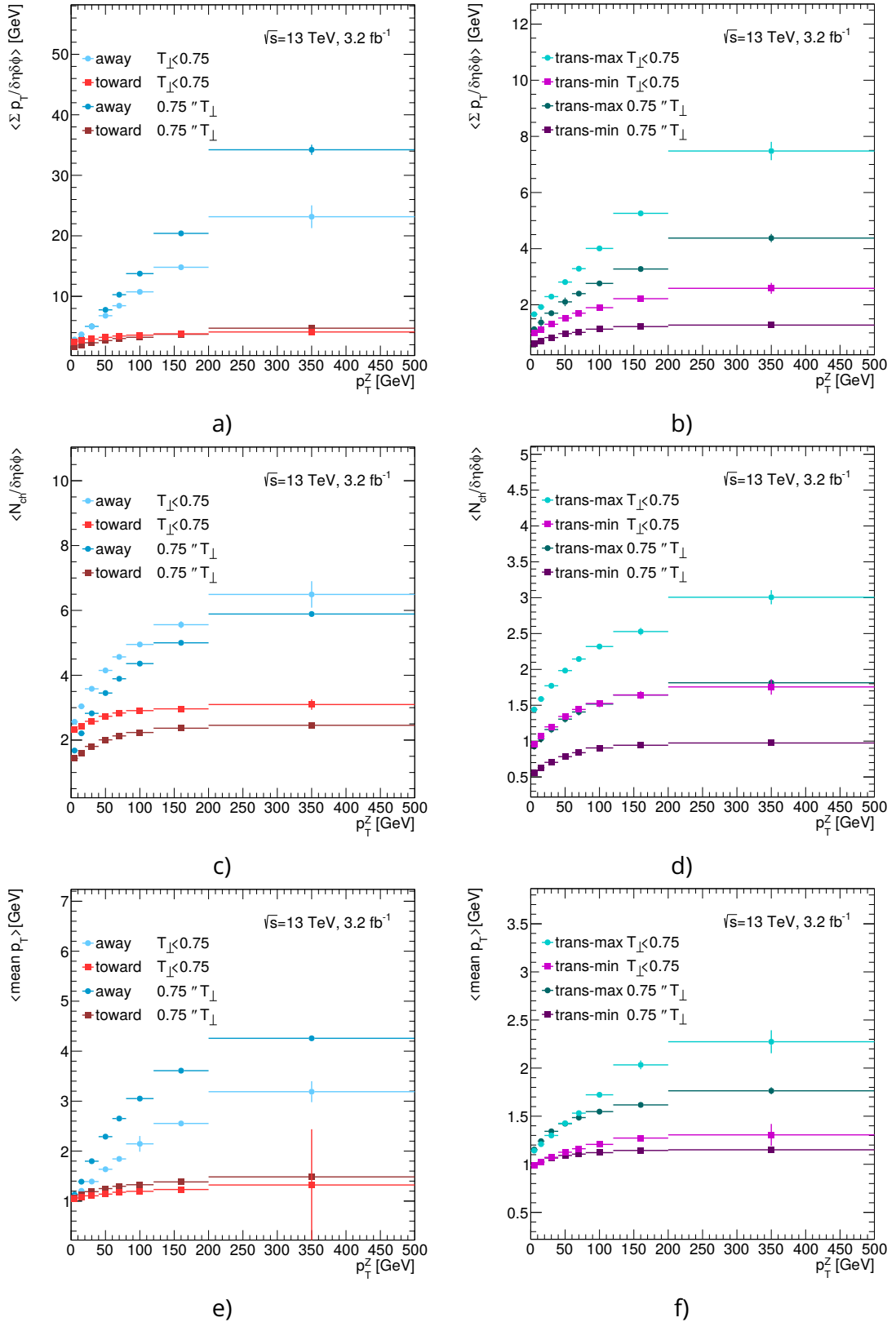


Figure 6.14: Comparison of the activities in the different regions of the transverse plane as a function of p_T^Z . The results are additionally distinguished in thrust. From top to bottom: arithmetic mean of the scalar sum of the transverse momenta, mean number of charged particles both presented per unit η - ϕ and the mean of mean p_T .

6.7.2 Differential distributions and generator performance

Trans-min region

Figures 6.15 to Fig. 6.18 show the unfolded observables with different selections on transverse thrust (T_{\perp}). The comparison of the MPI enhanced regions (low thrust: $T_{\perp} < 0.75$) to the high and inclusive thrust selections probes the ability of the generators to predict the MPI activity. The first columns of Fig. 6.16 to Fig. 6.18 present the differential distributions in a bin of low transverse momentum of the Z boson ($10 < p_{T}^Z < 20$ GeV). It is unlikely that the recoiling jets of the Z boson leak into the fiducial volume of the trans-min region, and in addition the direction of the Z is sufficiently well reconstructed. The second column shows the mean values of N_{ch} , Σp_{T} and mean p_{T} as function of p_{T}^Z to visualize possible dependencies on the hard scatter process. The predictions from POWHEG+PYTHIA8, SHERPA, and HERWIG++ are compared with the data. The ratio of prediction to data is shown beneath each plot. The data distributions of the mean values equal the Figures from the previous Sec. 6.7.1.

None of the tested MC generators describes all aspects of the data well and the differences exceed even the 70% level in particular bins.

Generally, the MC generators predict a higher number of particles with small p_{T} ($p_{\text{T}} < 0.75$ GeV) than is observed in data (see Fig. 6.15 (a)). The bins of higher p_{T} are consequently undershot by POWHEG+PYTHIA8. SHERPA and HERWIG++ overshoot the data in the tail of the distribution again, but suffer from statistical fluctuations. This performance is not affected by the different selections on thrust.

The prediction of a softer p_{T} spectrum compared to data is consistent with the MC predictions tending to lower values of mean p_{T} , as is shown in Fig. 6.16 (e). The largest differences between data and simulation are at lower values of N_{ch} and Σp_{T} , and arise due to the steeper transverse momentum spectrum of charged particles in MC simulations. POWHEG+PYTHIA8 and SHERPA predict a higher fraction of events with fewer charged particles and consistently smaller values for Σp_{T} . However, HERWIG++ slightly overestimates the fraction of particles with $p_{\text{T}} > 2.5$ GeV and is qualitatively closer to the shape of the distributions of N_{ch} and Σp_{T} .

With rising p_{T}^Z , the data p_{T} spectrum becomes harder, and N_{ch} , Σp_{T} , and mean p_{T} increase. The relative discrepancy remains the same in comparisons with the generator predictions. The respective Figures of high p_{T}^Z are not displayed here, as they are less meaningful for the effects of the UE.

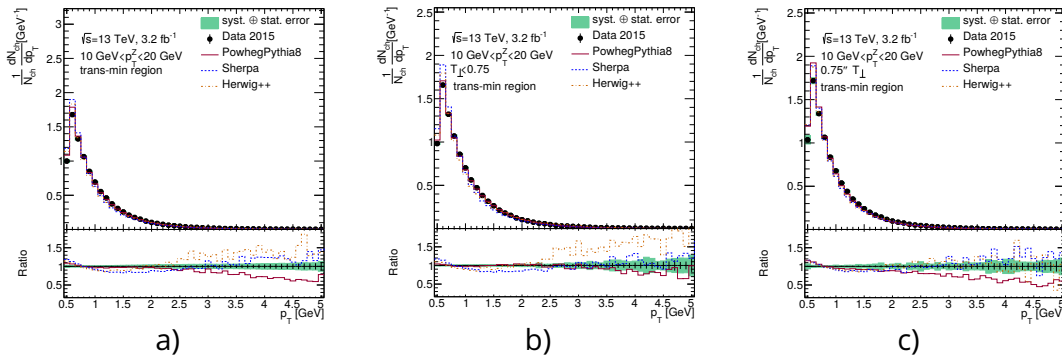


Figure 6.15: Spectrum of the transverse momentum of the charged particles in the trans-min region. (a) inclusive in thrust, (b) MPI-enriched ($T_{\perp} < 0.75$) and (c) $0.75 \leq T_{\perp}$. Predictions of POWHEG+PYTHIA8, SHERPA, and HERWIG++ are compared with the data. The ratios shown are predictions over data.

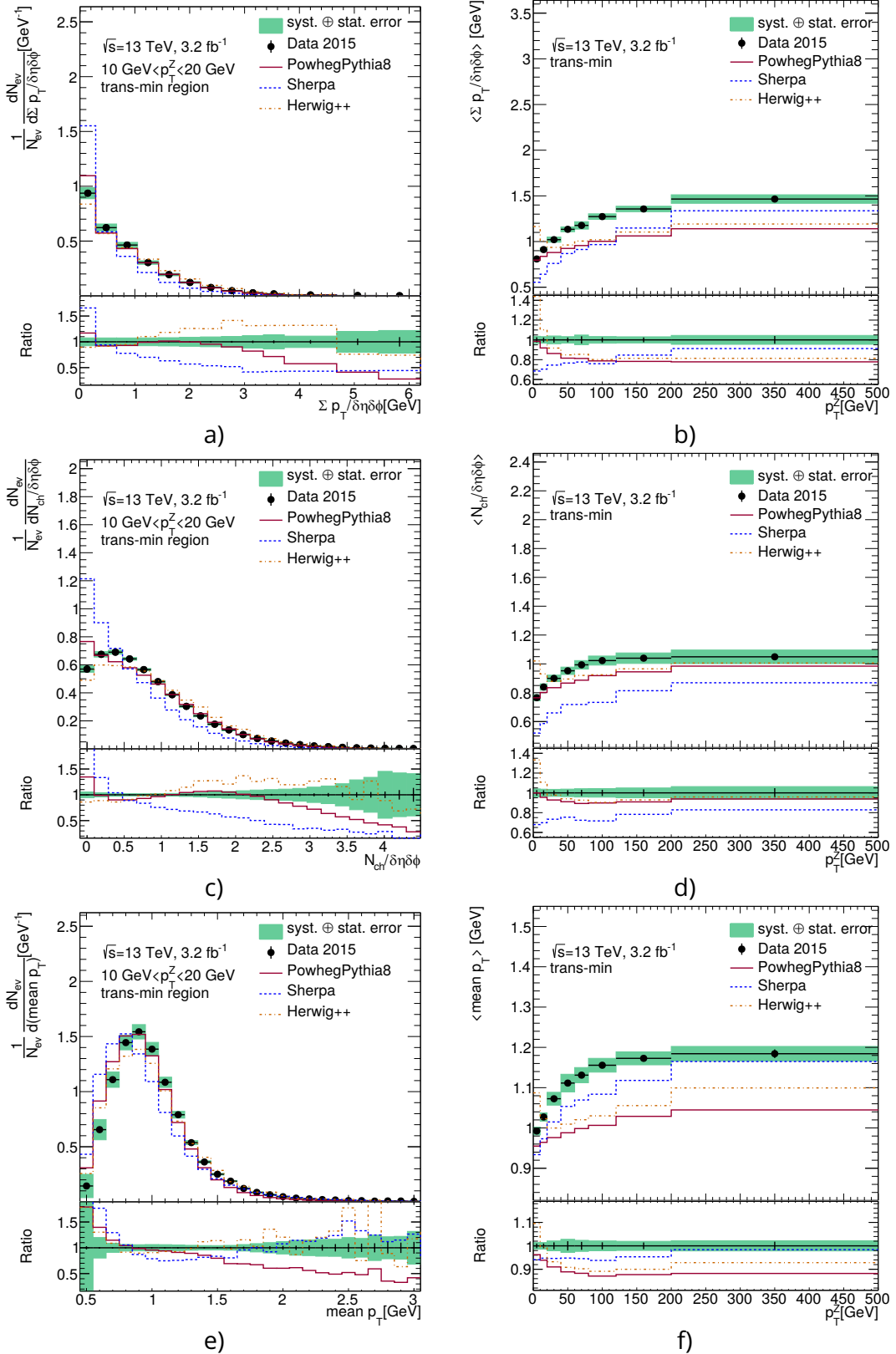


Figure 6.16: The left hand plots present the differential results for $10 < p_T^Z < 20 \text{ GeV}$, compared to the corresponding mean values as a function of p_T^Z in the right column, all inclusive in thrust in the trans-min region. From top to bottom: the sum of transverse momenta, the number of charged particles, and the arithmetic mean of p_T . Predictions of POWHEG+PYTHIA8, SHERPA, and HERWIG++ are compared with the data. The ratios shown are predictions over data.

The dependence on T_{\perp} is illustrated in Figures 6.17, 6.18 and in Fig. 6.15 (b), Fig. 6.15 (c) for the p_{T} spectrum. The most striking difference between the different regions in T_{\perp} is observed for the POWHEG+PYTHIA8 generator when focusing on the low p_{T}^Z bins for $dN_{\text{ev}}/d(N_{\text{ch}}/\delta\eta\delta\phi)$ and $dN_{\text{ev}}/d(\Sigma p_{\text{T}}/\delta\eta\delta\phi)$. It is visible for instance in Fig. 6.17 (c) compared to Fig. 6.18 (c). The distribution of N_{ch} by POWHEG+PYTHIA8 is shifted towards higher numbers of charged-particles relative to the data in the MPI enhanced selection. More precisely, POWHEG+PYTHIA8 overshoots the data in the range $1 \leq N_{\text{ch}}/\delta\eta\delta\phi \leq 2.5$. But in the high thrust region the MC generator underestimates the data almost over the full range except for the first two bins. In contrast, the performances of SHERPA and HERWIG++ are consistent when comparing the low and high thrust regions for N_{ch} ; HERWIG++ overestimates N_{ch} , and SHERPA underestimates it. The same effect is observed for the distributions of Σp_{T} (see Fig. 6.17 (a), Fig. 6.18 (a)). As pointed out in Ref. [136], the regions of high values of T_{\perp} are dominated by extra jet activity which is not adequately modelled in POWHEG+PYTHIA8. Consequently, POWHEG+PYTHIA8 manages to describe $\text{mean } p_{\text{T}}$ for the MPI enriched selection (Fig. 6.17 (e)), but is shifted to lower values for the high thrust one (Fig. 6.18 (e)). It should be noted, that for $\text{mean } p_{\text{T}}$ the mean value within $10 < p_{\text{T}}^Z < 20$ GeV is equal for the low and high thrust selection (e.g. see Fig. 6.14 (f)). But only the mean value for the low thrust events is sufficiently described by POWHEG+PYTHIA8. All other generators are off in both cases.

The MC modelling of individual measurements is further investigated by comparing the measured arithmetic means of the N_{ch} , Σp_{T} , and $\text{mean } p_{\text{T}}$ as functions of p_{T}^Z (right hand column of Fig. 6.16, Fig. 6.17 and Fig. 6.18). None of the MC generators is able to describe the observables over the full range of p_{T}^Z . All generators underestimate the UE activity for the selection on high thrust.

In total POWHEG+PYTHIA8 performs best in describing the MPI enriched events as function of p_{T}^Z , but it diverges from data for $p_{\text{T}}^Z > 80$ GeV. The discrepancy to data increases up to about $p_{\text{T}}^Z = 100$ GeV for the inclusive and low thrust measurement, but then approaches the data for higher values of p_{T}^Z . This indicates, that the hard scatter contributions are not well modelled for the low p_{T}^Z regime, but stabilize for a higher recoil of the Z boson.

SHERPA is in agreement with data for $\langle \text{mean } p_{\text{T}} \rangle$, $p_{\text{T}}^Z < 120$ GeV, in the MPI enriched selection, but it underestimates the activities within all other regions. In the low thrust region, the prediction by SHERPA improves, e.g. for N_{ch} the discrepancy shrinks from about 30% to roughly 10%. SHERPA provides the best description of the data in $\langle \text{mean } p_{\text{T}} \rangle$. It approaches the data with increasing p_{T}^Z , which indicates a better modelling of the contributions from the hard scatter interaction.

For $p_{\text{T}}^Z > 20$ GeV, HERWIG++ predicts a slower rise in the UE activity with rising p_{T}^Z than in the measured distributions. The predictions of HERWIG++ in the trans-min region improve with higher values of p_{T}^Z and also in events of lower T_{\perp} . However, the discrepancy between HERWIG++ and the data in the lowest bins remains regardless of the selected region.

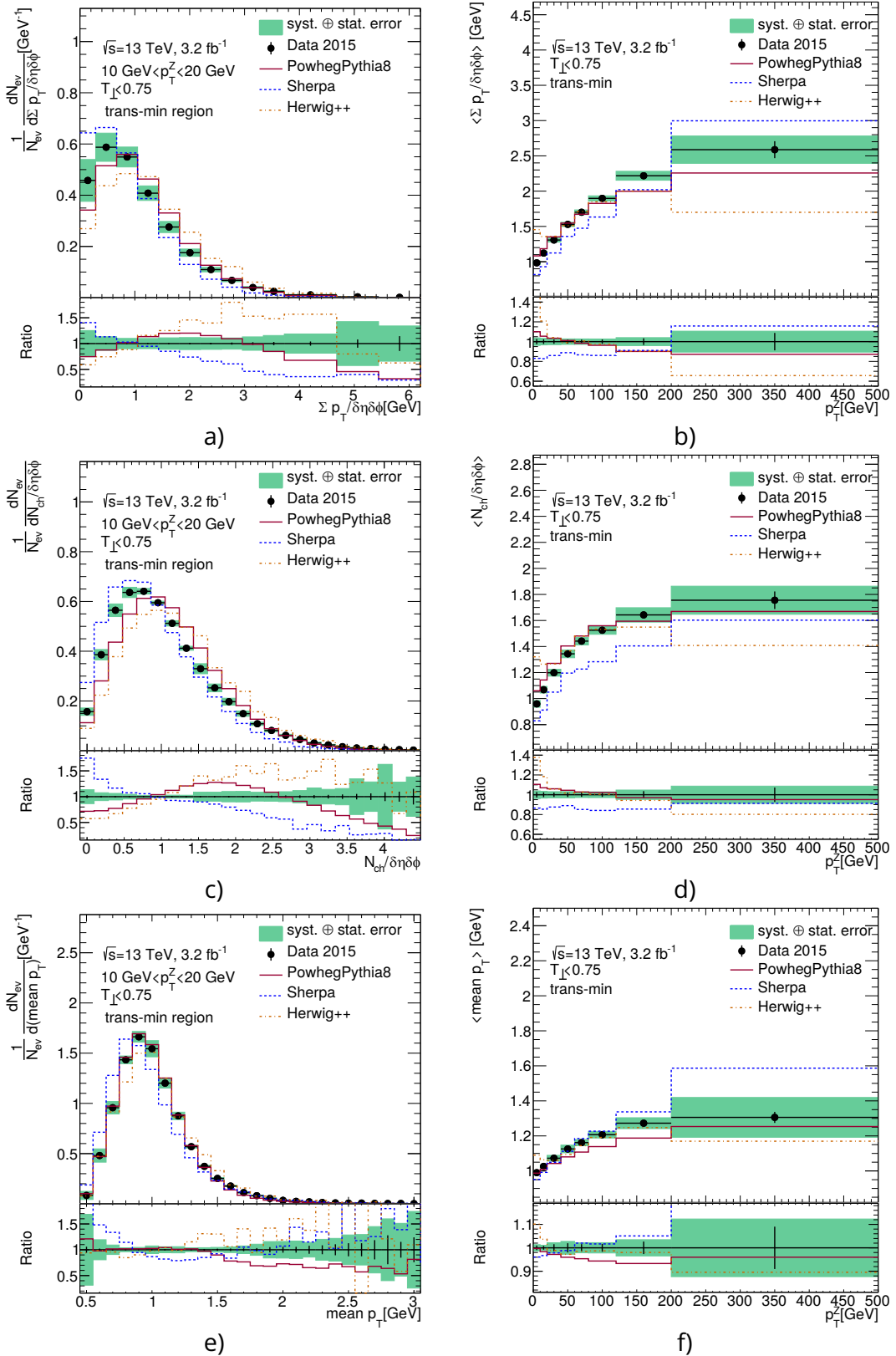


Figure 6.17: The left hand plots present the differential results for $10 < p_T^Z < 20 \text{ GeV}$, compared to the corresponding mean values as a function of p_T^Z in the right column, all with the MPI enriched selection ($T_{\perp} < 0.75$) in the trans-min region. From top to bottom: the sum of transverse momenta, the number of charged particles, and the arithmetic mean of p_T . Predictions of POWHEG+PYTHIA8, SHERPA, and HERWIG++ are compared with the data. The ratios shown are predictions over data.

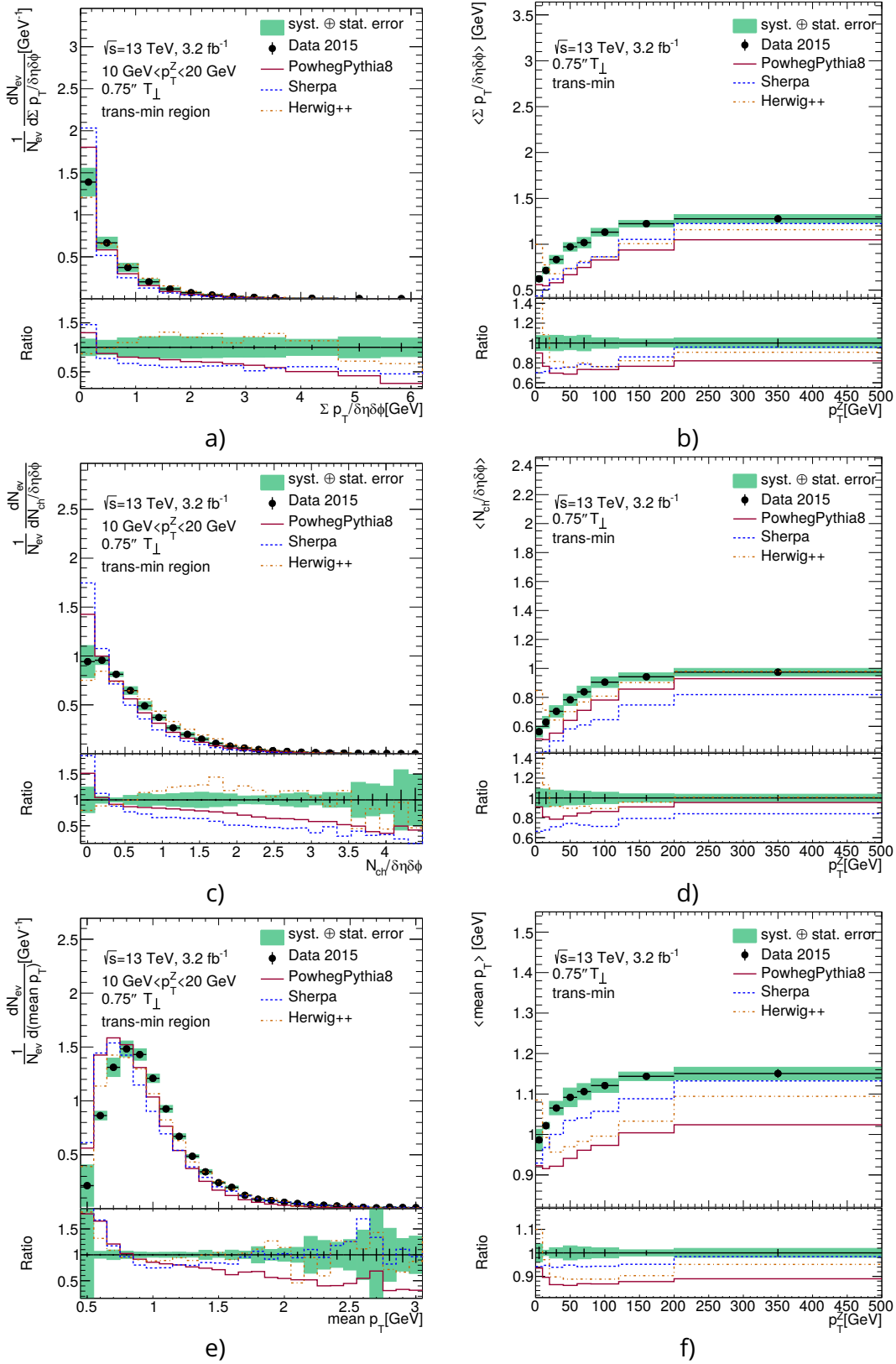


Figure 6.18: The left hand plots present the differential results for $10 < p_T^Z < 20 \text{ GeV}$, compared to the corresponding mean values as a function of p_T^Z in the right column, measured in the trans-min region, all events require $0.75 \leq T_{\perp}$. From top to bottom: the sum of transverse momenta, the number of charged particles, and the arithmetic mean of p_T . Predictions of POWHEG+PYTHIA8, SHERPA, and HERWIG++ are compared with the data. The ratios shown are predictions over data.

Trans-max region

The trans-max region is required to contain a larger value of Σp_T than the trans-min region (cf. Sec. 6.2.1). The trans-max region also includes more charged particles than the trans-min region, because the number of charged particles is directly connected to its Σp_T . The p_T spectrum becomes harder (compare Fig. 6.19 (a) and Fig. 6.15 (a)) and the mean p_T (cf. Fig. 6.20 (e)) rises accordingly compared to the trans-min region. Recoil jets of the Z boson are more likely to leak into the trans-max region, hence it is expected that more charged particles of overall higher p_T are present. These general properties are well reflected in the data and are qualitatively described by all generators. The generator performance is compatible for the trans-max and trans-min region.

One encounters discrepancies of the same order except for the bins representing events of low activity in the differential distributions. POWHEG+PYTHIA8 and especially SHERPA predict for $\Sigma p_T/\delta\eta\delta\phi < 0.6$ GeV (Fig. 6.20 (a)) and $N_{\text{ch}}/\delta\eta\delta\phi < 0.5$ (Fig. 6.20 (c)) almost twice the fraction of events as actually present in data. SHERPA is not able to describe qualitatively the shape of $dN_{\text{ev}}/d(\Sigma p_T/\delta\eta\delta\phi)$ and $dN_{\text{ev}}/d(N_{\text{ch}}/\delta\eta\delta\phi)$, but the underlying causes seem to compensate in $dN_{\text{ev}}/d(\text{mean } p_T)$.

The selection on thrust as well as the dependence on p_T^Z show similar features for POWHEG+PYTHIA8 and HERWIG++ as already pointed out for the trans-min region.

It should be noted that for SHERPA the performance for $\langle \text{mean } p_T \rangle$ alters compared to the trans-min region, when differentiated in thrust. SHERPA is in agreement with data for $\langle \text{mean } p_T \rangle$ in $0.75 \leq T_\perp$ over the full range of p_T^Z (cf. Fig. 6.21 (d)), but constantly overshoots it for $T_\perp < 0.75$. SHERPA first approaches and finally overshoots the data with rising p_T^Z . The strong correlation with p_T^Z indicates, that SHERPA models too hard particles within the ISR, that leak into the trans-min and trans-max regions (see also the tail of Fig. 6.19). The too hard particles within the trans-max region balance the Z boson recoil and create rather spherically balanced events. Hence, this mismodelling is more prominent in the selection with $T_\perp < 0.75$. It compensates the underestimation of the UE activity in bins of low p_T^Z (trans-min), but leads to the overshoot for a higher recoil of the Z boson especially in regions with a naturally higher contribution from ISR (trans-max).

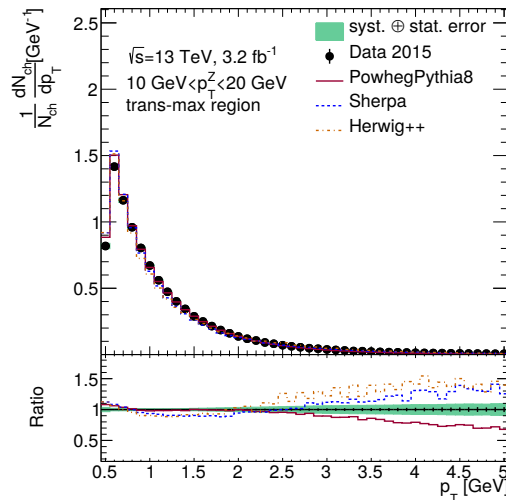


Figure 6.19: Spectrum of the transverse momentum of the charged particles in the trans-max region, inclusive in thrust. Predictions of POWHEG+PYTHIA8, SHERPA, and HERWIG++ are compared with the data. The ratios shown are predictions over data.

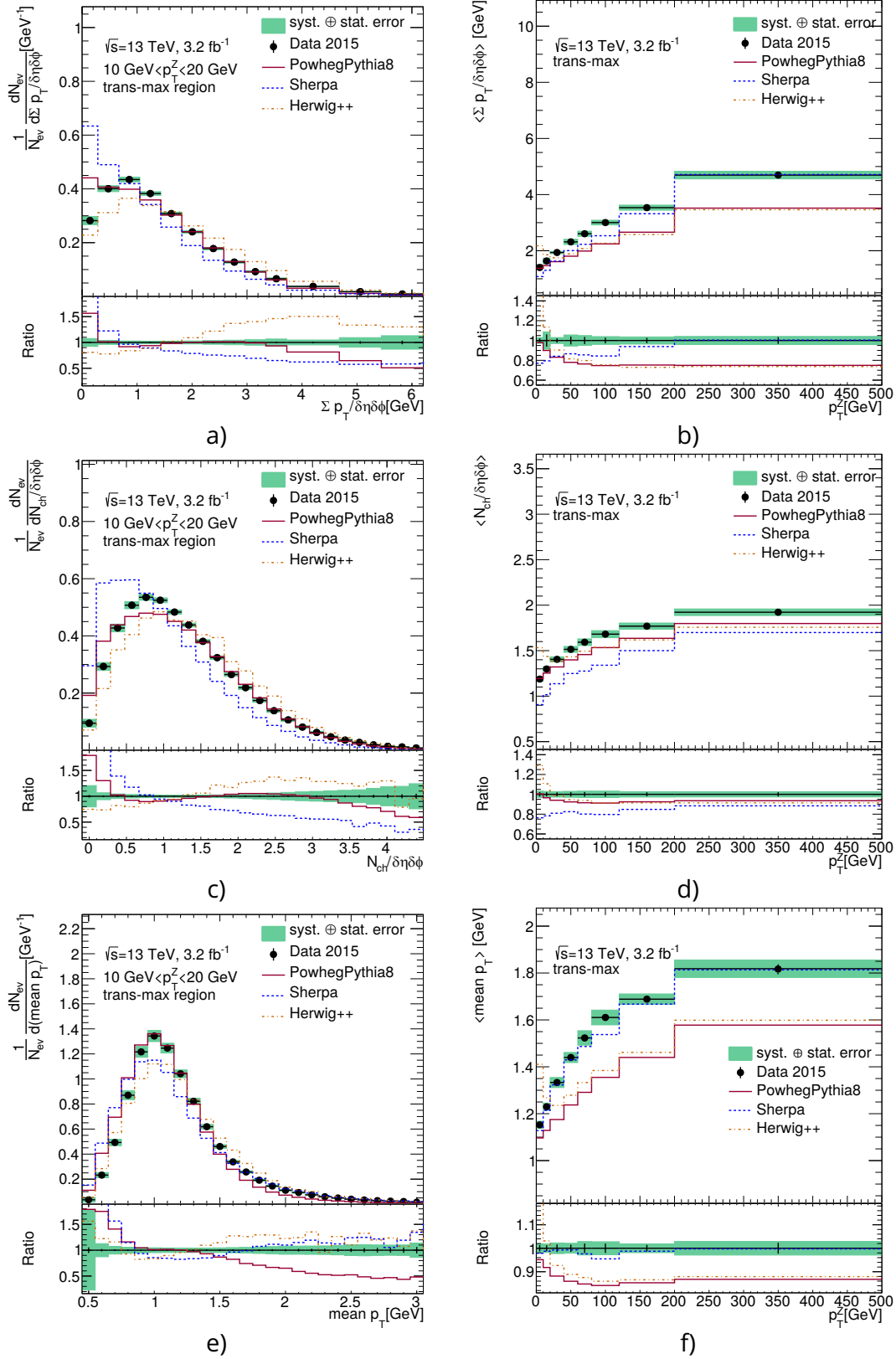


Figure 6.20: The left hand plots present the differential results for $10 < p_T^Z < 20 \text{ GeV}$, compared to the corresponding mean values as a function of p_T^Z in the right column, all inclusive in thrust in the trans-max region. From top to bottom: the sum of transverse momenta, the number of charged particles, and the arithmetic mean of p_T . Predictions of POWHEG+PYTHIA8, SHERPA, and HERWIG++ are compared with the data. The ratios shown are predictions over data.

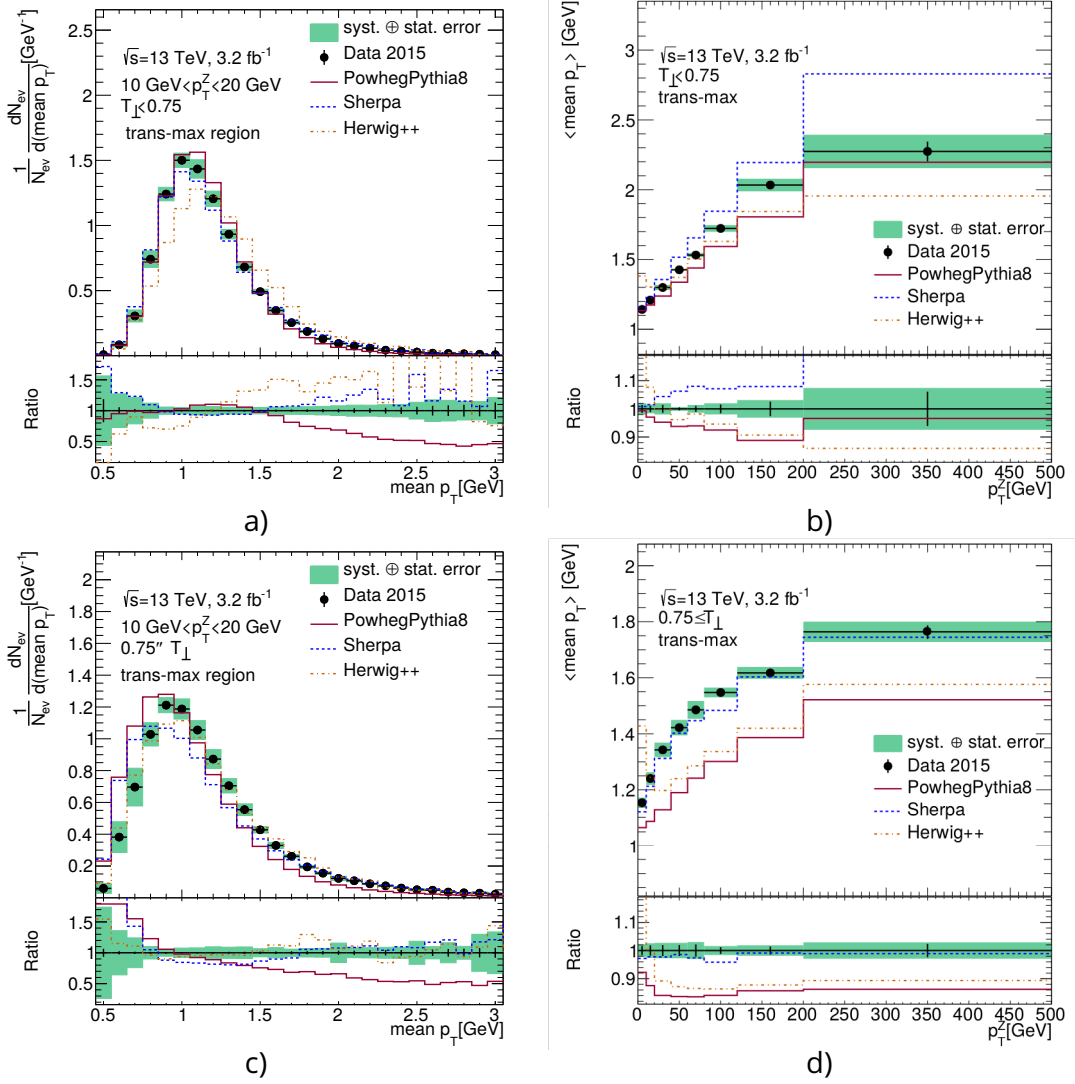


Figure 6.21: The left hand plots present the differential results for $mean\ p_T$ in $10 < p_T^Z < 20$ GeV, compared to the corresponding mean values as a function of p_T^Z in the right column. The top row shows results for the MPI enriched events ($T_{\perp} < 0.75$) and the bottom row for $0.75 \leq T_{\perp}$. Predictions of POWHEG+PYTHIA8, SHERPA, and HERWIG++ are compared with the data. The ratios shown are predictions over data.

Transverse region

The activity in the transverse region is originally referenced as the UE activity [129]. It combines the previously described trans-max and trans-min regions. The main effects stated in the previous paragraphs hold true for the transverse region, too. Hence only a reduced selection of plots is presented, which focuses on the MPI effects. Figure 6.22 highlights that POWHEG+PYTHIA8 performs well in describing the p_T -spectrum for the MPI enriched events, but tends to predict too soft particles for events with $0.75 \leq T_\perp$. No significant effect is visible for SHERPA, but HERWIG++ improves in describing the tail of the p_T distribution for $0.75 \leq T_\perp$.

Figure 6.23 also illustrates the difference between the MPI enriched and rather pencil-shaped events. POWHEG+PYTHIA8 predicts too many particles in the MPI sensitive selection (cf. Fig. 6.23 (a)). This discrepancy relaxes for higher values of p_T^Z (see Fig. 6.23 (b)). It inverts for the opposite selection, $0.75 \leq T_\perp$, where POWHEG+PYTHIA8 predicts too little events (Fig. 6.23 (c) and Fig. 6.23 (d)). SHERPA and HERWIG++ perform consistently for the selection on thrust, while the first generator undershoots and the second one overshoots the number of charged particles for $10 < p_T^Z < 20$ GeV. But HERWIG++ approaches the data for increasing values of p_T^Z .

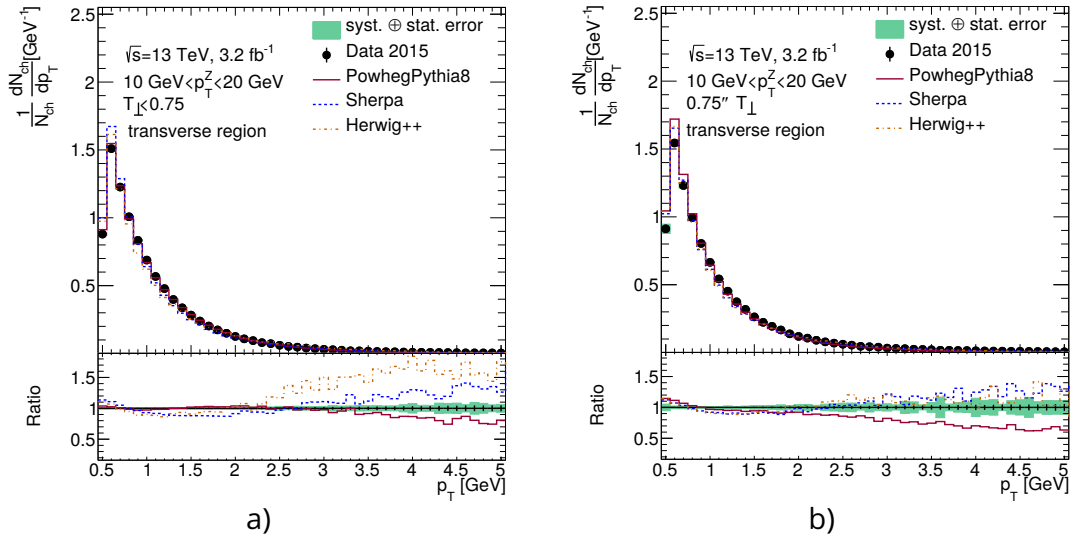


Figure 6.22: Spectrum of the transverse momenta of charged particles in the transverse region with $10 < p_T^Z < 20$ GeV for (a) MPI enriched events ($T_\perp < 0.75$) and (b) events with $0.75 \leq T_\perp$. Predictions of POWHEG+PYTHIA8, SHERPA, and HERWIG++ are compared with the data. The ratios shown are predictions over data.

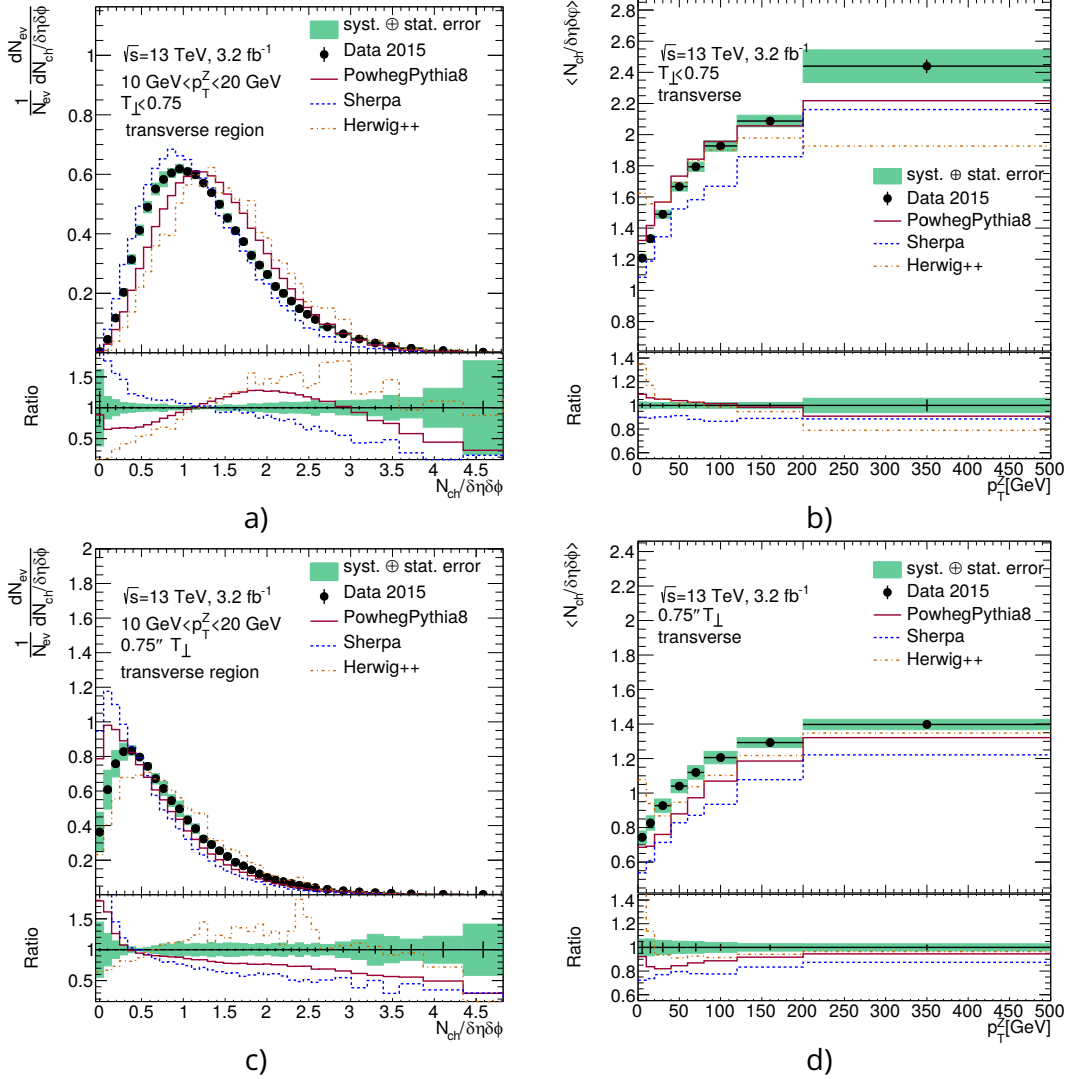


Figure 6.23: The left hand plots present the differential results for N_{ch} in $10 < p_T^Z < 20$ GeV, compared to the corresponding mean values as a function of p_T^Z in the right column. The top row shows results for the MPI enriched events ($T_\perp < 0.75$) and the bottom row for $0.75 \leq T_\perp$. Predictions of POWHEG+PYTHIA8, SHERPA, and HERWIG++ are compared with the data. The ratios shown are predictions over data.

Toward region

The toward region is of similar sensitivity to the UE activity as the trans-min region due to the suppressed contributions from the hard scattering. It is less likely that ISR leaks into the toward region and there is no gluon radiation (FSR) in the leptonic final state. But the effects of the selections in thrust are less dominant than for the trans-min region as already stated in Sec. 6.7.1.

The generator performances are compatible for the trans-min and toward regions. The only meaningful difference appears for the mean values predicted by POWHEG+PYTHIA8: The discrepancy to data grows with increasing p_T^Z (see Fig. 6.24 (a) and Fig. 6.24 (b)) in the toward region, while the divergence ends and levels out for $p_T^Z > 100$ GeV in the trans-min region (see e.g. Fig. 6.16 (d)).

The results of the toward region exemplify the need to investigate the differential distributions of the observables and not only the mean values. SHERPA performs well in describing the $\langle \text{mean } p_T \rangle$, but predicts the differential distribution of $dN_{\text{ev}}/d(\text{mean } p_T)$ too flat for $10 < p_T^Z < 20$ GeV (see Fig. 6.24 (c) and Fig. 6.24 (d)).

Away region

The results measured in the away region are not sensitive to activity of the UE, because they are dominated by the recoiling jets of the Z boson. Nevertheless, they complete the studies of the MC generator performance, as they link to the modelling of these recoiling jets.

All three MC generators perform best in describing the distributions measured in the away region in comparison to the other regions. The performance improves with rising p_T^Z . POWHEG+PYTHIA8 is in agreement with the data for $p_T^Z > 20$ GeV. It describes the $dN_{\text{ch}}/dp_T^{\text{ch}}$ and $\text{mean } p_T$ in the lowest p_T^Z bins, but N_{ch} is predicted too flat in low p_T^Z bins. POWHEG+PYTHIA8 shows the same behaviour in the away region as for the other regions when differentiating in T_{\perp} . Overall POWHEG+PYTHIA8 meets the expectations in the away region with a qualitatively good prediction. POWHEG+PYTHIA8 with the AZNLO-tune is adjusted to describe the p_T^Z -spectrum, hence also the p_T -related observables measured in the away region.

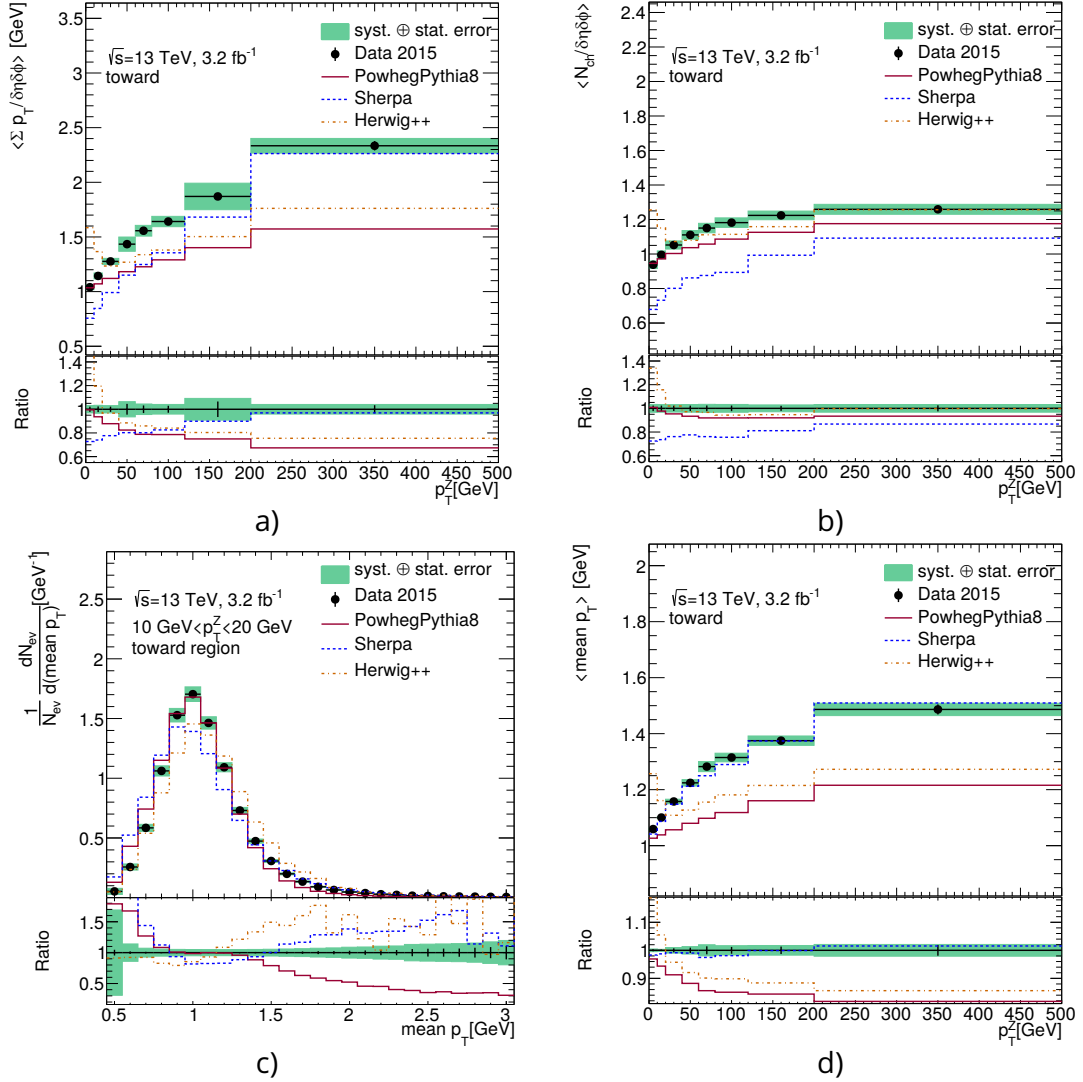


Figure 6.24: Mean sum of transverse momenta (a) and mean number of charged particles (b) in the toward region, inclusive in thrust. (c) The differential results for $\text{mean } p_T$ in $10 < p_T^Z < 20$ GeV and the corresponding (d) arithmetic mean values as function of p_T^Z in the toward region, inclusive in thrust. Predictions of POWHEG+PYTHIA8, SHERPA, and HERWIG++ are compared with the data. The ratios shown are predictions over data.

6.7.3 Comparison with other centre-of-mass energies

Figure 6.25 presents a comparison of the measured $\langle N_{\text{ch}} \rangle$ and $\langle \Sigma p_{\text{T}} \rangle$ for different centre-of-mass energies. The results for $\sqrt{s} = 7$ TeV are taken from the previous ATLAS measurement of the UE activity in Z boson events [130]. The event selection criteria are similar to the analysis presented in this paper, but the previous measurement also includes the $Z \rightarrow e^+e^-$ channel. The CDF measurements at $\sqrt{s} = 1.96$ TeV [152] are also included in the comparison. The CDF analyses used Drell-Yan lepton pairs in a smaller invariant mass window ($70 < m_{\mu\mu} < 110$ GeV) in $p\bar{p}$ collisions. The relative uncertainties of the two ATLAS measurements are of similar sizes, while the CDF measurement suffers from large statistical fluctuations for $p_{\text{T}}^{Z/\mu\mu} > 30$ GeV. All three measurements show qualitatively the same behaviour, i.e. a growing UE activity with higher values of p_{T}^Z . The UE activity further is damped in the high p_{T}^Z region, because effects such as the presence of MPI saturate at a given energy.

Nevertheless, more energy is available for the processes forming the UE when centre-of-mass energy is increased. The PDF contributions from sea quarks and gluons increase with higher energies, which leads to a higher probability of MPI. Hence, the rise of the UE activity as a function of \sqrt{s} is expected.

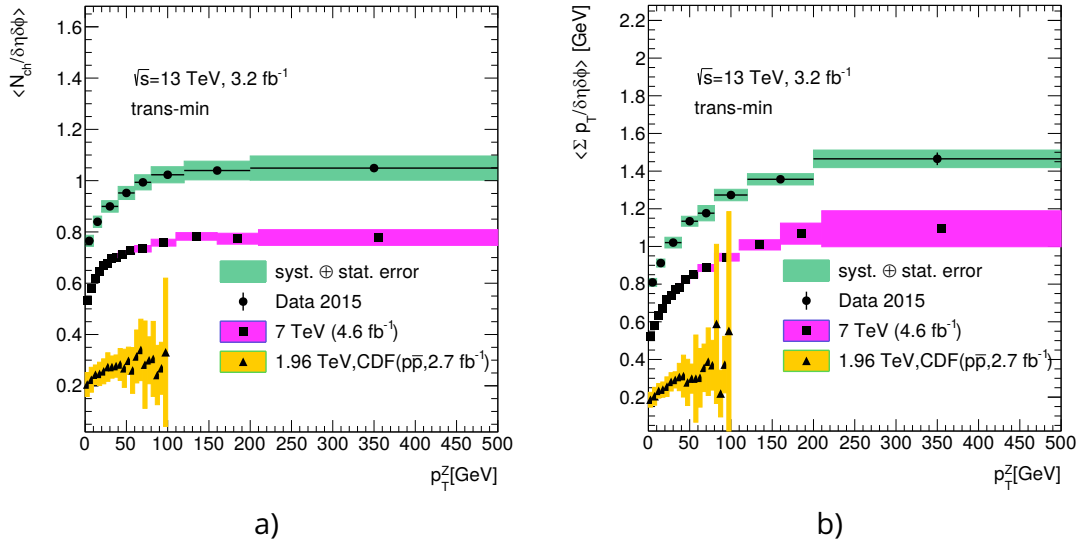


Figure 6.25: The distributions of $\langle N_{\text{ch}} \rangle$ and $\langle \Sigma p_{\text{T}} \rangle$ measured at $\sqrt{s} = 13$ TeV compared with the results of the previous ATLAS measurements at $\sqrt{s} = 7$ TeV [130] and the CDF measurements at $\sqrt{s} = 1.96$ TeV [152]. The error bars correspond to the full uncertainties of the corresponding measurement.

6.8 Conclusion

The previous Sec. 6.7 presents measurements of four observables sensitive to the activity of the UE in $Z \rightarrow \mu\mu$ events using 3.2 fb^{-1} of $\sqrt{s} = 13 \text{ TeV}$ pp collision data collected with the ATLAS detector at the LHC in 2015. Those observables are the transverse momentum spectrum of charged particles, the number of charged particles per event (N_{ch}), the sum of charged-particle p_{T} per event (Σp_{T}), and the mean of charged-particle p_{T} per event ($\langle \text{mean } p_{\text{T}} \rangle$). They are measured in intervals of the Z boson transverse momentum, and in different azimuthal regions of the detector relative to the Z boson direction. The arithmetic means of the distributions are plotted as functions of the p_{T}^Z and further distinguished in regions of transverse thrust or inclusive in transverse thrust.

The predictions from three Monte Carlo generators (POWHEG+PYTHIA8, SHERPA and HERWIG++) are compared with the data. In general, all tested generators and tunes show significant deviations from the data distributions regardless of the observable. The arithmetic means of the observables deduced from the predictions of POWHEG+PYTHIA8 and SHERPA match the main features of the UE activity in the fiducial region. The turn-on effect, i.e. the rising activity as a function of the hard-scatter scale (here p_{T}^Z), is visible as is a saturation of this effect for higher values of p_{T}^Z . In contrast to the other generators, HERWIG++ fails to reproduce the turn-on effect at low p_{T}^Z as it predicts that the UE activity decreases as a function of p_{T}^Z when considered only in the $p_{\text{T}}^Z < 20 \text{ GeV}$ region.

All generators underestimate the activity of the UE when quantified as the arithmetic mean of the observables for inclusive T_{\perp} . The generators are in better agreement with the data for the mean values, when focusing on the MPI sensitive regions. POWHEG+PYTHIA8 matches with the data within the uncertainties for $\langle N_{\text{ch}} \rangle$ and $\langle \Sigma p_{\text{T}} \rangle$, which indicates an adequate handling of the MPI activity. However, the simulation needs to be improved for other sources of UE activity, because predictive power of POWHEG+PYTHIA8 shrinks for the region with $0.75 \leq T_{\perp}$ in comparison to the inclusive measurement. Reference [136] points out that this selection is dominated by extra jet activity, which yields a first indication for a possible improvement of the Monte-Carlo generator prediction. This conclusion is valid for POWHEG+PYTHIA8 in various regions of p_{T}^Z .

The performance of HERWIG++ is consistent for $p_{\text{T}}^Z > 20 \text{ GeV}$ in comparison with the measurements at $\sqrt{s} = 7 \text{ TeV}$ [130]. Both measurements use the energy-extrapolation tunes [141] provided by the HERWIG++ authors, i.e. UE-EE-3 for $\sqrt{s} = 7 \text{ TeV}$ and in the analysis presented here UE-EE-5. The latter tune was additionally validated against Tevatron and LHC measurements at $\sqrt{s} = 900 \text{ GeV}$ and $\sqrt{s} = 7 \text{ TeV}$ [153]. The prediction of HERWIG++ is slightly better for the distributions of $\langle N_{\text{ch}} \rangle$ and $\langle \Sigma p_{\text{T}} \rangle$ at higher values of p_{T}^Z . In the previous measurements, the divergence increased with p_{T}^Z , which might be related to improper modelling of the impact parameter. Apart from overestimating the mean activity, HERWIG++ improved relative to the $\sqrt{s} = 7 \text{ TeV}$ measurements in the description of the shape of differential distributions in the presented p_{T}^Z -bins. Qualitatively it performs better than the other two generators.

POWHEG+PYTHIA8 performs as well at $\sqrt{s} = 13 \text{ TeV}$ as it does at $\sqrt{s} = 7 \text{ TeV}$, but it is tuned with AU2⁵ in the previous measurements. Nevertheless, this indicates that the MPI energy extrapolation of PYTHIA8 works well, which is in agreement with the better description for distributions at low T_{\perp} . On the other hand, POWHEG+PYTHIA8 generally predicted too many charged particles within the UE, while their p_{T} spectrum is in good agreement with the data. Possible tuning efforts could therefore address the hadronization model or the implementation of the splitting functions.

⁵AU2 tunes only the MPI part by using ATLAS $\sqrt{s} = 7 \text{ TeV}$ UE data.

While SHERPA version 1.4.0 with the CT10 PDF set consistently overestimates the UE activity metrics $\langle N_{\text{ch}} \rangle$ and $\langle \Sigma p_{\text{T}} \rangle$ at $\sqrt{s} = 7$ TeV by 5% to 15%, the present analysis and SHERPA version reveal a continuous underestimation. The discrepancy relative to the data decreases with higher values of p_{T}^Z for the measurement at $\sqrt{s} = 13$ TeV. SHERPA therefore requires major tuning in the low momentum regime.

All in all, the three generators offer great potential for future tuning efforts. The findings of the presented work need now to be incorporated in the corresponding models by theory experts. POWHEG+PYTHIA8 already provides an adequate modelling of MPI contributions, and could therefore serve as the mean of choice for precision measurements, which are sensitive to the UE activity. The measurement of the hadronic recoil is the example promoted in this thesis. The better description of the UE activity will allow to further optimize the determination of hadronic recoil of the W boson and subsequently lower the corresponding uncertainties on the measurement of m_W .

7.

Conclusion and final remarks

This thesis is dedicated to the measurement of the parameters of the W boson with highest possible precision. The results of the first part in Chapter 5 lead the way to an improved measurement of m_W and the first measurement of Γ_W with LHC data at $\sqrt{s} = 7$ TeV. The central part of the enhanced precision is the introduced PLH fit approach, which replaces the legacy fit based on χ^2 -minimization. Both approaches are successfully validated against each other as a first proof of the applicability of the new functionality. The advantage of the PLH fit is the direct incorporation of the systematic uncertainties as NP into the fit process. The PLH fit approach is able to improve the modelling uncertainties related to the choice of the PDF set by about 2 MeV to 5 MeV compared to the legacy measurement. The new results are:

$$\begin{aligned} m_W(p_T^\mu) &= 80\,372.6 \pm 19.1 \text{ MeV} \\ m_W(m_T) &= 80\,365.6 \pm 22.1 \text{ MeV} \end{aligned} \quad (7.1)$$

Figure 7.1 illustrates the comparison to the world average, the electroweak fit result and the legacy measurement. The presented results will drag the world average towards the electroweak fit result. The successful uncertainty reduction suggests to transfer the new fit approach also to the ongoing measurements of m_W at $\sqrt{s} = 5.02$ TeV and $\sqrt{s} = 13$ TeV. The same technique is exploited to measure the decay

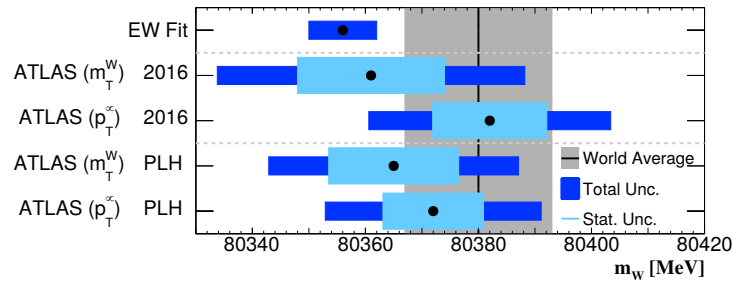


Figure 7.1: Overview of the results for the legacy ATLAS measurement of m_W (2016) [72] compared to the results of this thesis using the PLH fit (PLH). The grey area presents the world average of $m_W^{global} = 80380 \pm 13$ MeV and the first entry displays the value of the electroweak fit $m_W^{EW} = 80356 \pm 6$ MeV [27].

width of the W boson. The value of Γ_W is determined with a fit to the distributions of p_T^μ . The resulting precision already competes with the uncertainty of the current world average, although further improvements are anticipated. The blinded result with a preliminary set of profiled systematic uncertainties is:

$$\Gamma_W(p_T^\mu) = 2\,165.5(+blinding) \pm 29.3 \text{ MeV} \quad (7.2)$$

The results for m_W and Γ_W are currently under review within the ATLAS Collaboration. Given the various possible improvements, such as reduced uncertainties related to the choice of the PDF set or the extension of the investigated fit range, it is expected, that two new world leading precision measurements on the properties of the W boson will

be published within the coming months. Moreover, both measurements indicate, that a precision compatible to the electroweak global fit in case of m_W or the world average in case of Γ_W is reachable, which is remarkable for a hadron collider measurement.

Both measurements will further benefit from the measurement of the activity of the UE, which is presented in the second part of this thesis in Chapter 6. The modelling of the UE activity limits the precision of the hadronic recoil measurement, which is fundamental to the measurements of m_W and Γ_W .

The presented measurements of the UE activity are designed to have an enhanced sensitivity to MPI in pp collisions by a selection in transverse thrust. Hence, they provide insight into the structure and long-range low-momentum scale interactions of the proton. The results are presented as unfolded differential cross-sections for charged particle multiplicity and charged particle transverse momentum in regions of azimuth measured with respect to the Z boson direction. None of the presented theory predictions is able to describe the data. These discrepancies highlight the importance of improved tunes of Monte-Carlo generators based on this measurement. Additionally, more fundamental changes or even new approaches to simulate the UE should be considered.

The combination of both parts of this thesis contributes to a better understanding of the major uncertainties, which limit the precision of the experimental value of m_W . The finalized measurements will reinforce the sensitivity and significance of the electroweak fit and the consistency of the SM, and therefore possibly hint to signs of new physics beyond the SM. In any case, they will shape our knowledge of the SM.



Acknowledgement

... There are many people, whom I have to thank for my chance to work at the frontier of human knowledge. I never forget, that the creation of this thesis is a privilege, which is made possible by the wealth of our society and my fortune to be part of it.

Nevertheless, there are extraordinary individuals, who supported me in different manners. I give thanks to my wife, who showed me, that there is more to the world than physical laws. I am grateful for my parents, who empowered me with the skills required to cope such a project. And I thank my sister and grandparents, who challenged me to translate the secrets of the ivory tower named particle physics.

There are plenty of people, who contributed in several ways to the richness of this thesis. First of all, all members of the Lichtenberg Group, who made it more than standard modelled physics. I thank my supervisor [REDACTED] for providing the bigger picture in the abundant tasks, cross checks and flood of numbers. Special thanks goes to the professional programmers of our working group, [REDACTED] and [REDACTED]. Without you I would still be fighting software issues instead of exploring results. I thank [REDACTED] for sharing the adventure in the measurement of the W mass. [REDACTED] deserves my thanks for all his contributions to the measurement of the underlying event and who provided help beyond his contract bounds. I am grateful for the chance to experience a new scientific culture at SLAC. I thank [REDACTED], who made this such an rewarding experience.



Part III
Appendix



Bibliography

- [1] ATLAS Collaboration, "Observation of a new particle in the search for the Standard Model Higgs boson with the ATLAS detector at the LHC," *Phys. Lett.*, vol. B716, pp. 1–29, 2012.
- [2] CMS Collaboration, "Observation of a new boson at a mass of 125 GeV with the CMS experiment at the LHC," *Phys. Lett.*, vol. B716, pp. 30–61, 2012.
- [3] ATLAS Collaboration, "Measurement of distributions sensitive to the underlying event in inclusive Z boson production in pp collisions at $\sqrt{s} = 13$ TeV with the ATLAS detector," *The European Physical Journal C*, vol. 79, no. 8.
- [4] P. A. Dirac, "On the Theory of quantum mechanics," *Proc. Roy. Soc. Lond. A*, vol. A112, pp. 661–677, 1926.
- [5] A. Bellerive, "Review of solar neutrino experiments," *Int. J. Mod. Phys. A*, vol. 19, pp. 1167–1179, 2004.
- [6] P. W. Higgs, "Broken symmetries and the masses of gauge bosons," *Phys. Rev. Lett.*, vol. 13, pp. 508–509, Oct 1964.
- [7] David Galbraith and Carsten Burgard, "A standard diagram of the current standard model of physics," *CERN Bulletin*, vol. 35, August 2012. Programmed in TikZ by Carsten Burgard during Webfest 2012 @CERN.
- [8] R. P. Feynman, "The Theory of positrons," *Phys. Rev.*, vol. 76, pp. 749–759, 1949.
- [9] M. E. Peskin and D. V. Schroeder, *An introduction to quantum field theory*. Reading, Mass. [et.al.]: CRC Press, 5., (corr.) printing ed., 1997.
- [10] C. S. Wu, E. Ambler, R. W. Hayward, D. D. Hoppes, and R. P. Hudson, "Experimental test of parity conservation in beta decay," *Phys. Rev.*, vol. 105, pp. 1413–1415, Feb 1957.
- [11] F. Englert and R. Brout, "Broken symmetry and the mass of gauge vector mesons," *Phys. Rev. Lett.*, vol. 13, pp. 321–323, Aug 1964.
- [12] M. Gell-Mann, "A Schematic Model of Baryons and Mesons," *Phys. Lett.*, vol. 8, pp. 214–215, 1964.
- [13] G. Zweig, "An SU(3) model for strong interaction symmetry and its breaking. Version 1," *CDS*, 1 1964.
- [14] J. C. Collins and D. E. Soper, "Parton distribution and decay functions," *Nuclear Physics B*, vol. 194, no. 3, pp. 445 – 492, 1982.
- [15] J. C. Collins, D. E. Soper, and G. F. Sterman, "Factorization of Hard Processes in QCD," 1989.
- [16] G. Altarelli and G. Parisi, "Asymptotic Freedom in Parton Language," *Nucl. Phys. B*, vol. 126, pp. 298–318, 1977.

- [17] V. Gribov and L. Lipatov, "Deep inelastic $e p$ scattering in perturbation theory," *Sov. J. Nucl. Phys.*, vol. 15, pp. 438–450, 1972.
- [18] Y. L. Dokshitzer, "Calculation of the Structure Functions for Deep Inelastic Scattering and $e^+ e^-$ Annihilation by Perturbation Theory in Quantum Chromodynamics," *Sov. Phys. JETP*, vol. 46, pp. 641–653, 1977.
- [19] A. Vogt, S. Moch, and J. Vermaseren, "The Three-loop splitting functions in QCD: The Singlet case," *Nucl. Phys. B*, vol. 691, pp. 129–181, 2004.
- [20] H. Abramowicz *et al.*, "Combination of measurements of inclusive deep inelastic $e^\pm p$ scattering cross sections and QCD analysis of HERA data," *Eur. Phys. J. C*, vol. 75, no. 12, p. 580, 2015.
- [21] A. Cooper-Sarkar and K. Wichmann, "QCD analysis of the ATLAS and CMS W^\pm and Z cross-section measurements and implications for the strange sea density," *Phys. Rev. D*, vol. 98, no. 1, p. 014027, 2018.
- [22] T.-J. Hou *et al.*, "New CTEQ global analysis of quantum chromodynamics with high-precision data from the LHC," 12 2019.
- [23] A. D. Martin, W. J. Stirling, R. S. Thorne, and G. Watt, "Parton distributions for the LHC," *Eur. Phys. J.*, vol. C63, pp. 189–285, 2009.
- [24] Y. Fukuda *et al.*, "Evidence for oscillation of atmospheric neutrinos," *Phys. Rev. Lett.*, vol. 81, pp. 1562–1567, 1998.
- [25] V. C. Rubin and J. Ford, W. Kent, "Rotation of the Andromeda Nebula from a Spectroscopic Survey of Emission Regions," *Astrophysical Journal*, vol. 159, p. 379, Feb. 1970. Provided by the SAO/NASA Astrophysics Data System.
- [26] M. Markevitch, A. Gonzalez, D. Clowe, A. Vikhlinin, L. David, W. Forman, C. Jones, S. Murray, and W. Tucker, "Direct constraints on the dark matter self-interaction cross-section from the merging galaxy cluster 1E0657-56," *Astrophys. J.*, vol. 606, pp. 819–824, 2004.
- [27] J. Erler and M. Schott, "Electroweak Precision Tests of the Standard Model after the Discovery of the Higgs Boson," *Prog. Part. Nucl. Phys.*, vol. 106, pp. 68–119, 2019.
- [28] M. Awramik, M. Czakon, A. Freitas, and G. Weiglein, "Precise prediction for the w -boson mass in the standard model," *Phys. Rev. D*, vol. 69, p. 053006, Mar 2004.
- [29] A. Sirlin, "Radiative corrections in the $SU(2)_L \times U(1)$ theory: A simple renormalization framework," *Phys. Rev. D*, vol. 22, pp. 971–981, Aug 1980.
- [30] G. Pásztor, "Precision tests of the Standard Model at the LHC with the ATLAS and CMS detectors," *PoS*, vol. FFK2019, p. 005. 14 p, 2019.
- [31] S. Schael *et al.*, "Precision electroweak measurements on the Z resonance," *Phys. Rept.*, vol. 427, pp. 257–454, 2006.
- [32] F. Marcastel, "CERN's Accelerator Complex. La chaîne des accélérateurs du CERN." General Photo, Oct 2013.
- [33] CERN, *CAS - CERN Accelerator School: Intermediate Course on Accelerator Physics*, (Geneva), CERN, 2006.

- [34] J. Pequenaο, "Computer generated image of the whole ATLAS detector." General Photo, Mar 2008.
- [35] M. Schott and M. Dunford, "Review of single vector boson production in pp collisions at $\sqrt{s} = 7$ TeV," *Eur. Phys. J.*, vol. C74, p. 2916, 2014.
- [36] J. Pequenaο, "Computer generated image of the ATLAS inner detector." General Photo, Mar 2008.
- [37] ATLAS Collaboration, "ATLAS pixel detector electronics and sensors," *JINST*, vol. 3, p. P07007, 2008.
- [38] ATLAS Collaboration, "ATLAS Insertable B-Layer Technical Design Report." ATLAS-TDR-19, 2010.
- [39] ATLAS Collaboration, "Operation and performance of the ATLAS semiconductor tracker," *JINST*, vol. 9, p. P08009, 2014.
- [40] ATLAS Collaboration, "Performance of the ATLAS Transition Radiation Tracker in Run 1 of the LHC: tracker properties," *JINST*, vol. 12, p. P05002, 2017.
- [41] J. Pequenaο, "Computer generated image of the ATLAS Muons subsystem." General Photo, Mar 2008.
- [42] J. Pequenaο and P. Schaffner, "How ATLAS detects particles: diagram of particle paths in the detector." General Photo, Jan 2013.
- [43] ATLAS Collaboration, "Concepts, Design and Implementation of the ATLAS New Tracking (NEWT)," *CDS*, 3 2007.
- [44] R. Fruhwirth, "Application of Kalman filtering to track and vertex fitting," *Nucl. Instrum. Meth. A*, vol. 262, pp. 444-450, 1987.
- [45] T. G. Cornelissen, M. Elsing, I. Gavrilenko, J. Laporte, W. Liebig, M. Limper, K. Nikolopoulos, A. Poppleton, and A. Salzburger, "The global χ^2 track fitter in ATLAS," *J. Phys. Conf. Ser.*, vol. 119, p. 032013, 2008.
- [46] M. Cacciari, G. P. Salam, and G. Soyez, "The anti- k_t jet clustering algorithm," *JHEP*, vol. 04, p. 063, 2008.
- [47] ATLAS Collaboration, "Performance of the ATLAS Trigger System in 2010," *Eur. Phys. J. C*, vol. 72, p. 1849, 2012.
- [48] ATLAS Collaboration, "Performance of the ATLAS Trigger System in 2015," *Eur. Phys. J. C*, vol. 77, p. 317. 76 p, Nov 2016.
- [49] T. Sjöstrand, S. Mrenna, and P. Z. Skands, "PYTHIA 6.4 physics and manual," *JHEP*, vol. 05, p. 026, 2006.
- [50] T. Sjöstrand, S. Mrenna, and P. Z. Skands, "A brief introduction to PYTHIA 8.1," *Comput. Phys. Commun.*, vol. 178, pp. 852-867, 2008.
- [51] T. Gleisberg, S. Hoeche, F. Krauss, M. Schonherr, S. Schumann, F. Siegert, and J. Winter, "Event generation with SHERPA 1.1," *JHEP*, vol. 02, p. 007, 2009.
- [52] M. Bähr *et al.*, "Herwig++ physics and manual," *Eur. Phys. J. C*, vol. 58, pp. 639-707, 2008.

- [53] J. Alwall, R. Frederix, S. Frixione, V. Hirschi, F. Maltoni, O. Mattelaer, H. S. Shao, T. Stelzer, P. Torrielli, and M. Zaro, "The automated computation of tree-level and next-to-leading order differential cross sections, and their matching to parton shower simulations," *JHEP*, vol. 07, p. 079, 2014.
- [54] S. Alioli, P. Nason, C. Oleari, and E. Re, "NLO vector-boson production matched with shower in POWHEG," *JHEP*, vol. 07, p. 060, 2008.
- [55] F. Siegert, *Monte-Carlo event generation for the LHC*. PhD thesis, Institute for Particle Physics Phenomenology, Durham University, 9 2010.
- [56] C. Patrignani *et al.*, "Review of Particle Physics," *Chin. Phys.*, vol. C40, no. 10, p. 100001, 2016.
- [57] B. Andersson, S. Mohanty, and F. Soderberg, "Recent developments in the Lund model," in *36th Annual Winter School on Nuclear and Particle Physics (PINP 2002) and 8th St. Petersburg School on Theoretical Physics*, 12 2002.
- [58] R. D. Field and S. Wolfram, "A QCD Model for e^+e^- Annihilation," *Nucl. Phys. B*, vol. 213, pp. 65–84, 1983.
- [59] P. Bartalini and L. Fano, eds., *Proceedings, 1st International Workshop on Multiple Partonic Interactions at the LHC (MPlo8): Perugia, Italy, October 27-31, 2008*, (Hamburg), DESY, June 2009.
- [60] T. Sjostrand and M. van Zijl, "A Multiple Interaction Model for the Event Structure in Hadron Collisions," *Phys. Rev. D*, vol. 36, p. 2019, 1987.
- [61] D. Acosta *et al.*, "The underlying event in hard interactions at the Tevatron $\bar{p}p$ collider," *Phys. Rev. D*, vol. 70, p. 072002, 2004.
- [62] M. Bahr, J. M. Butterworth, and M. H. Seymour, "The Underlying Event and the Total Cross Section from Tevatron to the LHC," *JHEP*, vol. 01, p. 065, 2009.
- [63] S. Agostinelli *et al.*, "GEANT4—A simulation toolkit," *Nucl. Instrum. Meth. A*, vol. 506, pp. 250–303, 2003.
- [64] ATLAS Collaboration, "Early Inner Detector Tracking Performance in the 2015 data at $\sqrt{s} = 13$ TeV," Tech. Rep. ATL-PHYS-PUB-2015-051, CERN, Geneva, Dec 2015.
- [65] ATLAS Collaboration, "Charged-particle distributions in $\sqrt{s}=13$ TeV pp interactions measured with the ATLAS detector at the LHC," Tech. Rep. ATLAS-CONF-2015-028, CERN, Geneva, Jul 2015.
- [66] ATLAS Collaboration, "Studies of the ATLAS Inner Detector material using $\sqrt{s} = 13$ TeV pp collision data," Tech. Rep. ATL-PHYS-PUB-2015-050, CERN, Geneva, Nov 2015.
- [67] ATLAS Collaboration, "Alignment of the ATLAS Inner Detector with the initial LHC data at $\sqrt{s} = 13$ TeV," Tech. Rep. ATL-PHYS-PUB-2015-031, CERN, Geneva, Jul 2015.
- [68] ATLAS Collaboration, "Study of alignment-related systematic effects on the ATLAS Inner Detector tracking," Tech. Rep. ATLAS-CONF-2012-141, CERN, Geneva, Oct 2012.
- [69] ATLAS Collaboration, "Muon reconstruction performance of the atlas detector in proton–proton collision data at $\sqrt{s} = 13$ tev," *The European Physical Journal C*, vol. 76, p. 292, May 2016.

- [70] ATLAS Collaboration, "Measurement of the muon reconstruction performance of the ATLAS detector using 2011 and 2012 LHC proton–proton collision data," *Eur. Phys. J.*, vol. C74, no. 11, p. 3130, 2014.
- [71] C. Grupen and B. Shwartz, "Particle detectors," 2008.
- [72] ATLAS Collaboration, "Measurement of the W -boson mass in pp collisions at $\sqrt{s} = 7$ TeV with the ATLAS detector," *Eur. Phys. J. C*, vol. 78, no. 2, p. 110, 2018. [Erratum: *Eur.Phys.J.C* 78, 898 (2018)].
- [73] N. Vranjes, T. Petersen, and M. Karnevskiy, "Measurement of m_W at 7 TeV: Muon momentum corrections and uncertainties," Tech. Rep. ATL-COM-PHYS-2014-1433, CERN, Geneva, Nov 2014.
- [74] C. Zimmermann, M. Schott, and M. Karnevskiy, "Measurement of m_W at 7 TeV : Muon efficiency corrections and uncertainties," Tech. Rep. ATL-COM-PHYS-2015-073, CERN, Geneva, Feb 2015.
- [75] W. Buttinger, "Using Event Weights to account for differences in Instantaneous Luminosity and Trigger Prescale in Monte Carlo and Data," Tech. Rep. ATL-COM-SOFT-2015-119, CERN, Geneva, May 2015.
- [76] ATLAS Collaboration, "Measurement of the Inelastic Proton–Proton Cross Section at $\sqrt{s} = 13$ TeV with the ATLAS Detector at the LHC," *Phys. Rev. Lett.*, vol. 117, p. 182002, 2016.
- [77] ATLAS collaboration, "Performance of primary vertex reconstruction in proton–proton collisions at $\sqrt{s} = 7$ TeV in the ATLAS experiment," in *35th International Conference on High Energy Physics, Paris, France, 22 - 28 Jul 2010, 7 2010*.
- [78] S. Schael *et al.*, "Electroweak Measurements in Electron-Positron Collisions at W-Boson-Pair Energies at LEP," *Phys. Rept.*, vol. 532, pp. 119–244, 2013.
- [79] CDF Collaboration, "Combination of CDF and Do W -Boson Mass Measurements," 2013.
- [80] N. Besson, M. Boonekamp, E. Klinkby, T. Petersen, and S. Mehlhase, "Re-evaluation of the LHC potential for the measurement of M_W ," *Eur. Phys. J. C*, vol. 57, pp. 627–651, 2008.
- [81] ATLAS Collaboration, "Measurement of the production of a W boson in association with a charm quark in pp collisions at $\sqrt{s} = 7$ TeV with the ATLAS detector," *JHEP*, vol. 05, p. 068, 2014.
- [82] S. Amoroso *et al.*, "Les Houches 2019: Physics at TeV Colliders: Standard Model Working Group Report," in *11th Les Houches Workshop on Physics at TeV Colliders: PhysTeV Les Houches*, 3 2020.
- [83] A. Denner and T. Sack, "The W boson width," *Z. Phys. C*, vol. 46, pp. 653–663, 1990.
- [84] D. Kara, "Corrections of Order $\alpha\alpha_s$ to W Boson Decays," *Nucl. Phys.*, vol. B877, pp. 683–718, 2013.
- [85] P. Renton, "Updated SM calculations of σ_W / σ_Z at the Tevatron and the W boson width," 2008.

- [86] CDF Collaboration, "A Direct measurement of the W boson width in $p\bar{p}$ collisions at $\sqrt{s} = 1.96\text{-TeV}$," *Phys. Rev. Lett.*, vol. 100, p. 071801, 2008.
- [87] CDF Collaboration, "First measurement of the W boson mass in Run II of the Tevatron," *Phys. Rev. Lett.*, vol. 99, p. 151801, 2007.
- [88] C. A. Pruneau, "Data analysis techniques for physical scientists," 2017.
- [89] Do Collaboration, "Measurement of the W Boson Mass," *Phys. Rev. Lett.*, vol. 103, p. 141801, Oct 2009.
- [90] ATLAS Collaboration, "Improved luminosity determination in pp collisions at $\sqrt{s} = 7\text{ TeV}$ using the ATLAS detector at the LHC," *Eur. Phys. J. C*, vol. 73, p. 2518, 2013.
- [91] S. Alioli, P. Nason, C. Oleari, and E. Re, "A general framework for implementing NLO calculations in shower Monte Carlo programs: the POWHEG BOX," *JHEP*, vol. 06, p. 043, 2010.
- [92] J. Pumplin, D. R. Stump, J. Huston, H. L. Lai, P. M. Nadolsky, and W. K. Tung, "New Generation of Parton Distributions with Uncertainties from Global QCD Analysis," *JHEP*, vol. 07, p. 012, 2002.
- [93] ATLAS Collaboration, "Measurement of the Z/γ^* boson transverse momentum distribution in pp collisions at $\sqrt{s} = 7\text{ TeV}$ with the ATLAS detector," *JHEP*, vol. 09, p. 145, 2014.
- [94] P. Golonka and Z. Was, "PHOTOS Monte Carlo: A precision tool for QED corrections in Z and W decays," *Eur. Phys. J. C*, vol. 45, pp. 97–107, 2006.
- [95] ATLAS Collaboration, "The ATLAS Simulation Infrastructure," *Eur. Phys. J. C*, vol. 70, p. 823, 2010.
- [96] ATLAS Collaboration, "Further ATLAS tunes of PYTHIA6 and Pythia 8," 11 2011.
- [97] ATLAS Collaboration, "Measurement of the jet fragmentation function and transverse profile in proton–proton collisions at a center-of-mass energy of 7 TeV with the ATLAS detector," *Eur. Phys. J. C*, vol. 71, p. 1795, 2011.
- [98] ATLAS Collaboration, "Precision measurement and interpretation of inclusive W^+ , W^- and Z/γ^* production cross sections with the ATLAS detector," *Eur. Phys. J. C*, vol. 77, p. 367, 2017.
- [99] D. Bardin, A. Leike, T. Riemann, and M. Sachwitz, "Energy Dependent Width Effects in $e^+ e^-$ Annihilation Near the Z Boson Pole," *Phys. Lett. B*, vol. 206, pp. 539–542, 1988.
- [100] N. Andari, J.-B. Blanchard, M. Boonekamp, S. Camarda, A. Dimitrievska, R. Hanna, C. Hays, M. Karnevskiy, O. Kivernyk, M. Schott, G. Siragusa, R. Stroehmer, N. Vranjes, S. Webb, and C. Zimmermann, "Measurement of m_W with 7 TeV data: W boson mass measurement," Tech. Rep. ATL-COM-PHYS-2014-1569, CERN, Geneva, Dec 2014.
- [101] R. Gauld, A. Gehrmann-De Ridder, T. Gehrmann, E. Glover, and A. Huss, "Precise predictions for the angular coefficients in Z -boson production at the LHC," *JHEP*, vol. 11, p. 003, 2017.

- [102] C. Calame, M. Chiesa, H. Martinez, G. Montagna, O. Nicosini, F. Piccinini, and A. Vicini, "Precision Measurement of the W-Boson Mass: Theoretical Contributions and Uncertainties," *Physical Review D*, vol. 96, 12 2016.
- [103] A. Arbuzov, D. Bardin, S. Bondarenko, P. Christova, L. Kalinovskaya, G. Nanava, and R. Sadykov, "One-loop corrections to the Drell-Yan process in SANC. I. The Charged current case," *Eur. Phys. J. C*, vol. 46, pp. 407–412, 2006. [Erratum: *Eur.Phys.J.C* 50, 505 (2007)].
- [104] J. Gao, M. Guzzi, J. Huston, H.-L. Lai, Z. Li, P. Nadolsky, J. Pumplin, D. Stump, and C. P. Yuan, "CT10 next-to-next-to-leading order global analysis of QCD," *Phys. Rev.*, vol. D89, no. 3, p. 033009, 2014.
- [105] S. Catani, L. Cieri, G. Ferrera, D. de Florian, and M. Grazzini, "Vector boson production at hadron colliders: a fully exclusive QCD calculation at NNLO," *Phys. Rev. Lett.*, vol. 103, p. 082001, 2009.
- [106] T. Hahn, "CUBA: A Library for multidimensional numerical integration," *Comput. Phys. Commun.*, vol. 168, pp. 78–95, 2005.
- [107] J. C. Collins, D. E. Soper, and G. F. Sterman, "Transverse Momentum Distribution in Drell-Yan Pair and W and Z Boson Production," *Nucl. Phys.*, vol. B250, pp. 199–224, 1985.
- [108] G. A. Ladinsky and C. P. Yuan, "The Nonperturbative regime in QCD resummation for gauge boson production at hadron colliders," *Phys. Rev.*, vol. D50, p. R4239, 1994.
- [109] C. Balazs and C. P. Yuan, "Soft gluon effects on lepton pairs at hadron colliders," *Phys. Rev.*, vol. D56, pp. 5558–5583, 1997.
- [110] S. Catani, D. de Florian, G. Ferrera, and M. Grazzini, "Vector boson production at hadron colliders: transverse-momentum resummation and leptonic decay," *JHEP*, vol. 12, p. 047, 2015.
- [111] ATLAS Collaboration, "Measurement of differential production cross-sections for a Z boson in association with b-jets in 7 TeV proton-proton collisions with the ATLAS detector," *JHEP*, vol. 10, p. 141, 2014.
- [112] ATLAS Collaboration, "Measurement of the transverse momentum distribution of W bosons in pp collisions at $\sqrt{s} = 7$ TeV with the ATLAS detector," *Phys. Rev. D*, vol. 85, p. 012005, 2012.
- [113] ATLAS Collaboration, "Measurement of the angular coefficients in Z-boson events using electron and muon pairs from data taken at $\sqrt{s} = 8$ TeV with the ATLAS detector," *JHEP*, vol. 08, p. 159, 2016.
- [114] L. Harland-Lang, A. Martin, P. Motylinski, and R. Thorne, "Parton distributions in the LHC era: MMHT 2014 PDFs," *Eur. Phys. J. C*, vol. 75, no. 5, p. 204, 2015.
- [115] S. Dulat, T.-J. Hou, J. Gao, M. Guzzi, J. Huston, P. Nadolsky, J. Pumplin, C. Schmidt, D. Stump, and C. Yuan, "New parton distribution functions from a global analysis of quantum chromodynamics," *Phys. Rev. D*, vol. 93, no. 3, p. 033006, 2016.
- [116] J. Pumplin, D. Stump, R. Brock, D. Casey, J. Huston, J. Kalk, H. L. Lai, and W. K. Tung, "Uncertainties of predictions from parton distribution functions. ii. the hessian method," *Physical Review D*, vol. 65, Dec 2001.

- [117] M. Schott, G. Siragusa, J. Cuth, and T.-h. Lin, "Measurement of m_W at 7 TeV: Reconstruction of the hadronic recoil," Tech. Rep. ATL-COM-PHYS-2014-1435, CERN, Geneva, Nov 2014.
- [118] A. Dimitrievska, N. Vranjes, M. Schott, and M. Boonekamp, "Measurement of m_W at 7 TeV: Hadronic recoil corrections," Tech. Rep. ATL-COM-PHYS-2015-344, CERN, Geneva, Apr 2015.
- [119] L. Devroye, *Non-Uniform Random Variate Generation*. Springer-Verlag, 1986.
- [120] G. Cowan, *Statistical Data Analysis*. Oxford science publications, Clarendon Press, 1998.
- [121] K. Cranmer, G. Lewis, L. Moneta, A. Shibata, and W. Verkerke, "HistFactory: A tool for creating statistical models for use with RooFit and RooStats," 6 2012.
- [122] R. Brun and F. Rademakers, "ROOT: An object oriented data analysis framework," *Nucl. Instrum. Meth.*, vol. A389, pp. 81–86, 1997.
- [123] F. James, "MINUIT Function Minimization and Error Analysis: Reference Manual Version 94.1," 1994.
- [124] ATLAS Collaboration, "A morphing technique for signal modelling in a multidimensional space of coupling parameters," Tech. Rep. ATL-PHYS-PUB-2015-047, CERN, Geneva, Nov 2015.
- [125] A. C. DÜdder, *First Measurement of the Branching Ratio Fraction $BR(W \text{ to } \tau \nu \text{ to } \mu \nu \nu)/BR(W \text{ to } \mu \nu)$ in $\sqrt{s} = 7 \text{ TeV}$ Proton-Proton Collisions with the ATLAS Detector and Realization of a Production Facility for Large Scale Micromegas Drift Boards*. PhD thesis, Johannes Gutenberg-Universitaet, Mainz, Mainz, 2019.
- [126] D. Collaboration, "Direct measurement of the W boson width," *Phys. Rev. Lett.*, vol. 103, p. 231802, 2009.
- [127] CDF Collaboration, "A Direct measurement of the W boson width in $p\bar{p}$ collisions at $\sqrt{s} = 1.96\text{-TeV}$," *Phys. Rev. Lett.*, vol. 100, p. 071801, 2008.
- [128] L. Adam, S. Webb, and M. Schott, "Measurement of distributions sensitive to the underlying event in inclusive Z -boson production in pp collisions at $\sqrt{s} = 13 \text{ TeV}$ with the ATLAS detector," Tech. Rep. ATL-COM-PHYS-2018-188, CERN, Geneva, Mar 2018.
- [129] CDF Collaboration, "Charged jet evolution and the underlying event in $p\bar{p}$ collisions at 1.8 TeV," *Phys. Rev. D*, vol. 65, p. 092002, 2002.
- [130] ATLAS Collaboration, "Measurement of distributions sensitive to the underlying event in inclusive Z -boson production in pp collisions at $\sqrt{s} = 7 \text{ TeV}$ with the ATLAS detector," *Eur. Phys. J. C*, vol. 74, p. 3195, 2014.
- [131] CMS Collaboration, "Measurement of the underlying event in the Drell-Yan process in proton-proton collisions at $\sqrt{s} = 7 \text{ TeV}$," *Eur. Phys. J. C*, vol. 72, p. 2080, 2012.
- [132] CMS Collaboration, "Measurement of the underlying event activity in inclusive Z boson production in proton-proton collisions at $\sqrt{s} = 13 \text{ TeV}$," *JHEP*, vol. 07, p. 032, 2018.

- [133] G. Marchesini and B. R. Webber, "Associated transverse energy in hadronic jet production," *Phys. Rev.*, vol. D 38, p. 3419, 1988.
- [134] J. Pumplin, "Hard underlying event correction to inclusive jet cross-sections," *Phys. Rev.*, vol. D 57, pp. 5787–5792, 1998.
- [135] ATLAS Collaboration, "Measurements of underlying-event properties using neutral and charged particles in pp collisions at $\sqrt{s} = 900$ GeV and $\sqrt{s} = 7$ TeV with the ATLAS detector at the LHC," *Eur. Phys. J. C*, vol. 71, p. 1636, 2011.
- [136] D. Kar and D. S. Rafanoharana, "Probing underlying event in Z-boson events using event shape observables," *Int. J. Mod. Phys. A*, vol. 34, p. 1950022, 2018.
- [137] A. Banfi, G. P. Salam, and G. Zanderighi, "Phenomenology of event shapes at hadron colliders," *JHEP*, vol. 06, p. 038, 2010.
- [138] ATLAS Collaboration, "Measurement of event-shape observables in $Z \rightarrow \ell^+\ell^-$ events in pp collisions at $\sqrt{s} = 7$ TeV with the ATLAS detector at the LHC," *Eur. Phys. J. C*, vol. 76, p. 375, 2016.
- [139] ATLAS Collaboration, "Measurements of the production cross section of a Z boson in association with jets in pp collisions at $\sqrt{s} = 13$ TeV with the ATLAS detector," *Eur. Phys. J.*, vol. C77, no. 6, p. 361, 2017.
- [140] R. D. Ball *et al.*, "Parton distributions for the LHC Run II," *JHEP*, vol. 04, p. 040, 2015.
- [141] S. Gieseke, C. Rohr, and A. Siodmok, "Colour reconnections in Herwig++," *Eur. Phys. J.*, vol. C72, p. 2225, 2012.
- [142] P. Z. Skands, "Tuning Monte Carlo generators: The Perugia tunes," *Phys. Rev. D*, vol. 82, p. 074018, 2010.
- [143] ATLAS Collaboration, "Measurement of the WW cross section in $\sqrt{s} = 7$ TeV pp collisions with the ATLAS detector and limits on anomalous gauge couplings," *Phys. Lett. B*, vol. 712, p. 289, 2012.
- [144] ATLAS Collaboration, "Measurement of the top quark pair production cross section in pp collisions at $\sqrt{s} = 7$ TeV in dilepton final states with ATLAS," *Phys. Lett. B*, vol. 707, p. 459, 2012.
- [145] ATLAS Collaboration, "Measurement of the transverse momentum distribution of Drell–Yan lepton pairs in proton–proton collisions at $\sqrt{s} = 13$ TeV with the ATLAS detector," *Eur. Phys. J. C*, vol. 80, no. 7, p. 616, 2020.
- [146] F. Spanò, "Unfolding in particle physics: A window on solving inverse problems," *EPJ Web of Conferences*, vol. 55, pp. 03002–, 07 2013.
- [147] G. D'Agostini, "A Multidimensional unfolding method based on Bayes' theorem," *Nucl. Instrum. Meth. A*, vol. 362, pp. 487–498, 1995.
- [148] G. D'Agostini, "Improved iterative Bayesian unfolding," 2010.
- [149] O. Behnke, "Data analysis in high energy physics : a practical guide to statistical methods," 2013.
- [150] J. W. Monk and C. Oropenza-Barrera, "The HBOM method for unfolding detector effects," *Nucl. Instrum. Meth. A*, vol. 701, pp. 17–24, 2013.

- [151] H. Schulz, *Measurement of the Underlying Event using track-based event shapes in $Z \rightarrow l^+l^-$ events with ATLAS*. PhD thesis, Mathematisch-Naturwissenschaftlichen Fakultät der Humboldt-Universität zu Berlin, 9 2014.
- [152] CDF Collaboration, "Studying the underlying event in Drell-Yan and high transverse momentum jet production at the Tevatron," *Phys. Rev. D*, vol. 82, p. 034001, 2010.
- [153] M. H. Seymour and A. Siodmok, "Constraining MPI models using σ_{eff} and recent Tevatron and LHC Underlying Event data," *JHEP*, vol. 10, p. 113, 2013.
- [154] A. Collaboration", "Modelling radiation damage to pixel sensors in the ATLAS detector," *Journal of Instrumentation*, vol. 14, pp. P06012–P06012, jun 2019.
- [155] L. Adam, M. Benoit, M. Bomben, R. Carney, M. Garcia-Sciveres, L. Meng, B. P. Nachman, V. Wallangen, T. Lari, L. Rossini, G. Giugliarelli, J.-c. Beyer, A. Ducourthial, A. Macchiolo, J. Llorente Merino, N. Dann, C. Da Via, P. Miya-gawa, and I. Dawson, "A model for pixel digitization including radiation damage effects," Tech. Rep. ATL-COM-INDET-2016-068, CERN, Geneva, Sep 2016.
- [156] Apollinari G. et. al., *High-Luminosity Large Hadron Collider (HL-LHC): Technical Design Report V. 0.1*. CERN Yellow Reports: Monographs, Geneva: CERN, 2017.
- [157] ATLAS Collaboration, "Athena – ATLAS software framework." <https://atlassoftwaredocs.web.cern.ch/athena/athena-intro/>, 2017.

List of Figures

2.1	Summary table of all SM particles ordered in the different families. The surrounding black rectangles indicate to which force the fermions on the left couple. The figure is based on [7].	10
2.2	(a) The lowest order diagram for the Drell-Yan process, usually referred to as LO diagram. (b) Higher order correction with a virtual fermion loop. It corresponds to a NNLO correction.	12
2.3	Illustration of the 'Mexican hat'-shaped Higgs potential. The position A is the unstable symmetric center. As soon as the system transfers to position B somewhere on the circle of minima, the original symmetry will be broken.	16
2.4	The PDF set MSTW 2008 NLOPDF provided by [23]. The form factor is presented in dependence of the Bjorken- x for different quark flavours and gluons. The left figure corresponds to $Q^2 = 10\text{GeV}^2$ and the right one to $Q^2 = 10^4\text{GeV}^2$	20
2.5	Rapidity Distribution for the leading-order production of Z and W bosons in $\sqrt{s} = 7\text{ TeV } pp$ collisions. The differential cross-section is calculated with two different PDF sets.	22
2.6	Production of the W at NLO and its subsequent decay. The final state includes an additional (a) gluon or (b) quark, which manifest in jets within the detector. The recoil against the ISR initiates the transverse momentum of the vector-boson.	23
2.7	Feynman diagrams exemplifying loop corrections to the W boson propagator and the $Z \rightarrow b\bar{b}$ vertex, which affect the vector coupling. The figure is taken from [27].	27
2.8	(a) illustrates the estimate of the Higgs Boson mass in the Standard Model from electroweak precision measurements. The excluded area by direct searches is shown in yellow, while the blue band illustrate the χ^2 distribution of the global electroweak fit. (b) illustrates a χ^2 distribution for m_W derived with (blue) and without (orange) including the Higgs boson mass using the Gfitter program. The filled blue and yellow areas indicate The theoretical uncertainties. The χ^2 distribution is also evaluated with an alternative software (GAPP). The grey band presents the current world average of the measurements with 1σ uncertainty. The plots are taken from [27] and are based on results from [31].	28
3.1	Schematic drawing of the accelerator complex at CERN. The yellow dots refer to the experiments placed at the interaction points. The figure is courtesy of CERN [32]	31
3.2	(a) is a cut-away view of the ATLAS detector. The figure highlights the three different detector regions: The central barrel region and the two endcap regions, which close up the cylinder top and bottom side. The figure is courtesy of CERN [34]. (b) illustrates the ATLAS coordinate system. The sketch is taken from [35].	34
3.3	(a) is a cut-away view of the ID. The figures are courtesy of CERN [36].	35
3.4	A cut-away view of the MS. The figure is courtesy of CERN [41].	37

3.5	Schematic cross-section of an ATLAS detector segment. The paths of different particles are visualized. Solid lines correspond to reconstructable particle trajectories, while the dashed lines are invisible to the detector. Proton, Neutron, electron and photon shower in the corresponding calorimeters. The figure is courtesy of CERN [42].	39
3.6	Illustration of the particle track parameters. The left hand side presents the definition of d_0 in the transverse plane of the detector. The right hand side visualizes the longitudinal impact parameter. IP is the design interaction point and C is the center of the track seed, i.e. a circle with radius ρ . The tangent is needed to define the angle Φ_0	40
4.1	Pictorial representation of the event generation with a Monte-Carlo generator. The big red blob illustrates the hard interaction (here $t\bar{t}H$ production plus a QCD jet), the corresponding products decay subsequently. The purple blob visualizes an additional parton-parton interaction (MPI). The hadronization of the final state partons is initiated with the light green blobs, followed by hadron decays (dark green). The yellow lines represent photon emission. The figure is taken from Ref.[55].	46
4.2	Distribution of the average number of reconstructed vertices as function of the average number of interactions per bunch crossing. The azure boxes show the mean number of reconstructed vertices per minute of data taking. The plot is taken from Ref. [77].	54
5.1	Overview of selected measurements of m_W , including the most precise measurements from LEP [78], Tevatron [79] and the LHC [72]. The grey area presents the world average of $m_W = 80380 \pm 13$ MeV. The figure is taken from Ref. [27].	58
5.2	Illustration of the geometrical relations between the hadronic recoil, u_T , which serves as reference for p_T^W , the lepton momentum, p_T^ℓ , and the missing transverse energy, \vec{E}_T^{miss} . The latter approximates the momentum of the undetected neutrino and is inferred from the imbalance of measured vectorial energies. The blue area symbolizes energy deposits in the calorimeters.	61
5.3	Templates of the p_T^μ (a) and m_T (b) distributions for three different values of m_W . The templates are forward-folded with the response of the ATLAS detector. Both are taken from [72].	62
5.4	(a) Cumulative luminosity versus time delivered to (green), recorded by ATLAS (yellow), and certified to be good quality data (blue) during stable beams and for pp collisions at $\sqrt{s} = 7$ TeV in 2011. (b) Luminosity-weighted distribution of the mean number of interactions per crossing for the 2011 and 2012 data. Both plots are made publicly available by the ATLAS collaboration.	65

- 5.5 Example template fits to the \bar{p}_T^{miss} (a), m_T (b), and p_T^ℓ/m_T (c) distributions in the FR1 kinematic region, in the muon decay channels. Multijet templates are derived from the data requiring $0.2 < I_\mu < 0.4$. The data are compared to the simulation including signal and background contributions. (d) And the extrapolation to estimate the number of multijet-background events for both fit regions and the three variables. The linear extrapolations are indicated by the solid lines. The thick crosses show the results of the linear extrapolation of the background estimate to the signal region, including uncertainties from the extrapolation only. The thin crosses also include the uncertainty induced by the contamination of the control regions by electroweak and top-quark processes. All figures are taken from [72]. 72
- 5.6 (a) Differential Z boson cross section as a function boson rapidity, and (b) differential W^+ and W^- cross sections as a function of charged decay-lepton pseudorapidity at $\sqrt{s} = 7$ TeV [98]. The measured cross sections are compared to the POWHEG+PYTHIA8 predictions, corrected to NNLO using DYNNLO with the CT10NNLO PDF set. The error bars show the total experimental uncertainties, including luminosity uncertainty, and the bands show the PDF uncertainties of the predictions. The plots are taken from [72]. 76
- 5.7 (a) Residual muon momentum scale corrections as a function of muon $1/\langle p_T \rangle$ in four pseudorapidity regions. The extrapolation applies linear fits. (b) Sagitta bias as a function of pseudorapidity and averaged over the azimuthal angle. (c) Scale factors for the muon reconstruction, trigger and isolation efficiency obtained with the tag and probe method as a function of p_T^μ . All three plots show statistical uncertainties only. The plots are taken from [72]. 79
- 5.8 Distributions of (a) $\sum E_T^*$ and (b) the azimuth direction Φ of the recoil in data and simulation for $Z \rightarrow \mu\mu$ events. Both plots illustrates the effect of the transformation and correction respectively. The lower ratio plots show statistical uncertainties only. 81
- 5.9 The top plot presents the p_T^ℓ distribution in data (black) compared to different templates. The blue line corresponds to the highest template value of m_W , red to the lowest and purple to the best one with the lowest value of χ^2 . The lower plot presents the χ^2 values as function of the template values of m_W relative to the nominal mass value. The red curve illustrates the parabola fit. 84
- 5.10 (a) Example for linear interpolation of bin content. The parameter Θ_t controls the pull of the NP. (b) The full distribution in p_T^μ for an exemplary systematic uncertainty. 89
- 5.11 (a) Green corresponds to a template of lower mass value of m_W , blue to a higher one. Grey presents the linear combination of both templates and reproduces here the template of the central nominal value. (b) Bin content for an exemplary bin as function of the template shift of m_W . The linear approximation is suitable over the full range presented for m_W 90
- 5.12 Bin content for an exemplary bin as function of the template shift of Γ_W . (a) The linear approximation is not suitable over the full range presented Γ_W . (b) The zoom reveals, that the linear approximation is sufficient for a template separation of about $\Delta\Gamma_W = 100$ MeV. 90

5.13	Comparison between the central fits of the legacy analysis (grey), the resurrected χ^2 fit for the reanalysis (blue) and the PLH fit (PLH) on the very same data set. (a) are the results for the fits in p_T^μ and (b) in m_T . All fits are shown with statistical uncertainties only.	91
5.14	Results of the m_W fit using a PLH approach on the distributions in (a) p_T^μ and (b) m_T . The fits profiled all uncertainties listed in Tab. 5.5. The grey shades correspond to the fit results of the χ^2 fit applied in the legacy analysis including all uncertainties. The corresponding central values are already presented in Fig. 5.13.	94
5.15	Ranking plot for profiling the combination fit of p_T^μ . It lists the ten NPs with the largest impact for a better overview. An overview of all NPs for p_T^μ and m_T are displayed in Fig. B.1. The blue blocks indicate the pre- and post-fit impact and belong to the top x-axis. The black dots indicate the pulls and refer to the bottom axis. Only the ten most impacting NPs are listed.	98
5.16	Results of the Γ_W fit using a PLH approach on the distributions in p_T^μ . The fits presented with green and black bars profiled all uncertainties listed in Tab. 5.5, but exclude the Monte-Carlo statistical uncertainties. The red bars illustrate the results for profiling only data statistical uncertainties. These are put in direct comparison to the χ^2 -minimization results (grey squares), which include only statistical uncertainties. The vertical dotted lines reference the world average and its uncertainties ($\Gamma_W^{global} = 2.085 \pm 0.042 \text{ GeV}$). But all results for the central values of Γ_W are still blinded, so the world average serves only for the comparison of the uncertainties.	100
6.1	The activity of the UE (green) contributes to the overall energy deposit in the calorimeters (blue). Its contribution needs to be subtracted to properly determine the hadronic recoil u_T	104
6.2	Illustration of away, transverse, and toward regions in the transverse plane defined relative to the direction of the Z boson.	107
6.3	(a) Illustration of an isotropic and a balanced event topology in the transverse plane with their corresponding values of thrust T_\perp . In these figures, the beams are travelling perpendicular to the plane of the page. (b) The picture exemplifies, that MPI activity is likely to produce an event topology of low thrust.	110
6.4	(a) Total Integrated Luminosity and Data Quality in 2015 Cumulative luminosity versus time delivered to ATLAS (green), recorded by ATLAS (yellow), and certified to be good quality data (blue) during stable beams for pp collisions at $\sqrt{s} = 13 \text{ TeV}$ centre-of-mass energy in 2015. (b) The luminosity-weighted distribution of the mean number of interactions per crossing ($\langle \mu \rangle$).	115
6.5	Detector level distributions of (a) the spectra of p_T , (b) the charged-particle multiplicity N_{ch} , (c) the scalar sum of the transverse momentum of those particles Σp_T , and (d) the mean transverse momentum mean p_T in the trans-min region, inclusively in T_\perp for events with $10 < p_T^Z < 20 \text{ GeV}$. The data are presented before the unfolding step and the background and signal samples are presented as a stack. The multijet background is statistically limited.	119
6.6	The non-fiducial signal correction (a) and event efficiency correction (b) according to Eq. 6.4. The values are evaluated on the two main Monte-Carlo generators. The response matrix (c) completes the inputs for Eq. 6.3. And (d) presents the result of unfolding real data.	123

- 6.7 The different iteration steps for unfolding $dN_{\text{ch}}/dp_{\text{T}}^{\text{ch}}$ (a) and $dN_{\text{ev}}/d(N_{\text{ch}}/\delta\eta\delta\phi)$ (b) exemplarily in $10 < p_{\text{T}}^{\text{Z}} < 20$ GeV. The errors indicate the statistical uncertainty evaluated for the iteration. The ratio is calculated with respect to iteration step 8. The second and third iteration are almost similar for (a), while in (b) the convergence is visible for iteration 7 and 8. The values of the corresponding purity and stability indicate (c,d), that the convergence of $dN_{\text{ev}}/d(N_{\text{ch}}/\delta\eta\delta\phi)$ requires a higher number of iterations than $dN_{\text{ch}}/dp_{\text{T}}^{\text{ch}}$ 126
- 6.8 Data distributions of $dN_{\text{ev}}/d(N_{\text{ch}}/\delta\eta\delta\phi)$ split in different regions of $\langle\mu\rangle$ before the unfolding (a) and after the unfolding procedure (b). (b) displays the unfolded data with the statistical uncertainties. The different $\langle\mu\rangle$ regions are in agreement within these uncertainties after unfolding. The ratio is calculated with respect to the middle region [11,13]. 131
- 6.9 (a) Example of the HBOM iterations. D_1 is the actual data distribution on detector level, and D_0 is the same distribution, but cleaned from pile-up. The back-extrapolation step from D_1, \dots, D_6 to D_0 is presented in (b) for the gray shaded bin in plot (a). 134
- 6.10 Example of the result of the HBOM algorithm (D_0) compared to the nominal unfolding for (a) $dN_{\text{ev}}/d(N_{\text{ch}}/\delta\eta\delta\phi)$ and (b) $dN_{\text{ch}}/dp_{\text{T}}^{\text{ch}}$. The error bars correspond to unfolding and pile-up related uncertainties. 135
- 6.11 A summary of the systematic uncertainties in the arithmetic mean of the N_{ch} and Σp_{T} spectra in the trans-min region as a function of p_{T}^{Z} . Here ‘Prior’ combines the two approaches to estimate the unfolding-related uncertainties. ‘Detector’ includes the modelling of the detector and the pile-up conditions. 140
- 6.12 Breakdown of systematic uncertainties in the p_{T} spectrum (a), the charged-particle multiplicity (N_{ch} , (b)), the scalar sum of the transverse momenta (Σp_{T} , (c)) and the mean transverse momentum (mean p_{T} , (d)) for events with $10 < p_{\text{T}}^{\text{Z}} < 20$ GeV in the trans-min region inclusively in T_{\perp} . Here ‘Prior’ combines the two approaches to estimate the unfolding-related uncertainties. ‘Detector’ includes the modelling of the detector and the pile-up conditions. 141
- 6.13 Comparison of the activities in the different regions of the transverse plane as a function of p_{T}^{Z} . From top to bottom: arithmetic mean of the scalar sum of the transverse momenta, mean number of charged particles both presented per unit $\eta-\phi$ and the mean of mean p_{T} 144
- 6.14 Comparison of the activities in the different regions of the transverse plane as a function of p_{T}^{Z} . The results are additionally distinguished in thrust. From top to bottom: arithmetic mean of the scalar sum of the transverse momenta, mean number of charged particles both presented per unit $\eta-\phi$ and the mean of mean p_{T} 146
- 6.15 Spectrum of the transverse momentum of the charged particles in the trans-min region. (a) inclusive in thrust, (b) MPI-enriched ($T_{\perp} < 0.75$) and (c) $0.75 \leq T_{\perp}$. Predictions of POWHEG+PYTHIA8, SHERPA, and HERWIG++ are compared with the data. The ratios shown are predictions over data. 147

- 6.16 The left hand plots present the differential results for $10 < p_T^Z < 20$ GeV, compared to the corresponding mean values as a function of p_T^Z in the right column, all inclusive in thrust in the trans-min region. From top to bottom: the sum of transverse momenta, the number of charged particles, and the arithmetic mean of p_T . Predictions of POWHEG+PYTHIA8, SHERPA, and HERWIG++ are compared with the data. The ratios shown are predictions over data. 148
- 6.17 The left hand plots present the differential results for $10 < p_T^Z < 20$ GeV, compared to the corresponding mean values as a function of p_T^Z in the right column, all with the MPI enriched selection ($T_\perp < 0.75$) in the trans-min region. From top to bottom: the sum of transverse momenta, the number of charged particles, and the arithmetic mean of p_T . Predictions of POWHEG+PYTHIA8, SHERPA, and HERWIG++ are compared with the data. The ratios shown are predictions over data. 150
- 6.18 The left hand plots present the differential results for $10 < p_T^Z < 20$ GeV, compared to the corresponding mean values as a function of p_T^Z in the right column, measured in the trans-min region, all events require $0.75 \leq T_\perp$. From top to bottom: the sum of transverse momenta, the number of charged particles, and the arithmetic mean of p_T . Predictions of POWHEG+PYTHIA8, SHERPA, and HERWIG++ are compared with the data. The ratios shown are predictions over data. 151
- 6.19 Spectrum of the transverse momentum of the charged particles in the trans-max region, inclusive in thrust. Predictions of POWHEG+PYTHIA8, SHERPA, and HERWIG++ are compared with the data. The ratios shown are predictions over data. 152
- 6.20 The left hand plots present the differential results for $10 < p_T^Z < 20$ GeV, compared to the corresponding mean values as a function of p_T^Z in the right column, all inclusive in thrust in the trans-max region. From top to bottom: the sum of transverse momenta, the number of charged particles, and the arithmetic mean of p_T . Predictions of POWHEG+PYTHIA8, SHERPA, and HERWIG++ are compared with the data. The ratios shown are predictions over data. 153
- 6.21 The left hand plots present the differential results for mean p_T in $10 < p_T^Z < 20$ GeV, compared to the corresponding mean values as a function of p_T^Z in the right column, The top row shows results for the MPI enriched events ($T_\perp < 0.75$) and the bottom row for $0.75 \leq T_\perp$. Predictions of POWHEG+PYTHIA8, SHERPA, and HERWIG++ are compared with the data. The ratios shown are predictions over data. 154
- 6.22 Spectrum of the transverse momenta of charged particles in the transverse region with $10 < p_T^Z < 20$ GeV for (a) MPI enriched events ($T_\perp < 0.75$) and (b) events with $0.75 \leq T_\perp$. Predictions of POWHEG+PYTHIA8, SHERPA, and HERWIG++ are compared with the data. The ratios shown are predictions over data. 155
- 6.23 The left hand plots present the differential results for N_{ch} in $10 < p_T^Z < 20$ GeV, compared to the corresponding mean values as a function of p_T^Z in the right column, The top row shows results for the MPI enriched events ($T_\perp < 0.75$) and the bottom row for $0.75 \leq T_\perp$. Predictions of POWHEG+PYTHIA8, SHERPA, and HERWIG++ are compared with the data. The ratios shown are predictions over data. 156

- 6.24 Mean sum of transverse momenta (a) and mean number of charged particles (b) in the toward region, inclusive in thrust. (c) The differential results for mean p_T in $10 < p_T^Z < 20$ GeV and the corresponding (d) arithmetic mean values as function of p_T^Z in the toward region, inclusive in thrust. Predictions of POWHEG+PYTHIA8, SHERPA, and HERWIG++ are compared with the data. The ratios shown are predictions over data. 158
- 6.25 The distributions of $\langle N_{\text{ch}} \rangle$ and $\langle \Sigma p_T \rangle$ measured at $\sqrt{s} = 13$ TeV compared with the results of the previous ATLAS measurements at $\sqrt{s} = 7$ TeV [130] and the CDF measurements at $\sqrt{s} = 1.96$ TeV [152]. The error bars correspond to the full uncertainties of the corresponding measurement. 159
- 7.1 Overview of the results for the legacy ATLAS measurement of m_W (2016) [72] compared to the results of this thesis using the PLH fit (PLH). The grey area presents the world average of $m_W^{\text{global}} = 80380 \pm 13$ MeV and the first entry displays the value of the electroweak fit $m_W^{\text{EW}} = 80356 \pm 6$ MeV [27]. 164
- A.1 (a) A schematic diagram illustrating the components of the digitizer model. The minimal ionizing particle (MIP) induce electron (-) and hole (+) pairs in the sensor bulk. Both are dragged to the readout ends due to the electric field from the applied bias voltage. The moving charge carriers might be trapped, deflected by the magnetic field, or decelerated due the depleted electric field. (b) Profile of the electric field as a function of the sensor depth (Z) for different radiation dosages. 198
- A.2 (a) represents the procedure for the spline based approach to estimate the electric field at $\Phi = 7.6 \cdot 10^{14} \frac{n_{\text{eq}}}{\text{cm}^2}$, $U = 500V$ and $z = 3\mu\text{m}$. The colored dots represent electric field values available from TCAD simulations for a fixed depth of $z = 3\mu\text{m}$. The horizontal grey lines represent the first step, i.e. the interpolation while keeping the bias voltage fixed. The vertical line corresponds to the second step interpolating over the bias voltages while keeping the fluence fixed. (b) and (c) correspond to the grey solid lines in (a). The first plot shows the interpolation of the TCAD electric field values (*) with a spline (red line) for a fixed bias voltage $U_i = 150V$. The second plot presents the second interpolation step, i.e. interpolating the values obtained from the first interpolation step while keeping the fluence constant (here $\Phi = 7.6 \cdot 10^{14} n_{\text{eq}}/\text{cm}^2$). 199
- B.1 Ranking plot for profiling the combination fit of (a) m_T and (b) p_T^μ with all available NPs. The blue blocks indicate the pre- and post-fit impact and belong to the top x-axis. The black dots indicate the pulls and refer to the bottom axis. Only the ten most impacting NPs are listed. 201
- B.2 Results of the Γ_W fit using a PLH approach on the distributions in m_T . The fits presented with read bars profiled all uncertainties listed in Tab. 5.5, but exclude the Monte-Carlo statistical uncertainties. The red bars illustrate the results for profiling only data statistical uncertainties. The vertical dotted lines reference the world average and its uncertainties ($\Gamma_W^{\text{global}} = 2.085 \pm 0.042 \text{GeV}$). But all results for the central values of Γ_W are still blinded, so the world average serves only for the comparison of the uncertainties. 202

C.1	Example for the different scaling steps to create the UE observable representation. It starts with the basic observable without any scaling in (a). The observable is transformed into a density by scaling the x-axis (b). The contents are scaled to the bin width (c). And finally the full integral is normalized (d).	205
C.2	Example plots for forward closure for (a) the differential distributions and (b) the mean observables: ZeroPU refers to the distribution constructed on detector level from the MC sample originally produced without pile-up contamination, but in this case one iteration of the artificial pile-up is added. POWHEG+PYTHIA8 refers to the according detector level distribution of the (originally pile-up contaminated) baseline MC sample.	206
C.3	Exemplary distributions presenting the backward closure of the HBOM algorithm for (a) the differential distributions and (b) the mean observables. ZeroPU refers to the distribution constructed on detector level from the Monte-Carlo sample originally produced without pile-up contamination.	207

List of Tables

5.1	Summary of categories and kinematic distributions used in the m_W and Γ_W measurements.	62
5.2	Summary of the simulated background samples. The contribution is stated as relative fraction of the template sample in percent. The uncertainty on the cross-section relative to the signal sample is also given in percent.	68
5.3	Cutflow comparison for the process $W \rightarrow \mu\nu$. The simulation samples are normalized to the corresponding cross-section. Data taking periods L3 and L4 are discarded due to a timing problem in the RPC.	69
5.4	Validation of the different uncertainty categories. The values for the legacy analysis are taken from [72], while the reanalysis reevaluates the uncertainties based on pseudo experiments.	92
5.5	Summary of the systematic uncertainties, which are profiled in the PLH fit. A similar summary is found in [125], which employs the same set of simulation samples.	93
5.6	Summary of the results from the legacy analysis (χ^2 fit) with the uncertainties compared to the results of the profile likelihood approach. The latter profiled all available uncertainties. The toy based ones and the uncertainty on the MJ shape are excluded by now. The legacy numbers are unmodified and quoted from Ref.[72]. Tab. 5.7 provides the legacy uncertainty cleaned from the contributions, which are not included in the profile likelihood fit.	95
5.7	Summary of the impact of different NP categories on the profile likelihood fit compared to the corresponding uncertainty from the legacy analysis (Leg.). <i>Shift</i> states the difference between profiling the NP category and profiling only statistical uncertainties. <i>PLH</i> lists the uncertainty on m_W related to this category of NP. The first category, <i>Full Profiling</i> , profiled only systematic uncertainties. The statistical uncertainties are not profiled in this case, but added afterwards. This results in a slightly higher total uncertainty for PLH than it is stated in Tab. 5.6. The total uncertainty of the legacy analysis is cleaned from the contributions, which are not profiled, in order to guarantee compatibility of the results.	97
5.8	Summary of the impact of different NP categories on the profile likelihood fit of Γ_W . <i>Shift</i> states the difference between profiling the NP category and profiling only (data) statistical uncertainties. <i>Impact</i> lists the uncertainty on Γ_W related to this category of NP. The first category, <i>Full Profiling</i> , profiled all available uncertainties and presents the blinded results for the central values of Γ_W	101
6.1	Summary on observable reconstruction. The event characteristics target the sensitivity to the general UE components. The regions distinguish UE activity and hard-scattering. The observables are measured in all combinations of these categories.	109
6.2	Overview of the Monte-Carlo generator setup used for the simulation of the signal process $Z \rightarrow \mu\mu$	116

6.3	The table lists the total number of events passing the different cut-levels listed in Sec. 6.3.1. The simulation based samples are simulated equivalent to the trigger stage and scaled with respect to their cross-section and the data luminosity (3.2 fb^{-1}). The last line states the relative uncertainty on the background estimation and cross-section respectively. 'All events' refers to the number of events provided as datasets, hence the data already passed low quality criteria to be recorded.	118
6.4	A summary of the fiducial volume definition of the measurement, the particle-level definition, and the main observables. The first row lists selection criteria for the signal muons (indicated with an μ as superscript) limited by the detector geometry, while the cut on the dimuon invariant mass $m^{\mu\mu}$ yields a low background contamination.	122
B.1	The table presents the numerical values for Fig. 5.13. The column Legacy list the central fit results taken from [72] including the statistical uncertainties. The Column Reanalysis presents the fit results based on the resurrected samples and χ^2 fit. The third column lists the corresponding difference to display the closure, while the last column presents the results of the PLH fit using only statistical uncertainties.	200
B.2	Summary of the impact of different NP categories on the profile likelihood fit of Γ_W applied to distributions of m_T . <i>Shift</i> states the difference between profiling the NP category and profiling only (data) statistical uncertainties. <i>Impact</i> lists the uncertainty on Γ_W related to this category of NP. The first category, <i>Full Profiling</i> , profiled all available uncertainties and presents the blinded results for the central values of Γ_W	203

List of Abbreviations

Symbols | A | B | C | D | E | F | G | H | I | L | M | N | P | Q | R | S | T | U

Symbols

$\langle\mu\rangle$

average number of interactions per bunch crossing. 32, 53, 65, 81, 82, 114, 130, 131, 137, 138, 186

A

ATLAS

A Thoroidal LHC AparatuS. 2, 3, 8, 24, 27, 32–34, 36, 38–42, 44, 48, 49, 53, 58–60, 62–68, 75, 77, 81, 83, 87, 101, 102, 104, 105, 111–114, 116, 120, 125, 136, 160, 164, 182, 183, 188, 197

B

BSM

beyond the Standard Model. 26, 30, 58

C

CDF

Collider Detector at Fermilab. 59, 61, 84, 102, 105

CERN

Conseil Européen pour la Recherche Nucléaire. 31, 34, 35, 37, 39, 182, 183

CKM

Cabibbo-Kobayashi-Maskawa mixing matrix. 21, 59

CMS

Compact Muon Solenoid. 105

CSC

Cathode Strip Chambers. 37

D

DØ

detector at Tevatron collider. 61, 84, 102

DIS

Deep Inelastic Scattering. 19

E

EF

Event Filter - precise software trigger. 42

electroweak

electromagnetic and weak. 15, 26–28, 58, 72, 73, 93, 100, 164, 165, 182, 184

EM

ElectroMagnetic layers of calorimeter. 41, 42

F**FSR**

Final State Radiation. 25, 45, 73, 74, 106, 107, 115, 116, 129, 142, 157

G**GEANT4**

GEANT4 is a platform for the simulation of the passage of particles through matter using Monte Carlo methods – GEometry ANd Tracking. 44, 48, 49, 116

GRL

Good-Runs-List. 111

H**HBOM**

Hit-backspace-once-more. 105, 130–135, 186, 205–207

High Energy Physics

High Energy Physics. 3, 25, 44, 105

HLT

High Level Trigger. 42, 112

I**IBL**

Insertable *b*-layer. 34, 35, 38, 50, 111, 197

ID

Inner Detector. 33–39, 41, 42, 49–51, 53, 63, 70, 78, 79, 106–108, 112, 113, 182

ISR

Initial State Radiation. 22–25, 45, 64, 65, 73, 74, 106, 107, 115, 142, 152, 157, 182

L**L1**

First Hardware trigger. 112

L1

First Level hardware trigger. 42

L2

Fast software trigger. 42

LEP

Large Electron-Positron collider. 58, 183

LHC

Large Hadron Collider. 2, 3, 8, 16, 18–20, 30–33, 35, 58, 59, 65, 66, 98, 111, 114, 160, 164, 183, 197

LINAC2

LINear ACcelerator in CERN. 31

LO

Leading order. 11, 12, 182

Lumi-block

Time period of run, when beam condition are constant. 53, 111

M**MBTS**

Minimum Bias Trigger Scintillators. 42

MDT

Mini Drift Tubes. 37

MJ

multi-jet. 70–73, 80, 83, 87, 93, 95, 117, 190

Monte-Carlo

First, electronics-based level of trigger system.. 3, 22, 25, 44–49, 51, 53, 54, 61, 62, 65–68, 70–83, 85, 89, 91, 92, 99, 100, 105, 106, 108, 111–118, 120, 121, 123–125, 127, 128, 130–132, 134, 136, 138–140, 160, 165, 183, 185, 188–190, 197, 202, 205–207

MPI

Multi-parton interaction. 46–48, 104, 106, 108, 110, 115, 116, 142, 145, 147, 149, 150, 154–156, 159–161, 165, 183, 185, 187

MS

Muon spectrometer. 37, 38, 41, 42, 53, 63, 79, 106, 111, 112, 182

N**NLO**

Next-to-Leading order. 23, 45, 182

NNLO

Next-to-Next-to-Leading order. 11, 12, 19, 74–76, 182, 184

NP

nuisance parameter. 59, 86–89, 92–94, 96–101, 164, 184, 185, 188, 190, 191, 201–203

P**p.o.i.**

parameter of interest. 86–89

PDF

Parton Distribution Function. 19–22, 27, 44, 45, 47, 48, 59, 62, 66, 74–77, 83–86, 93, 94, 96, 98, 100, 101, 115, 116, 159, 164, 182

pile-up

Other interaction vertices during one bunch-crossing.. 32, 42, 53, 54, 60, 64–67, 80–82, 105, 112, 114, 116, 120, 124, 125, 130–135, 137–140, 186, 189, 205–207

Pixel

Pixel detector. 34, 35, 38, 197

PLH

Profile Likelihood Ratio. 59–61, 76, 77, 83, 86–89, 91–94, 96, 98–102, 164, 185, 188, 190, 191, 200, 202

primary vertex

Vertex with largest sum of track transverse momentum.. 32, 51, 54, 63, 64, 67, 112, 113

PS

Proton Synchrotron. 31

PSB

Proton Synchrotron Booster. 31

Q**QCD**

Quantum Chromodynamics. 10, 17–19, 22, 24, 46–48, 73–77, 100, 102, 106, 183

QED

Quantum Electrodynamics. 12–14, 24, 73, 76, 129

QFT

Quantum Field Theory. 17

R**RESBOS**

Drell-Yan Monte-Carlo generator using resummation calculation. 66

RoI

Region of Interest. 42

RPC

Resistive Plate Chambers. 37, 69, 190

RUN 1

First operational run period of the LHC (2009-2013). 30-32, 34, 38, 42, 49-51

RUN 2

Second operational run period of the LHC (2015-2018). 30-32, 34, 38, 42, 59

S

SCT

Semiconductor Tracker. 35, 38, 50

SF

Scaling Factor. 49, 51, 52, 137

SM

Standard Model. 2, 8-12, 16, 17, 25-27, 44, 58, 59, 67, 86, 115, 117, 120, 165, 182

SPS

Super Proton Synchrotron. 31

T

Tevatron

hadron collider in Fermilab. 58, 66, 160, 183

TGC

Thin Gap Chambers. 37

TRT

Transition Radiation Tracker. 35, 39, 50

U

UE

Underlying Event. 2, 3, 25, 27, 38, 41, 44, 47, 48, 53, 60, 64, 66, 80-82, 102, 104-111, 113-116, 122, 124, 125, 127-130, 138-140, 142, 143, 145, 147, 149, 152, 155, 157, 159-161, 165, 185, 189, 190, 204, 205, 207

A.

Track reconstruction with irradiated sensors

A.1 A model for pixel digitization including radiation damage effects

Disclaimer: Parts of the following were previously published in [154] and form the basis of an internal ATLAS note [155] within the context of this work.

The ATLAS Pixel detector is closest to the interaction point and is exposed to an immense amount of radiation dosage over its lifetime. The performance of its modules is subject to the amount of radiation, as it introduces defects to the silicon lattice structure of the sensors. The final consequence is a dependency between the tracking performance and the radiation damage. The effects will become relevant for the future high-luminosity upgrade of the LHC [156], which will increase the luminosity by a factor of 10 beyond the current LHC design value. The luminosity is converted into a common measure of the radiation damage, namely non-ionizing energy loss. It is expressed as the equivalent damage of a fluence of 1MeV neutrons (n_{eq}/cm^2) and determined via simulation due to the dependence on the shape of the particle cascades. For example, the IBL and second innermost layer had received integrated fluences of approximately $\Phi = 6 \cdot 10^{14} n_{eq}/cm^2$ and $\Phi = 3 \cdot 10^{14} n_{eq}/cm^2$, respectively, by the end of the pp collision runs in 2017. The goal of Ref. [154] is to present a model for radiation damage to silicon sensors that is fast enough to be incorporated directly into the digitization step of the ATLAS Monte-Carlo simulation, i.e. the conversion from energy depositions from charged particles to digital signals sent from module front ends to the detector read-out system. General details of the corresponding models are outlines in Sec. A.1.1, and a core part for the reduction of the run time is presented in Sec. A.1.2.

A.1.1 Radiation damage effects

Non-ionizing radiation causes defects in the sensor bulk that deforms the electric field resulting from an applied bias voltage. This directly impacts the charge collection, as the time it takes for charge carriers to reach the electrode depends on this field. In addition to changes in the electric field, the defects result in charge trapping when electrons and holes are absorbed before being collected. Since moving charges induce a current in the collecting electrode, charge is collected from the trapped charges even though they do not reach the top or bottom of the sensor. The applied model includes several physical effects, which are schematically summarized in Fig. A.1. It includes other effects that are not specific to radiation damage, but which are affected by it through the electric field. The correct modelling of the electric field as a function of the applied bias voltage and the exposed fluence is essential to the digitization modelling. The electric fields for benchmark values of the bias voltage (U) and the fluence (Φ) are provided with Technology Computer Aided Design (TCAD) simulations. However, fluence and bias voltage are continuous variables and the TCAD simulation are computational expensive. Hence, the final digitizer design is needed to be independent of the TCAD simulation to meet the required (timing) performance. The solution is an interpolation method, which exploits a small subset of electric fields as benchmarks to produce the electric field for any desired value of bias voltage or fluence. The corresponding algorithm is introduced in the following section.

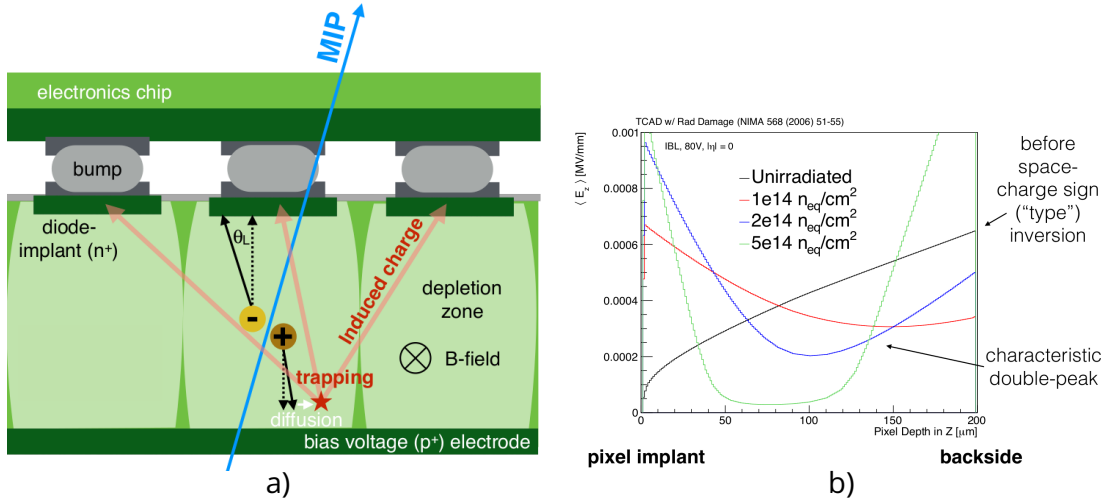


Figure A.1: (a) A schematic diagram illustrating the components of the digitizer model. The minimal ionizing particle (MIP) induce electron (-) and hole (+) pairs in the sensor bulk. Both are dragged to the readout ends due to the electric field from the applied bias voltage. The moving charge carriers might be trapped, deflected by the magnetic field, or decelerated due to the depleted electric field. (b) Profile of the electric field as a function of the sensor depth (Z) for different radiation dosages.

A.1.2

Interpolation method for an irradiated electric field

Imagining the ideal case, that the electric field profile can be realized as a smooth function depending on the bias voltage (U), the fluence (Φ) and the pixel depth (z), an interpolation method purely based on spline interpolation is implemented. The electric field value is interpolated for a fixed pixel depth, e.g. the TCAD samples hold information about the electric field profile for all integer values between $z = 3 \mu\text{m}$ and $z = 198 \mu\text{m}$ (the edge values are not reliably simulated and therefore ignored). For all of those the following steps are performed to estimate the electric field corresponding to the fluence Φ_{aim} and bias voltage U_{aim} of interest:

1. The bias voltage values are kept fixed. The samples belonging to the same bias voltage value (U_i) are listed by the according value of the fluence. A spline of third order is aligned to these values and evaluated at Φ_{aim} yielding $E(U_i, \Phi_{aim})$.
2. The same way the different values $E(U_i, \Phi_{aim})$ are processed. They are ordered by U_i and a spline of third order is aligned to it. This is evaluated at U_{aim} yielding the final value $E(U_{aim}, \Phi_{aim})$.

Some exemplary distributions are given in Fig. A.2. The interpolation is guaranteed to result in physically relevant values by demanding only positive results. Of course, the two steps could be applied in opposite order. Finally, it is anticipated to be of higher interest for the real case to interpolate to a higher fluence while keeping the bias voltage constant. Therefore, the according step is of higher priority.

The electric field profiles obtained by this spline based algorithm reproduce the general shape of the TCAD electric field profiles to great detail. Even profiles corresponding to high fluences and therefore not fully depleted sensors are of reasonable shape. The main limitation observed is coming from the density of available TCAD simulations in the vicinity of the fluence and bias voltage of interest. The more TCAD samples are available, the better the algorithm performs in reproducing the electric field profile.

The spline based approach is capable to cope with discontinuities in between the electric field parameters. Nevertheless, the splines lack of the ability to extrapolate, so that this approach is only valid if a sufficient range of TCAD samples are available. The interpolation algorithm is integrated in the simulation framework ATHENA [157]

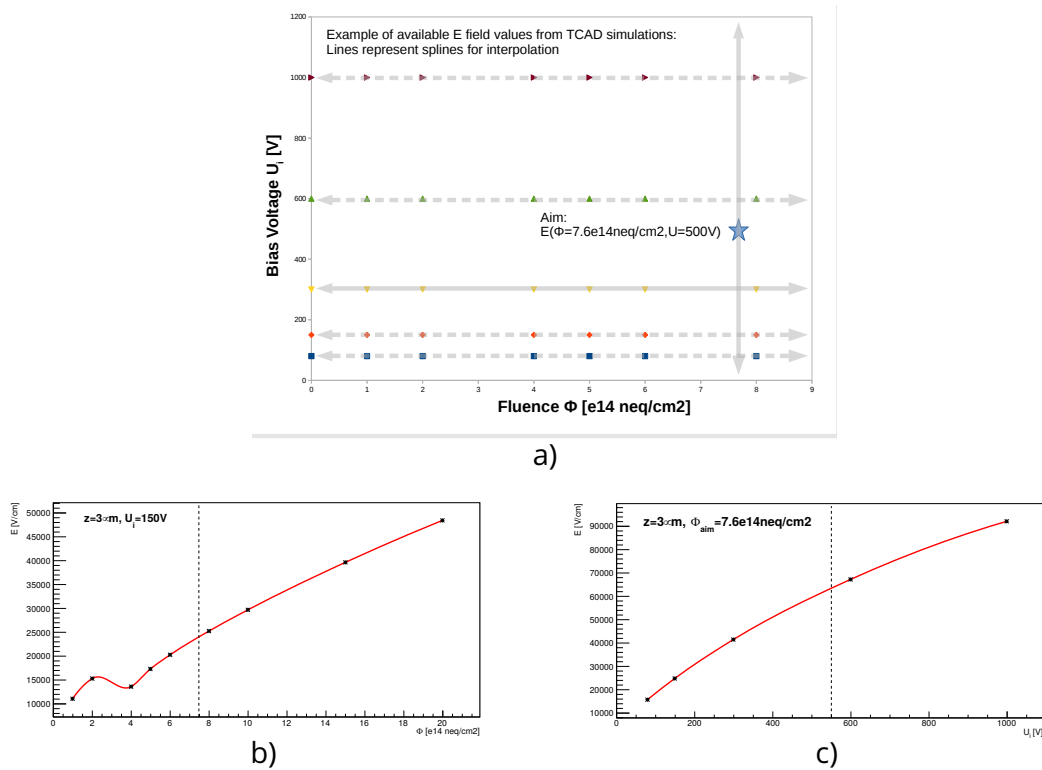


Figure A.2: (a) represents the procedure for the spline based approach to estimate the electric field at $\Phi = 7.6 \cdot 10^{14} \frac{\text{neq}}{\text{cm}^2}$, $U = 500\text{V}$ and $z = 3\mu\text{m}$. The colored dots represent electric field values available from TCAD simulations for a fixed depth of $z = 3\mu\text{m}$. The horizontal grey lines represent the first step, i.e. the interpolation while keeping the bias voltage fixed. The vertical line corresponds to the second step interpolating over the bias voltages while keeping the fluence fixed. (b) and (c) correspond to the grey solid lines in (a). The first plot shows the interpolation of the TCAD electric field values (*) with a spline (red line) for a fixed bias voltage $U_i = 150\text{V}$. The second plot presents the second interpolation step, i.e. interpolating the values obtained from the first interpolation step while keeping the fluence constant (here $\Phi = 7.6 \cdot 10^{14} \text{neq}/\text{cm}^2$).

and successfully validated with a closure test. The quality of the interpolation is estimated by removing one TCAD sample from the list of all available TCAD samples ($E(U_{\text{closure}}, \Phi_{\text{closure}})$). Then the algorithm is used to produce the E field profile according to the sample which was removed based on the remaining samples. The resulting E field profile is compared to the original TCAD simulation. The χ^2 value and Kolmogorov-Smirnov test serve as a measure for the compatibility. The closure is further investigated for the time-over-threshold (ToT), which is based on the interpolated (or original TCAD) E field profile. The ToT is the central value from which the track properties are derived.

B.

Additional material for the measurement of m_W and Γ_W

B.1 Validation of the reanalysis process

Channel	Legacy analysis		Reanalysis		Difference		Profile Likelihood	
	Central	Stat. Unc.	Central	Stat. Unc.	Central	Stat. Unc.	Central	Stat. Unc.
$m_T \eta < 0.8 W^+$	80371.3	29.2	80371.2	29.1	0.1	1.7	80373.1	24
$m_T \eta < 0.8 W^-$	80375.5	30.6	80376.2	30.7	0.1	1.7	80373.8	25.8
$m_T 0.8 < \eta < 1.4 W^+$	80354.1	32.1	80356.5	31.9	0.2	1.6	80354.2	26.9
$m_T 0.8 < \eta < 1.4 W^-$	80417.5	36.4	80415.2	36.3	0.1	1.3	80415.1	30
$m_T 1.4 < \eta < 2.0 W^+$	80426.3	30.2	80426.1	30.2	0	2.2	80422.7	25.6
$m_T 1.4 < \eta < 2.0 W^-$	80379.4	35.6	80377.9	35.6	0	2.2	80382.9	29.4
$m_T 2.0 < \eta < 2.4 W^+$	80334.6	40.9	80334.8	40.8	0.1	7.3	80331.7	33.8
$m_T 2.0 < \eta < 2.4 W^-$	80334.2	52.4	80335.6	52.2	0.2	7.6	80321.6	43.3
$p_T^\mu \eta < 0.8 W^+$	80327.7	22.1	80329.7	22.2	0.1	2.4	80326.7	18.3
$p_T^\mu \eta < 0.8 W^-$	80427.8	23.3	80431.9	23.4	0.1	1.9	80427.1	19.4
$p_T^\mu 0.8 < \eta < 1.4 W^+$	80357.3	25.1	80360	25.3	0.2	2	80355.6	21
$p_T^\mu 0.8 < \eta < 1.4 W^-$	80395.6	27.9	80396	28	0.1	1.6	80397.2	23.4
$p_T^\mu 1.4 < \eta < 2.0 W^+$	80446.9	23.9	80449.4	23.9	0	2.9	80448.1	20
$p_T^\mu 1.4 < \eta < 2.0 W^-$	80380.6	28.1	80385.8	28.1	0	2.3	80380.3	23
$p_T^\mu 2.0 < \eta < 2.4 W^+$	80334.1	34.5	80325.1	34.7	0.2	10.9	80338.4	28.5
$p_T^\mu 2.0 < \eta < 2.4 W^-$	80315.2	45.5	80316.4	45.8	0.3	10	80307.3	37.5

Table B.1: The table presents the numerical values for Fig. 5.13. The column Legacy list the central fit results taken from [72] including the statistical uncertainties. The Column Reanalysis presents the fit results based on the resurrected samples and χ^2 fit. The third column lists the corresponding difference to display the closure, while the last column presents the results of the PLH fit using only statistical uncertainties.

B.2 Ranking plots for the measurement of m_W using a profile likelihood ratio fit

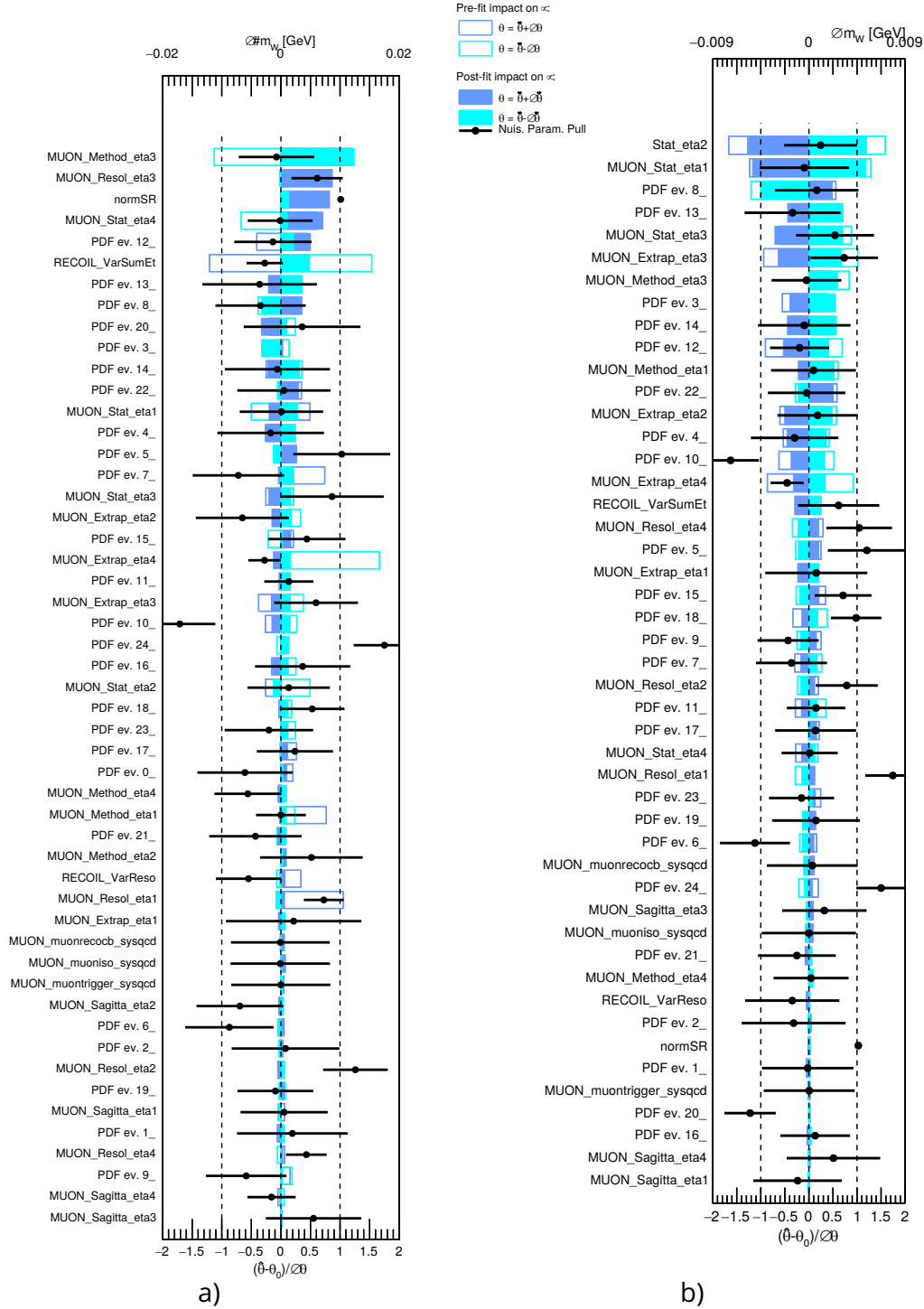


Figure B.1: Ranking plot for profiling the combination fit of (a) m_T and (b) p_T^μ with all available NPs. The blue blocks indicate the pre- and post-fit impact and belong to the top x-axis. The black dots indicate the pulls and refer to the bottom axis. Only the ten most impacting NPs are listed.

B.3 First results for Γ_W using a profile likelihood ratio fit in m_T

The following results present the measurement of Γ_W using template fits for distributions of m_T . The fit range corresponds to the interval of $60 \text{ GeV} < m_T < 100 \text{ GeV}$, which is originally optimized for the measurement of m_W . The fit results are not robust, if the interval bounds are varied in steps of 5 GeV. The investigated fit range needs to be extended above $m_T > m_W$ to become more sensitive to Γ_W and produce stable results. The results for the different channels in muon pseudorapidity and charge are presented in Fig. B.2, but they lack an error estimation for the low sensitivity of the fit. They serve only for a preliminary demonstration, that the fit framework is able to handle the setup. They can also provide a first glance on the estimate of the systematic uncertainties included in this measurement. The combination of all channels for distributions in m_T is:

$$\begin{aligned} \Gamma_W(m_T) &= 2122.6(+blinding) \pm 30.4 \text{ MeV} \\ &= 2122.6(+blinding) \pm 23.3(\text{syst.}) \pm 19.5(\text{stat.}) \text{ MeV} \end{aligned} \quad (\text{B.1})$$

The relation between the measurement in distributions of m_T and p_T^μ is comparable to the measurement of m_W , i.e. the precision of p_T^μ is better. In case of measuring m_W , this is due to the dominating uncertainty on the hadronic recoil. In the case of measuring Γ_W no definite answer is possible due to the missing convergence for the distributions of m_T . The individual impacts of the NP categories are listed in Tab. B.2 for completeness.

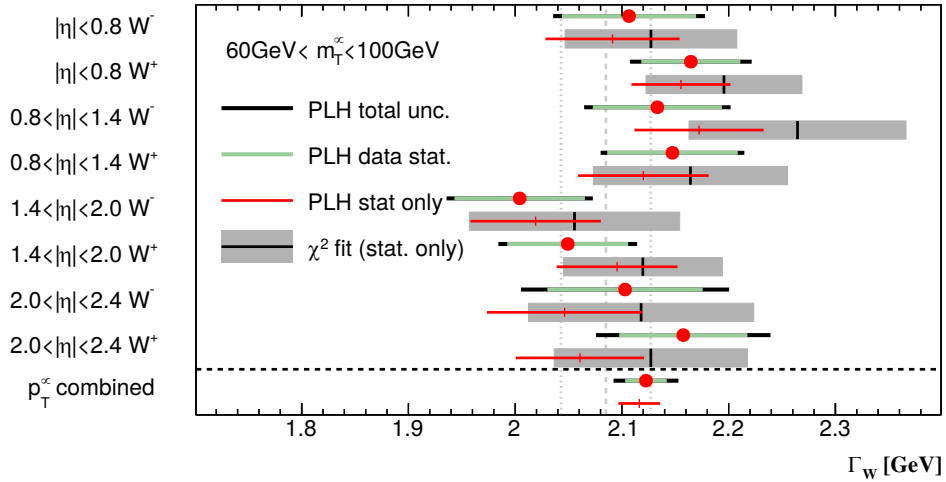


Figure B.2: Results of the Γ_W fit using a PLH approach on the distributions in m_T . The fits presented with read bars profiled all uncertainties listed in Tab. 5.5, but exclude the Monte-Carlo statistical uncertainties. The red bars illustrate the results for profiling only data statistical uncertainties. The vertical dotted lines reference the world average and its uncertainties ($\Gamma_W^{\text{global}} = 2.085 \pm 0.042 \text{ GeV}$). But all results for the central values of Γ_W are still blinded, so the world average serves only for the comparison of the uncertainties.

Channel m_T -fit	Full Profiling [MeV]			Muon NPs		Recoil NPs		Bkg. NPs		PDF NPs		Stat. Unc.
	Central Value	Full Unc.	Shift	Shift	Impact	Shift	Impact	Shift	Impact	Shift	Impact	Impact
$W^- \eta < 0.8$	2106.4	71.1	15.2	-9.1	9.2	4.7	13.1	2	16.8	2.3	10.5	62.8
$W^+ \eta < 0.8$	2164.5	57	9.1	-5.2	21.6	9.2	32.4	-2.3	11.5	10.3	17.6	46.4
$W^- 0.8 < \eta < 1.4$	2134.1	68.6	-38.2	1	12.4	-20.7	43.9	0.6	13.5	2.2	58.4	60.5
$W^+ 0.8 < \eta < 1.4$	2144.7	67.3	24.6	12.7	9.7	18.9	16.4	-0.5	17.6	7.6	9.1	61.1
$W^- 1.4 < \eta < 2.0$	2003.3	68.5	-15.9	-12.2	13	-18.8	20.5	-0.3	28	0.6	18.6	61.1
$W^+ 1.4 < \eta < 2.0$	2049	65	-46.5	-19.3	5.5	-41.1	13.3	-2	12.5	-26.2	25	56.6
$W^- 2.0 < \eta < 2.4$	2102.6	97.5	56.3	24.8	38.6	7.1	24.2	10.6	53	62	19.4	72.7
$W^+ 2.0 < \eta < 2.4$	2155.5	81.7	94.7	48.6	39.1	1.3	12	16.8	43.3	74.7	14	60.1
m_T^W combined	2122.6	30.4	6.2	41.3	9.6	-12.3	4.6	-4.9	17.8	6.3	13.4	19.5

Table B.2: Summary of the impact of different NP categories on the profile likelihood fit of Γ_W applied to distributions of m_T . Shift states the difference between profiling the NP category and profiling only (data) statistical uncertainties. Impact lists the uncertainty on Γ_W related to this category of NP. The first category, Full Profiling, profiled all available uncertainties and presents the blinded results for the central values of Γ_W .

C.

Additional material for the measurement of the UE activity

C.1 Convention for the visualization of the UE activity

This thesis visualizes the observables, which are sensitive to the UE, using the conventional representation. The results are either presented as mean values like in Sec. 6.7.1 or differential distributions as displayed in Sec. 6.7.2. Especially the latter representation is not intuitive with the threefold denominator on the y-axis. The following section breaks down the convention based on the example of $dN_{ev}/d(N_{ch}/\delta\eta\delta\phi)$. The mean valued will be explained at the very end.

The quantity on the y-axis is calculated per event and per UE region, which is the combination of a region in the transverse plane, a range in p_T^Z and an optional distinction in transverse thrust. The example picks the trans-min region, with $10 < p_T^Z < 20$ GeV inclusive in thrust. The event selection fills the fundamental histogram, which counts the number of events N_{ev} as a function of the tracks or charged particles N_{ch} . It is displayed in Fig. C.1(a).

The event activity will be compared in different transverse regions, which are of different size in the ϕ -plane. The observables are therefore transformed into a density, e.g. number of charged particles per volume $\delta\eta\delta\phi$. This is realized by scaling the bins of the x-axis by $1/(\delta\eta\delta\phi)$, as presented in Fig. C.1(b). Only the bin edges are scaled, while the bin contents remain untouched in this step.

The bin sizes of the x-axis are varying and the bin contents are therefore scaled by the bin width to make them compatible. This yields the total number of events per charged particle density on the y-axis, namely: $\frac{dN_{ev}}{d(N_{ch})/(\delta\eta\delta\phi)}$. The corresponding scaling is illustrated in Fig. C.1(c).

The final transformation is the normalization to unity, i.e. scaling by the total number of events $1/N_{ev}$, because the analysis focuses on a shape comparison and drops the information on the total event count. It is therefore presented by $dN_{ev}/d(N_{ch}/\delta\eta\delta\phi)$ as function of $d(N_{ch}/(\delta\eta\delta\phi))$, which visualizes a probability to measure a event with a certain particle density in this UE region.

The presentation of the mean values is much simpler, as it involves no subsequent scaling steps. The differential distribution, like the one of the previous example, is condensed to single number as function of p_T^Z . The presented value is the mean value of the x-axis, which demonstrates the UE observable. Of course, other properties, such as the standard deviation or the skewness, could be displayed as well, but these are redundant, if the differential distributions are available. The presentation of the mean observables as function of p_T^Z as it is presented in Sec. 6.7.1 is constructed by joining the mean values of the corresponding differential distributions.

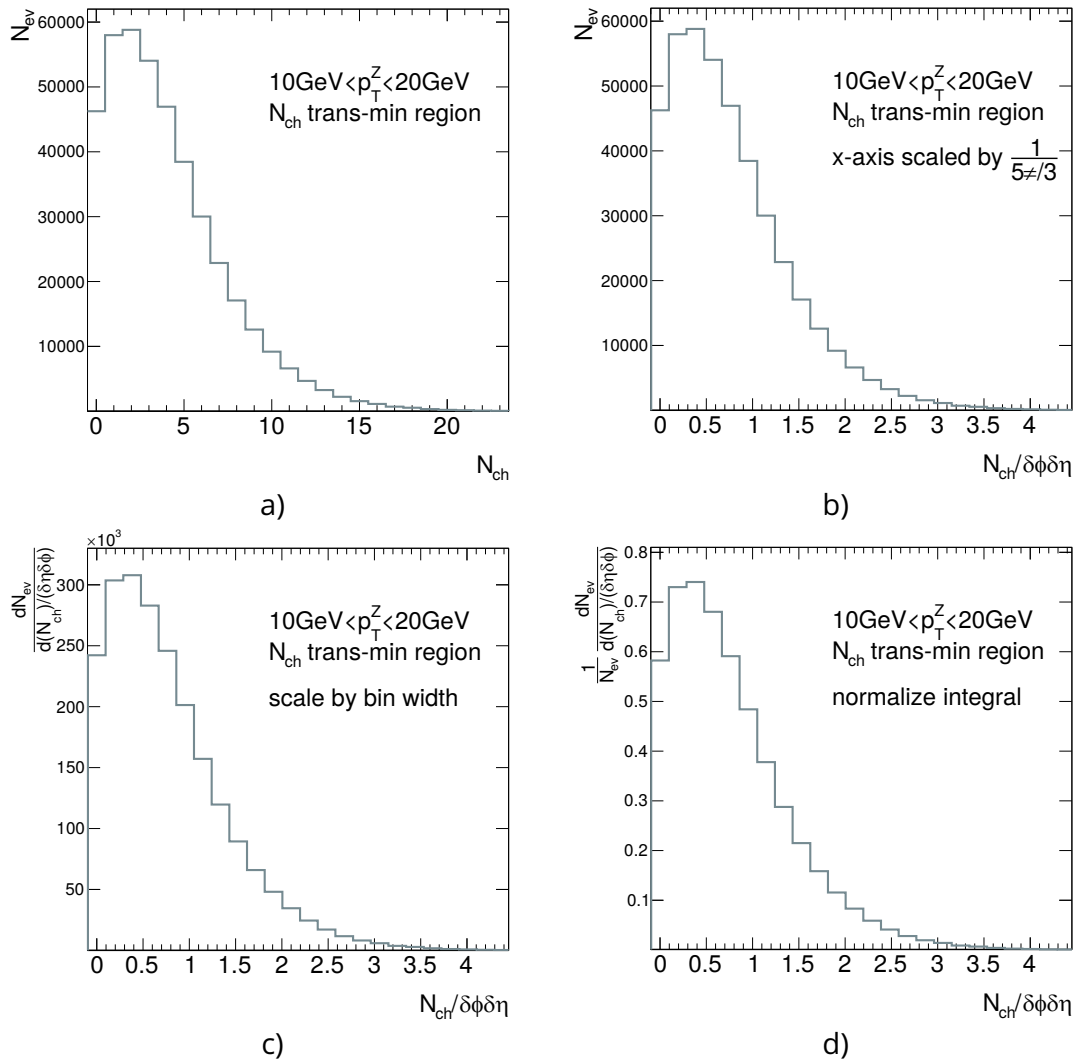


Figure C.1: Example for the different scaling steps to create the UE observable representation. It starts with the basic observable without any scaling in (a). The observable is transformed into a density by scaling the x-axis (b). The contents are scaled to the bin width (c). And finally the full integral is normalized (d).

C.2 The HBOM algorithm

C.2.1 Validation of the HBOM Algorithm

The HBOM algorithm is validated using samples coming from Monte-Carlo simulations. For the validation it is crucial that two compatible samples are available: one sample including a simulation of pile-up and the identical sample without the simulation of pile-up. Details about these two samples produced with POWHEG+PYTHIA8 are listed in Sec. 6.3.3. There are two different ways to validate the HBOM algorithm, the forward and the backward closure.

Forward Closure

The forward closure is used as a validation on an early stage of the HBOM algorithm, because it includes the pile-up library but not the back-projection. It is implemented as following: The regular selection procedure for the observables is performed on the MC sample, which was produced without any pile-up. The selection is then polluted

once with artificial pile-up as described in Sec. 6.5.2. The artificial pile-up follows the pile-up library created from the default Monte-Carlo sample which includes the simulation of pile-up. The distributions coming from the zero pile-up sample including the HBOM pile-up should then equal the distributions of default Monte-Carlo pile-up sample. Indeed, the forward closure is generally within deviations of less than 5%. Some exemplary plots are shown in figure Fig. C.2. Since the creation of artificial pile-up is a statistical process some minor deviations are expected.

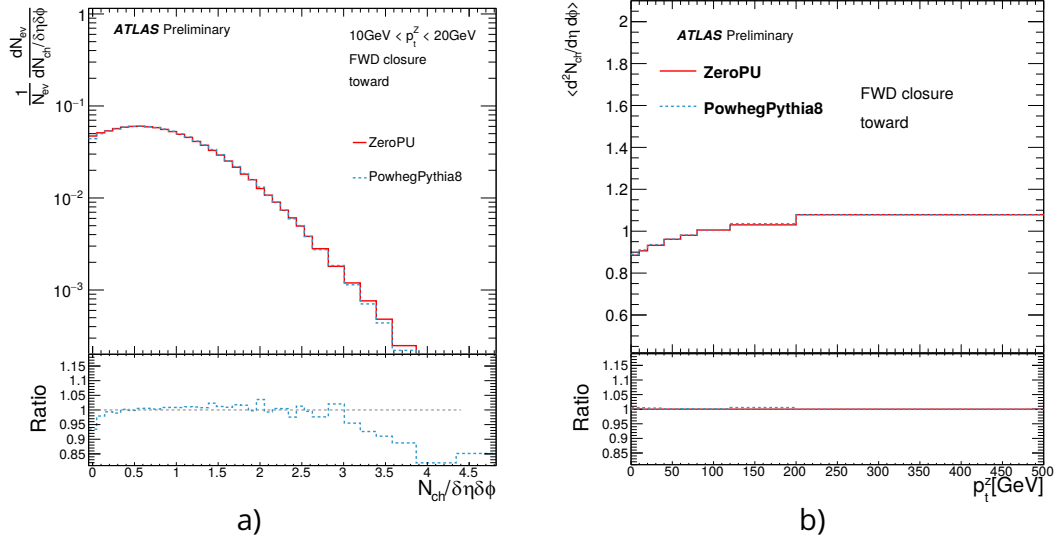


Figure C.2: Example plots for forward closure for (a) the differential distributions and (b) the mean observables: ZeroPU refers to the distribution constructed on detector level from the MC sample originally produced without pile-up contamination, but in this case one iteration of the artificial pile-up is added. POWHEG+PYTHIA8 refers to the according detector level distribution of the (originally pile-up contaminated) baseline MC sample.

Backward Closure

The backward closure follows the same idea as the forward closure, i.e. a validation based on the zero pile-up Monte-Carlo sample. But in this case, the full HBOM correction is applied. In detail, the observables selected from the default MC sample are polluted several times with artificial pile-up. Then the bin-wise back-projection is applied to obtain distributions corrected for pile-up. The resulting distributions are designated to agree with the ones constructed from the zero pile-up sample. In order to reduce further detector effects, the pile-up corrected default MC sample is unfolded with the zero pile-up sample. The comparison of the zero pile-up distributions on particle level and the pile-up corrected and unfolded ones represents the backward closure.

In general, one yields an adequate closure: Within areas of sufficient statistics, the pile-up corrected distributions deviate roughly from 2% to 5% from the ones corresponding to the zero pile-up sample, e.g. see Fig. C.3. Just the bins of lowest activity ($dN_{ev}/d(N_{ch}/d\eta d\phi) < 2$, $dN_{ev}/d(\Sigma p_T/d\eta d\phi) < 2$ GeV) yield a larger deviation larger than 10%. This is consistent with the results of the data-driven pile-up estimate and previous studies related to the HBOM algorithm.

These bins of lowest or rather zero activity suffer from the non-smooth behaviour due the cut on p_T . In general, when pile-up is added to an observable, the events migrate naturally to higher activities. In all other regions this loss is balanced by

events coming from regions of lower activity. But the regions of lowest activity just lose events due to pile-up without any compensation.

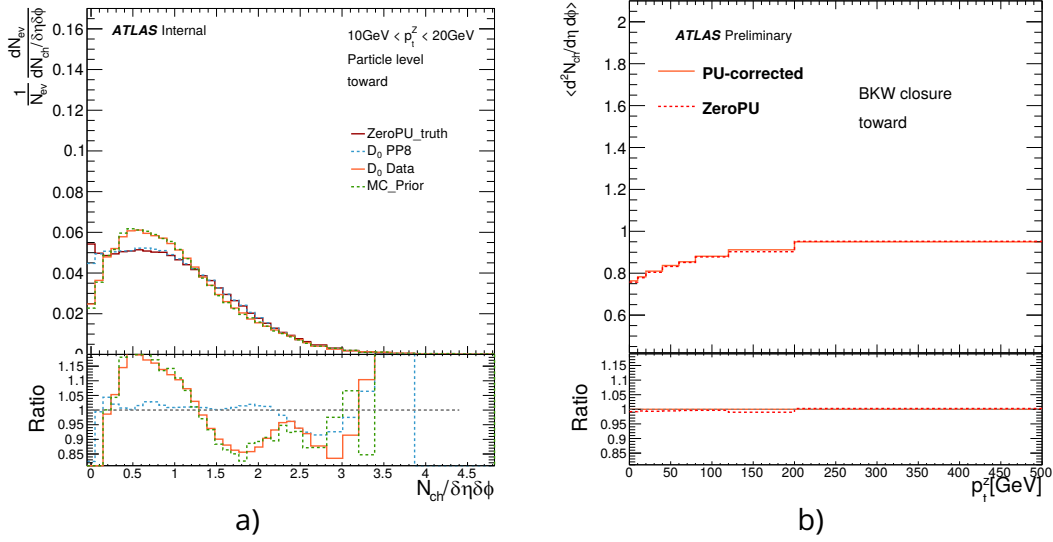


Figure C.3: Exemplary distributions presenting the backward closure of the HBOM algorithm for (a) the differential distributions and (b) the mean observables. ZeroPU refers to the distribution constructed on detector level from the Monte-Carlo sample originally produced without pile-up contamination.

Uncertainty on the choice of the pile-up library

The choice of pile-up vertices added to the pile-up library affects the overall performance of the HBOM algorithm. The final selection is found to be best reproducing the forward and backward closure and aims to select a representative sample of pile-up activity. The pile-up vertices which are included in the pile-up library are required to be separated by at least 60 mm from any other collision vertex. But it has to be acknowledged the smaller the vertex spacing is chosen the more likely it is to record activity from more than one pile-up vertex if these overlap. In contrast, a higher value for the vertex spacing decreases the number of selected pile-up vertices and shrinks the statistical significance. Furthermore, more pile-up vertices from the periphery of the collision point are recorded. These show a reduced activity hence result in a reduced activity correction for the HBOM algorithm. In order to estimate the systematic uncertainty related to the choice of the vertex spacing the HBOM algorithm is additionally performed with a vertex spacing of 40 mm and 80 mm. The resulting differences to the default algorithm are combined and assigned as uncertainty to the HBOM results.

D.

Curriculum vitae

Lennart Adam

Curriculum vitae

✉ lennart.adam@cern.ch

Ausbildung

- 01/2021 - **Promotionsstudium**, *Schwerpunkt Teilchenphysik, statistische Datenanalyse*,
01/2017 Johannes Gutenberg-Universität, Mainz.
 - Dissertation innerhalb internationaler Großkollaboration (ATLAS, CERN)
 - Big Data Anwendungen, Programmierung und Detektorsimulation
 - Projektleitung "Muon Data Quality"
 - Mehrjährige Lehrtätigkeit
- 10/2017 - **DAAD Reisestipendium: Gastwissenschaftler**,
05/2017 SLAC National Accelerator Laboratory, Stanford University, CA.
- 10/2016 - **Master of Science, Physik**, Johannes Gutenberg-Universität, Mainz.
10/2014 Gesamtnote: *sehr gut (1,2)* - Nebenfach Informatik
 - Arbeitsschwerpunkt: Statistische Datenanalyse in der Hochenergiephysik
 - Vorlesungsauswahl zur Teilchen- und Medizinphysik
 - Deutschlandstipendium
- 10/2014 - **Bachelor of Science Physik**, Johannes Gutenberg-Universität, Mainz.
04/2011 Gesamtnote: *sehr gut (1,5)* - Nebenfach Informatik
 - Bachelorarbeitstitel: Untersuchung der geometrischen Schnittstelle zwischen Szintillator und Photomultiplier
 - Arbeitsschwerpunkt: Optimierung der Szintillatorform bezüglich Lichtausbeute mit Hilfe einer Raytracing Software
- 06/2014 - **ERASMUS Auslandsstipendium**,
09/2013 University of Birmingham, UK.
Enrolled: Session 2013/14 - UG Physics
- 03/2011 - **Zivildienst**, Rettungsdienst Rheinhessen-Nahe gGmbH.
05/2010 Ausbildung zum Rettungssanitäter
- 03/2010 **Allgemeine Hochschulreife**, Gymnasium am Römerkastell, Alzey.
Durchschnittsnote: *sehr gut (1,0)*
 - Auszeichnung "Bestes Abitur"

Praxiserfahrung

- 11/2016 - **Betriebspraktikum d-fine GmbH**, Unternehmensberatung, Risk & Finance.
10/2016
- o Projekt zur Vorbereitung einer IRBA-Prüfung
 - o Überprüfung interner Modelle zu Kreditentscheidungen (Fehler- und Abweichungsanalysen)

Auszeichnungen (Auswahl)

- 2017 DAAD Reisestipendium für Doktoranden
2015,2016 Deutschlandstipendium
2010 Preis für das beste Abitur

EDV-Kenntnisse

Programmiersprachen C++, Python, JAVA

Sprachkenntnisse

Deutsch Muttersprache
Englisch verhandlungssicher
Französisch Grundkenntnisse

Soziales Engagement

Vermittler Netzwerk Teilchenwelt.

Betreuung (internationale) Teilchenphysik-Masterclass für Schülerinnen und Schüler

Ehrenamtliche Tätigkeit in der Jugendarbeit,

Evangelische Jugend in Hessen und Nassau Dekanat Alzey.

Projekte für Kinder und junge Erwachsene, z.B. Leitung von Sommerfreizeiten

TuS Saulheim - Basketball,

Jugendtrainer, Spieler, Schiedsrichter.

Mainz, 05. Februar 2021 ,



